Physical properties of a thermally cracked andesite and fluid-injection induced rupture at laboratory scale

Zhi Li

PSL
UNIVERSITÉ PARIS

THÈSE DE DOCTORAT
DE L'UNIVERSITÉ PSL

Préparée à [Ecole Normale Superieure]

Physical properties of a thermally cracked andesite and fluid-injection induced rupture at laboratory scale

Soutenue par
ZHI LI
Le 22 March 2019

Ecole doctorale n°560
Sciences de la terre et de l'environnement et physique de l'univers, Paris

Spécialité
Géophysique

ENS
ÉCOLE NORMALE SUPÉRIEURE

Composition du jury : Frédéric Pellet

Siavash Ghabezloo CR, Ecole des Ponts Paristech		*Rapporteur*
Sergio, Vinciguerra Professor, Vinciguerra		*Rapporteur*
Frédéric Pellet Professor, Ecole des mines de Paris		*Examinateur*
Sophie, Violette MCF, Ecole Normale Supérieure		*Examinateur*
DianSen, Yang Professor, Chinese Academy of science		*Examinateur*
Aurelien, Nicolas Ingénieur de recherche,	Eurofins	invité
Jérome, Fortin CR-CNRS, Ecole Normale Supérieure		*Directeur de thèse*
Yves, Guéguen Professor, Ecole Normale Supérieure		Co-*Directeur de thèse*

Abstract

The physical properties and mechanical behavior of andesite are of interest in the context of geothermal reservoir, CO2 sequestration and for several natural processes.

The effects of thermal crack damage on the physical properties and rupture processes of andesite were firstly investigated under triaxial deformation at room temperature. Thermal cracking was induced by slowly heating and cooling samples. The effects of heat treatment temperatures ranging between 500°C and 1100°C on the P-wave velocities and on the microstructure were investigated. Then, the mechanical properties of andesite samples heat-treated at 930°C were investigated under triaxial stress at room temperature using constant strain rate tests and confining pressures ranging between 0 and 30 MPa. Similar triaxial experiments were conducted on non-heat-treated samples. Our results show that 1) for heat treatments at temperatures below 500°C, no significant changes in the physical properties are observed; 2) for heat treatments in the temperature range of 500-1100°C, crack density increases; and 3) thermal cracking has no influence on the onset of dilatancy but increases the strength of the heat-treated samples. This last result is counterintuitive but seems to be linked with the presence of a small fraction of clay (3%) in the intact andesite. Indeed, for heat treatment above 500°C, some clay melting is observed and contributes to sealing the longest cracks.

Secondly, we present samples artificially altered at different levels after heat-treatment. We report results of hydrostatic and triaxial loading experiments performed on untreated, unaltered heat-treated and artificially altered samples, all originally from the exact same lithology. The evolution of the mineralogy with both the heat treatment and the artificial alteration was carefully tracked. Our results show that (1) Elastic moduli of altered andesite increases compared to heat treated andesite. (2) Peak stress of altered andesite decreases compared to

heat treated andesite. The weakening is stronger as alteration is higher. (3) Smectite is observed to precipitate in cracks in artificially altered samples. (4) A decrease of the friction coefficient in cracks due to the presence of smectite might explain the mechanical weakening of altered sample.

At last, a series of experiments were performed in order to investigate the effect of fluid pressure variation i) on the mechanical behavior of andesite samples and ii) on acoustic emissions activities. Fluid pressure was raised in a sample submitted to a stress state close to the onset of dilatancy (which corresponds to the critical stress state in field), and the injection was continued until the rupture (the axial stress and confining pressure were kept constant). Fault propagation was monitored by the acoustic emissions. Our results show that (1) A time dependent behavior was observed in the fluid-injection induced rupture experiment. (2) Spatial heterogeneity of crack development was observed before rupture. More cracks were developed at downstream while upstream remains silent and the rupture began from the downstream end. (3) Critical crack length is inverted and estimated to be in the range of 129μm~223μm. Finally, in a second series of experiments, we employed optic fiber sensors to measure the fluid pressure at different positions in the sample during the pressure diffusion process. Axial strain and radial strain were recorded during the whole process. After experiment, CT-scan was performed on the sample after fluid injection experiment to observe the fractures network. Our results show that (1) permeability heterogeneity is observed during the fluid-injection experiment. (2) Subcritical crack growth influences the permeability and pore pressure spatial temporal distribution.

Keywords: Thermal crack; fluid injection; physical property; mechanical property

Résumé

Comprendre et connaitre les propriétés physiques et le comportement mécanique de l'andésite est important pour des applications industrielles comme la géothermie ou le stockage de CO2 mais aussi pour comprendre différents processus naturels.

Dans une première partie, on étudie l'effet des fissures d'origine thermique sur les propriétés physiques et les processus de rupture de l'andésite. Le comportement mécanique est étudié via des tests triaxiaux à taux de déformation constante et à température ambiante. La fissuration thermique a été induite en chauffant et en refroidissant lentement des échantillons. Les effets de des traitements thermiques pour des amplitudes comprises entre 500 ° C et 1100 ° C sur la vitesse des ondes P et sur la microstructure ont été étudiés. Ensuite, les propriétés mécaniques des échantillons d'andésite traités à 930 ° C ont été étudiées sous contrainte triaxiale et à température ambiante en utilisant des tests à taux de déformation constant et à des pressions de confinement comprises entre 0 et 30 MPa. Nos résultats montrent que 1) pour les traitements thermiques inférieures à 500 ° C, aucun changement significatif des propriétés physiques n'est observé; 2) pour les traitements thermiques dans la plage de températures de 500-1100 ° C, la densité de fissures augmente; et 3) la fissuration thermique n'a pas d'influence sur l'apparition de la dilatance mais augmente la résistance mécanique des échantillons traités thermiquement. La présence d'une petite fraction d'argile (3%) dans l'andésite intacte peut expliquer ce résultat. En effet, pour les traitements thermiques supérieurs à 500°C, une partie de l'argile fond et colmate les fissures les plus longues.

Deuxièmement, nous avons effectué des recherches sur les effets de l'altération sur le comportement mécanique et sur la minéralogie. Nos résultats montrent que (1) les modules élastiques de l'andésite altéré au laboratoire augmentent en fonction du degré d'altération. (2) Par contre on observe une diminution de la contrainte maximale admissible par la roche.

L'affaiblissement est d'autant plus fort que l'altération est élevée. (3) On observe que la smectite précipite dans les fissures pour les échantillons altérés au laboratoire. (4) Une diminution du coefficient de frottement dans les fissures en raison de la présence de smectite pourrait expliquer l'affaiblissement mécanique de l'échantillon altéré.

Enfin, une série d'expériences a été réalisée afin d'étudier l'effet de la variation de la pression du fluide i) sur le comportement mécanique des échantillons d'andésite et ii) sur les activités d'émissions acoustiques.. La pression du fluide a été augmentée dans un échantillon soumis à un état de contrainte proche du seuil de dilatance (ce qui correspond à l'état de contrainte critique sur le terrain), et l'injection a été poursuivie jusqu'à la rupture (la contrainte axiale et la pression de confinement ont été maintenues constantes). Nos résultats montrent qu'un (1) comportement dépendant du temps est observé dans l'expérience de rupture induite par injection de fluide. (2) Une hétérogénéité spatiale du développement de la fissuration est observée avant la rupture. (3) La longueur critiques des fissures est inversée et estimée entre 129 μm et 223 μm. Dans une seconde série d'expérience, nous avons utilisé des capteurs à fibres optiques pour mesurer la pression du fluide à différentes positions de l'échantillon pendant le processus de diffusion de la pression. Après l'expérience, un scanner a été réalisé sur l'échantillon pour observer le réseau de fractures. Nos résultats montrent qu'(1) une hétérogénéité spatiale de la perméabilité est observée au cours de l'expérience d'injection de fluide. (2) La croissance de la fissure sous-critique influence la perméabilité et la distribution spatio-temporelle de la pression interstitielle.

Mots Clés : Fissure thermique; injection de fluide; propriété physique; propriété mécanique

Acknowledgement

I am deeply grateful for my three supervisors: Dr. Jerome Fortin, Prof. Yves Gueguen, Prof. Chunhe Yang for their support and patience at all times. Jerome is always happy, optimistic, and with a lot of ideas, he gives me a lot of confidence and valuable advices in the long uncertain research process. It has been a pleasure to work with him. He helped and supported me so much both in academic and in life that I can finish my PhD smoothly in a foreign country. Yves is like a big detective, he provided visions and philosophical concepts in research, and he is always patient with young researchers. He is a real gentleman and I learned more from him except from research. I give my deep gratitude to Prof. Yang who supported me a lot and gave me opportunity to go abroad.

I would like to thank Dr. Aurelien Nicolas who has given me a lot of help on doing experiments and processing data, and discussion during my PhD. Many thanks to Lea levy, Sissmann, Cedric Bailly, Jan Borgomano, Chao Sun for their help on microstructure analysis and model construction. I wish to thank Dr. G. Blocher, C.Kluge, and Dr. H. Milsch in GFZ for their kind help in the experiments and discussion. I express my gratitude to Prof. Chopin, Dr. Thomas Ferrand and Dr. Sarah Incel for their discussion with me, and Damien Deldicque for his help in SEM and XRD analysis. My special thanks to Fredric Pellet and Dominique Bruel for attending my committee during my PhD.

I would like to thank Mr. Stephane Richard and Mr. Phillipe who helped me a lot in the administrative procedures and visa issues. I'm sincerely grateful for Laure Meynadier, Helene Lyon-caen, and Clement Narteau who have given me a lot of encouragement and teach me to balance between life and academic.

I would like to thank many people who have supported me a lot during most difficult times and depressed times. I am grateful for senior researchers in the lab who have helped me a lot,

Alexandre Schubnel, Christophe Vigny, Harsha Bhat, Manuel Pubellier, Matthias Delescluse, Matio, Romain Jolivet, Luce Fleitout and Cedric Bulois. Deep thanks to my dear friends, Paoline Prevost, Eva Kanari, Sungping Chang, Hanjn Yin, Gianina,Valentin Tschannen, Lavynia Tunini, Chao Sun, Louise Cordrie, Samanul Chapman, Yao Liang, JB, JD, Manon Dlsn, Kurama Okubo, DJ, Juan Martin de Blas, Thomas Chartier, Arefeh Mrf, Amin Kahrizi, Menglan He, Wei Wei, Ying Zhu, Yue Jiang, Alice Wang, Zhikai Wang, Zhiyi Qiu, Zhi Geng, Jialan Wang, Yijing Wu, Jingjing Lu, Guanglei Cui, Qi He, Jingtian Xu, Xiaoping Yuan, Lei Wang, Zhenkun Hou, Shuai Heng, Yunlong Wei, Mingjie Gao. My special thanks to my landlady Madame Chiffert and Mr. Olivier Chiffert, and Sichelle Chiffert.

This research is sponsored by China Scholarship Council and GEOTREF France, my special thanks to them and to ENS and ISRM, Chinese Academy of Sciences, which gave me the chance to do PhD.

I wish to greatly appreciate the help and support of Dr. Fei Zheng for being with me at best times and worst times.

At last to my beloved family, I am deeply grateful that my younger brother and my parents are always beside me no matter what happens.

Table of Contents

Introduction

Research background

In geothermal systems, the physical properties and mechanical behavior of andesite are of interest for the understanding of several natural processes and for engineering design. Natural processes include ground deformation due to magma rising below volcanoes (Jaupart,1998; Costa et al. 2009; Heap et al.2014), eruption activity and formation of dikes (Gudmundsson, 2006,2011; Browning et al. 2015), or fault activity (Rowland and Sibson, 2001). Industrial contexts are geothermal reservoir engineering (Siratovich et al., 2014) and CO_2 sequestration (Trias et al. 2017).

As geothermal fields usually locate in tectonically active areas, crustal stresses are near to critical stress. In addition, tectonically active areas mean "fractured rock reservoir". Several authors have investigated the effect of micro-fracture on mechanical strength, porosity, elastic wave velocities, and elastic moduli of rocks (Wu et al. 2000; Guéguen and Schubnel 2003; Smith et al. 2009, Pereira and Arson 2013; Faoro et al. 2013; Pola et al. 2014; Heap et al. 2014). The link between micro-fractures and permeability (Nara et al. 2011) has been also investigated, with micro-fractures proving to enhance permeability.

Fluid pressure variation has influence on different aspects of geothermal systems. Fluid pressure variation can be associated with seismicity observed in natural processes such as seasonality of ground water recharge (Hainzl *et al.* 2006; Saar and Manga, 2003), water level fluctuations in water reservoirs (Chander, 1997; Talwani 1997), petroleum exploration (Davies et al., 2013; Rutqvist et al., 2013) , geothermal field (Baisch et al., 2010; Deichmann and Giardini, 2009; Brodsky et al., 2000; Prejean et al. ,2004; Giardini 2009), wastewater disposal (Horton, 2012; Kim, 2013; Keranen et al., 2014; Frohlich et al, 2014), or CO_2 sequestration

(Zoback and Gorelick, 2012; Mazzoldi et al., 2012; Cappa and Rutqvist, 2011). Note that fluid pressure variation could trigger earthquake (Yamashita 1998; El Hariri et al., 2010) in long space and time scales (Hummel and Müller, 2009; Shapiro *et al*., 1997, 2003;).

Scientific problems addressed in this thesis

1. Thermal effect on mechanical properties of geothermal/volcano systems

In volcanic areas, where hot fluids circulate, temperature is a parameter that should be taken into account when investigating mechanical behavior. Temperature variations can induce intragranular cracks and intergranular cracks or even melting of the rock (Friedman et al. 1979, Wong 1989), leading to large changes in the microstructure.

Many studies have been performed on the role of thermal effects on the mechanical behavior of igneous rocks, including intrusive and extrusive rocks (Heap et al. 2014, 2015, 2016; Vinciguerra et al. 2005; Fortin et al.2011; Stanchits et al. 2006; Meredith et al. 2005; Wang et al. 2013). Note that, in contrast to intrusive rocks, extrusive rocks have a different microstructure resulting from fast cooling: a fine groundmass and phenocrysts.

Increasing temperature can modify fluid transport properties (Vinciguerra et al. 2005, Nasseri 2009, Faoro, 2013, Darot, 1992, Geraud 1994), elastic wave velocities (Walsh 1965, Nasseri 2007), and mechanical properties (Faulkner et al. 2003, Wang et al. 2013). Thermal cracking has been shown to weaken different rocks, including granite (Homand-Etienne and Houpert, 1989; Chaki et al. 2008), gabbro (Keshavarz et al. 2010), calcarenite (Brotóns et al. 2013), and carbonate (Sengun et al. 2014;). P-wave velocity changes due to thermal cracking are expected. Such changes are important for seismic tomography inversion of volcano systems and may be useful for investigating magma chamber activity and dike eruption. Because induced seismicity is possible during geothermal exploration, it is important to systematically determine the geo-mechanical behavior and to characterize its evolution resulting from thermal stresses.

2. Hydro-thermal effect of alteration on the properties of geothermal system

In volcanic geothermal systems [e.g. Reyes, 1990; Meunier, 2005], subduction zones [e.g. Hyndman et al., 1997;Passellegue et al., 2014] and some major faults [e.g. Chester et al., 2013; Yamaguchi et al., 2011], where hot fluid circulates in the host rock [e.g. Adelinet et al., 2011], the presence of alteration minerals is susceptible to significantly modify the mechanical behaviour of rock, as compared to pure and healthy rock. Alteration results in microstructural changes [e.g. Heap et al., 2014; Siratovich et al., 2014], which in turn modifies the physical (porosity, open crack density, velocity of propagation of elastic waves, permeability) and mechanical properties of the rock [Pola et al., 2012; Meller and Kohl, 2014; Frolova et al., 2014; Wyering et al., 2014]. Small changes in microstructural parameters, such as porosity [e.g. Vajdova et al., 2004], pore size [e.g. Zhu et al., 2010], crack density and mean length [e.g. Keshavarz et al., 2010], significantly affect the mechanical behavior of volcanic rocks.

3. Fluid pressure variation induced seismicity

The potential risk of inducing seismicity by diffusion of elevated pore pressure is known for decades (Ellsworth 2013). In addition, since 2008, fluid injection used for shale gas production appears to be the trigger of earthquakes in the mid-continent of United States which has become seismically active (Frohlich et al. 2012,2013,2014; Horton 2012; Keranen et al. 2013; Ellsworth 2013; Justinic et al. 2013; McGarr et al. 2014,2017). As an example, a magnitude of 4.8 earthquake occurred near Timpson, Texas, a region where the seismicity was rare prior to this earthquake event (Frohlich et al, 2014). In Europe, the Deep Heat Mining Project in Basel, Switzerland used fluid injection to increase the permeability of the reservoir (fractures in granite) and caused a event with a magnitude of 3.4 (Giardini 2009, McGarr et al. 2014,2017). Geothermal systems are commonly hosted in altered and fractured rock reservoir (Wu et al. 2000; Pereira and Arson 2013; Faoro et al. 2013; Pola et al. 2014; Heap et al. 2014). As

geothermal fields usually locate in tectonically active areas, crustal stresses are near to critical stress (Ellsworth 2013; Zoback et al. 1997), thus fluid injection in these reservoirs could induce seismicity.

At field scale, time lag effect of induced seismicity due to fluid injection has been observed. Shirazi et al. (2016) used INSAR data to estimate pore pressure and volumetric strain. As soon as the injection is stopped, the authors show that the pore pressure has an inhomogeneous spatial distribution: the areas with high permeability are associated with the largest pore pressure decay, whereas the areas associated with low permeability are associated with high fluid pressure.

4. Spatiotemporal pattern of seismicity related to hydraulic diffusion

Different hydraulic diffusivity and seismic criticality (mechanical property) of rocks lead to different spatiotemporal pattern of seismicity activity (Do Nascimento et al., 2005; Shapiro *et al*., 1997, 2003). Hummel and Müller, (2009) included the permeability change in the model of the fluid pressure diffusion. Yilmaz et al. (1994) investigated pore fluid pressure distribution in fractured and compliant rocks by simulating 1-D pore-fluid pressure profiles with a pressure-dependent permeability. Pore pressure propagation is highly influenced by the permeability heterogeneity of the crust (Lee et al., 1998; Clifton et al., 2003; Do Nascimento et al., 2005;). It's important to account for geologic complexity when estimate the transmission of pore poressre while investigate seismicity (Simpson and Narasimhan, 1992; Lee et al., 1998; Do Nascimento et al., 2005).

Geodynamic setting: La Guadeloupe

The Guadeloupe archipelago (Islands of Basse-Terre, Grande-Terre, les Saintes, Marie-Galante and Désirade) lies in the northern part of The Lesser Antilles Arc which spreads over 850 km

long between the island of Saba in the North and Grenade in the South. Most of the magmatic products found in the island arc are related to the subduction of the North American Plate below the Carribean plate since at least 40 Ma (Bouysse et al., 1990). Being part of the northern part of the arc, Guadeloupe displays both the recent active volcanic arc and the old extinct arc (Bouchot et al., 2011).

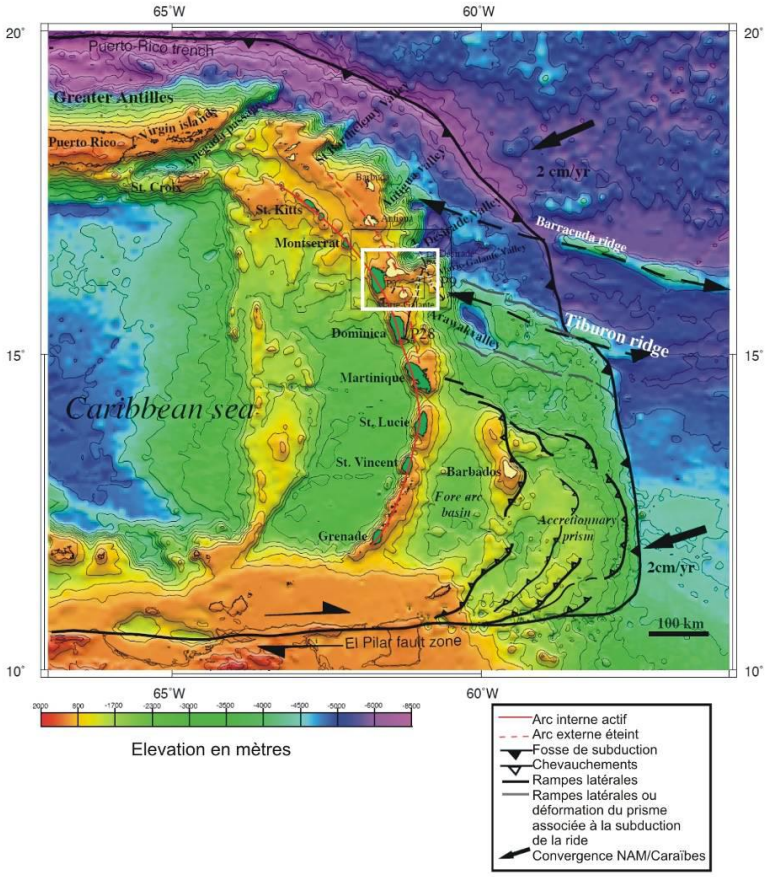

Figure 1. Geodynamical map of the Lesser Antilles showing the old extinct arc (dotted redline) and the recent active are (plain red line). Guadeloupe Archipelago is showed within the white box. (Feuillet et al., 2001; Bouchot et al., 2011).

Regional seismicity affecting Guadeloupe is related to the oblique subduction of the North American plate below the Caribbean plate as well as to movements along normal faults and has been responsible for damaging shallow-depth M ≥5 earthquakes in 1851 and 1897. Although this is still subject to some debate, Feuillet et al. (2001; 2002) suggested that these

earthquakes are related to the volcanic complex (La Soufrière) formed at the western tip of a prominent E-W oriented graben, whose normal faults extend from the prominent Marie-Galante rift system.

Basse Terre is a volcanically active island located in the central part of the Lesser Antilles volcanic arc. The northern part of the island is made of the NNW–SSE-elongated Northern Chain. This part of the island is the oldest one (Davidson et al., 1983; Bouysse et al.,1990; Samper 2008;), and is formed from high eruption rates and/or low viscosity magma that propagated within extensional structures parallel to the volcanic front. The morphology of this island has been substantially modified by erosion. The southern part of the island (the youngest part) is made of volcanoes with more circular bases, formed by lower eruption rates and/or more viscous magma that exploited the NW–SE-striking Montserrat-Bouillante fault zone.

Sample material

GEOTREF (A project aimed at improving understanding fractured geothermal reservoirs) is planning a new geothermal project in the area from which the samples were taken. For the purpose of our research we selected six andesitic blocks from different areas in La Guadeloupe. Two blocks are from the quarry of Deshaio are used for the research in this thesis.

Figure 2. Quarry of Deshaio

Note that the temperature of 930°C that we will used in the next chapter, for the amplitude of the heat-treatment, corresponds to the temperature of the second magma chamber in La Soufière (Villemant et al. 2014), which is where the dikes begin (Villemant 2014).

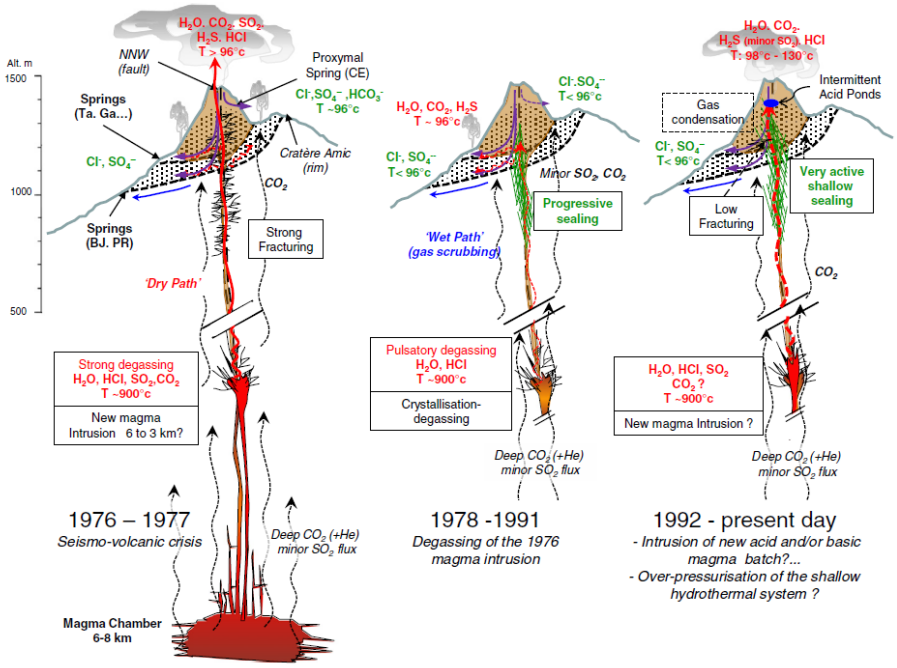

Figure 3. Villemant et al., 2014

Research Outline

Chapter I gives a review on methodology and theoretical background. The experimental set-up of the tri-axial cell, strain measurements, hardware and software of acoustic survey system are described. Theoretical models employed in this research are reviewed, including effective medium theory, fracture mechanics, wing crack model, subcritical crack growth, nonlinear diffusion equation.

Chapter II presents the effects of thermal crack damage on the physical and mechanical properties of an andesite. Thermal cracking was induced by slowly heating and cooling samples. The effect of the temperature of the heat-treatment ranging between 500 °C and 1100°c was investigated on the P-wave velocities and on the microstructure. Then, the

mechanical properties of andesite samples treated to 930 °C were investigated under triaxial stress at room temperature, using constant strain rate tests and at confining pressure ranging between 0 and 30 MPa. Similar triaxial experiments were conducted on non-heat-treated samples. This chapter has led to a paper under press in Rock Mechanics and Rock Engineering.

Chapter III presents samples artificially altered at different levels after heat-treatment. We report results of hydrostatic and triaxial loading experiments performed on untreated, unaltered heat-treated and artificially altered samples, all originally from the exact same lithology. During these experiments, evolution of P- and S wave velocities were measured to track the evolution of cracking. Acoustic emissions were also recorded and localized. The evolution of the mineralogy with both the heat treatment and the artificial alteration was also carefully tracked, with a special focus on smectite and other clay minerals precipitation. This chapter has led to a paper that will be submitted soon.

Chapter IV shows a series of experiments done in order to investigate the effect of fluid pressure variation i) on the mechanical behavior of andesite samples and ii) on acoustic emissions activities. In particular fluid pressure was raised in a sample submitted to a stress state close to the onset of dilatant point (corresponds to the critical stress state in field), and the injection was continued until the rupture (the axial stress and confining pressure were kept constant). Fault propagation were monitored by the acoustic emissions, and their locations were compared with the fractures observed in the sample after the experiment. The mechanism of delayed time before the main rupture is discussed.

Chapter V investigates the fluid pressure diffusion in rock submitted to stresses closed to the criticality. We performed a fluid injection experiment on the thermally treated andesite and monitored pore pressure in a space-time domain. Firstly, hydrostatic loading is applied on the sample to 40MPa, then differential loading was increased until stress state reaches beginning of dilatancy. Then, fluid pressure was increased at one boundary of the sample and kept at a

constant value (35 MPa), until the whole sample reaches failure. We employed optic fiber sensors to measure the fluid pressure at different positions of the sample during the pressure diffusion process, axial strain and radial strain are recorded during the whole process. After experiment, CT-scan was performed on the sample after fluid injection experiment to observe the fractures formed after experiment.

Chapter I Methodology and Theoretical Background

1.1 Methodology

1.1.1 Experiment apparatus

Experiments were performed using a tri-axial cell installed in Laboratoire de Geologie at Ecole Normale Supérieure in Paris. This apparatus allows for hydrostatic and deviatoric loading, pore pressure and temperature to be applied independently on a cylindrical specimen (diameter 40 mm length 80 mm). The hydrostatic and deviatoric stresses are servo-controlled with an accuracy of 0.01 MPa, and oil is used to confine the whole sample within the cell. The pore pressure, the confining pressure and the deviatoric stress can be increased respectively up to 100, 100 and 700 MPa. Temperature can be increased up to 200°C but only room temperature data are reported in this work. Room temperature is controlled with an accuracy of ±0.5 C around 20°C. A schematic diagram of the setup is presented in Figure 1.1.

1.1.2 Strain and ultrasonic measurements

Eight Tokkyosokki TML FCB strain gages (four axial and four circumferential) were glued directly onto the surface sample (Figure 1.2). Each strain gauge is used in conjunction with a one-fourth Wheatstone bridge. The strain measurement is recorded every two seconds. An external gap sensor using Foucault currents is employed to measure the total displacement of the piston during axial loading and provides, once corrected, a global axial strain measurement.

The measured axial strain ε_1 and radial strain ε_3 allow for the estimation of the volumetric strain $\varepsilon_v = \varepsilon_1 + 2\varepsilon_3$ and the calculation of the static Young modulus. Axial strain ε_1 and radial strain ε_3 are calculated using the average values of the four vertically oriented strain gauges

and the four horizontally oriented strain gauges, respectively. The compressive stresses and strains are denoted as positive.

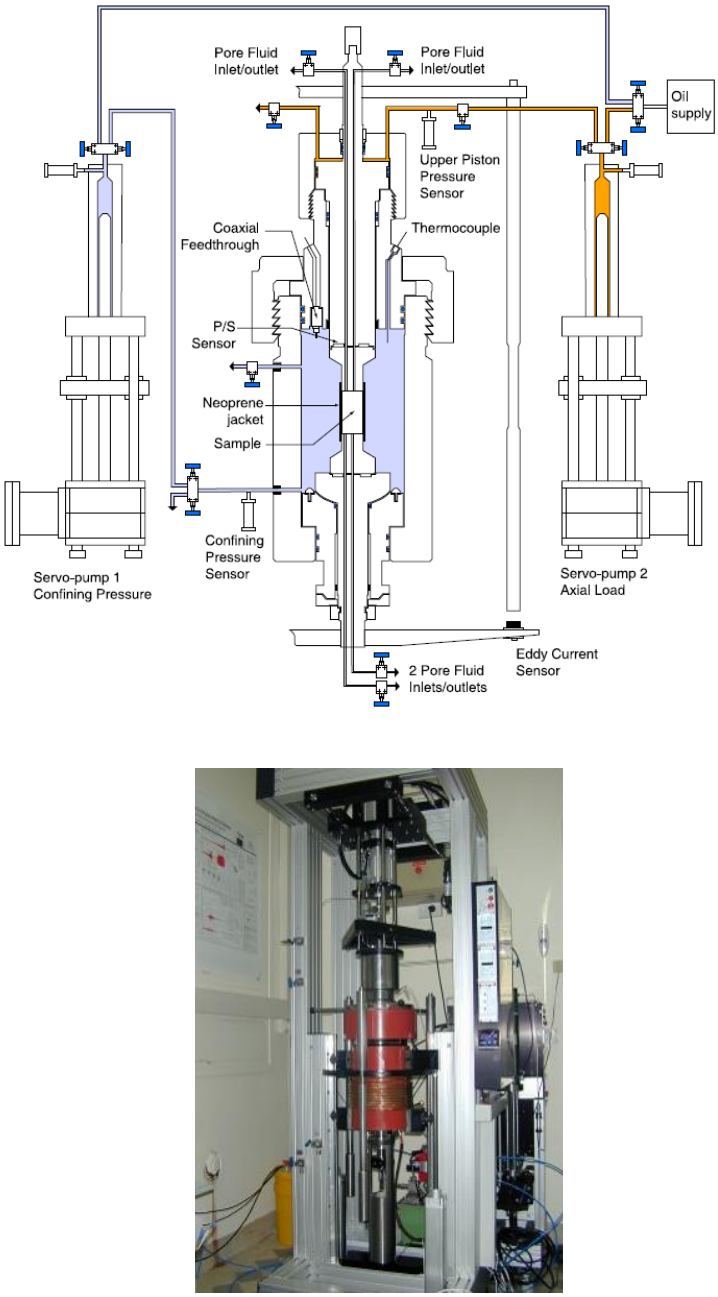

Figure 1.1 Tri-axial cell installed at École Normale Supérieure (Ougier-simonin et al., 2010, 2011)

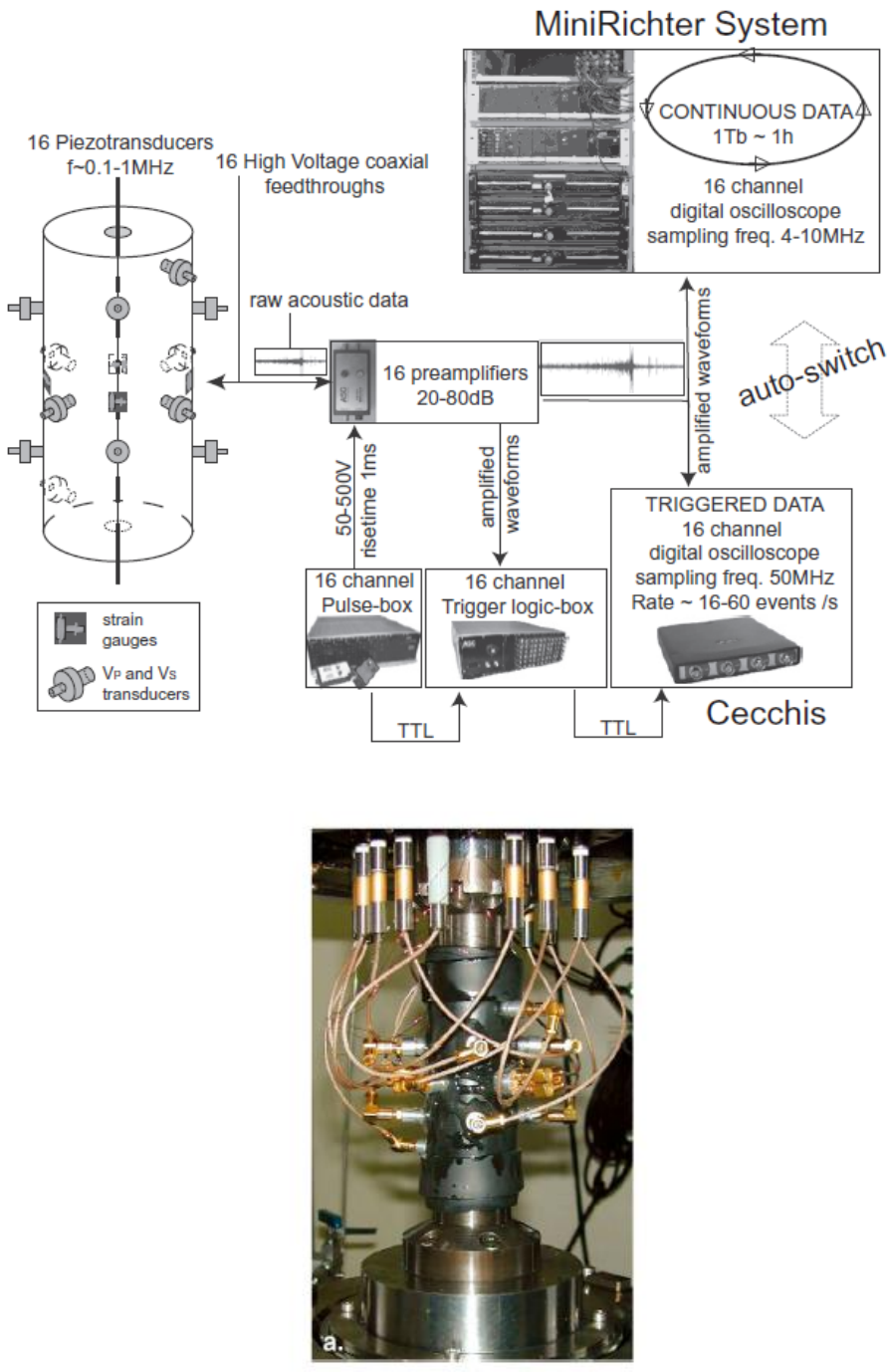

Figure 1.2 Ultrasonic sensors and strain gauges glued on samples (from Ougier-Simonin et al., 2010, 2011)

1.1.3 The brittle regime: definition of the stress states C' and D'

The failure of brittle rocks has been investigated by many researchers (Brace et al.,1966; Bieniawski, 1967; Byerlee and Brace, 1968; Scholz, 1968; Wawersik and Fairhurst, 1970; Martin and Chandler, 1994; Wong et al., 1997). They have shown that the stress-strain curves for a brittle material can be divided into five regions (Figure 1.3) (Martin and Chandler 1994).

The initial region of the stress-strain curve represents the closure of existing micro-cracks in the sample and may or may not be present, depending on the initial crack density and crack geometry (Martin and Chandler 1994).

Once the existing cracks are closed, the strain-stress curve is usually linear (Figure 1.3 - region II). The elastic properties could be determined from this part of stress-strain curves.

The onset of dilation marks the beginning of region III. Brace et al. (1966) found that dilation begins at a stress level of about 40-60% of the peak strength. This stress level is referred to as the crack initiation stress σ_c (C' point). These cracks are stable cracks since an increase in load is required to cause further cracking. Crack initiation is difficult to identify from the laboratory stress-strain curves, particularly if the sample already contains a high density of micro-cracks (Martin and Chandler, 1994; Wong et al., 1997; Brace et al., 1966; Scholz, 1968; Baud et al. 2000; Richart et al. 1928). The crack initiation stress is best determined using a plot of volumetric strain versus axial strain (figure 1.3). First the elastic volumetric strains are calculated using the elastic constants (E, υ) from the linear portion of stress-strain curves in region II by

$$\frac{\Delta V}{V_{elastic}} = \frac{1-2\upsilon}{E}(\sigma_1 - \sigma_3) ,$$

Then, the elastic volume strain are subtracted from the total measured volumetric strains to determine the volumetric strains caused by axial cracking (figure 1.3). σ_c (C' Point) is the axial stress at which dilation just begins on the crack-volume plot (figure 1.3).

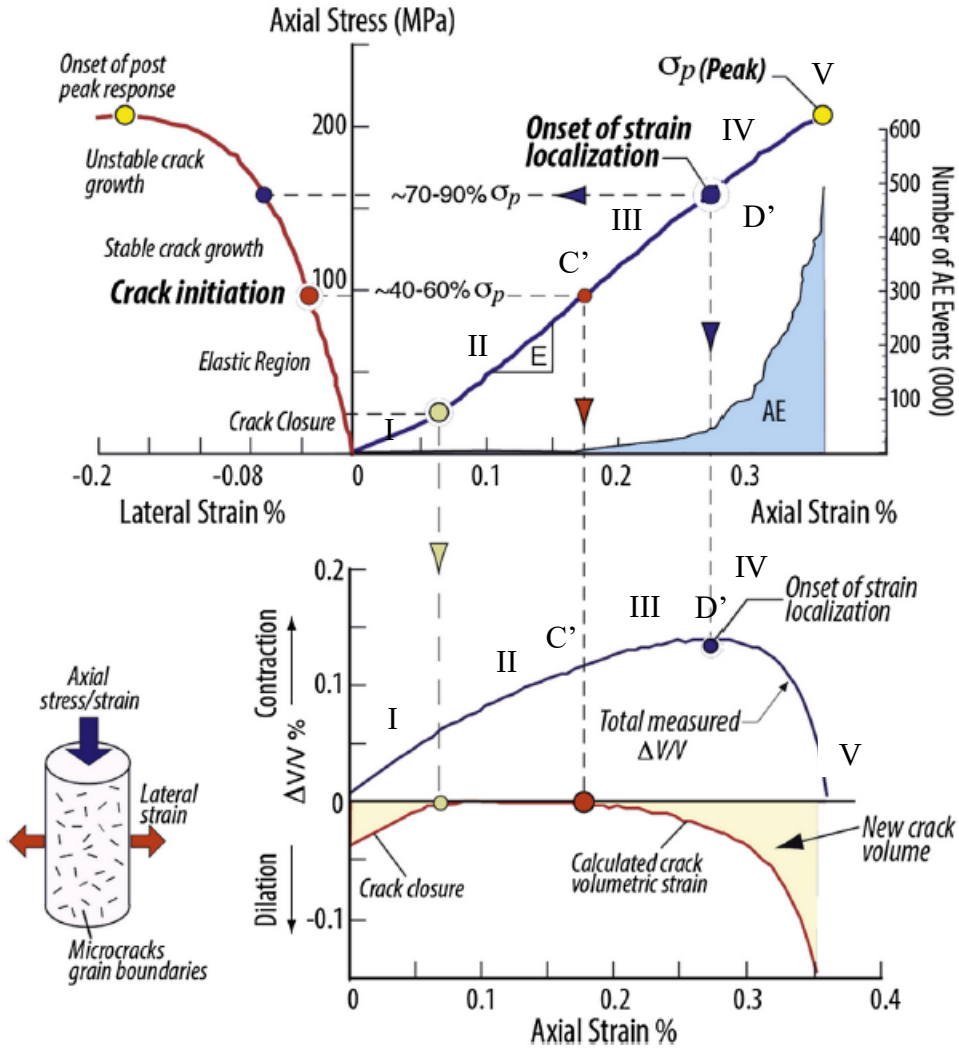

Figure 1.3 Martin and Christiansson, 2009

The axial stress level σ_D (D' point) where the total volumetric strain reverse from compaction to dilatancy marks the beginning of region IV (Figure 1.3) and represents the onset of unstable crack growth, as defined by Bienawaski (1967). It generally occurs at axial stress level between 70%-90% of the short-term peak strength. It is at this stress level that the axial strain departs from linearity (figure 1.3). Hallbauer et al. (1973) pointed out that this region is characterized by the most significant structural changes to the sample, with the density of micro-cracks increasing drastically.

The peak strength of the material marks the beginning of post-peak behavior, Region V, and is universally used to establish the failure strength envelope.

1.1.4 Ultrasonic measurements and acoustic emission (AE)

14 ultrasonic piezoelectric transducers (PZTS, Figure 1.2) were glued directly on the surface of the sample. The classical ultrasonic pulse transmission technique is used for velocity measurements between an emitting and a receiving transducer (Ougier-Simonin et al., 2011). It consists of measuring the travel time of an elastic pulse through the rock sample for a known travelling path length, the latter having been corrected for strains during the mechanical loading. In active velocity survey mode, a pulse of 250 V with a rise time of 1s is generated and transmitted successively to each transducer using a pulsing switchbox (ASC Ltd.). Each piezo-ceramic converts this electrical pulse into a mechanical vibration that propagates into the medium. In contrast, each receiving piezoceramic converts the received mechanical waveform into an electrical signal that is amplified at 40 dB using 16 pre-amplifiers. Signals are recorded using a 16 channels Cecchi digital oscilloscope. Waveforms are sampled at 50MHz. Velocity surveys were then fully automatically processed using cross-correlation techniques so that the error bar on wave velocity measurements are less than 2%. This specific arrangement permitted measurements of P-wave anisotropy in our sample throughout experiment. These measurements allowed us to identify the dynamic elastic constants.

In passive mode, each transducer signal is recorded using the ASC Ltd. MiniRichter streaming system, which stores continuous ultrasonic waveform data onto a 1 TB hard disk (Figure 1.2). Such continuous recording techniques at this sampling rate have been pioneered in the last years thanks to fast development of computing systems. Signals were amplified at 40 dB as well. In these conditions, the average electric noise was kept below 15 mV on most channels. Discrete acoustic emissions data was obtained after the experiment using a simple triggering technique (300 mV minimum amplitude, 5 ls time window) on waveform records. Time of the first arrivals were automatically picked on each channel for each AE event, using a simple RMS auto-picking technique (50 back windows, 35 front windows, 25 picking threshold).

Hypocenter locations were then determined using a collapsing grid search algorithm, assuming an evolutive medium (from isotropy to transverse isotropy using the velocity model calculated in active mode). The AE hypocenter location was used to determine the origin of the acoustic signals generated during fracturing.

1.1.5 Velocity model for AE hypocenter location

(1) Homogeneous isotropic

The homogeneous isotropic velocity structure assumes a half space containing the source and all receivers. Each raypath is calculated as a vector between the source and the receiver. Velocity is homogeneous throughout the volume and isotropic. For isotropic symmetry, the relation of elastic velocity and shear modulus G, bulk modulus K

$$V_P = (\frac{K + 4G/3}{\rho})^{0.5} \tag{1-1}$$

$$V_s = (\frac{G}{\rho})^{0.5} \tag{1-2}$$

(2) Transversely isotropic

For transversely isotropic velocity structure, velocity varies depending on the ray orientation through the volume with respect to an axis of symmetry. The direction of axis is defined by a vector a, in a North-East-Down Cartesian coordinate system using an azimuth from North and plunge down from the horizontal (Insite Appendices). The velocity (P or S wave velocity) is given by equation 3-1 where γ is the angle between the raypath l and the axis of symmetry a. V_I is the velocity parallel to the axis of symmetry, $V\_$ is the velocity perpendicular to the axis of symmetry. Their relationship is (Insite Appendices)

$$V\_ = \alpha V_I \tag{1-3}$$

Where α is the anisotropy factor. The velocity V_r along the raypath l is (Insite Appendices)

$$V_r = \left(\frac{V_I + V_-}{2}\right) - \left(\frac{V_I - V_-}{2}\right)\cos(\pi - 2\gamma) \quad (1\text{-}4)$$

1.1.6 Acoustic location algorithm

(1) Geiger routine

The Geiger algorithm solves for the origin time t_0, and source location (x_0, y_0, z_0), such that the sum of the square of the residuals is a minimum, where the residual r is equal to the observed time t_0 minus the calculated time at (x_0, y_0, z_0). The algorithm iterates towards the correct location using the magnitudes of the time derivatives. The Geiger method is an inverse least square problem. The source location is defined by four parameters:

$$\theta = (t_0, x_0, y_0, z_0) \quad (1\text{-}5)$$

The time residual r_i is the difference between the calculated arrival times T_i and the observed arrival times t_i corrected to the time zero of the event t_0:

$$r_i = t_i - t_0 - T_i \quad (1\text{-}6)$$

The function relating the arrival times and the location is nonlinear since there is no single step approach to find the best event location. The standard technique is to linearize the problem:

$$\theta = \theta^* + \Delta\theta \quad (1\text{-}7)$$

Where θ^* is a source location estimate near the true location, and $\Delta\theta$ is a small perturbation. Using the first term in the Taylor series expansion, the observed times may be approximated by

$$t_i = t_0^* + \Delta t_0 + T_i(h^*) + \frac{\partial T_i}{\partial h}\Delta h \quad (1\text{-}8)$$

The time residuals at the location h^* are given by:

$$r_i(h^*) = \Delta t_0 + \frac{\delta T_i}{\delta h}\Delta h \tag{1-9}$$

$$r_i(h^*) = \frac{\delta T_i}{\delta \theta}\Delta \theta \tag{1-10}$$

In matrix notation, equations could be expressed as

$$r = A\Delta\theta \tag{1-11}$$

Following Gibowicz and Kijko [1994], the minimization of the sum of the squared time residuals can be given by

$$b = B\Delta\theta \tag{1-12}$$

The Geiger location is found by choosing a starting location, solving the matrix problem (Singular Value Decomposition) for $\Delta\theta$, and then iterating until this adjustment parameter reaches a user set minimum.

(2) Collapsing grid search routine

The algorithm searches a 3D space defined for the minimum misfit between the measured travel times picked for every receiver and the theoretical travel times from the ray path and given velocity model.

A collapsed grid has a size (volume limits) and cell dimension defined by the previous grid, the dimension of a collapsed cell is given by

$$Dc_{i+1} = \frac{Dc_i}{R} \tag{1-13}$$

Where Dc_i is the Cell Dimension of the previous grid and R is the Collapsing Ratio. The starting grid defined by the user can have any cuboid volume, whereas collapsed grids are always a cube with side length given by

$$Dg_{i+1} = NDc_{i+1} \tag{1-14}$$

Where N is the average number of axial cells in the starting grid. The number of axial cells along each direction (North, East, and Down) in the starting grid is D_x/D_{c_1} and must always be ≥ 10. The cubic collapsed grid is defined by the user-specified Collapsing Buffer (B_c), as shown in figure 1.4, where B_c is the half width of the new grid measured in number of uncollapsed cells. The new grid thus has a side length of $Dg_{i+1} = 2B_cD_{c_i}$ centered on a given position in the uncollapsed grid. Thus if $B_c = 1$ then the new collapsed grid has a volume consisting of 8 uncollapsed cells (2×2×2) centered on the given position. If $B_c = 2$ then the new collapsed grid consists of 64 uncollapsed cells (4×4×4) and so forth.

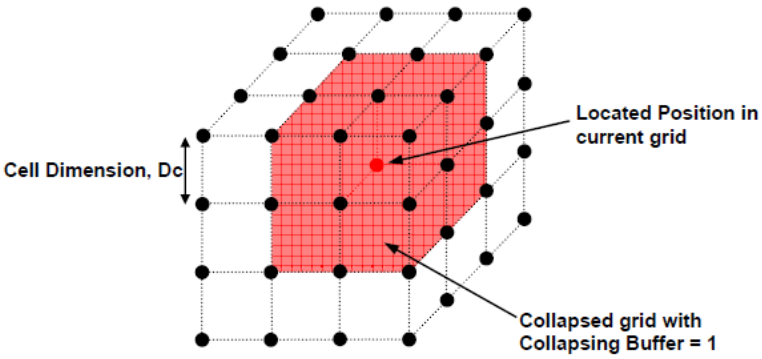

Figure 1.4 Definition of a collapsed grid volume (Insite Appendices)

The Collapsing Ratio, R defines the collapsed Cell Dimension with respect to the uncollapsed cell using first equation. The ratio is defined by

$$R = \frac{N}{2Bc} \tag{1-15}$$

Collapsing Ratio must have a value $R \geq 2.0$ to ensure effective and efficient collapsing. Collapsing grid search routine is applied for AE location in this thesis, it is more efficient as an initial coarse grid is first searched for minimum misfit position. The algorithms assume that the minimum value is close to the global minima and generate a smaller grid around this

position, then the minima is this collapsed grid will be found and another grid will be generated. The method continues until a specified resolution is obtained.

1.1.7 Permeability measurement

For our permeability measurement we used two methods: steady state and transient pulse. The steady state technique uses either a constant flow or a constant pore pressure gradient provided by two servo-controlled cylinders. Two symmetrical measures of permeability were performed by switching the flow direction in the sample. Permeability was then inferred using Darcy's law:

$$\frac{Q}{S} = -\frac{k\Delta P}{\eta L} \tag{1-16}$$

Where Q is the fluid flow (m^3s^{-1}), S the sample area (m^2), L the sample length (m), η the dynamic viscosity of the pore fluid (Pa·S), $\frac{\Delta P}{L}$ is the pore fluid pressure gradient (Pa). However, this method can only measure a permeability $k \geq 10^{-18}m^2$.

Transient pulse is used when permeability is lower ($< 10^{-18}m^2$). The fluid pressure on one side of the sample is instantaneously increased by ΔP. This allows us to measure the fluid diffusion through the sample. ΔP decays exponentially with time until equilibrium pressure is reached in the sample. Assuming the system geometry is known, the permeability could be computed from the time it takes for this transient pressure pulse to reach the equilibrium (Brace et al. 1968).

$$k = \alpha\eta\beta\frac{L}{S}\left(\frac{1}{\frac{1}{V_A}+\frac{1}{V_B}}\right) \tag{1-17}$$

With

$$P_A - P_f = \Delta P\frac{V_A}{V_A+V_B}e^{-\alpha t} \tag{1-18}$$

V_A and V_B(m^3) are the two cylinders reservoir volumes of the pore pressure pump respectively (including the volume of the connecting tubes). P_A is the pressure applied to V_A instaneously and P_f is the final equilibrium. β is the isothermal compressibility coefficient of the pore fluid (Pa^{-1}). α is the decay exponent. According to Bernabe (1987), this method can be partly modified by fixing the fluid pressure of the second cylinder constant. Thus the decay of the pressure transient occurs more rapidly and the equation above is simplified to equation.

$$k = \alpha\eta\beta\frac{L}{S}V_{pulse} \tag{1-19}$$

V_{pulse} is the total fluid volume. In this case, $V_{pulse} = V_A$ or $V_{pulse} = V_B$, depending on whether the pressure increment is applied on the cylinder V_A or V_B.

1.2 Theoretical background

1.2.1 Fracture mechanics

(1) Strain energy

All materials have defects originally, Griffith, (1921) proposed that the defects concentrate the stress, which lead with increasing stress to the final failure. Inglis, (1913) calculated the stress concentrations around elliptical holes, but the singularity of the solution at the crack tip leads to infinite stress. Griffith, (1921) employed an energy balance concept: the strain energy per unit volume in a thin plate of linear elastic material submitted to an axial load and contain a crack of radius c is

$$U_e = \frac{E\varepsilon^2}{2} = \frac{\pi\sigma^2 c^2}{E} \tag{1-20}$$

E is Young's modulus of the material, U_e is strain energy, σ is the axial stress, ε is the axial strain. The mechanical energy $U_m = -W + U_e$, where W is the energy provided by the loading system, one can show $W = 2U_e$, hence

$$U = -\frac{\sigma^2}{2E}\pi c^2 \tag{1-21}$$

The surface energy S associated with a crack of radius c is

$$S = 4\gamma c \tag{1-22}$$

γ is surface energy density. The total energy associated with the crack is then the sum of the (positive) energy absorbed to create the new surfaces, plus the (negative) mechanical strain energy released by allowing the regions near the crack flanks to become unloaded.

(2) Unstable crack growth

In the beginning, cracks grow only with stress increasing. As the cracks grow longer, the crack length reaches the critical crack length l_c, for which the crack growth is spontaneous and catastrophic.

The critical crack length l_c could be obtained by

$$\frac{\partial(S+U)}{\partial c} = 2\gamma - 2\frac{\sigma_f^2}{E}\pi c = 0 \tag{1-23}$$

$$\sigma_f = \sqrt{\frac{E\gamma}{\pi c}} \tag{1-24}$$

σ_f is the stress at failure. Irwin (1957) and Orawan (1949) suggested that in ductile materials the released strain energy is absorbed not by creating new surfaces but by energy dissipation due to plastic flow in the material near the crack tip. They suggested that the catastrophic fracture occurs when the strain energy is released at a rate sufficient to satisfy the needs of all these energy sinks. This critical strain energy release rate is denoted by the parameter G_c. The Griffith equation can be rewritten in the form:

$$\sigma_f = \sqrt{\frac{EG_c}{\pi a}} \tag{1-25}$$

The above model is valid for mode I, it has been extended to mode II and III.

(3) Stress Intensity factor

Three types of cracks termed mode I, II and III are defined. Mode I is under tensile stress with a normal-opening mode, while mode II and III are under shear stress with shear sliding modes. Westergaard et al. (1939) gave the stress distribution at crack tip with stress intensity factors.K_I, K_{II}, K_{III} are stress intensity factor for mode I, II, III fractures respectively. The critical stress intensity factor indicates the point where the material can withstand crack tip stresses up to a critical value.

In plane stress condition for mode I:

$$\sigma_f = \sqrt{\frac{EG_c}{2\pi c}} = \frac{K_{Ic}}{\sqrt{2\pi c}} \tag{1-26}$$

$$K_{Ic}^2 = EG_c \tag{1-27}$$

where G_c is the critical strain energy release rate, K_{IC} is fracture toughness, E is elastic modulus. In plane strain condition,

$$K_{IC}^2 = EG_c(1-\upsilon^2) \tag{1-28}$$

1.2.2 Effective Medium Theory

(1) Definition of crack density and aspect ratio

When defects sizes are smaller than the wavelength, effective medium theory is an appropriate method (Guéguen & Kachanov 2011).

The crack density ρ_c is defined as

$$\rho_c = \frac{1}{V}\sum\nolimits_1^N c_i^3 \tag{1-29}$$

Where c_i is the radius of the i-th crack, N is the number of cracks in the Representative Elementary Volume V.

The crack geometry is assumed to be penny-shaped (Bristow, 1960) and is indicated by average aspect ratio:

$$\zeta = w/c \tag{1-30}$$

Where, w is the half aperture of the crack, c is the radius of the crack.

(2) Crack closure pressure

Defects in geo-materials are mainly cracks and pores. Aspect ratio of pores is close to 1 while cracks have aspect ratio values < 0.01. Although cracks contribute little to porosity (<1%), cracks dominate the effective properties of rocks (Simmons and Brace, 1965; Walsh, 1965a, 1965b; Brace et al., 1968; Gueguen et al., 2011).The closure pressure P_{close} of cracks under hydrostatic pressure in dry condition is (Walsh, 1965a; Jaeger et al., 2007):

$$P_{close} = \frac{\pi \zeta E_0}{4(1-\upsilon_0^2)} \sim \zeta_0 E_0 \tag{1-31}$$

where, E_0 and υ_0 are the Young modulus (GPa) and Poisson's ratio of matrix, ζ_0 is the initial mean crack aspect ratio. Assuming for andesite $E_0 = 70$ GPa, for pores $\zeta_0 = 1$ and crack ζ_0=0.001, the closure pressure for pores are too high while for cracks the closure pressure is 70MPa approximately, showing a well know result that pores are stiffer to deform compared to cracks.

(3) Non-interactive assumption in effective medium theory

The simplest method of all Effective Medium Theory is the non-interactive theory (Kachanov 1994). In the non-interactive assumption, each crack is considered to be isolated and interactions between cracks are assumed to compensate each other on average. Non-interactive

effective medium theory was shown to be valid when cracks are distributed randomly and as long as crack density do not exceed 0.3 (Kachanov, 1994; Sayers and Kachanov, 1995; Schubnel and Gueguen, 2003; Fortin et al., 2006, 2007; Gueguen and Sarout, 2009). As a consequence, crack density and mean aspect ratio could be inverted directly from elastic wave velocities.

(4) Non-interactive assumption for randomly oriented cracks (including fluid effect)

In the framework of non-interaction approximation, the relation between elastic property parameters and micro-structure parameters could be linked by (Bristow, 1960; Walsh 1965; Fortin et al. 2006)

$$\frac{K_o}{K} = 1 + \rho_c \frac{h}{1 - 2v_o}\left(1 - \frac{v_o}{2}\right) \tag{1-32}$$

$$\frac{G_o}{G} = 1 + \rho_c \frac{h}{1 + v_o}\left(1 - \frac{v_o}{5}\right) \tag{1-33}$$

K and G are the effective bulk modulus and effective shear modulus respectively, which can be inverted from ultrasonic velocities. K_o and G_o are the bulk modulus and shear modulus of the crack-free matrix, v_o is the Poisson ratio of the matrix, h is a factor given by

$$h = \frac{16(1 - v_o^2)}{9\left(1 - \frac{v_o}{2}\right)} \tag{1-34}$$

Under saturated condition, the equations are:

$$\frac{K_0}{K_{sat}} = 1 + \rho_c \frac{16(1 - v_0^2)}{9(1 - 2v_0)}\left(\frac{\delta_f}{1 + \delta_f}\right) \tag{1-35}$$

$$\frac{G_0}{G_{sat}} = 1 + \rho_c\left[\frac{16(1 - v_0)}{15\left(1 - \frac{v_0}{2}\right)} + \frac{32(1 - v_0)}{45}\left(\frac{\delta_f}{1 + \delta_f}\right)\right] \tag{1-36}$$

With $\delta_f = \frac{\pi\zeta E_0}{4(1-\upsilon_0^2)}(\frac{1}{K_f} - \frac{1}{K_0})$. δ_f characterizes the effect of fluid pressure. K_f is the fluid bulk modulus.

(5) Non-interactive assumption for transversely isotropy symmetry

In the case of transversely isotropic distribution of crack orientation, a second rank crack density tensor α is substituted for the scalar crack density ρ_c (Fortin 2011; Ougier-Simonin et al.,2011; Wang et al., 2013; Nicolas et al., 2016)

$$\alpha = \frac{1}{V}\sum(a^3\boldsymbol{nn})^i \tag{1-37}$$

Where $\boldsymbol{n}$ is a unit normal to a crack and **nn** is a dyadic product. The linear invariant $\alpha_{kk} = \rho_c$ thus α is a natural tensorial generalization of ρ_c, β is the fourth rank crack density tensor(Fortin 2011; Ougier-Simonin et al.,2011; Wang et al., 2013; Nicolas et al., 2016)

$$\beta = \frac{1}{V}\sum(a^3\boldsymbol{nnnn})^i \tag{1-38}$$

Transversely isotropic orientation distribution of cracks is realistic for the crack induced under a deviatoric loading (Gueguen and Sarout, 2011; Fortin 2011; Ougier-Simonin et al.,2011; Wang et al., 2013; Nicolas et al., 2016). In this case, the total strain ε_{ij} (per representative volume V) is expressed as a summation of strain in solid matrix (ε_{ij}^0) and extra strains due to presence of multiple cracks ($\Delta\varepsilon_{ij}$)

$$\varepsilon_{ij} = S_{ijkl}^{eff}\sigma_{kl} = \varepsilon_{ij}^0 + \Delta\varepsilon_{ij} = (S_{ijkl}^0 + \Delta S_{ijkl})\sigma_{kl} \tag{1-39}$$

S_{ijkl}^{eff} is the effective compliance, σ_{kl} is the applied stresses, S_{ijkl}^0 is the compliance of solid matrix, ΔS_{ijkl} is the extra compliance due to pores and cracks. ΔS_{ijkl} for an isotropic matrix containing penny-shaped cracks could be expressed in the non-interactive assumption as

$$\Delta S_{ijkl} = h[\frac{1}{4}\left(\delta_{ik}\alpha_{jl} + \delta_{il}\alpha_{jk} + \delta_{jk}\alpha_{il} + \delta_{jl}\alpha_{ik}\right) + \psi\beta_{ijkl} \quad (1\text{-}40)$$

With $h = \frac{32(1-\upsilon_0^2)}{3(2-\upsilon_0)E_0}$, and E_0 and υ_0 are Young's modulus and Poisson ratio of solid matrix respectively, in addition :

$$\psi = \left(1 - \frac{\upsilon_0}{2}\right)\frac{\delta_f}{1+\delta_f} - 1 \quad (1\text{-}41)$$

As an example, the effective compliance of a rock containing only vertical cracks under dry and saturated cases in the laboratory could be written as (dry condition, $\psi = -\upsilon_0/2$)

$$\begin{gathered} S_{1111} = S^0_{1111} + h\rho_c(\frac{1}{2} + \frac{3\psi}{8}) \\ S_{3333} = S^0_{3333} \\ S_{1212} = S^0_{1212} + h\rho_c(\frac{1}{4} + \frac{\psi}{8}) \\ S_{2323} = S_{1313} = S^0_{1313} \\ S_{1122} = S^0_{1122} + h\psi\rho_c/8 \\ S_{1133} = S_{2233} = S^0_{2233} \end{gathered} \quad (1\text{-}42)$$

1.2.3 Wing crack model

Ashby and Sammis, (1990) developed the wing crack model: under compression, a population of small cracks extends in a stable way until a critical stress state where they interact and lead to final failure. A series of papers and reviews (Topponnier and Brace, 1976; Wawersik and Brace, 1971; Nemat-Nasser and Horii, 1982; Ashby and Hallam, 1986; Sammis and Ashby, 1986) have established that cracks grow until their length is comparable with their spacing.

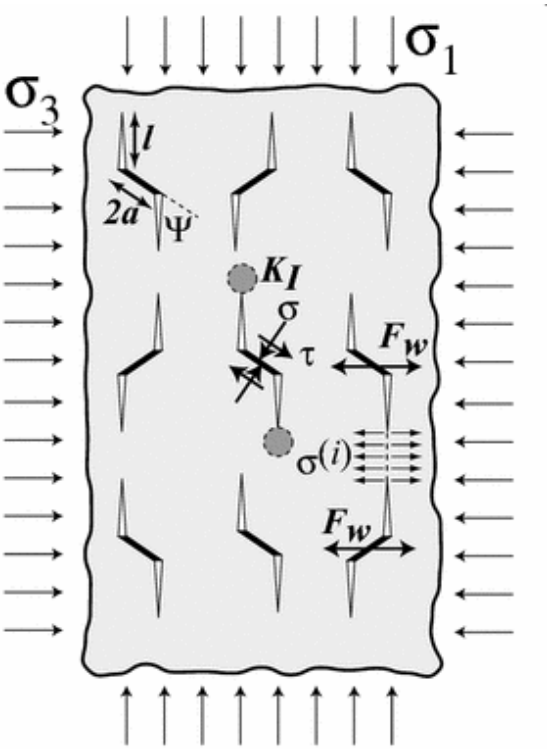

Figure 1.5 From Perol, T. and Bhat, H.S., 2016.

(1) Crack initiation

The criterion for crack initiation under axisymmetric loading has the form

$$\sigma_1 = c_1\sigma_3 - \sigma_0 \tag{1-43}$$

c_1 and σ_0 are material properties, σ_1 is the axial stress, and $\sigma_2 = \sigma_3$ are the radial stress. Cracks initiate when (Nemat-Nasser and Horii, 1982; Ashby and Hallam, 1986):

$$\sigma_1 = \frac{(1+\mu^2)^{1/2}+\mu}{(1+\mu^2)^{1/2}-\mu}\sigma_3 - \frac{\sqrt{3}}{(1+\mu^2)^{1/2}-\mu}\frac{K_{Ic}}{\sqrt{\pi a}} \tag{1-44}$$

Where μ is friction coefficient, K_{IC} is the fracture toughness of the material, and $2a$ is crack length.

(2) Crack growth after initiation

Once cracks are initiated, K_I is modified due to the presence of wing crack. The crack keeps growing while $K_I > K_{IC}$, i.e. a growth of crack length requires an increase in the loading stress

This stage occurs before cracks begin to interact strongly. The stress intensity K_I at the tip of each wing crack varies with the geometry and length of the newly formed surface. In 2D case, in an elastic medium containing cracks with a length of $2a$ inclined at an angle ψ to the σ_1,

$$\tau = \frac{\sigma_3 - \sigma_1}{2} sin2\psi \tag{1-45}$$

$$\sigma = \frac{\sigma_3 + \sigma_1}{2} + \frac{\sigma_3 - \sigma_1}{2} cos2\psi \tag{1-46}$$

Based on the work of Nemat-Nasser and Horii (1982), Ashby and Hallam (1986) and Nemat-Nasser (1986), Kemeny and Cook (1987), F_w is opening force parallel to σ_3(see Figure 1.5), acting at the midpoint of the wing crack with length of $2l$, and

$$\begin{aligned} F_w &= (\tau + \mu\sigma)2asin\psi \text{ , or} \\ F_w &= -(A_1\sigma_1 - A_3\sigma_3)a \end{aligned} \tag{1-47}$$

F_w creates a stress intensity tending to open the crack (Tada et al., 1985), and:

$$(K_I)_1 = \frac{F_w}{\sqrt{\pi l}} \tag{1-48}$$

The remote confining stress σ_3 acts on the wing crack of length l(Tada et al., 1985) and:

$$(K_I)_3 = \sigma_3\sqrt{\pi l} \tag{1-49}$$

Thus, the stress intensity factor is

$$K_I = \frac{F_w}{\sqrt{\pi(l+\beta)}} + \sigma_3\sqrt{\pi l} = -\frac{A_1\sigma_1\sqrt{\pi a}}{\pi\sqrt{L+\beta}} + \sigma_3\sqrt{\pi a}\left(\frac{A_3}{\pi\sqrt{L+\beta}} + \sqrt{L}\right) \tag{1-50}$$

Where $L = l/a$. The cracks extend until K_I becomes equal to K_{IC}. A_1 and A_3 are given by Nemat-Nasser and Horii (1982), Ashby and Hallam (1986),

$$A_1 = \frac{\pi\sqrt{\beta}}{\sqrt{3}}\left((1+\mu^2)^{\frac{1}{2}} - \mu\right) \tag{1-51}$$

$$A_3 = A_1\left(\frac{(1+\mu^2)^{\frac{1}{2}}+\mu}{(1+\mu^2)^{\frac{1}{2}}-\mu}\right) \tag{1-52}$$

$$\beta = 0.1 \tag{1-53}$$

In case where the interaction between cracks is unneglectable, the mean internal stress due to crack interaction is:

$$\sigma_3^i = \frac{F_w}{d^2} \tag{1-54}$$

Where d is the average distance between two cracks. Thus the last component of stress intensity factor became

$$(K_I)_3 = (\sigma_3 + \sigma_3^i)\sqrt{\pi l} \tag{1-55}$$

1.2.4 Subcritical crack growth

The subcritical crack growth is the phenomenon that taken placewhen the fracture toughness is not reached, but the crack begins to propagate (Mallet et al., 2015). This phenomenon is related to the presence of water and is amplified as temperature is increased.

(1) subcritical crack growth rate: exponential law

In the subcritical growth of cracks, the growth rate of crack is assumed to be thermally activated (Johnson and Paris, 1968; Lawn and Wilshaw, 1975; Mallet et al., 2015). Crack growth rate is (Darot and Guéguen, 1986):

$$\frac{dl}{dt} = l_0 e^{\left(\frac{-E_a}{kT}\right)} e^{\left[\frac{s}{kT}\left(\frac{K_I^2}{E_0}-2\gamma\right)\right]} \tag{1-56}$$

where T is the temperature, l_0 is a characteristic crack speed, which is the product of the interatomic distance b and atomic vibration frequency υ, $l_0 \cong 10^4$m s^{-1}(Lawn and Wilshaw, 1975), E_0 is the Young's modulus, γ is the thermodynamic surface energy, and K_I is the stress

intensity factor. Combining with the wing crack model (Ashby and Sammis, 1990; Deshpand and Evans, 2008; Bhat et al., 2011) . The stress intensity factor K_I at crack tip is

$$K_I = \frac{F_w}{(\pi(l(t) + \beta c))^{3/2}} - \frac{2}{\pi}(\sigma_3' - \sigma_i')\sqrt{\pi l(t)} \tag{1-57}$$

Crack length evolution could be described with the two equations above. Then strain evolution could be expressed (Deshpande and Evans, 2008) using

$$\Delta\epsilon_{ij} = \frac{\delta W}{\delta \sigma_{ij}} \tag{1-58}$$

Where, W is total free energy, composed of two parts: uncracked solid strain energy density W_0 and contribution of cracks $N_c \Delta W$. For more explanation on this model, the reader can refer to the the work of Mallet et al. 2015.

1.2.5 Stress-dependent permeability

Transport properties, (permeability and diffusivity) have been observed to be strongly stress-dependent (Nur et al. 1980; Yilmaz et al. 1994). Gavrilenko and Gueguen (1989) developed a model of pressure-dependent permeability, connecting permeability with statistical distribution of crack geometry. More recently, Yilmaz et al. 1994 suggested a model in which the diffusion coefficient D is related to the pore fluid pressure P by

$$D = D_0 e^{\kappa p} \tag{1-59}$$

κ is the permeability compliance, defined and dicussed in 1.2.6.

1.2.6 Construction of a nonlinear diffusion equation

Assuming that the medium is homogeneous and isotropic, Darcy's law is

$$q = \frac{k}{\mu}\frac{\partial P}{\partial x} \tag{1-60}$$

q is the is flow rate (the volumetric rate of flow per unit area), μ is the fluid viscosity, k is the permeability of the medium, P is pore pressure. The mass conservation implies:

$$\frac{\partial(\rho\phi)}{\partial t} + \nabla(\rho q) = 0 \tag{1-61}$$

Where, ρ is the fluid density, ϕ is the porosity, q is flow rate.

If define c_ϕ the porosity compressibility (Geertsma 1957; Zimmerman et al. 1986), c_f is the fluid compressibility, κ is the permeability compliance. We will also assuming that μ is constant and that ρ, ϕ, k depend only on effective pressure. Under constant confining pressure,

$$\begin{aligned} c_\phi &= \frac{1}{\phi}\frac{\partial\phi}{\partial p} \\ c_f &= \frac{1}{\rho}\frac{\partial\rho}{\partial p} \\ \kappa &= \frac{1}{k}\frac{\partial k}{\partial p} \end{aligned} \tag{1-62}$$

Consider c_ϕ, c_f, κ to be pressure invariant, this leads to :

$$\begin{aligned} c_\phi p_p &= \ln(\frac{\phi}{\phi_0}) \\ c_f p_p &= \ln(\frac{\rho}{\rho_0}) \\ \kappa p_p &= \ln(\frac{k}{k_0}) \end{aligned} \tag{1-63}$$

ϕ_0, ρ_0, k_0 are reference values of porosity, fluid density, and permeability respectively. Combining Darcy law, continuity equation, considering porosity compressibility, fluid compressibility and permeability compliance, this leads to:

$$\frac{\mu\phi}{k}\left(c_\phi + c_f\right)\frac{\partial p}{\partial t} = \sum_{i=1}^{3}\frac{\partial^2 p}{\partial x_i^2} + (c_f + \kappa)\sum_{i=1}^{3}(\frac{\partial p}{\partial x_i})^2 \tag{1-64}$$

The values of κ have magnitudes of one to three orders larger than values of c_ϕ, c_f. (Dake 1978; Newman 1973; Jones 1975; Nur et al., 1980; Jones and Owens 1980), this for large κ, the non-linearity of flow essentially depends on the permeability compliance κ. In 1D flow, the equation could be written as

$$\frac{\partial p(x;t)}{\partial t} = D_0 \frac{\partial}{\partial x} \left(e^{kp(x;t)} \frac{\partial p(x;t)}{\partial x}\right) \tag{1-65}$$

For certain boundary condition and initial condition and geometry, there are analytical solutions for this problem. Note that these solutions have been used for field case in the work of Yilmaz et al.,1994, Crank 1979 and Parlange 1992.

Chapter II Physical and Mechanical Properties of Thermally Cracked Andesite Under Pressure

This paper has been accepted by Rock Mechanics and Rock Engineering by Zhi Li, Jérôme Fortin, Aurélien Nicolas, Damien Deldicque and Yves Guéguen

Abstract

The effects of thermal crack damage on the physical properties and rupture processes of andesite were investigated under triaxial deformation at room temperature. Thermal cracking was induced by slowly heating and cooling samples. The effects of heat treatment temperatures ranging between 500°C and 1100°C on the P-wave velocities and on the microstructure were investigated. Then, the mechanical properties of andesite samples treated at 930°C were investigated under triaxial stress at room temperature using constant strain rate tests and confining pressures ranging between 0 and 30 MPa. Similar triaxial experiments were conducted on non-heat-treated samples. Our results show that 1) for heat treatments at temperatures below 500°C, no significant changes in the physical properties are observed; 2) for heat treatments in the temperature range of 500-1100°C, crack density increases; and 3) thermal cracking has no influence on the onset of dilatancy but increases the strength of the heat-treated samples. This last result is counterintuitive but seems to be linked with the presence of a small fraction of clay (3%) in the non-heat-treated andesite. Indeed, for heat treatment above 500°C, some clay melting is observed and contributes to sealing the longest cracks.

Keywords: Andesite, Thermal crack, Ultrasonic velocity, Crack density, Onset of dilatancy, Brittle Strength, Partial melting, Crack sealing.

2.1 Introduction

The physical properties and mechanical behavior of andesite are of interest for the understanding of several natural processes and for engineering design. Natural processes include ground deformation due to magma rising below volcanoes (Jaupart,1998; Costa et al. 2009; Heap et al.2014), eruption activity and cessation of dikes (Gudmundsson, 2006,2011; Browning et al. 2015), or fault activity in volcano systems (Rowland and Sibson, 2001). Industrial contexts are geothermal reservoir engineering (Siratovich et al., 2014) and CO_2 sequestration (Trias et al. 2017).

In volcanic areas, where hot fluids circulate, temperature is a parameter that should be taken into account when investigating mechanical behavior. Temperature variations can induce intragranular cracks and intergranular cracks or even melting of the rock (Friedman et al. 1979, Wong 1989), leading to large changes in the microstructure. A common way to investigate the effect of temperature on the mechanical behavior is to use heat-treated samples.

Many studies have been performed on the role of thermal effects in the mechanical behavior of igneous rocks, including intrusive and extrusive rocks (Heap et al. 2014, 2015, 2016; Vinciguerra et al. 2005; Fortin et al.2011; Stanchits et al. 2006; Meredith et al. 2005; Wang et al. 2013). Increasing temperature can modify fluid transport properties (Vinciguerra et al. 2005, Nasseri 2009, Faoro, 2013, Darot, 1992, Geraud 1994), elastic wave velocities (Walsh 1965, Nasseri 2007), and mechanical properties (Faulkner et al. 2003, Wang et al. 2013). Thermal cracking has been shown to weaken different rocks, including granite (Homand-Etienne and Houpert, 1989; Chaki et al. 2008), gabbro (Keshavarz et al. 2010), calcarenite (Brotóns et al. 2013), and carbonate (Sengun et al. 2014;). P-wave velocity changes due to thermal cracking are expected. Such changes are important for seismic tomography inversion of volcano systems and may be useful for investigating magma chamber activity and dike eruption. According to

Griffith et al. (2017) and Browning et al. (2016), more cracks are created during the cooling stage than during the heating stage.

In contrast with intrusive rocks, extrusive rocks have a different structure resulting from fast cooling: a fine groundmass and phenocrysts. Note that the ultrasonic velocities and transportation properties of andesite have been investigated in previous studies (Fortin et al., 2011; Fatquharson et al., 2015; Heap et al., 2014, 2015 ; Siratovich et al., 2015; Heap and Kennedy, 2016;).

The selected rock for this study is an andesite from Guadeloupe, France. Guadeloupe is located in the Lesser Antilles arc. This arc results from the subduction of the North American Plate under the Caribbean Plate (Bouysse et al., 1990). The Bouillante (Guadeloupe, France) geothermal power plant has been operating for 30 years (Jaud and Lamethe, 1985). GEOTREF (A project aimed at improving understanding fractured geothermal reservoirs) is planning a new geothermal project in the area from which the samples were taken. Faults and active fluids are present in the volcano system and cause significant seismicity activity (Feuillet et al. 2001; 2002). Because induced seismicity is possible during geothermal exploration, it is important to systematically determine the geomechanical behavior and to characterize its evolution resulting from thermal stresses. This paper aims to investigate the effect of heat treatment on the mineralogical composition, microstructural parameters (porosity, crack density), and petrophysical parameters (permeability, elastic wave velocities) of andesite. For this purpose, we selected an andesitic block from a quarry located in Guadeloupe, France, and samples were heat-treated at different temperatures. Then, petrophysical and mechanical properties were measured.

2.2 Material & Methods

2.2.1 Materials

(1) Rock samples

The samples of andesite were cored from a single block, which was obtained from a quarry located in Déhaies (Guadeloupe, France). Cylindrical samples were cored with diameters of 40 mm and lengths of 80 mm. No bedding related to volcanic features was identified in the block. After coring, boundary surfaces were polished to ensure smooth horizontal surfaces.

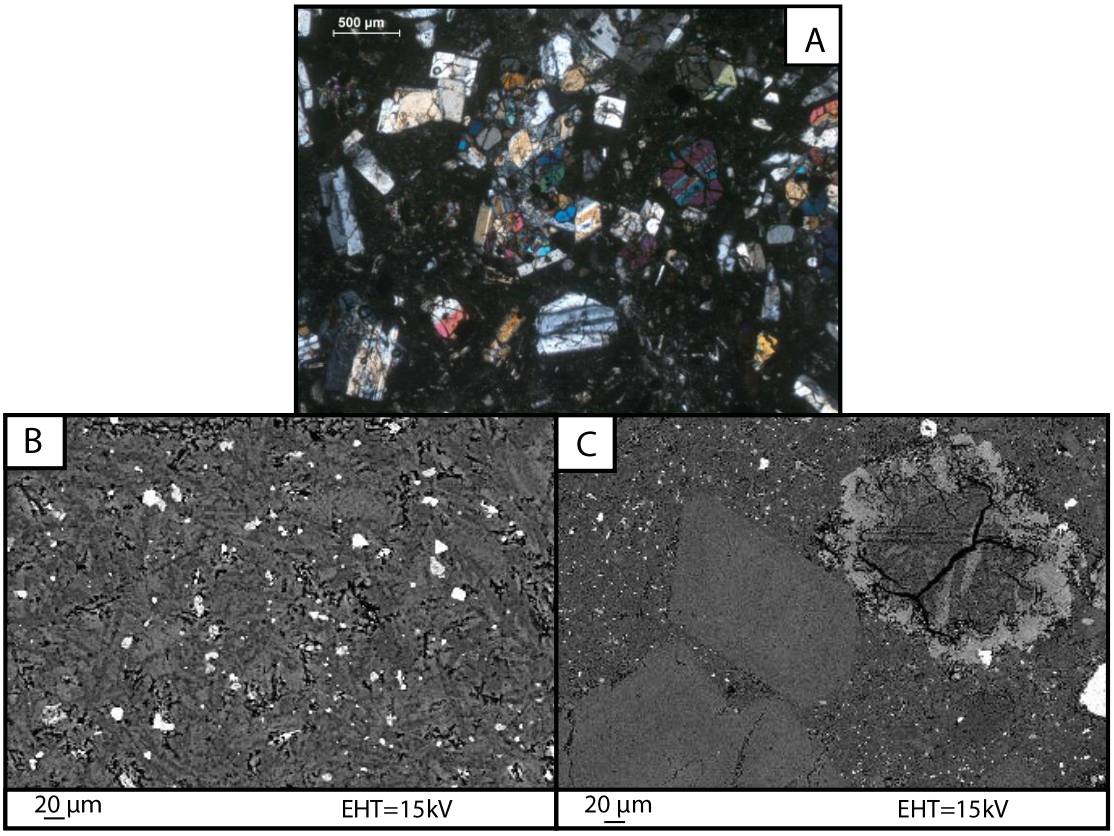

Figure 2.1: a) SEM images of a non-heat-treated andesite sample at low magnitude. b) high magnification view of the matrix. c) high magnification view of the phenocrysts.

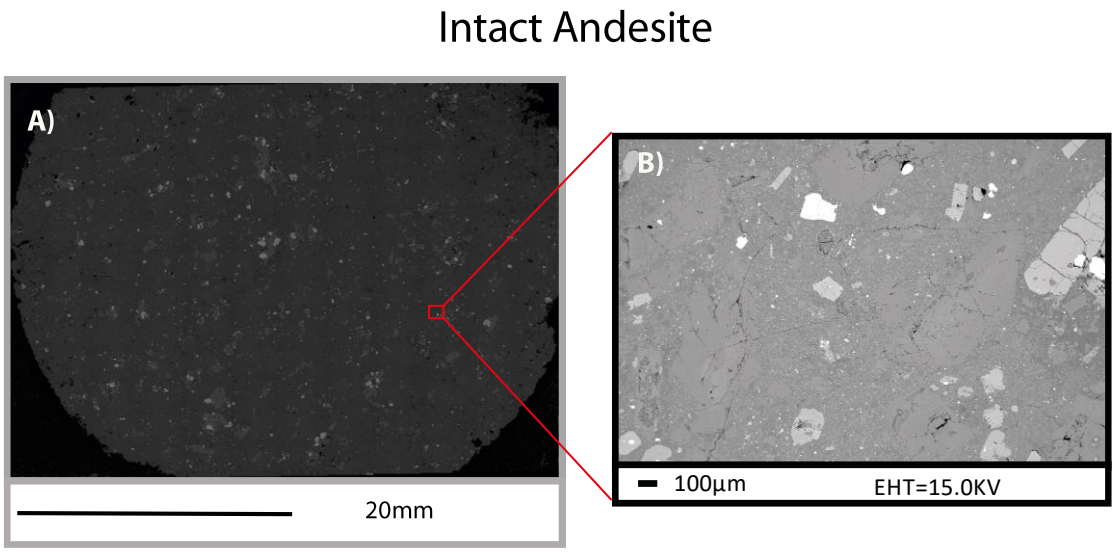

Figure 2.2: Cracks in the matrix. The longest cracks have a length of 300 µm -500 µm.

The samples have a mean density of 2670 kg/m^3, and the porosity varies between 1.5% and 2.3% with a mean porosity of 1.9%. The porosity is estimated by comparing the weight of a water-saturated sample with the weight of the same sample dried under a vacuum at 40°C for 4 days. The permeability of the non-heat-treated andesite is approximately 10^{-21} m^2. The P-wave velocity of the non-heat-treated andesite samples is 5400 m/s with a measurement error of 200 m/s.

The andesite is composed of a fine groundmass with large phenocrysts (Figure 2.1). The matrix is composed of quartz and plagioclase (50-60%). The mean grain size of the matrix is 2 µm. Phenocrysts are plagioclase (25-35%), pyroxene (15-20%) and oxides (4-5%). The mean grain size of phenocrysts is 100 µm (Figure 2.1).

Figure 2.1 shows that this andesite is naturally microcracked. Cracks can be observed inside the phenocrysts (Figure 2.1c). Figure 2.2 also shows that the andesite sample has a few long cracks in the matrix, with lengths on the order of 300 µm-500 µm.

(2) Procedure of the heat treatment

Samples were heat treated to four different temperatures: 500°C, 800°C, 930°C, and 1100°C. Samples were placed in a programmable Meker MHT-3 furnace (Nicolas et al. 2016), and the temperature was increased at a rate of 140°C/h to the target temperature. The furnace atmosphere was not controlled by air-oxygen fugacity. The target temperature was held constant for 2 hours. Samples were slowly cooled to room air temperature. The cooling rate was controlled by the thermal inertia of the oven and remained slow (~10 hours to decrease from 930°C to room temperature). The effects of the heat treatment amplitude on the petrophysical properties of the andesite are presented in section 2.3.1. The particular temperature of 930°C was selected for a detailed triaxial deformation test. This temperature corresponds to that of the second magma chamber temperature in La Soufière, Guadeloupe (Villemant et al. 2014), which is where the dikes begin (Villemant 2014). The mechanical properties of the heat-treated andesite samples are investigated and compared to the mechanical properties of the non-heat-treated samples.

2.2.2 Experimental Methods

(1) Experimental apparatus

Triaxial deformation experiments are performed on the triaxial cell installed at the Laboratoire de Géologie at École Normale Supérieure in Paris (Figure 1 in appendix). The axial load is applied by an axial piston with a maximum load of 680 MPa and is measured with a sensor with an accuracy of approximately 10^{-3} MPa. The confining pressure is applied by a volumetric servo pump that can provide pressure up to a maximum of 100 MPa and is measured by a pressure transducer with an accuracy of 10^{-3} MPa (Ougier-Simonin et al. 2011, Nicolas et al. 2016). The pressure-conducting medium is silicone oil.

(2) Strain and ultrasonic instrumentation

Four groups of strain gauges are glued at different positions directly on the sample. (Figure 2 in appendix). Each group is composed of one axial gauge and one radial gauge. Strain gauges *Tokyo Sokki TML FCB 2-11* are employed. The axial strain ε_a, and radial strain ε_r are both averaged across the four strain gauges in each orientation. The volumetric strain is deduced as $\varepsilon_v = \varepsilon_a + 2\varepsilon_r$. Neoprene tubing is used to separate the sample from the oil of the confining medium. Then, 12 P-wave sensors (*PI 255 PI Ceramics*, 1 MHz resonance frequency) and 4 polarized S-wave sensors (*Shear PZT plate*) are glued directly on the surface of the rock and sealed with a two-component epoxy (Figure 2 in appendix). The network of ultrasonic sensors used allows us to record i) acoustic emissions (passive mode) and ii) the evolution of the ultrasonic velocities in different directions (active mode). For the ultrasonic wave velocity survey, a 250 V high-frequency signal is pulsed every 2 minutes on each sensor while the others are recording. In passive mode, these sensors can record the acoustic emissions (AE) that take place in the sample. The AEs are amplified at 40 dB and can be discretely recorded with a maximum rate of 12 AE/s. (Schubnel et al., 2006, 2007; Brantut et al., 2011; Ougier-Simonin et al., 2011; Nicolas et al., 2016).

(3) Experimental procedure

For all the samples, the P-ultrasonic wave velocity is measured at room temperature and atmospheric pressure. Permeability is measured with water using transient pulse or steady flow methods at 2.5 MPa effective confining pressure. For non-heat-treated samples and samples heat-treated to 500°C, permeability is measured using the transient pulse (Brace et a., 1968) (two symmetrical measures are performed by switching the flow direction in the sample); for samples heat-treated to 800°C and 930°C, permeability is measured with steady state flow.

For non-heat-treated andesite samples and heat-treated (at 930°C) andesite samples, experiments are performed under dry conditions at room temperature, with confining pressures of 5, 15 and 30 MPa (non-heat-treated samples) and 0, 15 and 30 MPa (heat-treated samples). Differential loading is applied up to peak stress using a controlled constant strain loading rate of 10^{-6}/s. During triaxial deformation, ultrasonic measurements are made on all samples every 2 minutes.

In the following, we adopt the convention that compressive stresses and compactive strains are positive. The differential stress is noted by $Q = \sigma_1 - \sigma_3$, and the mean stress by $P = (\sigma_1 + 2\sigma_3)/3$, where σ_1 and $\sigma_3 = P_c$ are the vertically applied (maximum) stress and the confining pressure (minimum), respectively.

2.3 Results

2.3.1 Properties of samples heat-treated at different temperatures

(1) P-wave velocity, crack density and permeability

The samples were heat-treated at different temperatures: 500°C, 850°C, 930°C and 1100°C. The evolution of the P-wave velocity and permeability as functions of the temperature of the heat treatment are shown in Figure 2.3. In addition, we invert the P-wave velocity to obtain the crack density, as defined by $\rho = \sum_N \frac{l_i^3}{V}$, where l_i is the length of the *i*-th crack and N is the total number of cracks embedded in the representative elementary volume V. When the crack length is smaller than the wavelength, effective medium theory is an appropriate method (Ougier-Simonin et al., 2010). The effective elastic properties are mainly controlled by cracks (Gueguen and Kachanov 2012). A noninteractive assumption is employed (Kachanov, 1994). Noninteractive effective medium theory has been shown to be valid when cracks are distributed

randomly and crack density does not exceed 0.2-0.3 (Kachanov, 1994; Sayers and Kachanov, 1995; Gueguen and Sarout, 2009). The details of the inversion in crack density are given in the appendix "Crack density inversion method – Isotropic case" (Ougier-Simonin et al. 2010; Mallet et al. 2014; Fortin et al., 2011; Nicolas et al., 2016).

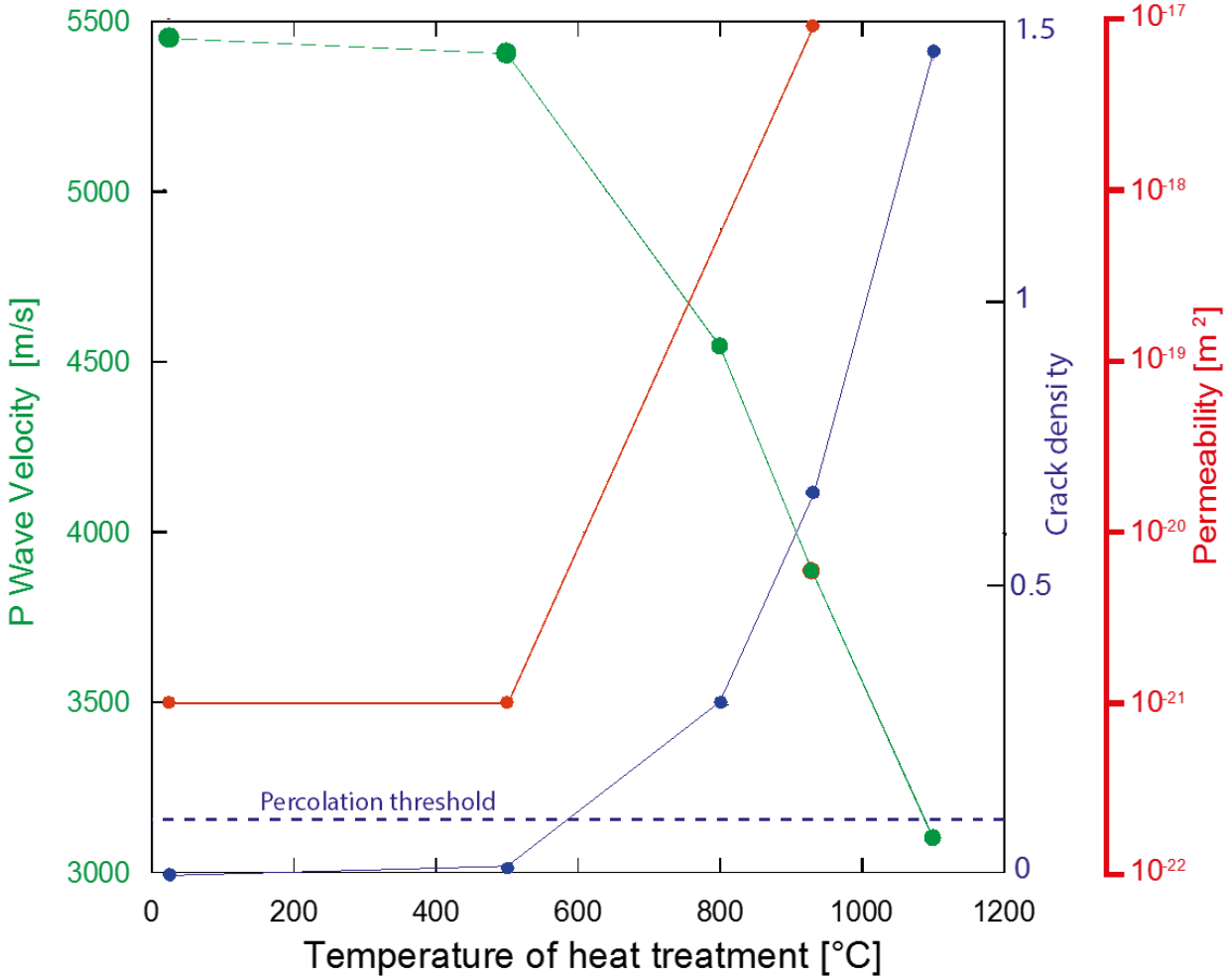

Figure 2.3: P-wave velocity (green curve), crack density (blue curve). Permeability (red curve). Note that the percolation threshold (crack density of 0.1) is indicated as a blue dashed line.

A small decrease in the P-wave velocity of 70 m/s (1.3%) is recorded (Figure 2.3) for a heat treatment of 500°C. However, the decrease reaches 1000 m/s (18%) for a temperature of 800°C and 2250 m/s (41%) for a temperature of 1100°C, indicating a major change at approximately 500°C, which should be associated with a significant change in microstructure. The crack

density inverted from the P wave velocity increases from 0.01 for a heat treatment of 500°C to 1.4 for a heat treatment of 1100°C. This last value is outside the range in which effective medium theory is valid. However, the value points to very intense cracking. The induced crack density reaches the percolation threshold of 0.1 (Guéguen and Dienes, 1989) for a heat treatment between 500°C and 800°C. This result is in good agreement with the permeability evolution, which shows no change below 500°C but shows an increase by 4 orders of magnitude for a heat treatment of 930°C (Figure 2.3).

(2) Microstructural observations of the heat-treated samples

The microstructures are shown in Figure 2.4. In the sample heat-treated at 500°C (Figure 2.4A, 2.4B), few cracks can be observed. In the samples heated at 800°C (Figure 2.4C, 2.4D) and 930°C (Figure 2.4E, 2.4F), cracks surrounding the large inclusions with lengths of 50 μm-200 μm can be observed, including intergranular and intragranular cracks. Small cracks begin to appear in the matrix. Partial melting occurs above 500°C; the details and effects of partial melting are presented in section 3.2. The sample treated at 1100°C shows the highest crack density (Figure 2.4G, 2.4H). In particular, in the matrix (Figure 2.4H), the number of cracks with lengths ranging between 1 μm and 20 μm is greatly increased, and most cracks are located at the boundaries of the crystal grains of quartz, tridymite and plagioclase. Overall, the evolution of the microstructure is in good agreement with the evolution of the P-wave velocity and the permeability (Figure 2.3).

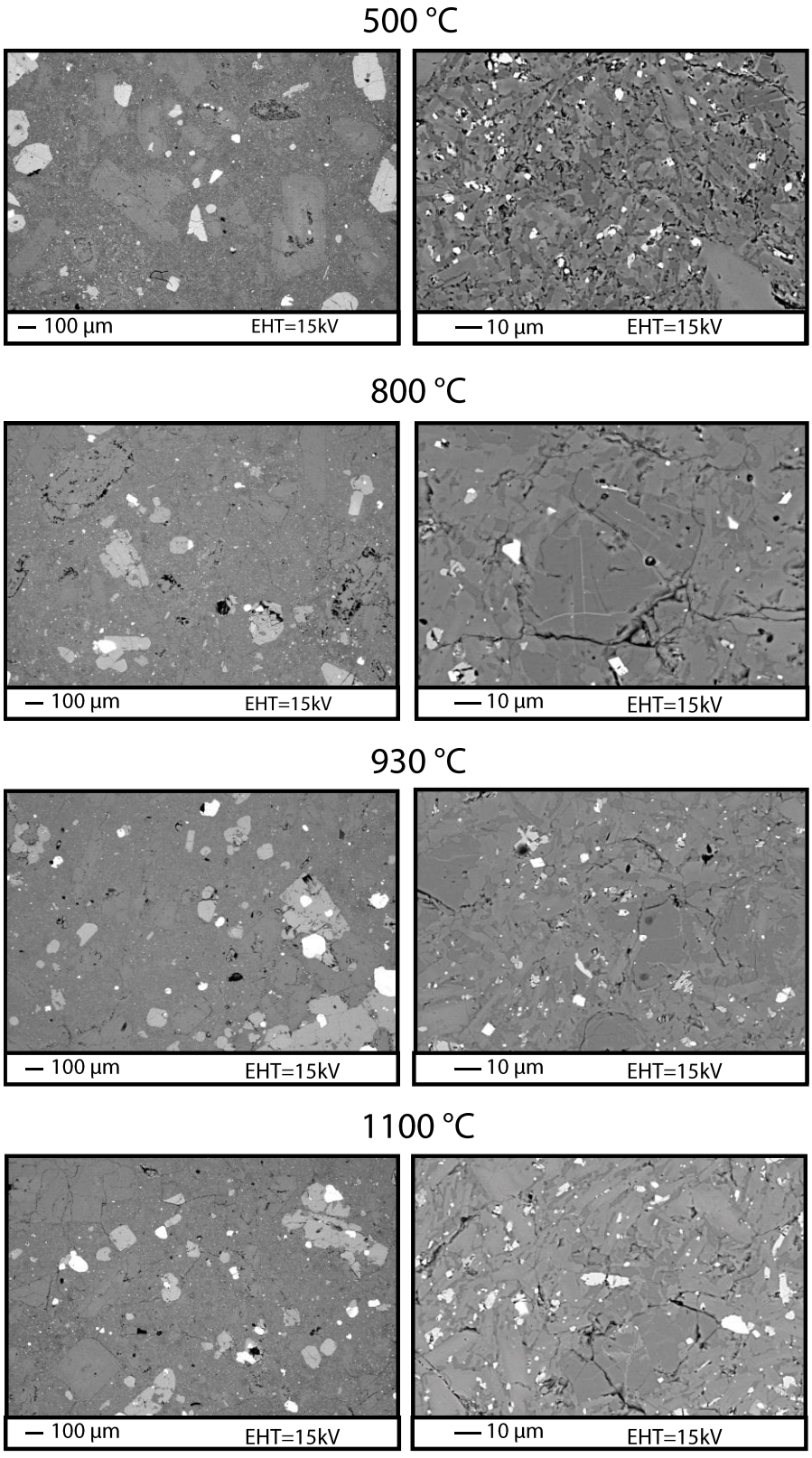

Figure 2.4: SEM pictures of andesite samples heat-treated to 500°C, 800°C, 930°C and 1100°C

2.3.2 Mineralogical effects of heat treatment on andesite

(1) Mineralogical Composition

The mineralogical compositions of non-heat-treated andesite samples and heat-treated andesite samples were analyzed with EBSD (electron backscatter diffraction) and XRD (X-ray diffraction.

Table 1 Chemical composition of andesite samples heat treated to different temperatures

Sample	Plagioclase	Pyroxene	Silicon	Iron-oxides	Smectite	Illite
Andesite	70.8%	14.1%	9.2%	2.5%	3.4%	0.0%
Andesite HT500	70.9%	15.5%	7.8%	2.2%	0.0%	3.5%
Andesite HT930	73.2%	14.4%	8.0%	1.9%	0.0%	2.5%
Andesite HT 1100	68.7%	13.6%	11.0%	2.9%	0.0%	3.9%

Appendix:

Table 2 Chemical composition of andesite samples heat treated to different temperatures

Classification	Mineral	Andesite	Andesite 500	Andesite 930	Andesite 1100
Plagioclase	Bytownite	7.4%	24.7%	23%	14.8%
	Sadine	10.6%	11.4%	12.7%	14.3%
	Albite	52.8%	34.8%	37.5%	39.6%
Pyroxene	Diopside	1.7%	2.3%	3.3%	0.8%
	Hypersthene	6.4%	8.4%	9.1%	6.4%
	Augite	6.1%	4.8%	2.1%	6.5%
Silicon	Tridymite	8.0%	7.2%	5.0%	9.2%
	SiO2	1.2%	0.6%	3.1%	0.8%
Iron-oxides	ilmentite	0.2%	0.0%	0.0%	1.9%
	Magnetite	2.4%	2.2%	1.9%	0.9%
Clay	Smectite	3.4%	0.0%	0.0%	0.0%
	Illite	0.0%	3.5%	2.5%	3.9%

For non-heat-treated andesite samples, the ratio of different phases is shown in Table 1. A more detailed composition is given in Appendix A. The non-heat-treated andesite sample is composed of 70.8% plagioclase (including bytownite, sanidine and albite), 14.1% pyroxene (including diopside, hypersthene and augite), 9.2% other silicates (including tridymite and quartz) and 2.5% iron oxides. The clay content is 3.4%, mainly smectite due to plagioclase alteration.

The mineralogical composition is slightly changed for samples heat-treated at 500°C and 930°C. In particular, the smectite (clay) disappears, and another form of clay appears: illite. The samples heat treated at 930°C and 1100°C are similar (disappearance of smectite); in addition, the proportion of plagioclase decreases by 2%, whereas the proportion of silicate increases by 2%, but this last result could be due to the heterogeneity existing in the samples. Irreversible dehydration and loss of swelling properties of smectite have been shown (e.g., Greene-Kelly 1953, Russel and Farmer 1964) to occur at temperatures between 350°C and 550°C, while dihydroxylation of smectite occurs at temperatures between 550°C and 800°C (Malek et al. 1997).

(2) Partial melting

The non-heat-treated andesite contains smectite (clay) related to the alteration of plagioclase, the smectite is mainly located in the vicinity of plagioclase (Figure 2.5.a).

As the heat treatment reaches 930°C, partial melting is observed in the samples from SEM images (Figure 2.5.a). Glass is visible in the porosity (Figure 2.5.b). Smectite melting results in voids with sizes ranging from 5 µm-10 µm, mainly located near plagioclase (where the smectite was located). In the matrix, small pores of 0.5 µm-1 µm are also observed, mostly at the boundaries of oxides. These pores may also be due to the melting of smectite.

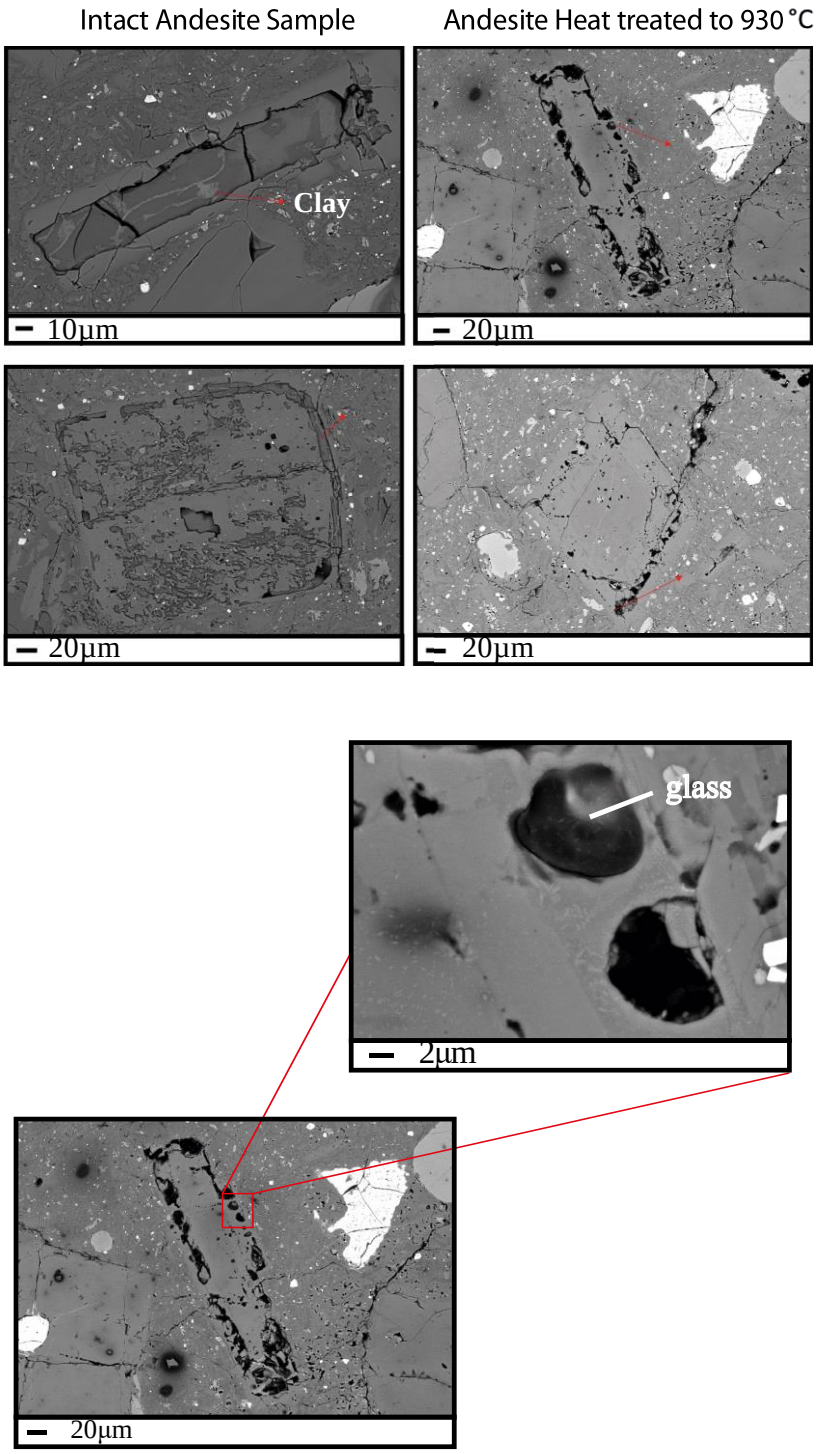

Figure 2.5: a) Partial melting, in samples heat-treated at 930°C. Melting occurs at the boundaries of the phenocrysts, i.e. where the clay (smectite) is located. b): Glass is spotted in the porosity, indicating partial melting.

2.3.3 Tri-axial deformation of non-heat-treated andesite and heat-treated andesite

(1) Stress-strain behavior of non-heat-treated andesite

Triaxial deformation tests were performed at confining pressures of 5 MPa, 15 MPa and 30 MPa under dry conditions at room temperature. The differential stress and mean stress are plotted versus axial strain and volumetric strain, respectively, in Figure 2.6.

The samples under confining pressures varying between 5 MPa and 30 MPa are deformed in the brittle regime. The differential stress reaches a peak stress followed by macroscopic failure. The peak stress is observed to increase with confining pressure: the maximum differential stress increases by 20% as the confining pressure increases from 5 MPa to 15 MPa and increases by 27% as the confining pressure increases from 5 MPa to 30 MPa. Note that at the beginning of the loading, the stress-strain curves (Figure 2.6) are almost linear, which indicates that the number of pre-existing cracks is very small.

Another result of interest is the identification of the D' point, which is the point where volumetric strain reverses (Figure 2.6). Beyond D', dilatancy dominates over compaction [Heap et al. 2014]. The differential stress for D' increases as the confining pressure is increased from 5 MPa to 30 MPa. The stress state of D' increases by 22% as the confining pressure increases from 5 MPa to 15 MPa and increases by 50% as the confining pressure increases from 5 MPa to 30 MPa.

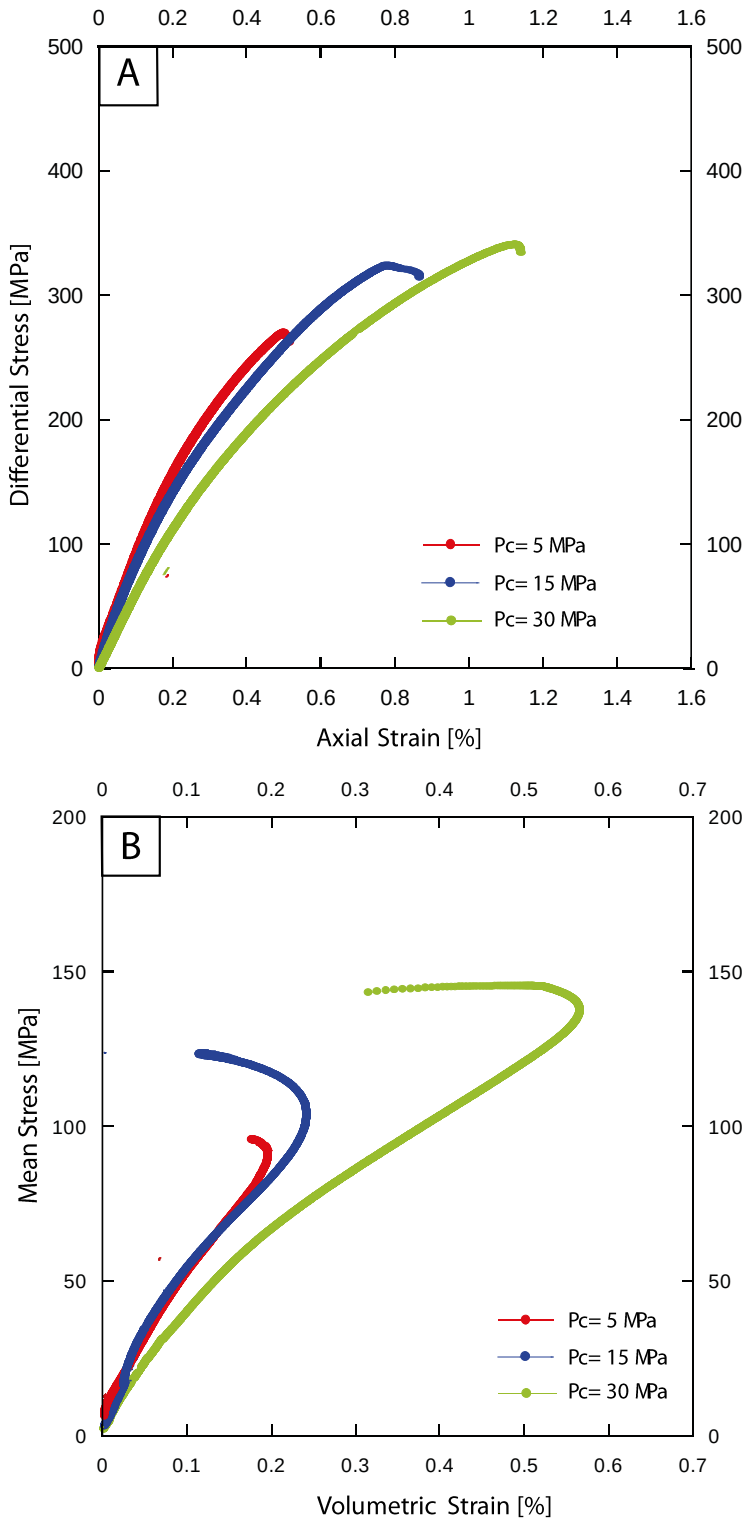

Figure 2.6: Conventional triaxial experiments on non-heat-treated andesite samples under dry condition. a) Differential stress versus axial strain under confining pressure of 5 MPa, 15 MPa and 30 MPa. b) Mean stress versus volumetric strain.

(2) Ultrasonic velocity evolution of non-heat-treated andesite

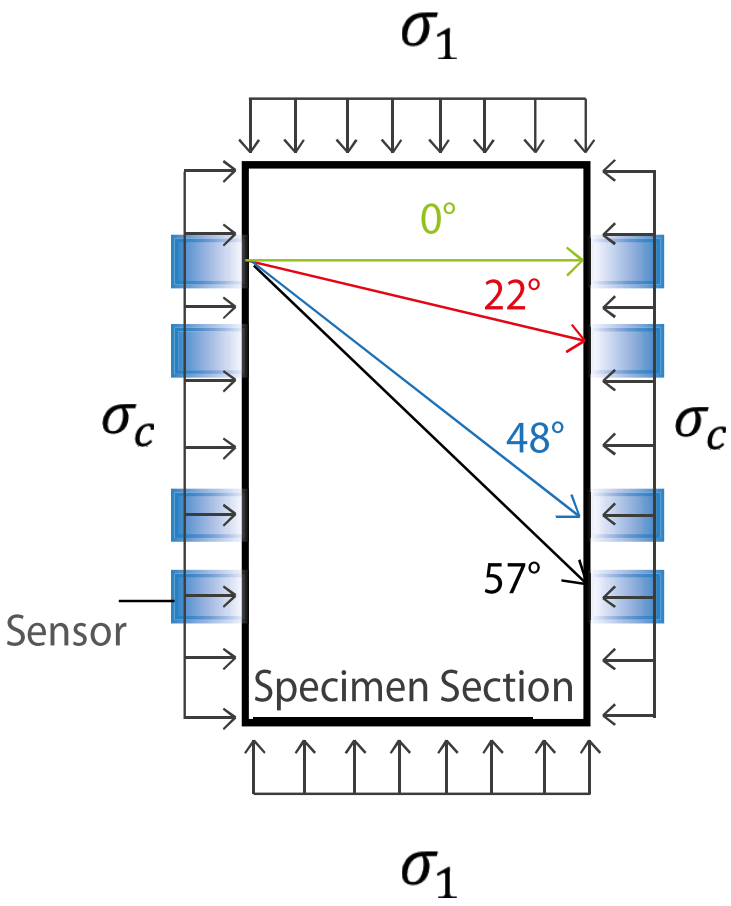

Figure 2.7: a) Sketch illustrating how P wave velocities are measured with different angles with respect to σ_1. b) (next page) P wave velocity and differential stress measured during triaxial deformation experiments on intact andesite samples under confining pressure of 5 MPa, 15 MPa and 30 MPa. P wave velocity and differential stress are plotted versus axial strain. P wave velocity and volumetric strain are plotted versus axial strain. The point C' indicates the onset of dilatancy, D' indicates dilation over dominates compaction, failure is marked.

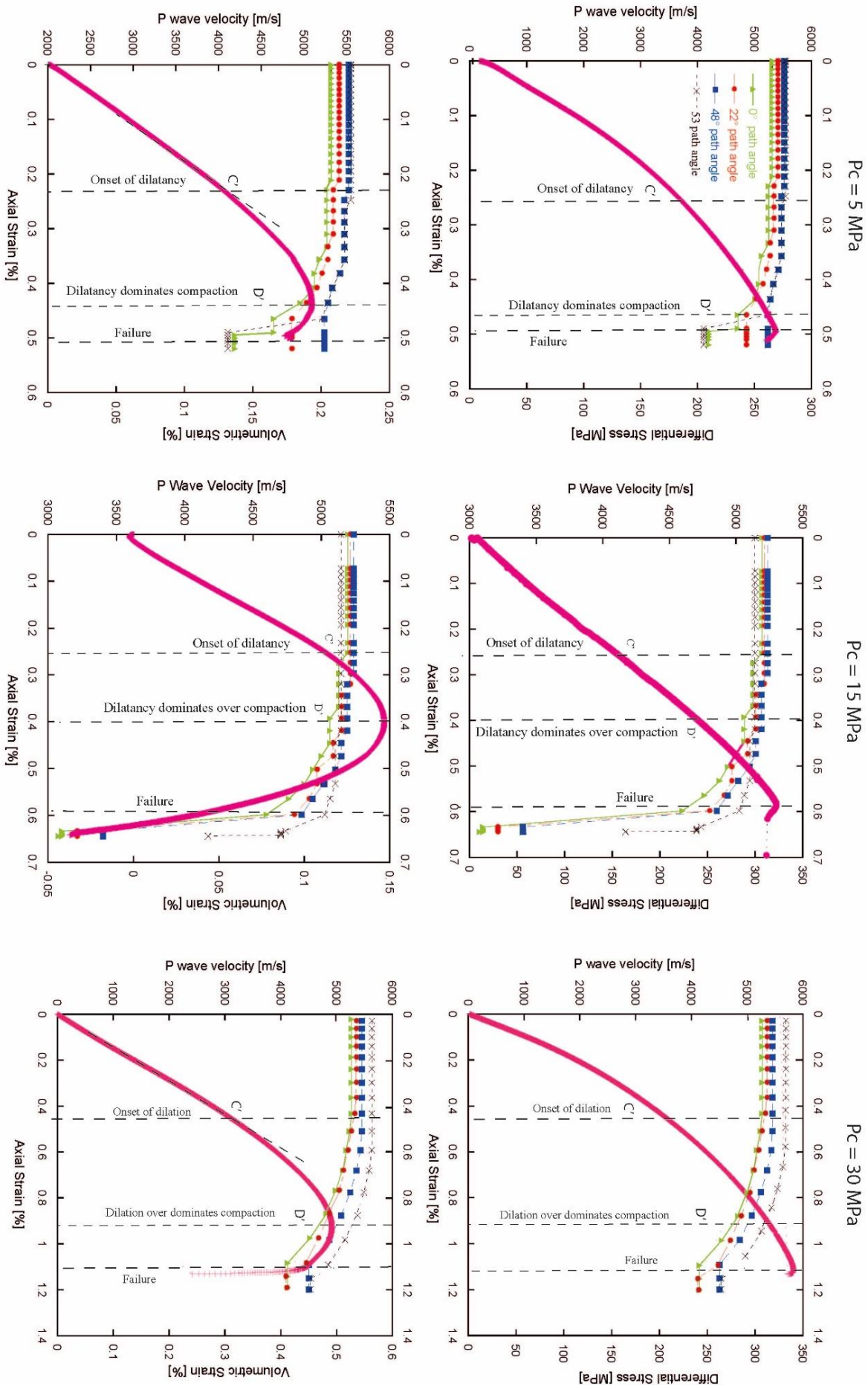
Pc = 5 MPa
P wave velocity [m/s]
Differential Stress [MPa]
Axial Strain [%]
Volumetric Strain [%]
0° path angle
22° path angle
48° path angle
53 path angle
Onset of dilatancy
Dilatancy dominates compaction
Failure
C'
D'
Pc = 15 MPa
P Wave Velocity [m/s]
Onset of dilatancy
Dilatancy dominates over compaction
Pc = 30 MPa
Onset of dilation
Dilation over dominates compaction

The P-wave velocity evolution during the triaxial deformation of andesite samples under confining pressures of 5 MPa, 15 MPa and 30 MPa is shown in Figure 2.7.b. In Figure 2.7.a, the rays of the different P-wave velocities are plotted. The P-wave velocities were measured at four fixed angles (0°, 22°, 48°, 53°). During the first phase of loading, in the quasi-elastic regime, the P-wave velocity is almost constant. This observation agrees with the almost linear stress-strain curve and indicates that the amount of crack porosity is very low [Walsh, 1965]. The P-wave velocity decreases at the onset of dilatancy, marked as point C' [Brace et al.,1966], as cracks nucleate and propagate. The stress state C' corresponds to the beginning of the P-wave velocity decrease (acoustic data) and to the stage where the volumetric strain curve deviates from linearity (mechanical data) (Brace et al. 1966), as shown in Figure 2.7.b.

For the three experiments, P-wave anisotropy is observed as the sample is deformed, with the P-wave velocity for rays at 90° with respect to the axial stress decreasing most.

(3) Stress-strain relation of heat-treated andesite

Triaxial experiments were performed on andesite samples heat-treated (at 930°C) under confining pressures of 0 MPa (ultrasonic sensor and strain gauges are glued directly on the sample, measured inside the triaxial cell), 15 MPa and 30 MPa under dry conditions. The differential stress and mean stress are plotted versus axial strain and volumetric strain, respectively, in Figure 2.8.

As in the case of the non-heat-treated andesite samples, the mechanical behavior of the heat-treated samples is brittle. The peak stress increases by 56% as the confining pressure increases from 0 MPa to 15 MPa and by 200% as the confining pressure increases from 0 MPa to 30 MPa.

A clear effect of pre-existing crack closure is shown on the stress-strain curve in Figure 2.8, which is denoted by the concave curve at the beginning of loading.

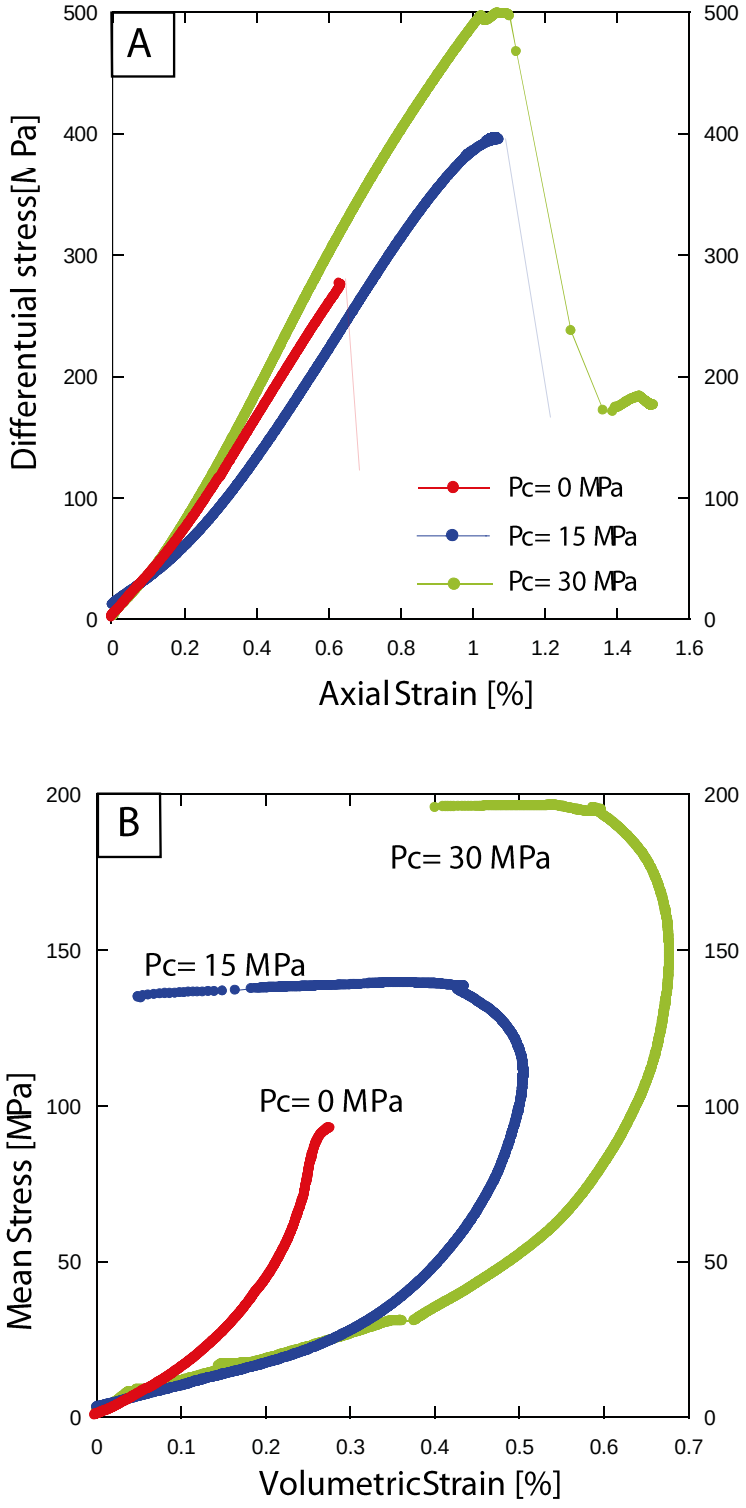

Figure 2.8: Conventional triaxial experiments on heat treated (at 930°C) andesite samples under dry condition. a) Differential stress versus axial strain under confining pressure of 0 MPa, 15 MPa and 30 MPa. b) Mean stress versus volumetric strain.

3.3.4 Ultrasonic velocity evolution of heat-treated andesite

The P-wave velocity evolution during the triaxial deformation of heat-treated andesite samples under confining pressures of 0 MPa, 15 MPa and 30 MPa is shown in Figure 2.9. In Figure 2.9, the evolution of P-wave velocities along different traces from 0° to 53° (Figure 2.7.a) is plotted. A clear difference can be observed in comparison with Figure 2.7.b: for heat-treated samples, the P-wave velocity increases at the beginning of loading, indicating the closure of pre-existing cracks (Stage I). This observation agrees with the stress-strain curve of heat-treated andesite samples, which is concave at the beginning of loading.

During stage II (from C' to D'), the P-wave velocity reaches a plateau. There is competition between pre-existing crack closure and new crack nucleation and propagation. The onset of dilatancy (point C') corresponds to new crack nucleation. Point C' is determined from both acoustic data and mechanical data, as shown in Figure 2.9. Regarding the acoustic data, point C' corresponds approximately to the stage where the radial P-wave velocity stops increasing. At stage III, from point D' to the failure point, a clear decrease in P-wave velocities is observed as well as clear P-wave anisotropy indicating the propagation and nucleation of mainly axial cracks.

Figure 2.9 (next page): P wave velocity and differential stress measured during triaxial deformation experiments on heat treated (at 930°C) andesite samples under confining pressure of 0 MPa, 15 MPa and 30 MPa. P wave velocity and differential stress are plotted versus axial strain. P wave velocity and volumetric strain are plotted versus axial strain. The point C' indicates the onset of dilatancy, D' indicates dilation over dominates compaction, failure is marked.

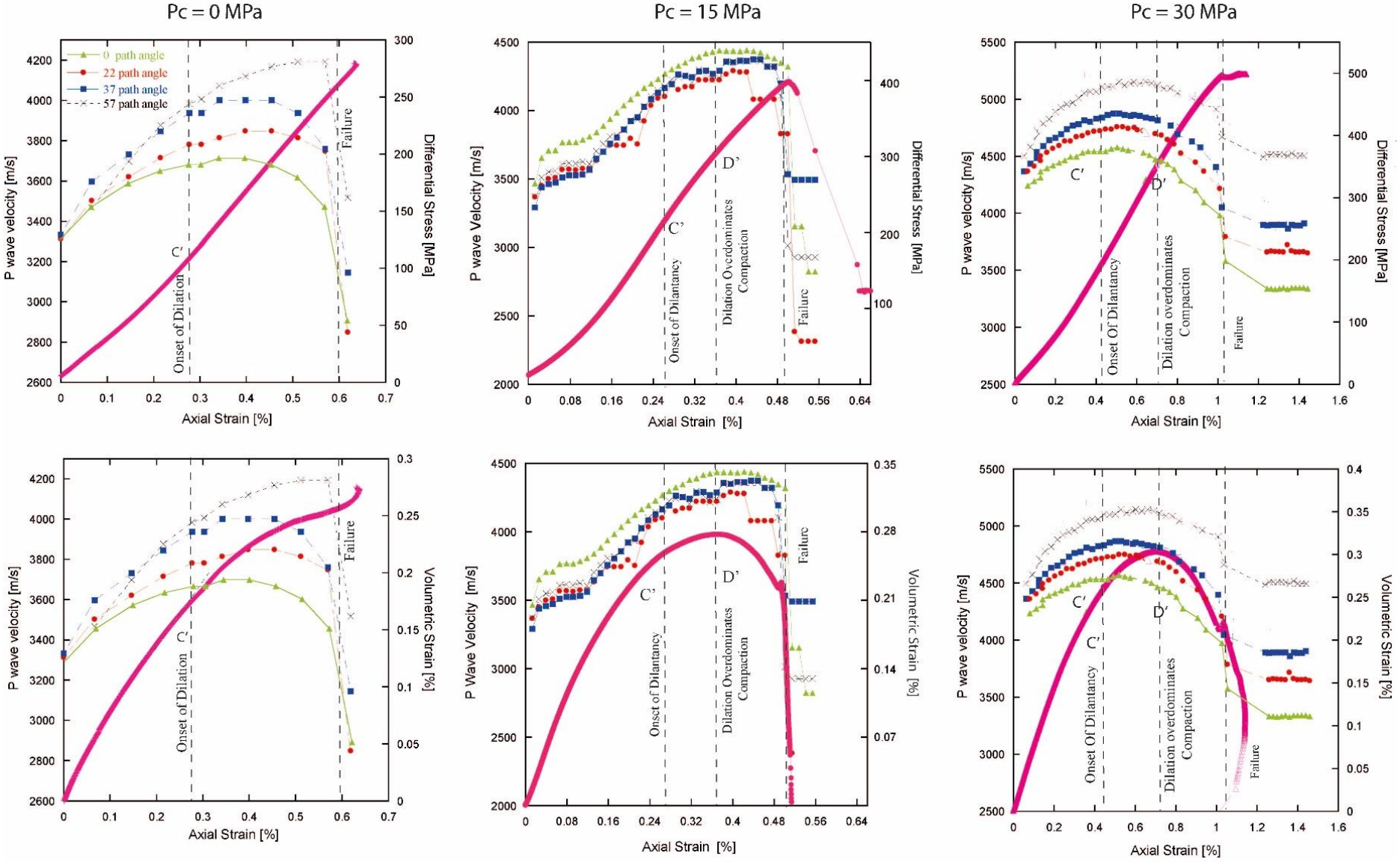
Pc = 0 MPa
Pc = 15 MPa
Pc = 30 MPa
0 path angle
22 path angle
37 path angle
57 path angle
P wave velocity [m/s]
P wave Velocity [m/s]
Differential Stress [MPa]
Volumetric Strain [%]
Axial Strain [%]
C'
D'
Onset of Dilation
Onset of Dilantancy
Onset Of Dilantancy
Dilation Overdominates Compaction
Dilation overdominates Compaction
Failure

2.4 Discussion

2.4.1 Effect of the heat treatment on the crack density

(1) Heat treatment and crack density

Cracks formed in heat-treated andesite are mainly due to thermal stresses because minerals or aggregates have different thermal expansion coefficients [Friedrich and Wong, 1986]. According to theoretical considerations based on thermoelasticity and fracture mechanics, the total surface of crack S (per unit volume) created during heat treatment and due to different thermal expansion of minerals is given by [Davidge and Green, 1968; Fredrich and Wong, 1986]:

$$S = \frac{1}{8G_{IC}}\left[\frac{E}{1-2v}\right](\Delta\alpha\ \Delta T)^2 \qquad (2\text{-}1)$$

where E is Young's modulus of the (intact) andesite (E=64.7 GPa), υ is Poisson's ratio of intact andesite (υ=0.28) and Δα is the thermal expansion contrast between plagioclase and quartz/tridymite or glass, which can be estimated as 14×10^{-6}/°C. ΔT is the temperature of the heat treatment. G_{IC} is the energy release rate of andesite under mode I and is estimated to be 5 J/m^2 - 6.5 J/m^2 (Fredrich and Wong, 1986; Tutluoglu and Keles, 2011; Mayukh Talukdar, 2018) In addition, the relationship between the total surface of the crack S and the crack density, $\rho = Nl^3/V$, is S=2 π ρ / c, where c is the mean radius of the crack in the volume V (l=2c).

Following Wang et al. (2013), and assuming that the average thermal crack size is that of the grain size, *l*, (i.e., *c=l/2*), we can estimate the crack density created i) in the matrix or ii) at the interface between the large inclusions and the matrix. In the matrix, grains of plagioclase and quartz/tridymite have an average length of 1 μm, which leads to a crack density of 0.04~0.053. However, the large inclusions have average lengths of 100 μm-200 μm, which lead to crack densities of 0.4~0.53, values much higher than the crack density generated in the matrix. The

estimated initial crack density is ρ = 0.6 (Figure 2.3) for andesite samples heat-treated at 930°C. Note that this figure is out of the range of validity for effective medium theory. However, this value quantitatively indicates a high degree of cracking.

In addition, we can define the aspect ratio $\xi = w/c$, where w is the crack half aperture. The total crack porosity is equal to $\Phi = 2\pi \rho \xi$, which is 3.7% after the heat treatment. This value leads to a crack aspect ratio of approximately 10^{-2}, an order of magnitude that agrees with those in previous studies [Wang et al. 2013; Adelinet et al. 2010].

(2) Crack density and anisotropy

The evolution of the crack density during loading can be deduced from the evolution of the elastic P-wave velocities (Fortin et al. 2011). More precisely, assuming a transversely isotropic symmetry, noninteraction and dry conditions, the two components of the crack density tensor can be deduced from the ultrasonic measurements (Gueguen and Kachanov, 2011). An alternative and equivalent method is to estimate, from the ultrasonic measurements, the vertical crack density and the randomly oriented crack density (Gueguen and Kachanov, 2011, Fortin et al. 2011, Nicolas et al. 2016). See also the appendix "Crack density inversion method – Transversely isotropic symmetry".

The evolution of the crack density for the experiments performed at Pc=30 MPa on the non-heat-treated samples and heat-treated samples is shown in Figure 2.10. In the non-heat-treated samples, the crack density evolution is directly correlated with the initiation and propagation of cracks at the onset of dilatancy. These induced cracks are mainly axial, and the density of the randomly oriented cracks is almost equal to zero during the loading (Figure 2.10a).

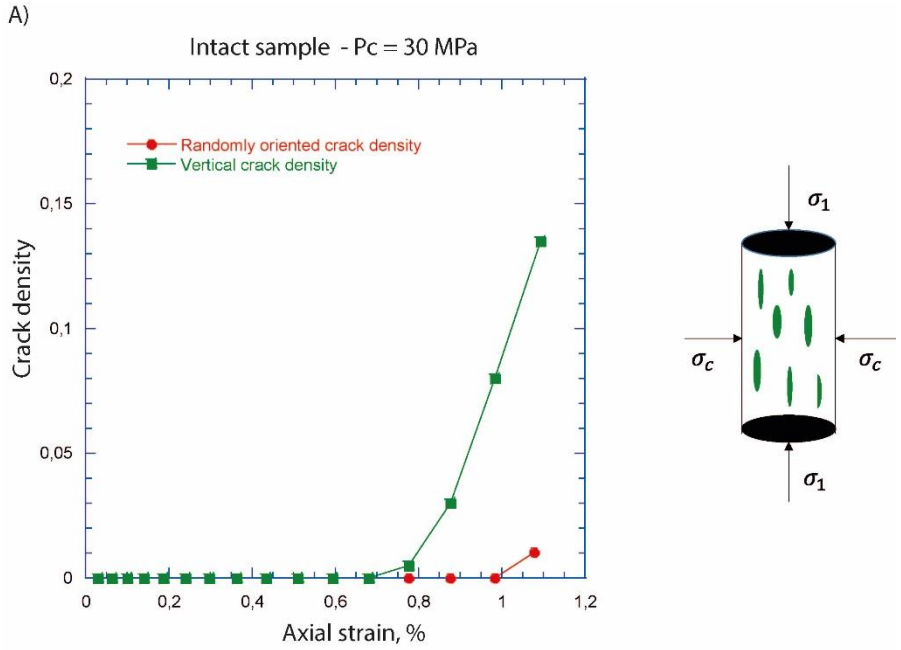

Figure 2.10: Axial crack density and randomly oriented crack density evolution versus axial strain during triaxial deformation experiments on a) non-heat-treated andesite samples under confining pressure of 30 MPa and

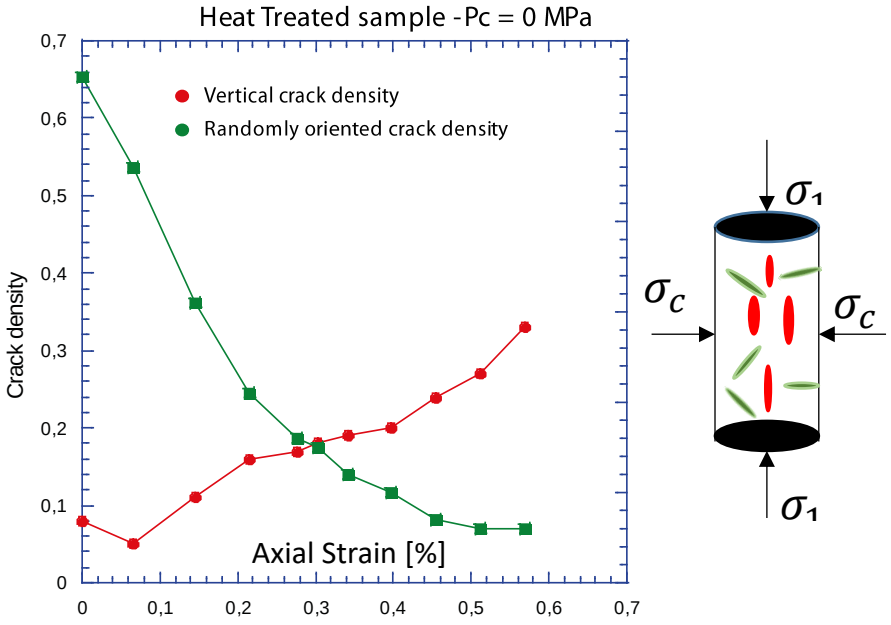

Figure 2.10 (b) heat-treated (at 930°C) andesite samples under confining pressure of 30 MPa.

In heat-treated samples that contain pre-existing thermal cracks, the randomly oriented crack density starts to decrease at the beginning of differential loading, while the axial crack density

increases significantly beyond the onset of dilatancy. The axial crack density in Figure 2.10b increases even before the onset of dilatancy. As the axial stress increases, the pre-existing randomly oriented cracks close while the axial cracks open. Crack opening causes a decrease in the P-wave velocity and an increase in the crack density.

Note that the crack density inverted in Figure 2.3 is based on the measurement of the P-wave velocity at ambient pressure, whereas the crack density inverted in Figure 2.10 is based on the measurement of the P-wave velocity under a confining pressure of 30 MPa. Due to the effect of pressure, the P-wave velocities increase as the pressure increases; thus, the crack density decreases as the confining pressure increases. This phenomenon explains why the initial crack density in Figure 2.10 is lower than that reported in Figure 2.3.

2.4.2 Effect of heat treatment on the microstructure: partial melting

The question is: where does the melt go? Figure 2.11 shows that the melt seals some cracks, especially the cracks with the largest apertures. We also observe that bubbles are distributed in the melt in agreement with the observations of Simmons and Richter [1976], Swanenberg [1980], and Roedder [1981], indicating that the bonding strength is recovered. The melt flows into the cracks, and as it cools, the glass bonds the two surfaces of cracks. Bubbles are clearly observed in the SEM (Figure 2.6). Since the spherical bubbles represent relatively stable pore shapes, we refer to the bubble planes as being strength recovered.

SEM and EBSD reveal that the melt content is an amorphous phase that contains Fe, K, and Mg. Partial melting probably results from the presence of smectite, which has lowered melting point of other minerals. Indeed, the melting point of pyroxene and plagioclase is 1400°C, whereas smectite melts at temperatures of 400-500°C.

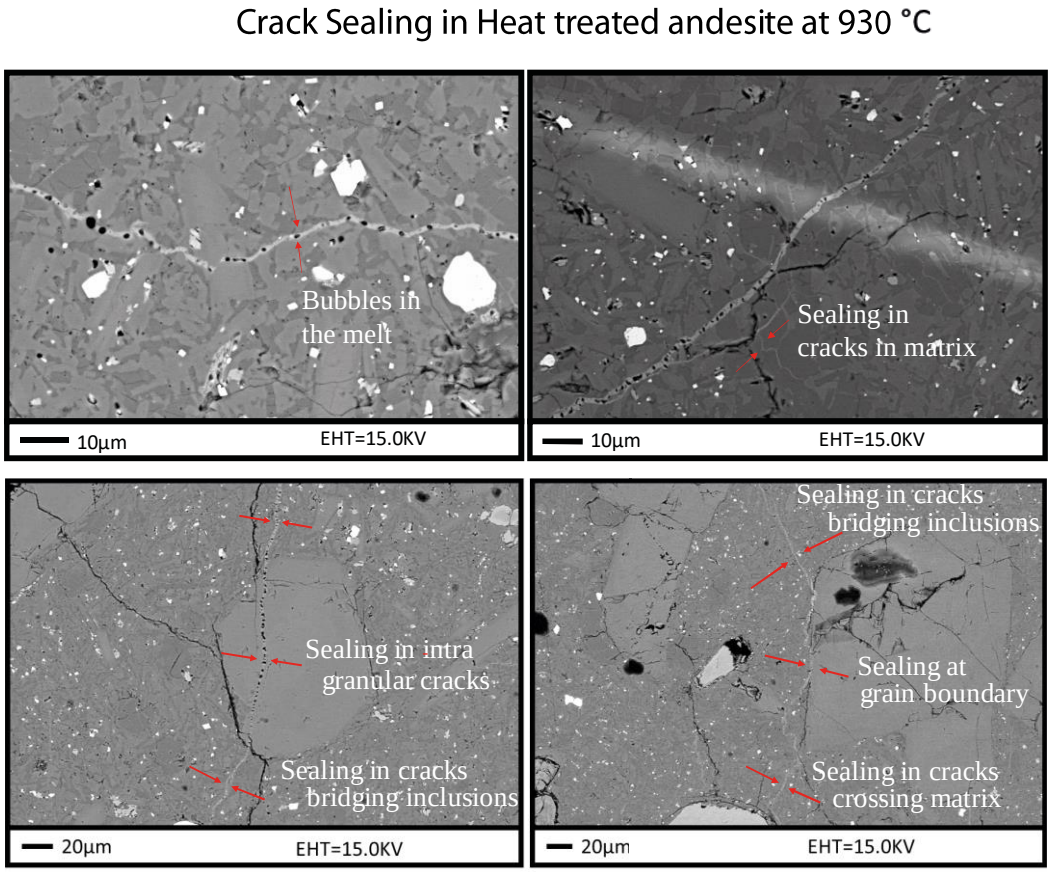

Figure 2.11: Crack sealing observed in intergranular cracks. Bubbles observed in the melt which seals the cracks.

2.4.3 Effect of heat treatment on mechanical strength

(1) Effect on the onset and development of dilatancy

The stress states at the onset of dilatancy (C') during constant strain rate triaxial deformation experiments of intact and heat-treated andesite samples are plotted in Figure 2.12. Heat treatment does not induce any change in the stress state at the onset of dilatancy despite the dramatic increase in damage (crack density). This result can be explained by the fact that C' is sensitive to crack nucleation or propagation regardless of the initial crack density.

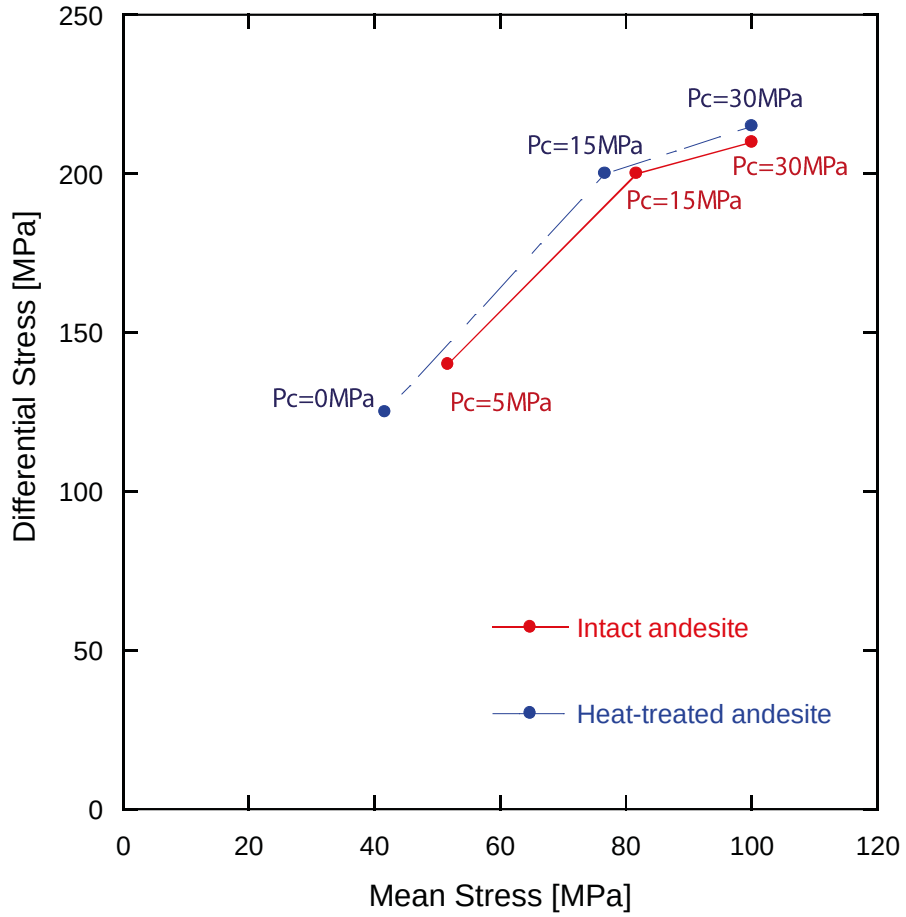

Figure 2.12: Stress states C' (onset of dilatancy) in non-heat-treated samples and heat-treated samples (at 930°C).

Wing crack damage models are currently used to quantitatively analyze the dilatancy evolution under axisymmetric loading. Brittle faulting can be modeled by a sliding wing crack model (Cotterell & Rice, 1980). Following Ashby and Sammis (1990), wings are expected to start to grow from pre-existing flaws at an axial stress equal to:

$$\sigma_1 = \frac{(1+\mu^2)^{1/2}+\mu}{(1+\mu^2)^{1/2}-\mu}\sigma_3 + \frac{\sqrt{3}}{(1+\mu^2)^{1/2}-\mu}\frac{K_{IC}}{\sqrt{\pi a}} \qquad (2\text{-}2)$$

where σ_1 and σ_3 are the maximum and minimum principal stresses, μ is the friction coefficient on pre-existing flaws, K_{IC} is the fracture toughness and a is the length of pre-existing flaws. Note that this criterion (eq. 2) is not directly sensitive to the crack density. The length of pre-existing flaws, a, is estimated to be in the range of 100 μm-300 μm, which corresponds to the

average length of large inclusions. Fitting the onset of dilatancy for triaxial deformation experiments performed at different confining pressures on intact samples, the friction coefficient μ is estimated to be equal to 0.57, and the fracture toughness K_{IC} is in the range from 1.1 MPa $m^{1/2}$-1.9 MPa $m^{1/2}$. The friction coefficient is in good agreement with the mean values found in rocks [Byerlee, 1978], and the fracture toughness is in the range of values obtained for andesite (1 MPa $m^{1/2}$-2 MPa $m^{1/2}$), as measured by Ouchterlony (1990), Tutluoglu and Keles (2011), and Nara et al. (2012).

The friction coefficient μ_{HT} is estimated to be 0.57, the same value as for non-heat-treated samples. The fracture toughness for heat-treated andesite samples $K_{IC\text{-}HT}$ is estimated in the range 1 MPa $m^{1/2}$-1.7 MPa $m^{1/2}$, values slightly lower than those for non-heat-treated samples.

(2) Effect on the peak strength

Heat-treated samples of andesite have higher peak stresses than intact samples (Figure 2.13).

The 2D damage model previously presented to analyze the onset of dilatancy can also be used to quantitatively model the failure of the samples (Ashby and Sammis, 1990; Kemeny & Cook, 1991; Baud et al., 2000; Mallet et al., 2015). This model leads to a brittle failure envelope that can be described as:

$$\sigma_1 = A(\mu, D_0)\sigma_3 + B(\mu, D_0)\frac{K_{IC}}{\sqrt{\pi a}} \qquad (2\text{-}3)$$

where A and B are constants that depend on the friction coefficient on pre-existing flaws and on the initial damage (D_0) defined as $D_0 = \frac{4}{3}\pi(\alpha a)^3 N_V$, where Nv is the number of sliding cracks initially present. According to the model prediction, peak strength decreases with initial damage, assuming a is a constant, which may seem to contradict our results showing an increase in peak stress after heat treatment despite an increase in initial damage.

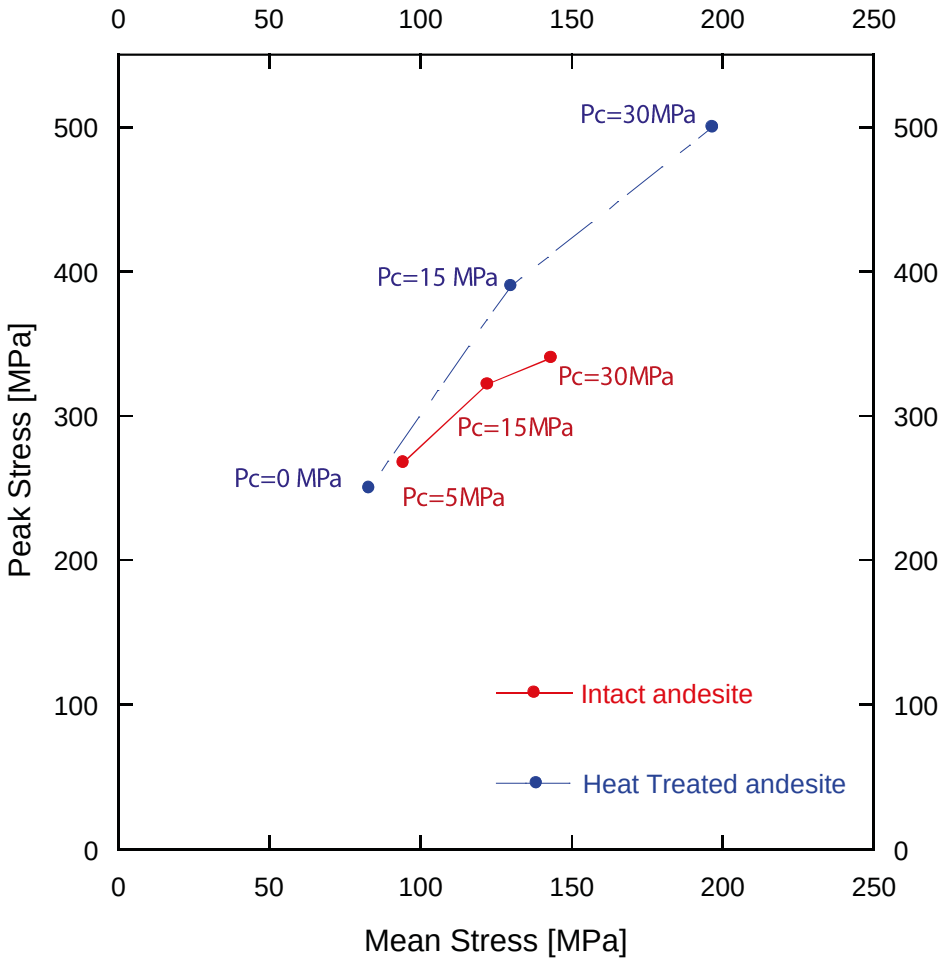

Figure 2.13: Stress states at failure in non-heat-treated samples and heat-treated samples (at 930°C).

However, the previous model is probably too simple for at least two reasons. First, the enhancement of heat-treated sample strength relative to those of intact samples could be related to a crack sealing process. Microstructural observations show that the longest and largest fractures passing through the matrix are sealed. During the temperature increase, partial melting of some minerals occurs, and the melt flowed along the cracks that had already formed first due to thermal stress (This interpretation implies that parameter a is not a constant and is likely to decrease). The melt filled part of the cracks and finally led to amorphous medium filling and sealing of cracks during cooling.

A second reason is that the most dangerous cracks are the longest ones. Crack sealing of the longest cracks implies an effective crack length decrease. The longest cracks are segmented into smaller length cracks. In contrast with elastic moduli, which depend on crack density, the mechanical strength is controlled by the longest cracks.

2.5 Conclusions and Perspectives

This investigation aimed to quantify thermal treatment effects on the microstructure (cracking) and the physical and mechanical properties of andesite. In situ conditions (high temperature) and the presence of fluid might modify our observed results. At elevated temperatures during triaxial deformation, the high temperature range (500°C-1100°C) could lead to a brittle-ductile transition and thus more complicated mechanical behavior (Violay et al., 2017).

The main results of this work are as follows:

(1) Due to thermal treatment, the P-wave velocity decreases by up to 50% as the temperature of heat treatment varies from room temperature to 1100°C. The crack density increases to 0.6.

(2) A clay content as low as 1.5% in the intact rock leads to partial melting for a temperature of heat treatment > 500°C. Partial melting modifies the microstructure and the characteristics of the rocks.

(3) A small amount of crack sealing changes the distribution of the crack size. The ultrasonic velocity is weakly modified, but the mechanical strength is enhanced.

(4) Thermal treatment could have a strengthening effect on a rock depending on the original microstructure of the rock and the mineral content. This result is counterintuitive but might be linked to the presence of clay in the andesite.

Acknowledgement

We thank Léa Lévy for help with SEM observation and XRD analysis, and thanks to Dr. Thomas Ferrand and Dr. Sarah Incel for discussion. This work is supported by the French State through the Future Investments funds under GROTREF project, which is a multidisciplinary platform for innovation and demonstration activities for the exploration and development of high geothermal energy in fractured reservoirs.

2.6 Appendix

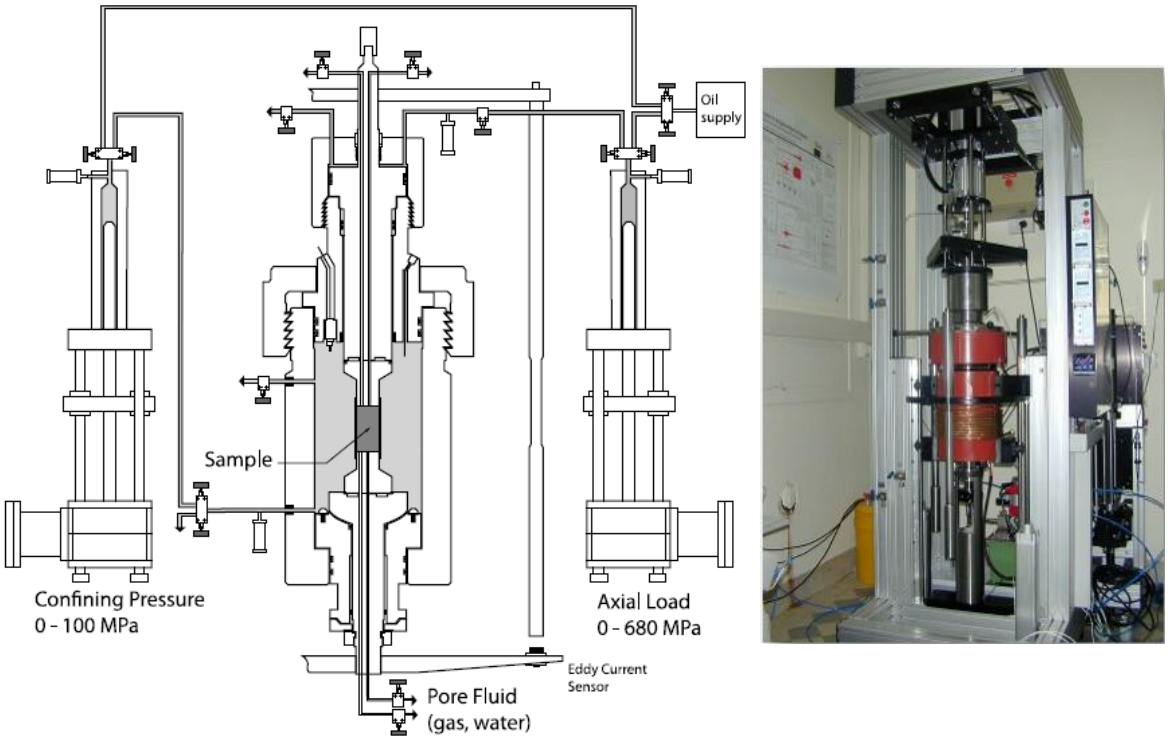

Figure 1. Triaxial cell installed at École Normale Supérieure (Adapted from Ougier-simonin et al., 2010,2011)

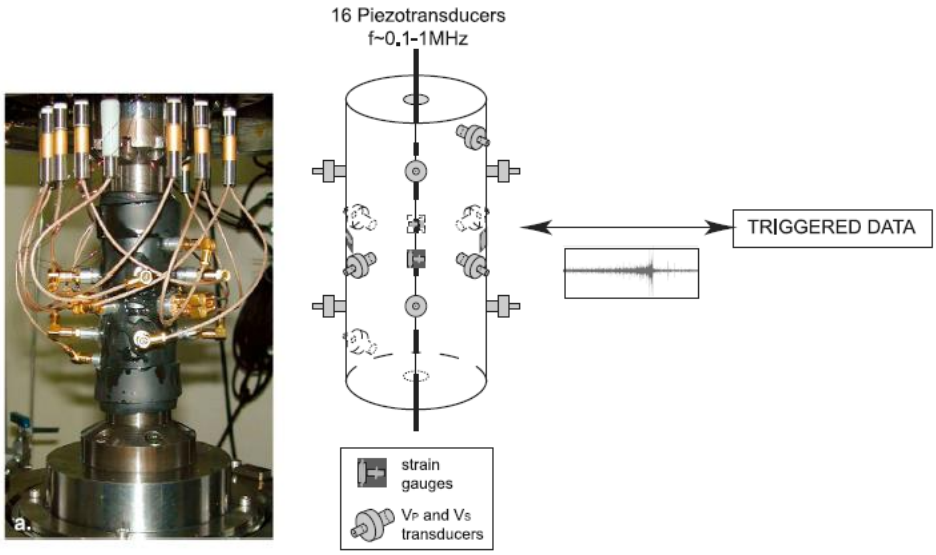

Figure 2. Ultrasonic sensors and strain gauges glued on samples (adapted from Ougier-Simonin et al., 2010, 2011)

Crack density inversion method – Isotropic case

In the noninteraction approximation, the effective elastic properties in the dry case are given by (Bristow 1960):

$$\frac{K_o}{K} = 1 + \rho_c \frac{h}{1 - 2\upsilon_o}\left(1 - \frac{\upsilon_o}{2}\right)$$

$$\frac{G_o}{G} = 1 + \rho_c \frac{h}{1 + \upsilon_o}\left(1 - \frac{\upsilon_o}{5}\right)$$

K is the effective bulk modulus that can be directly inverted from a combination of the P- and S-wave velocities, and G is the effective shear modulus that can be directly inverted from the S-wave velocities. K_o and G_o are the bulk and shear moduli of the crack-free matrix, and υ_o is the corresponding Poisson's ratio of this state. The value h is a factor given by

$$h = \frac{16(1 - \upsilon_o^2)}{9\left(1 - \frac{\upsilon_o}{2}\right)}$$

Crack density inversion method – Transversely isotropic symmetry

In a more general case when the orientation distribution is not isotropic, the overall moduli cannot be expressed in terms of ρ_c only. For a unified coverage of nonrandom orientations, a second rank tensor α is substituted for the scalar crack density ρ_c:

$$\alpha = \frac{1}{V}\sum (a^3 \boldsymbol{nn})^i$$

where $\boldsymbol{n}$ is a unit normal to a crack and **nn** is a dyadic product. The linear invariant $\alpha_{kk} = \rho_c$ so that α is a natural tensorial generalization of ρ_c; the fourth-rank tensor

$$\beta = \frac{1}{V}\sum (a^3 \boldsymbol{nnnn})^i$$

was identified as a fourth-rank crack density tensor. However, this tensor plays a relatively minor role in the dry case. A general transversely isotropic orientation distribution of cracks is realistic for the thermally treated rock under deviatoric stress.

For transversely isotropic symmetry along the axis, the crack density tensor α is (Fortin et al., 2011; Nicolas et al., 2016):

$$\alpha = \frac{\rho_i}{3}\begin{pmatrix} 1 & 0 & 0 \\ 0 & 1 & 0 \\ 0 & 0 & 1 \end{pmatrix} + \frac{\rho_v}{2}\begin{pmatrix} 1 & 0 & 0 \\ 0 & 1 & 0 \\ 0 & 0 & 1 \end{pmatrix}$$

where ρ_i is the randomly oriented crack density, associated to the thermal cracks in the paper, ρ_v is the axial crack density induced by the mechanical loading. Under the non-interacting approximation, the relation between the stiffness tensor C and α is (Sayers & Kachanov 1995; Nicolas et al., 2016):

$$\begin{cases} C_{11} + C_{12} = (\frac{1}{E_0} + \alpha_{33})/D \\ C_{11} - C_{12} = 1/(\frac{1+v_0}{E_0} + \alpha_{11}) \\ C_{33} = (\frac{1+v_0}{E_0} + \alpha_{11})/D \\ C_{44} = 1/(\frac{2(1+v_0)}{E_0} + \alpha_{11} + \alpha_{33}) \\ C_{13} = (\frac{v_0}{E_0})/D \\ C_{66} = 1/(\frac{2(1+v_0)}{E_0} + 2\alpha_{11}) \end{cases}$$

where

$$D = \left(\frac{1}{E_0} + \alpha_{33}\right)\left(\frac{1-v_0}{E_0} + \alpha_{11}\right) - 2(\frac{v_0}{E_0})^2$$

From the effective stiffness tensor, the wave phase velocities along the propagation angles ϕ corresponding to the sensors' setup are (Mavko et al. 1998; Nicolas et al., 2016):

$$V_p(\phi) = \left[\left(C_{11}sin^2(\phi) + C_{33}cos^2(\phi) + C_{44} + \sqrt{M}\right)/2\rho\right]^{1/2}$$

$$V_p(\phi) = \left[\left(C_{11}sin^2(\phi) + C_{33}cos^2(\phi) + C_{44} - \sqrt{M}\right)/2\rho\right]^{1/2}$$

$$V_p(\phi) = [(C_{66}sin^2(\phi) + C_{44}cos^2(\phi))/\rho]^{1/2}$$

where

$$M = ((C_{11} - C_{44})sin^2(\phi) - (C_{33} - C_{44})cos^2(\phi))^2 + ((C_{13} + C_{44})\sin(2\phi))^2$$

Then, a least square procedure is used to compare predicted synthetic data and measured ultrasonic velocities. The inverted axial crack density corresponds to the value with the minimum distance between predicted and measured velocities (Fortin et al., 2011; Nicolas et al., 2016).

Chapter III Influence of Hydrothermal Alteration on The Elastic Behavior and Failure of Heat-Treated Andesite from Guadeloupe

This paper is under review of Geophysics Journal International by A. Nicolas, L. Levy, L. Zhi, O. Sissmann, J. Fortin, B. Gibert and F. Sigmundsson

Abstract

Studies on the mechanical behaviour of rocks, including volcanic rocks, usually seek for the purest and healthiest material: unaltered, without macroscopic defects. However, natural volcanic rocks are often altered due to the circulation of hydrothermal fluids; and this alteration is susceptible to influence the rock mechanical and petrophysical properties. This study precisely focuses on the effect of alteration on the elastic and failure mechanical properties of andesite. A relatively fresh and homogeneous block of natural andesite was retrieved from a quarry. Three samples were heat-treated and artificially altered at different levels by soaking them in a brine for one month at a pressure of 20 MPa and temperatures of 80◦C, 180◦C and 280◦C, respectively. To characterize their mechanical behaviour, samples were hydrostatically loaded up to 50 MPa and unloaded while strains and elastic wave velocities were recorded. Then, samples were deformed triaxially at a constant strain rate under a confining pressure of 15 MPa, until failure. At ambient pressure, increasing alteration resulted in increased wave propagation velocity, indicating an increased elastic moduli. During hydrostatic loading, volumetric deformation at a given effecive pressure decreased with alteration. During triaxial loading, alteration decreases elastic compaction and the peak stress at failure. These observations are interpreted as the result of micro-cracks in-filling by alteration minerals, and in particular smectite, which has a low friction coefficient. Experimental results are modelled with a damage model based on crack propagation from pre-

existing flaws. A decreasing friction coefficient within the flanks of the cracks leads to a decrease of the peak stress and explains experimental observations. The effects of thermal crack damage on the physical properties and rupture processes of andesite were investigated under triaxial deformation at room temperature. Thermal cracking was induced by slowly heating and cooling samples.

Keywords: Mechanical behaviour; Elastic properties; Hydrothermal systems

3.1 Introduction

Understanding the mechanical behaviour of rocks in volcanic geothermal systems is important to predict induced seismicity and well bore failure in industrial contexts such as geothermal reservoir engineering and CO2 sequestration, as well as to prevent natural hazards related to fault-activation and to explain ground deformation in volcanic areas revealed by GPS and InSAR observations (e.g. Massonnet & Sigmundsson 2000; Pedersen & Sigmundsson 2004; Pagli et al. 2006). Numerous laboratory studies have exposed stress-strain relationships for a variety of unaltered volcanic rocks (e.g. Stanchits et al. 2006; Heap et al. 2009, 2011, 2015; Adelinet et al. 2010, 2013; Fortin et al. 2011; Nara et al. 2013). However, alteration minerals, and in particular expandable minerals, such as smectite, are abundant in volcanic geothermal systems (e.g. Reyes 1990; Meunier 2005), in subduction zones (e.g. Hyndman et al. 1997; Passele`gue et al. 2014) and in some major faults (e.g. Chester et al. 2013; Yamaguchi et al. 2011), where hot fluid circulates in the host rock (e.g.Geoffroy & Dorbath 2008; Adelinet et al. 2011), causing dissolution and secondary mineralization (e.g. Browne 1978; Zimbelman et al. 2005; Navelot et al. 2018). The presence of alteration minerals can significantly modify the mechanical behaviour of rocks, due to microstructural changes as compared to pure and healthy rock (e.g. Heap et al. 2014; Siratovich et al. 2014; Navelot et al. 2018). Indeed, microstructural changes modify the physical properties (porosity, open crack density, velocity of propagation

of elastic waves, permeability) and thus mechanical properties of the rock (Pola et al. 2012; Meller & Kohl 2014; Frolova et al. 2014; Wyering et al. 2014; Navelot et al. 2018). Small changes in microstructural parameters, such as porosity (e.g. Vajdova et al. 2004), pore size (e.g. Zhu et al. 2010), crack density and mean length (e.g. Keshavarz et al. 2010), significantly affect the mechanical behaviour of volcanic rocks. Yet, the specific influence of alteration on the mechanical behaviour of geothermal volcanic reservoirs is still poorly understood (Siratovich et al. 2016). Studying the specific influence of alteration on the elastic behaviour and failure properties of volcanic rocks requires the use of samples with identic microstructures but altered at different levels, which is difficult to find in nature (e.g. Heap et al. 2017). To overcome this obstacle, a single block of homogeneous andesite was used as starting material and samples from this block were artificially altered at different levels, after heat-treatment. We report results of hydrostatic and triaxial loading experiments performed on untreated, unaltered heat-treated and artificially altered samples, all coming originally from the same lithology. During these experiments, evolution of P and S wave velocities were measured to track the evolution of open porosity. Acoustic emissions were also recorded and localized. The evolution of the mineralogy with both the heat-treatment and the artificial alteration was also carefully tracked, with a special focus on smectite and other clay minerals precipitation.

3.2 Material and methods

3.2.1 Starting material, heat-treatment and artificial alteration

The ideal material would be different blocks of the exact same andesite, naturally altered at different levels. Because it was difficult to find that in the field, a single block of relatively fresh andesite was used and samples were artificially altered to different levels. The block was recovered from an outcrop below Mamelle pass (Guadeloupe, French West Indies). The original andesite is formed of a matrix with large inclusions from tenths to hundreds of microns

(Figure 3.1 a and 3.1b). All samples were cored in the same block), and thin sections were made in several samples to control the similarity of microstructures. Although no bedding was identified, all samples were cored parallel to each other, in order to avoid effects of preferential direction. After coring, faces were ground to ensure a good parallelism. The resulting cylindrical samples have a diameter of 40 mm and a length of 80 mm.

Due to the low permeability of the samples, thermo-fracturation by heat-treatment was needed to be able to saturate the samples with fluids and ensure a homogeneous artificial alteration, as much as possible. Samples were heat-treated at 930°C with a programmable Meker MHT-3 furnace, following the procedure described in Nicolas et al. (2014). Intact samples were heated at a rate of 120°C/h, up to 930°C, kept 2h at the maximal temperature, and then cooled at 120°C/h, to avoid any quenching or thermal shocking effect. All the samples show higher fracture density after heat treatment at 930°C compared to the intact sample (Figure 3.1). This intense microfracturing, increasing the crack surface area and permeability (e.g. Darot et al. 1992), is due to the different thermal expansion coefficients of minerals (e.g. Fredrich & Wong 1986) and the α-β transformation of quartz above 550°C (e.g. Glover et al. 1995).

Three heat-treated samples were altered during one month in an autoclave, saturated with a fluid at a pressure of 200 bar and a temperature of 80°C, 180°C and 280°C. The fluid was prepared to be as as close as possible to the seawater at Rocroy beach, next to the outcrop.

A description of the samples used in this study, along with their identification numbers, can be found in Table 3.1.

3.2.2 Characterization of mineral sand chemical contents

The primary minerals and artificial alteration products were characterised by means of quantitative analyses of X-Ray Diffraction (XRD) patterns, measured on powders from whole rock samples, XRD measurements on the fraction < 2µm of the samples, Cation Exchange

Capacity (CEC) measurements on powders from whole rock samples and Scanning Electron Microscope (SEM) observations on thin sections associated to chemical analyses by Energy Dispersion Spectroscopy (EDS).

The CEC was measured by back-titration of the molecule Copper-triethylenetetramine(II), which replaces all exchange cations in minerals subjects to cation exchanges. A protocol using this molecule, originally developed to measure the CEC on pure clay minerals (Meier & Kahr 1999), was adapted to measure the CEC of altered volcanic rocks (Levy et al. 2018) and used here. The CEC measurements for all samples can be found in Table 3.1, together with estimated uncertainties.

The XRD patterns were analysed with the Rietveld refinement method using the BGMN software to provide with a quantification of the mineralogy (Taut et al. 1998). The quantifications are detailed in Table 3.2.

Fluids were analyzed by Atomic Emission Spectroscopy in an Inductively Coupled Plasma (ICP-AES). The fluid compositions before contact with the rock, after equilibration with the unaltered samples and after alteration at 80, 180 and 280°C can be found in Table 3.3.

3.2.3 Petrophysical properties

Connected porosity values of the untreated samples were measured using a triple weight procedure at ambient pressure. The initial connected porosity is low (1% +/- 0.3%) (Figure 3.1 a). Initial P and S wave velocities are 4938 m/s and 2792 m/s, respectively (Figure 3.4 b). Density along the untreated samples was also measured using a medical CT-scan. These three measurements were repeated after heat-treatment and after alteration.

3.2.4 Experimental Apparatus

The pressure vessel used in this study is a conventional triaxial cell installed in the Laboratoire de Geologie at the Ecole Normale Superieure in Paris. Axial load was applied by an axial piston and measured with an accuracy of about 10^{-2} MPa. Radial pressure was controlled by a pump. The confining pressure ($\sigma_2 = \sigma_3$) is measured by a pressure transducer with an accuracy of about 10^{-2} MPa. A detailed description of the apparatus can be found in Brantut et al. (2011); Ougier-Simonin et al. (2011). Strains were measured using double strain gauges (Tokyo Sokki TML type FCB 2-11), directly glued on the sample. These gauges were composed of one axial and one radial gauge. The axial displacement was also measured with three displacement transducers (DCDT), mounted outside the pressure vessel between the moving piston and the fixed lower platen. For both strain gauges and DCDTs, mean displacements were considered. The DCDT measurements were corrected for the stiffness of the cell, using the strain gauge measurements. The strain uncertainty measured with gauges was estimated to 10^{-5}. DCDT signals have an accuracy of about 10^{-4}. The volumetric strain was calculated as $\varepsilon_v = \varepsilon_{ax} + 2\varepsilon_r$, where ε_{ax} and ε_r are the axial and radial strains, respectively.

Before the measurement, samples were dried in an oven at $\sim 40^{\circ}$C for several days. Neoprene tubing was used to separate the sample from oil confining medium. In addition to the gauges, sixteen piezoelectric transducers (PZTs; 1 MHz resonance frequency) were glued directly onto the sample surface through holes drilled in the jacket. Among the sensors, twelve are sensitive to P-waves and the others to S-waves. Transducers were used as sources and receivers (active mode) to measure the evolution of P and S wave velocities every 5 minutes during deformation (e.g. Fortin et al. 2007a; Wang et al. 2012). Arrival times were determined with an accuracy of 0.1s. This gives an accuracy of 5% for the elastic velocities. Acoustic sensors were also used in passive mode to record acoustic emissions occurring during rock deformation (e.g. Fortin et

al. 2006, 2009). A thorough description of the acoustic system can be found in Brantut et al. (2011).

To characterise the mechanical behaviour under pressure, confining pressure was increased from 0 MPa to 50 MPa at a rate of 3 MPa/min. The maximum pressure was maintained constant for around 10 min and the sample was then unloaded from 50 MPa to 0 MPa. After that, samples were reloaded hydrostatically up to the desired confining pressure of 15 MPa. The differential stress was then applied by deforming the sample at a controlled strain rate of $\sim 10^{-5}s^{-1}$, until failure.

3.3 Results

3.3.1 Evolution of mineralogy with heat-treatment and alteration

The content of major mineral phases is similar between untreated, heat-treated unaltered and heat-treated altered sample (see Table 2): 70% to 75% of plagioclases (labradorite, albite), 5% to 10% of K-feldspars (sanidine), 5% to 10% of pyroxene (augite), 2-3% of SiO2 (quartz, trydimite, crystobalite) and 2-3% of iron-oxide (ilmenite, hematite). Rietveld-refinements of XRD analyses do not allow drawing a clear trend for the evolution of these minerals with heat-treatment and alteration. This section focuses on the variations of the clay mineral content (minor phases) after heat-treatment and alteration.

(1) Effects of heat-treatment

Two different clay minerals are identified in the starting, untreated, material: smectite and biotite. The presence of chlorite is possible. The main desired effect of heat-treatment is to increase the connected porosity in order to increase the permeability and enable homogeneous fluid saturation for alteration. But a side effect is the dehydration and, most often, dehydroxylation of clay minerals

after they undergo a temperature of 930◦C.

Smectite is identified in two distinct samples taken from the original block of andesite: AL-NTT1 and AL-NTT2, both by XRD patterns on fine fraction (Figure 3.3) and chemical analyses of SEM images (Figure 3.1). Moreover smectite is consistently quantified by XRD patterns on whole rock (Table 3.2) and CEC measurements (Table 3.1), with 3 wt.% in sample AL-NTT1 and 1 wt.% in sample AL-NTT2. Indeed, the CEC of altered volcanic rocks, measured by Cu-trien, can be converted into weight fraction of smectite content: Smec . % $= \frac{CEC}{CEC_0}$, with $CEC_0 = 80{\sim}100$ meq/g being the CEC of pure smectite (Levy et al. 2018). Since AL-NTT1 is located inside the block, it has been less exposed to leaching than AL-NTT2, located outside the block. Therefore, the value of 3 wt.% is considered to be the intial quantity of smectite in the samples before heat-treatment. It is observed in Figure 1 that smectite is associated to pyroxene replacement in the rock mass. As a consequence, the presence of smectite in the untreated samples is interpreted as the product of slow, diagenetic transformation of the volcanic matrix, possibly aided by the presence of trapped fluids (e.g. residual magmatic water).

Table 3.1 Description of the six samples used in this study, with results from the CEC measurements

ID	Description	CEC
		meq/100g
AL-NTT1	Untreated sample, taken inside the block	3.26 ± 0.20
AL-NTT2	Untreated sample, taken outside the block	1.08 ± 0.14
AL-NA-TT	Heat-treated but unaltered, reference sample	0.00 ± 0.00
AL-80	Heat-treated and altered at 80˚C	0.00 ± 0.20
AL-180	Heat-treated and altered at 180˚C	0.00 ± 0.20
AL-280	Heat-treated and altered at 280˚C	0.48 ± 0.13

Table 3.2 Mineral content of all samples, according to Rietveld-refinement of XRD patterns

Sample	Labradorite	Albite	Sanidine	Augite	Quartz	Tridymite	Crystobalite	Ilmenite	Hematite	Smectite	Biotite
	%	%	%	%	%	%	%	%	%	%	%
AL-80	30.62	38.04	5.04	10.62	7.30	2.14	3.42	0.46	2.18	0.00	0.19
AL-180	32.09	40.88	6.30	6.48	6.15	2.47	2.24	0.56	2.22	0.00	0.61
AL-280	31.08	44.30	5.94	7.37	6.60	2.43	0.00	0.51	1.68	0.00	0.09
AL-NA-NTT1	66.99	5.03	6.46	6.83	7.82	2.51	0.00	0.00	1.21	3.15	0.00
AL-NA-NTT2	26.48	42.86	9.40	8.70	7.01	2.70	0.00	0.00	1.90	0.96	0.00
AL-NA-TT	32.23	34.66	9.04	10.67	7.77	2.35	0.00	0.64	2.46	0.00	0.18

Table 3.3 Fluid compositions by ICP-AES analysis

Fluid	Si ppm	Mn ppm	K ppm	Cu ppm	Ca ppm	Co ppm	Ni ppm	Zn ppm	Cr ppm	Ti ppm	Fe ppm	Ba ppm	Sr ppm
Initial	30.62	0	0	38.04	5.04	10.62	7.30	2.14	3.42	0.46	2.18	0.00	0.19
After saturation	32.09	0	0	40.88	6.30	6.48	6.15	2.47	2.24	0.56	2.22	0.00	0.61
Alteration-80	31.08	44.30	0	0	5.94	7.37	6.60	2.43	0.00	0.51	1.68	0.00	0.09
Alteration-180	66.99	5.03	0	0	6.46	6.83	7.82	2.51	0.00	0.00	1.21	3.15	0.00
Alteration-280	26.48	42.86	9.40	0	0	8.70	7.01	2.70	0.00	0.00	1.90	0.96	0.00

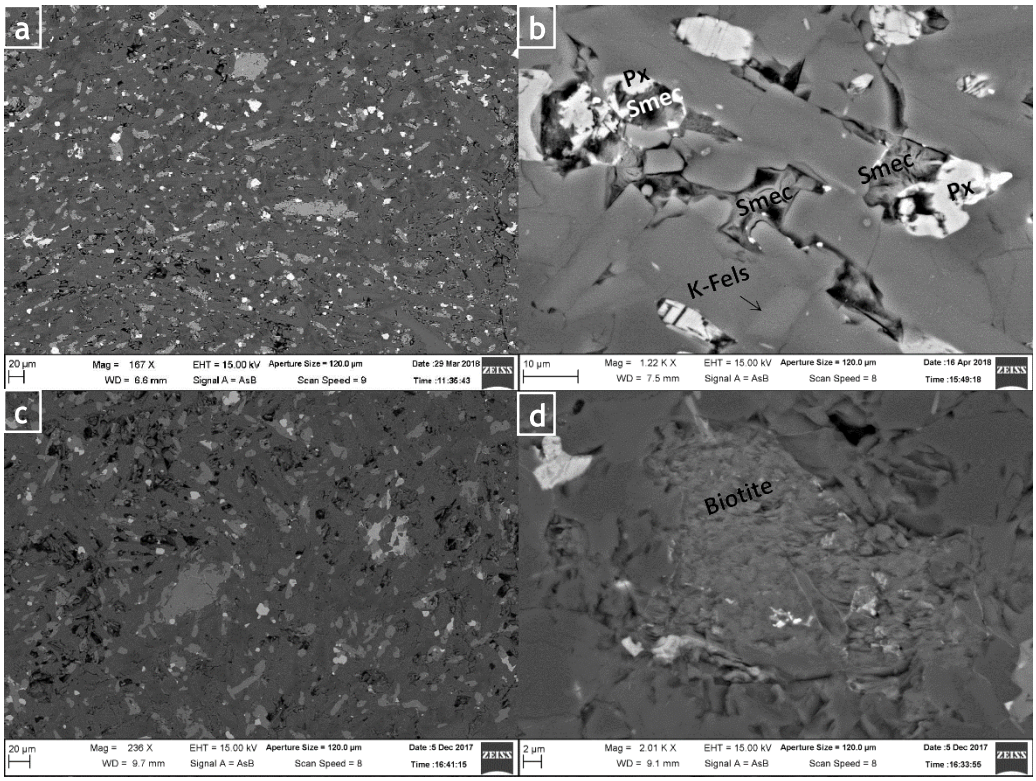

Figure 3.1 SEM observations of the mineralogy before ((a) and(b)) and after heat-treatment (c) and (d)).

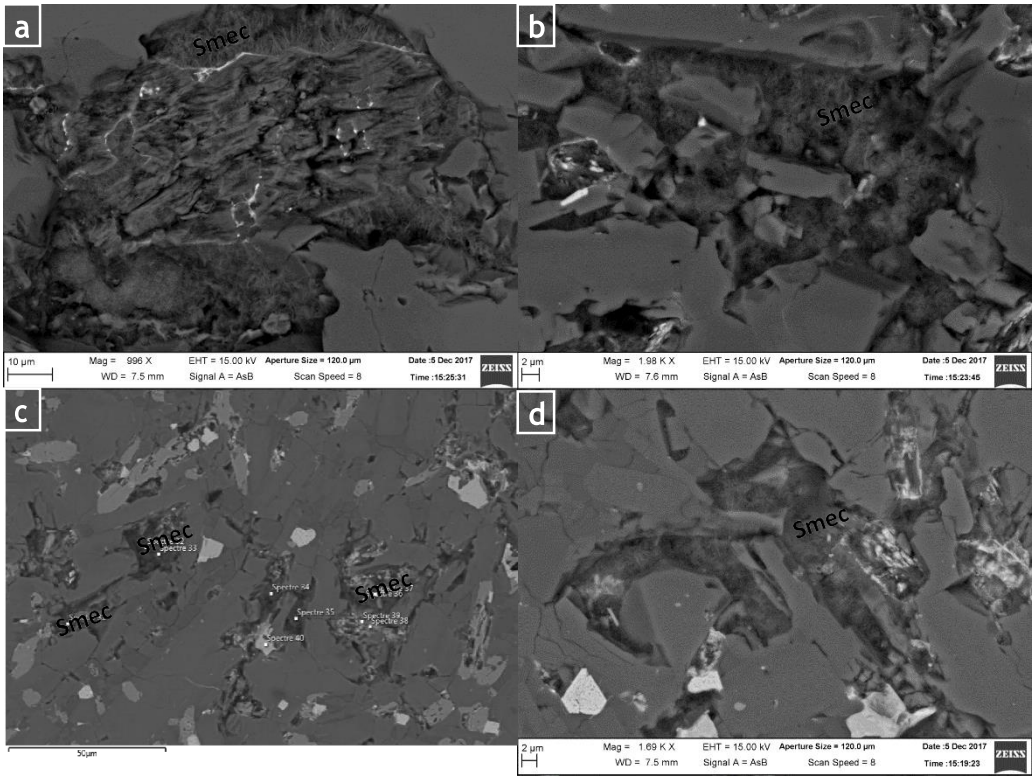

Figure 3.2 SEM observations of the sample altered at 280˚C

After heat-treatment, the smectite content drops to zero, according to CEC measurements and to the collapse of the characteristic 14Å peak observed in XRD patterns of the fine fraction (Figure

3.3). Irreversible dehydration and loss of swelling properties of smectiteoccur at temperatures between 350˚C and 550˚C (e.g. Greene-Kelly 1953; Russell & Farmer 1964) while dihydroxylation of smectite occur at temperatures between 500˚C and 800˚C (e.g. Mackenzie 1957; Grim & Rowland 1944; Malek et al. 1997). The heat-treatment at 930˚C therefore caused both an irreversible dehydration and a dehydroxylation of smectite crystals initially present.

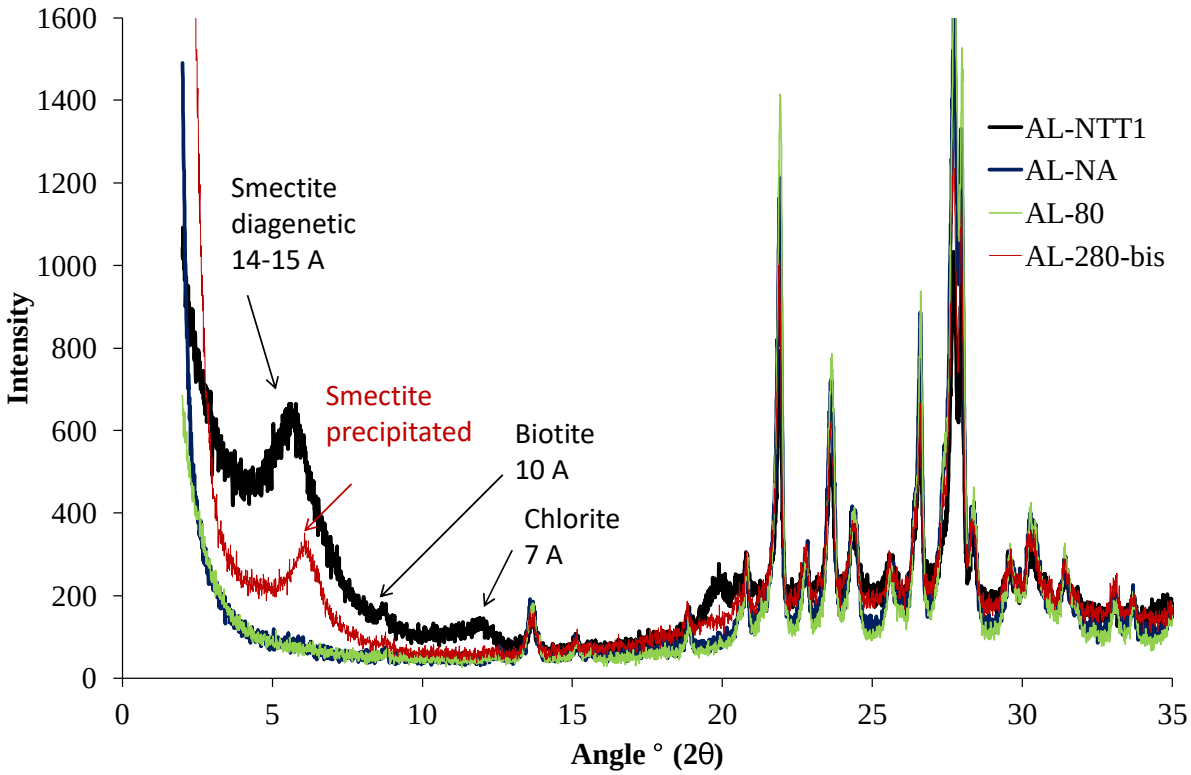

Figure 3.3 XRD patterns of all samples, normalized to the intensity at the lowest angle. The abscissa corre- sponds to twice the angle between the X-Ray beam and the horizontal plane. AL-NTT1 corresponds to the intact fresh andesite, AL-NA to the heat-treated andesite, AL-80 and AL-280-bis to andesite altered at 80 and 280◦C, respectively.

Biotite is inferred by a characteristic peak on the XRD diffraction pattern of the fine fraction (Figure 3.3). This peak alone does not allow the discrimination between biotite and illite. However, the presence of illite should be associated to the transformation of K-feldspar and therefore located in the vicinity of K-feldspar minerals, similarly to smectite slowly transforming pyroxenes. K-Feldpsar are unaltered, which indicates that the presence of illite is unlikely (Figure 3.1b). Since biotite is a common primary mineral in andesistic magmas, the presence of biotite rather than illite is inferred.

Chemical analyses suggest the persistence of biotite after heat-treatment AL-NA (Figure 3.1d). The characterstic 10Å peak observed in the untreated samples AL-NTT1 and AL-NTT2 is less intense in the heat-treated sample AL-NA but has not totally disappeared. This indicates that

the crystalline network of biotite had started to collapse by dehydroxylation when the heat-treatment stopped but that the vitrification of biotite was not complete. This interpretation is strengthened by the high-thermal stability of biotite, up to 1000°C (Skjerlie & Johnston 1992).

The presence of chlorite could explain the 7Å peak observed on the XRD patterns of fine fraction (Figure 3.3). Other characteristic peaks of chlorite diffraction (14Å, 4.7Å, 3.5Å) tend to confirm this interpretation, although the background diffraction of non-clay minerals biases the XRD pattern, with in particular plagioclases remaining in the fine fraction. Since chlorite is commonly found as replacement of biotite in andesistic minerals (Rimsaite 1975), its presence in the intact sample is possible. The collapse of all the characteristic peaks associated to chlorite after heat-treatment is consistent with the fact the dehydroxylation of chlorite occurs at temperatures lower than 930°C. (Zhan & Guggenheim 1995). Therefore, even if chlorite is present in the intact sample, it has disappeared after heat-treatment. As a consequence, the only clay mineral possibly remaining after heat-treatment is ill-crystallized biotite, located in the rock matrix (Figure 3.1d).

After alteration in an autoclave during one month at 280°C, hints of alteration are observed. Precipitation of new smectite is evidenced by the characterstic 14Å peak in sample AL-280, which has undergone the highest level of alteration (Figure 3.3). The presence of smectite in this sample is confirmed by CEC measurements: the same value of 0.48 meq/100g is found after a duplicate analysis using different quantities of rock powders. This value corresponds to about 0.5 smectite wt.%. Chemical analyses of SEM images confirm the presence of a phase having the chemical composition of a smectite, but this mineral is weakly crystallized (Figure 3.2). Although smectite may rehydroxylate upon cooling in the presence of water (Drits et al. 1995), swelling properties (and thus cation exchange properties) are definitely lost (Greene-Kelly 1953). Moreover, the XRD peak is slightly shifted towards higher angles, compared to the smectite peak in the untreated samples (Figure 3.3). Therefore, the increase of CEC and

new 14Å peak upon artificial alteration at 280°C is attributed to new precipitation of smectite in the connected fracture network.

In samples altered at 80°C and 180°C, weakly crystallized smectite may be present but is not observed. The XRD patterns of AL-80 and AL-180 do not show hints of smectite presence, while the CEC is 0. Yet the uncertainty of the CEC measurement is high (Table 3.1). However, fluid analyses confirm that smectite is at equilibrium in the solid and fluid phases (Table 3.3). Therefore, artificial alteration at 280°C of the heat-treated sample has led to an observable precipitation of smectite, whereas effects of artificial alteration at 80°C and 180°C cannot be observed with the mineralogical methods used here.

3.3.2 Evolution of petrophysical properties with heat-treatment and alteration

(1) Effects of heat-treatment

Heat treatment induces an increase in connected porosity from 1% +/- 0.3% to 2.6%+/- 0.1% (Figure 3.4a), which can be explained by the propagation and opening of cracks due to differences in the coefficient of thermal expansion of the minerals. P waves velocities drop from 4.9 to 2.8km/s (Figure 3.4b), showing a crack density increase. The propagation and opening of new cracks can also be inferred from the microstructural observations (Figure 3.1). P and S wave velocities under ambient pressure increase with alteration and the increase is more pronounced for higher alteration temperature: P-wave velocity increase from 2.8 km/s to 3.2 km/s after alteration at 180°C and to 3.9 km/s after alteration at 280°C (Figure 3.4b). Both P and S wave velocities are systematically higher under a confining pressure of 50 MPa than under ambient pressure (Figure 3.4b), which can be explained by crack closure with pressure (Walsh 1965).

Artificial alteration leads to a slight increase in porosity (+0.5%) (Figure 3.4a), more important with higher alteration temperature. This could be either due to new cracks or equant pores.

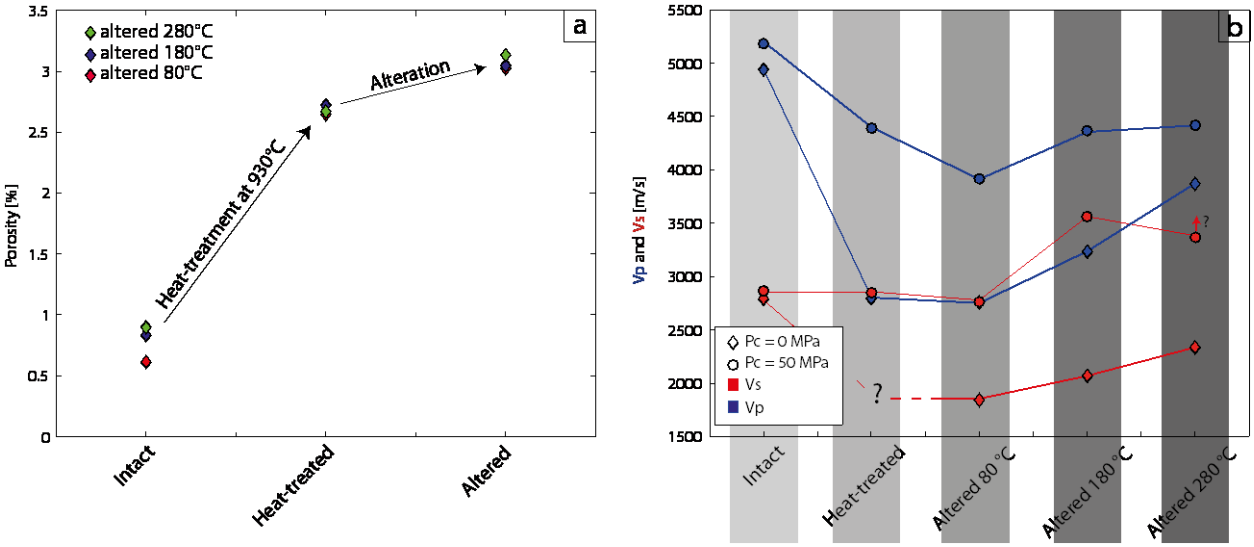

Figure 3.4 (a) Evolution of porosity during the alteration process of samples altered at 80◦C (red diamonds), 180◦C (blue diamonds) and 280◦C (green diamonds). (b) Evolution of Vp at ambient pressure (blue dia- monds), Vs at ambient pressure (red diamonds), Vp under a confining pressure of 50 MPa (blue circles), and Vs under a confining pressure of 50 MPa (red circles) during the alteration process of samples altered at 80◦C, 180◦C and 280◦C.

3.3.3 Evolution of the elastic behaviour under hydrostatic stress with heat-treatment and alteration

In this paper, compressive stresses and compactive strains are counted positive. The principal stresses will be denoted σ_1 and σ_3 , σ_1 being the highest principal stress and σ_3 the confining pressure. The differential stress $\sigma_1 - \sigma_3$ will be denoted Q and the mean stress $(\sigma_1 + 2\sigma_3)/3$ will be denoted P.

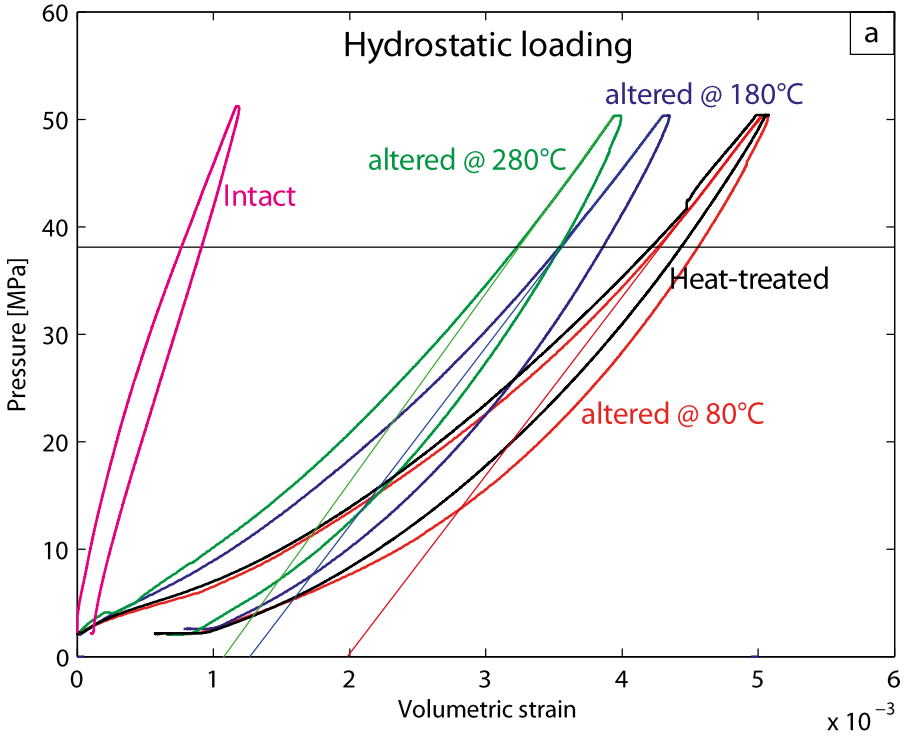
Hydrostatic loading
a
altered @ 180°C
altered @ 280°C
Intact
Heat-treated
altered @ 80°C
Pressure [MPa]
Volumetric strain
x 10 −3
0
10
20
30
40
50
60
0
1
2
3
4
5
6

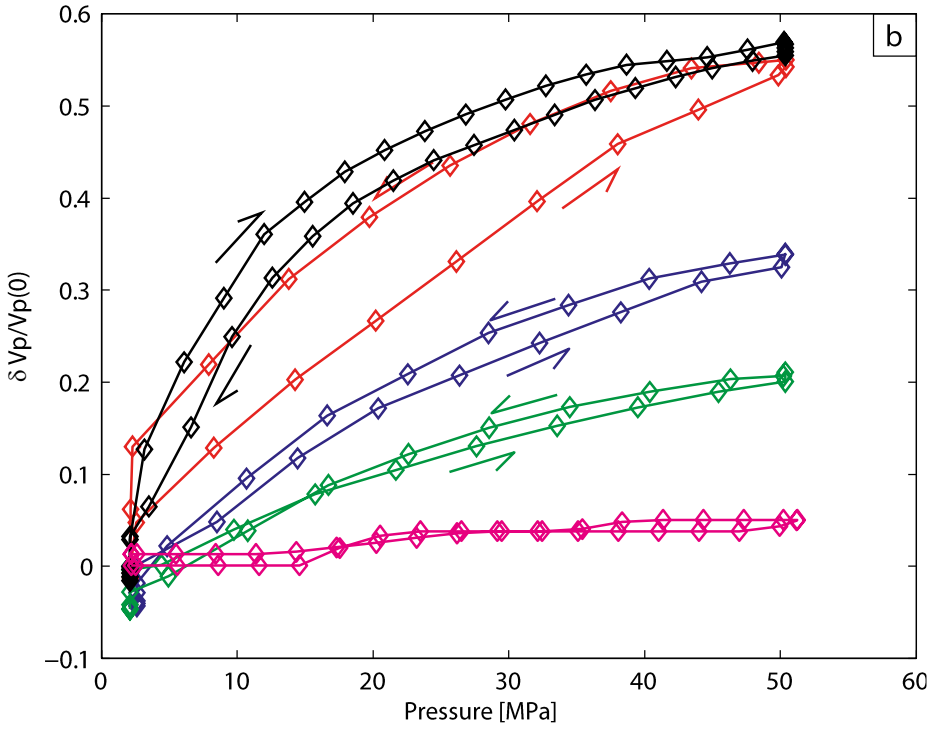
b
δ Vp/Vp(0)
Pressure [MPa]
0.6
0.5
0.4
0.3
0.2
0.1
0
−0.1
0
10
20
30
40
50
60

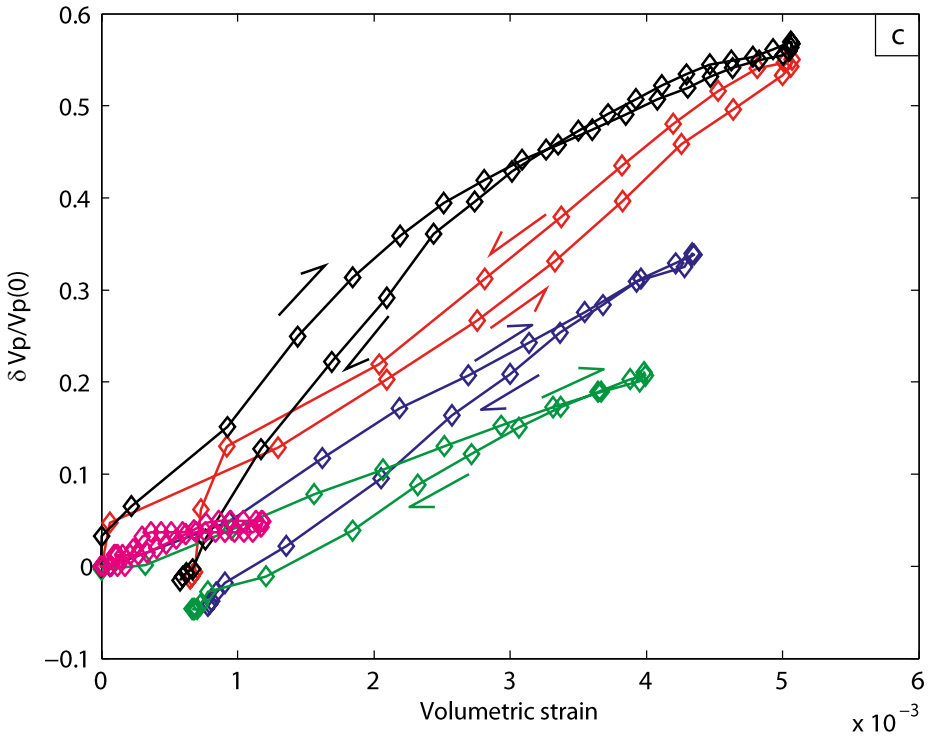

Figure 3.5 (a) Evolution of the volumetric strain plotted versus confining pressure for an intact sample (pink curve), a heat-treated sample (black curve), and samples altered at 80◦C (red curve), 180◦C (blue curve) and 280◦C (green curve). (b) Evolution of δVp/Vp0 (where Vp0 is the P wave velocity at the beginning of isostatic loading) is plotted as a function of pressure for the previous samples. (c) Evolution of δVp/Vp0 (where Vp0 is the P wave velocity at the beginning of isostatic loading) is plotted as a function of volumetric strain for the previous samples.

Results for a hydrostatic loading experiment with up to 50 MPa confining pressure performed on an intact sample, a heat-treated sample and samples altered at 80˚C, 180˚C, and 280˚C are presented in Figure 3.5a. The stress-strain curve of the intact sample is linear with a slope corresponding to a static bulk modulus of K= 47GPa. The mechanical behaviour of the heat-treated sample is different. Its hydrostatic response was non-linear up to a pressure of ~38 MPa, beyond which the stress-strain curve became linear with a slope corresponding to a static bulk modulus of K=15.9GPa. For altered samples, the hydrostatic response was non-linear up to a pressure of ~38MPa, beyond which the stress-strain curve became linear with a slope

corresponding to a static bulk modulus of K=15.9GPa, K=16.2GPa, and K= 17.2GPa for the samples altered at 80°C, 180°C, and 280°C, respectively (Figure 3.5a). The non-linearity observed below 38MPa can be explained by the progressive closure of pre-existing microcracks (e.g. Walsh 1965; Baud et al. 2000; Nicolas et al. 2016). The compaction has a hysteresis and after unloading, the volumetric deformation does not return to its initial value. Comparing the volumetric strain measured and the perfectly elastic trend, microcrack porosity can be estimated (Walsh 1965). We find $\varphi_c \sim 0.1\%$, $\varphi_c \sim 0.1\%$, $\varphi_c \sim 0.12\%$ and $\varphi_c \sim 0.2\%$ for the heat-treated sample and samples altered at 80°C, 180°C, and 280°C, respectively.

As pressure is increased from 0 to 50 MPa, P-wave velocity remains constant for the intact sample. For the heat-treated sample, P-wave velocity increases by 55% as pressure is increased from 0 to 50 MPa. As pressure is increased from 0 to 50 MPa on altered samples, P-wave velocities increase by 55%, 35% and 20% for samples altered at 80°C, 180°C, and 280°C, respectively (Figure 3.5b). Elastic wave velocities are directly related to the compaction of the samples (Figure 3.5c). This increase highlights the closure of pre-existing cracks (e.g. Fortin et al. 2005). Under hydrostatic stress conditions, our results show that ultrasonic wave velocities are independent from their pathway, indicating that the medium composed of matrix with embedded pores and cracks is isotropic, in agreement with previous observations by Vinciguerra et al. (2005).

3.3.4 Evolution of the mechanical behaviour during triaxial loading and failure with heat-treatment and alteration

For all samples, the mechanical behaviour observed during constant strain rate triaxial deformation of the samples are typical of the brittle faulting regime: The axial strain versus differential stress curves first show a linear trend typical of an elastic behaviour (Figure 3.6a). Then, the differential stress reaches a peak, beyond which strain softening is taking place

(Figure 3.6a). From the volumetric strain versus mean stress curves (Figures 3.6b), it can be seen that samples show an elastic compactant behaviour until a critical stress state denoted C' (Wong et al. 1997) beyond which the volumetric strain deviates from linear elasticity (onset of dilatancy). The critical stress state C' is determined manually at the point of divergence of the curve of volumetric strain versus mean stress and the linear elastic compaction of each experiment.

During triaxial loading of the non-altered sample, elastic compaction is followed by dilatancy, which leads to macroscopic failure. The two altered samples that were triaxially deformed show the same mean stress-volumetric strain relationship (Figure 3.6b). Elastic compaction is highest for the non-altered sample. Our results show that the peak stress (differential stress at failure) decreases with the degree of alteration (Figure 3.7).

The non-altered sample failed at a peak stress of 471 MPa, slightly higher than the sample altered at 180°C which failed at a stress of 464 MPa. The sample altered at 280°C failed at a peak stress of 418 MPa, which is 11% lower than the peak stress for the intact sample. Similarly to what is observed for the peak stress, the differential stress levels at the onset of dilatancy (C') shows a negative alteration dependence (Figure 3.7). Again, the stress at which dilatancy overcomes compaction decreases with the degree of alteration. For the intact sample, the onset of dilatancy (C') and dilatancy (D') are reached for stresses of 189 MPa and 362 MPa, respectively. This is higher than the stresses for the sample altered at 180°C, which reached the onset of dilatancy and dilatancy points at 165 MPa and 286 MPa, respectively. Finally, the sample altered at 280°C reached the onset of dilatancy and dilatancy at 165 MPa and 285 MPa, respectively.

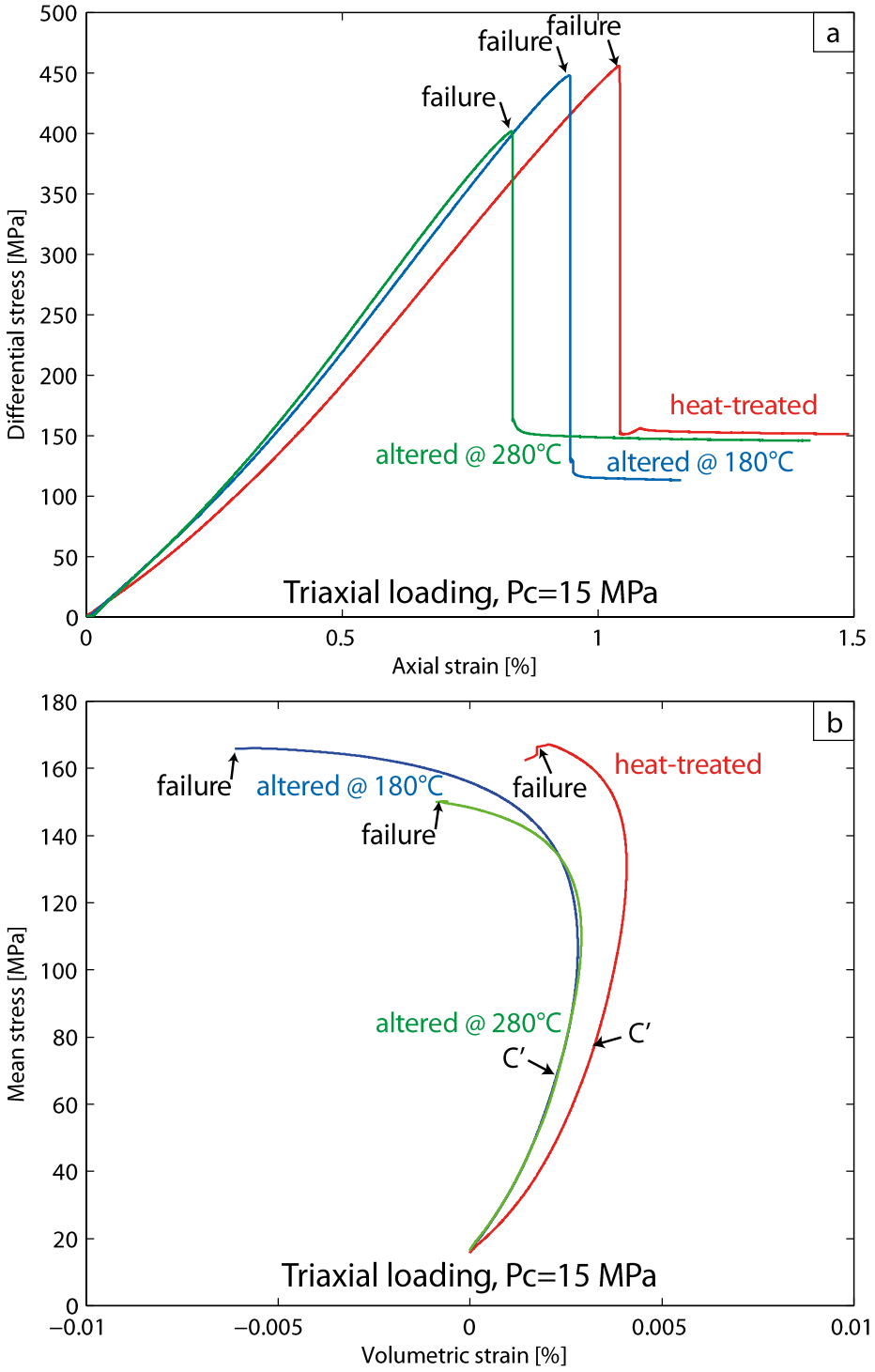

Figure 3.6 (a) The differential stress is plotted versus axial strain for constant strain rate deformation exper- iments performed on heat-treated sample, and samples altered at 180◦C and 280◦C at a confining pressure of 15 MPa. The mean stress versus volumetric strain curves for these three experiments are shown in panel (b).

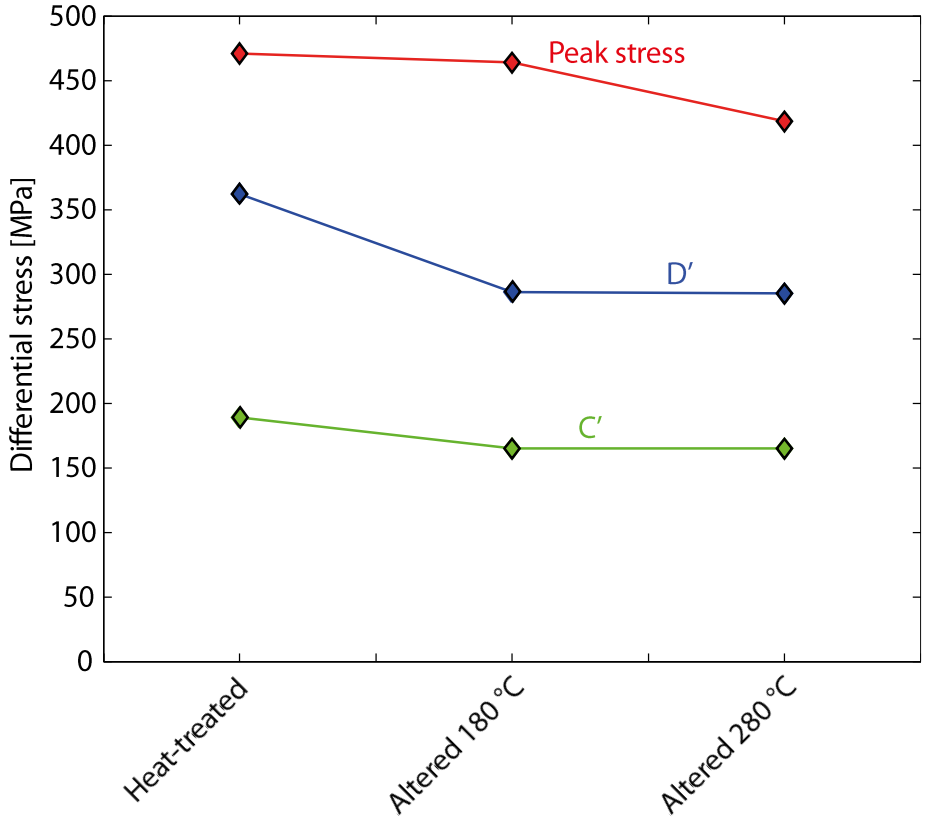

Figure 3.7 Peak stress (red diamonds), and thresholds for onset of dilatancy C' (green diamonds), and di- latancy D' (blue diamonds) are shown in the PQ space for an heat-treated sample, and samples altered at 180◦C and 280◦C. All samples were triaxially deformed at a confining pressure of 15 MPa.

During the initial stage of elastic loading, P-wave velocities (V_p) at all angles with respect to σ_1 and S wave velocities (V_s) increase with deformation for all samples (Figure 3.8). The increase is maximum for the highest angles with respect to σ_1 and decreases with the angle. P wave velocity increases reach 40%, 30% and 25% for non-altered, altered at 180˚C and altered at 280˚C samples, respectively. Then, V_p and V_s start decreasing at the onset of dilatancy (C') (Figure 3.8). Beyond C', velocities continue to decrease as the sample is deformed until failure at which velocities drop abruptly. The overall decrease for both V_p and V_s reaches 60% for the non-altered sample but tends to decrease with alteration. Under triaxial stresses, the maximum decrease is observed for the pathway perpendicular to σ_1 (90˚), which suggests that the

propagating and/or nucleating cracks are mainly axial (Mavko et al. 1995; Ayling et al. 1995; Fortin et al. 2011; Nicolas et al. 2016, 2017b). Thus, we invert ultrasonic wave velocities in terms of axial and randomly oriented crack densities (Sayers & Kachanov 1995) assuming: (1) a transverse isotropic crack geometry; (2) an isotropic matrix, in agreement with the isotropic ultrasonic waves velocities measured under hydrostatic conditions; (3) non-interacting cracks, an assumption which is valid for crack densities up to at least 0.15 and probably 0.2∼0.25 (Grechka & Kachanov 2006); (4) a random crack center distribution; and (5) penny-shape cracks of radius c and aperture w. The detailed procedure can be found in Fortin et al. (2011) and in Appendix A in Wang et al. (2013). When the differential stress is increased, the axial and background crack densities decrease during the elastic compaction of all experiments (Figure 3.8). Beyond that stage, the axial crack density increases immediately beyond the onset of dilatancy (C') and reaches values up to 2 at macroscopic failure (Figure 3.8d). Inverted crack densities increase less for altered samples. Acoustic emissions recorded during samples deformation and failure were re-localized using Insight Software (Figure 3.9). For re-localization, we use a constant velocity model with an anisotropy factor of 0.75 (ratio between axial and radial velocities). Acoustic emissions seem to be localised on a shear plane inclined with regards to the maximum principal stress, in agreement with post-mortem observations. It shows that all samples have a brittle behaviour.

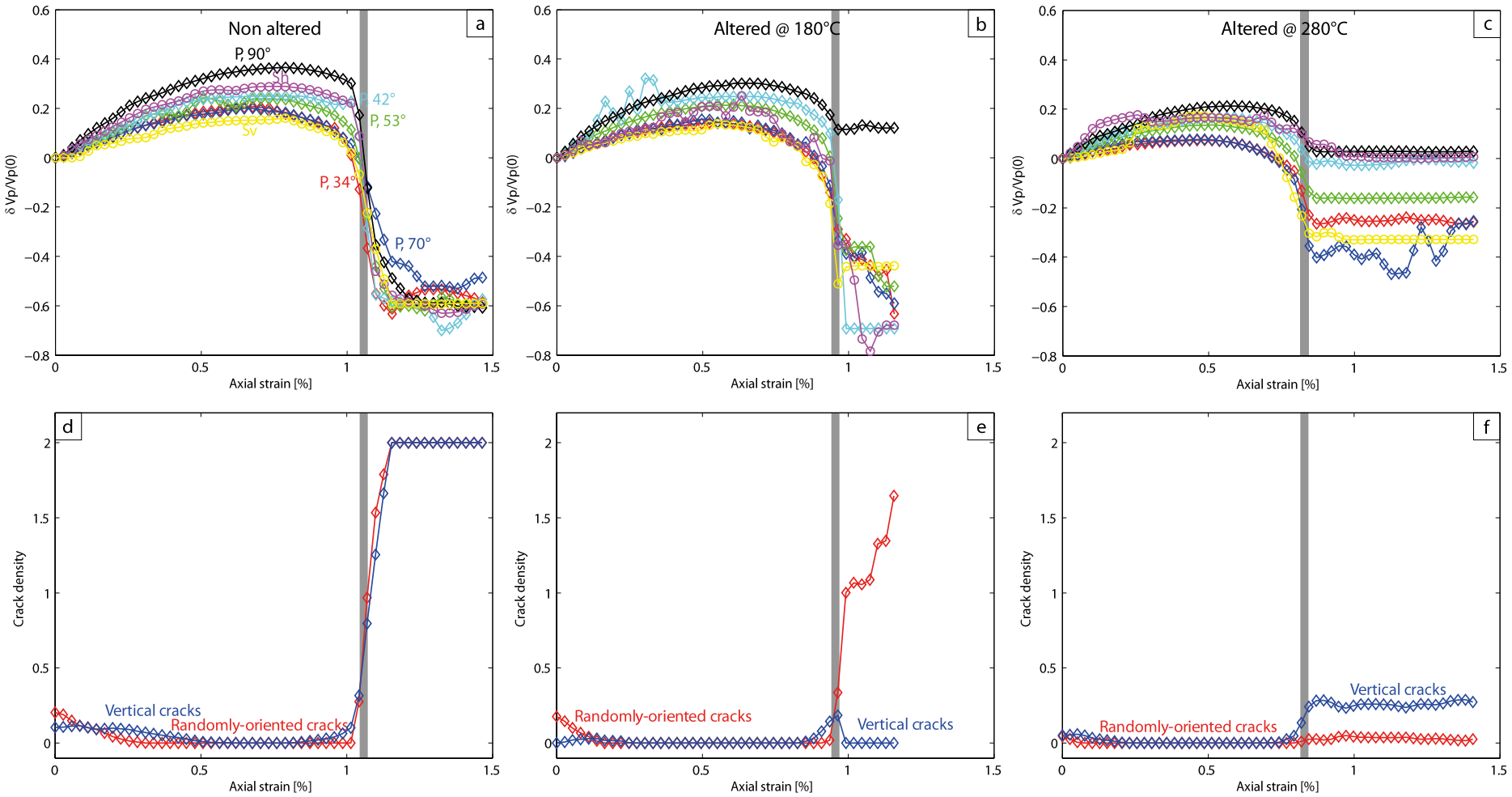

Figure 3.8 Evolution of δV/V0 (where V0 is the P or S wave velocity at the beginning of triaxial loading) at different angles with respect to σ_1 is plotted as a function of axial strain for an heat-treated sample (a), and samples altered at 180◦C (b) and 280◦C (c). Evolution of axial and randomly-oriented crack density as a function of axial strain for an heat-treated sample (d), and samples altered at 180◦C (e) and 280◦C (f).

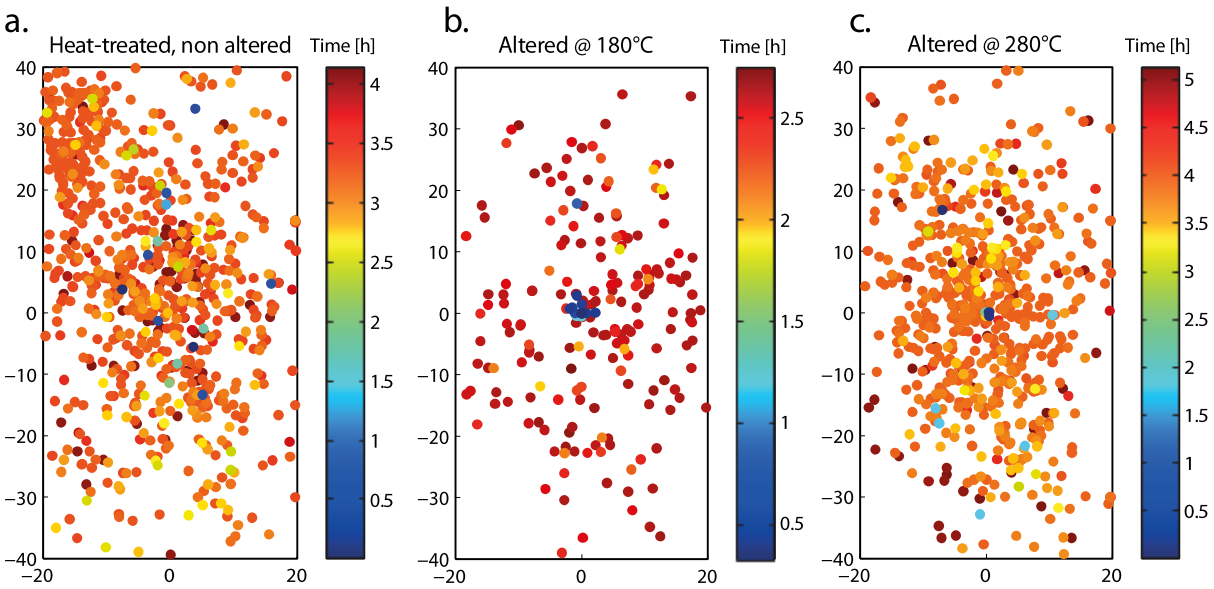

Figure 3.9 Re-located acoustic emissions for constant strain rate deformation experiments performed on samples heat-treated (a), altered at 180◦C (b) and altered at 280◦C (c).

3.4 Discussion

3.4.1 Alteration, porosity and density

Alteration leads to an increase of porosity. A positive correlation between porosity and quantity of alteration had also been noticed in natural samples from a hydrothermal system in Iceland (Levy et al. 2018). Levy and co-workers explained this correlation by a lithological control on both porosity and alteration. Given that the original lithology and porosity of all samples is very similar in this study, this explanation is not sufficient. An actual control of the alteration on the porosity seems to appear.

3.4.2 Can smectite precipitation in cracks explain the mechanical behaviour?

The presence of smectite in the sample altered at 280˚C is evidenced by SEM-EDS analyses, XRD on fine fraction and CEC measurements. Consistent increase of elastic wave velocities under room pressure with the level of alteration (none, 80˚C, 180˚C and 280˚C) is also an

indirect observation of smectite infilling in cracks because elastic wave velocities are much more sensitive to cracks than to equant porosity (Fortin et al. 2007b). The increase of alteration level induces an increase of the elastic mechanical modules, which results in an increase in the velocity of propagation of the elastic waves and a lower volumetric deformation with the increase of pressure. The increase of the alteration also causes a decrease of the compaction under isostatic conditions and a decrease of the stress state at which the onset of dilatancy (C') occurs, the stress state at which dilatancy overcomes compaction (D') and finally the differential stress at failure occurring in a brittle manner during constant strain rate deformation experiments. The decrease of compaction with increasing alteration is in good agreement with crack filling because it is well known that cracks tend to close first under isostatic loading. Under triaxial stresses, it is known that the mechanical behaviour of fragile environments (in terms of elasticity and rupture) is much more susceptible to cracks than to equant porosity, which may be in contradiction with the observations that crack porosity is filled by the products of alteration. However, damage models for brittle solids under compression show that the damage likely develops from pre-existing defects (e.g. cracks) and that the friction coefficient between the two flanks of the these defects is of the utmost importance on the mechanical behaviour. Phyllosilicate minerals, and in particular smectite, are known to have low friction coefficients (e.g. Saffer et al. 2001; Moore & Lockner 2007; Carpenter et al. 2011). Thus, our mechanical observations can be explained by the filling of pre-existing cracks by smectite. We thus conclude that alteration has led to the precipitation of smectite in cracks, which has induced an increase of elastic modulus of the material and a decrease of peak strength. Previous studies have also shown that phyllosilicates can have an influence on the mechanical behaviour (e.g. Bos & Spiers 2002; Collettini et al. 2009)

3.4.3 Modelisation

Triaxial constant strain rate experiments on heat-treated and altered samples of andesite are modelled using well-known wing crack damage models initially developed by Nemat-Nasser & Horii(1982), and later revisited by Ashby & Hallam (1986); Ashby & Sammis (1990); Bhat et al. (2011,2012); Mallet et al. (2015); Perol & Bhat (2016); Nicolas et al. (2017a), among others. Wings of length denoted l can grow from each end of the pre-existing penny-shaped crack of radius a inclined at an angle ψ with respect to the maximum principal stress, parallel to the maximum principal stress (Figure 3.10a). These wing cracks form an array of interacting cracks in an isotropic linear elastic surrounding medium subjected to compressive stresses (Figure 3.10b). The faces of the initial crack, in contact, can slide with some friction characterized by a Coulomb friction coefficient μ. We use Ashby & Sammis's approach to calculate the stress intensity factor K_I at the tip of the wings in a three-dimensional setting (Figure 3.10), the wing crack growth and the resulting volumetric strain. Cracks grow when the stress intensity at their tips K_I exceeds the fracture toughness K_{IC} of the solid. Then, cracks propagate until K_I falls to K_{Ic}.

Under compressive stresses as considered in this study, K_I decreases as l increases until the cracks start to interact strongly: each increment of crack advance requires an increment of load and growth is stable. As wing cracks grow, the current damage increases. The crack can also open. Thus, three regimes need to be considered (Deshpande & Evans 2008; Nicolas et al. 2017a): (i) Relative sliding on the flanks of the initial crack cannot take place because of friction, preventing cracks from growing. (ii) Relative sliding is possible and Ashby & Sammis' approach is used. Expression of the stress intensity KI at the tip of interacting cracks forming an array is given by equation 26 in Ashby & Sammis (1990). (iii) Contact between the flanks of the initial crack is lost and the situation reduces to the classical problem for a cracked elastic solid (Bristow 1960; Budiansky & O'Connell 1976; Tada et al. 2000). Precise description of

the model can be found in Nicolas et al. (2017a), excepted that intra-crystalline plasticity and new crack nucleation are not considered in this paper (thus only sections 3.2.1 and 3.2.2 should be considered in Nicolas et al.'s paper).

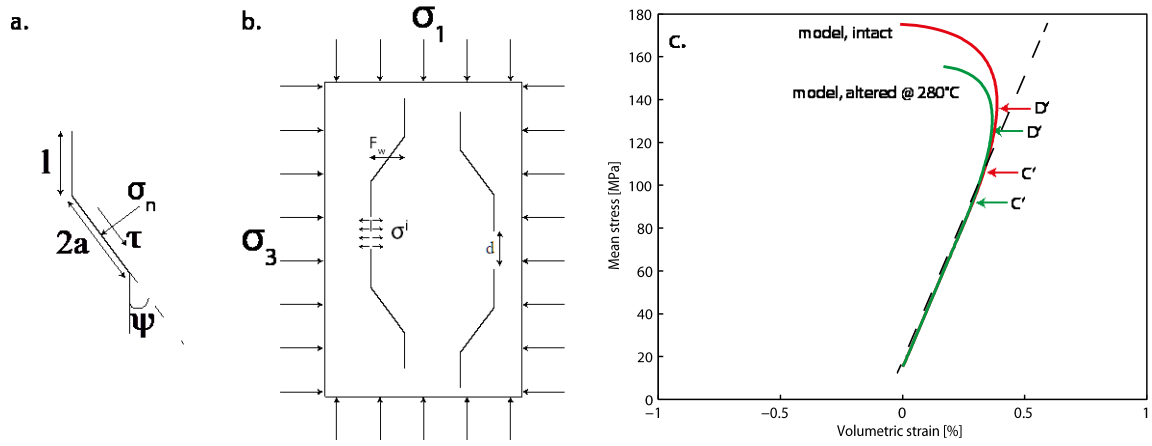

Figure 3.10 (a) An isolated wing-crack is subjected to remote stress. Wings develop from an initial flaw of radius a, parallel to the maximum principal stress σ1. (b) Geometry of the crack network used for the stress- intensity factor, K_I , calculated at a crack tip. (c) The model is run for a confining pressure of 15 MPa. Evolution of the mean stress as a function of volumetric strain for an heat-treated sample and a sample altered at 280◦C. The red and green curves correspond to the heat-treated and altered at 280◦C samples, respectively. Arrows represent the onset of dilatancy C' for each value of friction coefficient.

The elastic moduli of the uncracked porous medium used in this study are Young's modulus E_0 = 50GPa and Poisson's ratio υ_0= 0.15). Any other set of elastic constants are calculated from these values. The critical stress intensity factor for andesite is taken equal to K_{IC}=2MPa·m$^{1/2}$. This value corresponds to the value for dry andesite according to values measured by Nara et al. (2012) who found that fracture toughness for Kumamoto andesite is K_{IC}=2.01−4.10^{-3} × h_rMPa·m$^{1/2}$, where hr is relative humidity. This is good agreement with measurements by Nara & Kaneko (2005); Tutluoglu & Keles (2011); Siratovich et al. (2014) who found values ranging between 1 MPa·m$^{1/2}$ and 2 MPa·m$^{1/2}$. It is also of the order of

magnitude of the critical stress intensity factor measured for other volcanic rocks (e.g. Atkinson 1984).

Crack density (or initial damage) can be inferred from elastic wave velocity measurements (e.g. Sayers & Kachanov 1995; Fortin et al. 2005) or SEM images (e.g. Fredrich et al. 1989; Mallet et al. 2013). We use D_0=0.1, which is good agreement with inverted crack densities. Crack mean size can be inferred from SEM images (e.g. Mallet et al. 2013) or taken as equal to the grain size. We use $a = 2\times10^{-4}$ m for both altered and unaltered samples, which is in good agreement with direct SEM observations. Porosity can be measured using a triple weighting procedure, as done in this study. We use a porosity of 2%, which is the value measured for heat-treated samples. We do not take into account the slight porosity increase with alteration because porosity has very little influence on the predicted mechanical behaviour (Nicolas et al. 2017a). The friction coefficient on pre-existent penny-shaped cracks can be inferred from a linear failure envelope, assuming that friction is equal on a macroscopic fault and microcracks. Typical values for intact rocks are in the range [0.4-0.8], as shown by Byerlee (1978) for example. We use μ = 0.5 for the intact sample and μ=0.4 for the altered sample due to the filling of cracks by clay minerals that have low friction coefficients. This decrease of the friction coefficient is observed in many studies (e.g. Ohnaka 1975; Saffer et al. 2001), although some measurements may remain unclear (e.g. Moore & Lockner 2007).

Comparing model predictions for unaltered and altered samples, decreasing the friction coefficient has an influence and decreases the onset of dilatancy C' and dilatancy point (D') (represented by arrows), on the peak stress and on the volumetric strain at the peak stress (Figure 3.10c). Model predictions are then in good agreement with the experimental results and tend to confirm that the decrease of friction coefficient on pre-existing flaws due to clay minerals filling the cracks can explain the changes in the mechanical behaviour under triaxial loading.

3.4.4 Implications

Our mechanical results have implications in several domains related to volcanic areas. First, volcano are sometimes modelled as an infinite half-space using a constant set of elastic moduli (e.g.Mogi 1958; McTigue 1987). Inflation and deflation of deep magmatic chambers induce the deformation of Earth's crust (e.g. Dvorak & Dzurisin 1997; Walwer et al. 2016). Elastic properties

of volcanic rocks are used in models used to invert geodetic data measurements (deformation of volcanoes) to give information on the depth and pressure variations of volcanic chambers (e.g. Anderson 1937; Mogi 1958; McTigue 1987). Thus, volcanic rock mechanical properties and their variation with alteration are of the utmost importance. According to the most simple model (Mogi

1958), the volcano vertical surface uplift is proportional to the pressure increment in the magmatic chamber and inversely proportional to the elastic shear modulus (if the medium is considered as homogeneous). However, our results show that even though volcanoes may be made up of only one kind on rock, alteration due to hot fluid flows may induce changes of the mechanical properties of the rock. Thus, taking into account these elastic moduli dependence to alteration could be of interest.

Seismic velocities in volcanic areas sometimes vary (e.g. Ratdomopurbo & Poupinet 1995), due to the presence of pressurized fluids for example (e.g. Brenguier et al. 2014). Increase in elastic moduli could have an impact on the seismic effect during seismic campaigns: an increase in speed in the case of campaigns could indicate an area of altered rocks.

Some failure models (e.g. Main 1999; De la Cruz-Reyna & Reyes-Da´vila 2001; Connor et al. 2003) aim at predicting volcanic eruptions. Some of these models are based on the brittle characteristics of the materials forming volcanoes (e.g. Denlinger 1990). Fracture toughness is

used in some of these models (e.g. Gudmundsson 2009). Thus, our measurements of the influence of alteration on the peak strength of andesite can be used in volcanic eruption models.

3.5 Conclusion

The mechanical behaviour of volcanic rocks and its evolution with alteration is of the utmost importance for many fields of study related to volcanic eruptions or geothermal exploitation among others. Mots studies on the mechanical behaviur of volcanic rocks have focused on healthy rocks samples and the specific influence of alteration on the mechanical behaviour of geothermal volcanic reservoirs is still poorly understood. Yet, the presence of alteration minerals is susceptible to significantly modify the mechanical behaviour of rock, as compared to pure and healthy rock, because alteration results in microstructural changes, which in turn modifies the physical (porosity, open crack density, velocity of propagation of elastic waves, permeability) and therefore mechanical properties of the rock. Our experiments performed on samples artificially altered to different degrees have focused on the evolution of the mechanical behaviour under hydrostatic and differential stresses with alteration. Initial material was heat-treated samples of relatively fresh andesite. Alteration was quantified, and the samples were then loaded isostatically and in a triaxial setting for samples deformed at a constant strain rate. Mechanical results show that elastic moduli increase with alteration. On the contrary, peak strength of the samples decrease with alteration.

Numerical solutions of wing crack models show that a decrease of friction coefficient between the two flanks of pre-existing flaws could explain the mechanical observations. The decrease of friction coefficient can be explained by alteration, which could lead to the formation of smectite in the heat-treatment induced cracks.

Our mechanical results have implications in several domains related to volcanic areas, on a fundamental and applied point of view. In the field, alteration should quantified and taken into account in mechanical modelling and inversion of geodetic data.

Acknowledgments

Thanks Damian Walwer for its comments on volcano deformation. Data are available upon request to the first author. LL thanks the Icelandic Geosurvey (ISOR) for allowing CEC measurements in their facility. This study was performed in the frame of the GEOTREF project, aiming at improving our understanding of the behaviour of fractured geothermal reservoirs.

Chapter IV Fluid-Injection Induced Rupture in Thermally Cracked Andesite at Laboratory Scale

Abstract

A series of experiments are done in order to investigate the effect of fluid pressure variation i) on the mechanical behavior of andesite samples and ii) on acoustic emissions activities. In particular fluid pressure was raised in a sample submitted to a stress state close to the onset of dilatant point (corresponds to the critical stress state in field), and the injection was continued until the rupture (the axial stress and confining pressure were kept constant). Fault propagation was monitored by the acoustic emissions, and their locations were compared with the fractures observed in the sample after the experiment. The mechanism of delayed time before the main rupture is discussed. Our results show that: (1) Permeability of heat treated (at 930°C) andesite sample has shown a large decrease ($9\times10^{-18}m^2$~$2\times10^{-18}m^2$ under hydrostatic loading (0MPa~25MPa). (2) Heat treated andesite samples have shown a brittle characteristic under saturated conditions, and falls on the Mohr-Coulomb envelop of the intact samples.(3) A time dependent behavior was observed in the fluid-injection induced rupture experiment.(4) Heterogeneity of crack development was observed before rupture. More cracks were developed at downstream while upstream remains silent. The rupture began from the downstream end. (5) Critical crack space is inverted and estimated to be in the range of 129μm~223μm. Crack length growth with time is inverted during stage II where stress state was constant.

4.1 Introduction

Fluid injection into reservoirs is a method generally employed in geothermal systems, hydrocarbon reservoirs, in waste disposal sites and in CO_2 sequestration. By investigating into the mechanism of how fluid flow influences mechanical behavior at a laboratory scale, we could obtain an insight of how the fluid injection and induced seismicity are related at the laboratory and field scales. Fluid pressure variation in rocks which contain micro-cracks and pores could change the effective stress state and thus cause local deformation. This change in effective pressure could lead to instability at the macroscale (ie. initiation/propagation of a fracture), and the energy released in this process leads to induced seismicity.

The potential risk of inducing seismicity by diffusion of elevated pore pressure is known for decades (Ellsworth 2013). In addition, since 2008, fluid injection used for shale gas production appears to be the trigger in the mid-continent of United States which has become seismically active and the earthquake rate has increased (Frohlich et al. 2012,2013,2014; Horton 2012; Keranen et al. 2013; Ellsworth 2013; Justinic et al. 2013; McGarr et al. 2014,2017). As an example, a magnitude of 4.8 earthquake occurred near Timpson, Texas, a region where the seismicity was rare prior to this earthquake event (Frohlich et al, 2014). In Europe, the Deep Heat Mining Project in Basel, Switzerland used fluid injection to increase the permeability of the reservoir (fractured granite) and caused a event with a magnitude of 3.4 (Giardini 2009, McGarr et al. 2014,2017). Geothermal systems are commonly hosted in altered and fractured rock reservoir (Wu et al. 2000; Pereira and Arson 2013; Faoro et al. 2013; Pola et al. 2014; Heap et al. 2014). As geothermal fields usually locate in tectonically active areas, crustal stresses are near to critical stress (Ellsworth 2013; Zoback et al. 1997), thus fluid injection in these reservoirs could induce seismicity.

Two triggering mechanisms of induced seismicity at field scale have been described (Elsworth 2016). Fluid injection activity leads to an increase of the fluid pressure in the reservoir, resulting in a decrease of the effective pressure which possibly induce the fracture or sliding along pre-existing faults and to seismic events (Stanchits 2011; Nur and Booker,1972; Fletcher and Sykes,1977; Talwani and Acree, 1985; Zoback and Harjes, 1997). Another possibility is due to the stress variation in the vicinity of the fault resulting from remote stress change at fluid injection zone. These two different mechanisms act on similar time scales but are characterized by different length scales (Elsworth 2016).

At field scale, time dependence of induced seismicity due to fluid injection has been observed. Shirazi et al. (2016) used INSAR data to estimate pore pressure and volumetric strain. As soon as the injection is stopped, these authors show that pore pressure's spatial distribution is inhomogeneous: high permeability are associated with the largest pore pressure decay, whereas low permeability areas correspond to high fluid pressure.

Pore pressure can lead to mechanical instabilities and thus induced seismicity. Wassing et al. (2014) constructed a model based on the Soultz-sous-Forets GPK3 injection well where the rock mass is intersected by a dominant fracture zone, they investigated the role of fracture strength and frictional weakening. McClure et al. (2014) show that the amplitude of the induced seismicity is related to the mechanical properties and frictional properties.

There are a certain number of pioneering experiments that have been done in the laboratory. Lockner and Byerlee (1977) have shown in sandstone samples that failure mechanism depends on injection rate, i.e. a larger injection rate lead to tensile failure while a smaller injection rate cause shear failure. They analyzed the correlation between the failure mechanism and the pore pressure distribution. Masuda et al. (1990) performed an experiment of fluid injection in granite, and show using acoustic emissions (AE) locations that the fluid pressure is inhomogeneous. Kranz et al. (1990) performed experiments on cylindrical granite samples in which a hole was

drilled. The authors report that most AE are characterized by a shear motion and very few pure dilatational or compressional events occurred. Similar experiments were performed by Vinciguerra et al. (2004) on Darley Dale sandstone with an internal borehole. Schubnel et al. (2006) performed fracture experiment by raising fluid pressure in Fontainebleau sandstone samples, they record clear aftershocks maybe caused by heterogeneous pore pressure distribution along and across the fault plane. Similar results were obtained by Stanchits et al.(2011) in Flechtingen sandstone; in particular the authors show that the water injection process is accompanied by a induced activity of acoustic emissions located close to the migrating water front.

In this chapter, we present a series of experiments done in order to investigate the effect of fluid pressure variation i) on the mechanical behavior of andesite samples and ii) on acoustic emissions. In particular fluid pressure was raised in a sample submitted to a stress state close to the onset of dilatancy (corresponding to the critical stress state in field), and the injection was continued until the rupture (the axial stress and confining pressure were kept constant). Foreshock and aftershock were analyzed. Fault propagation was monitored at AE hypocenters and they were compared with the fractures observed in the sample after the experiment. The time to rupture is discussed.

4.2 Material & Methods

4.2.1 Materials

(1) Coring of rock samples

The samples of andesite were cored from a block obtained from a quarry located in Déhaies (Guadeloupe, French Antillas). Cylindrical samples were cored to a diameter of 40mm and are

80 mm-86mm in length. All samples are cored parallel. After coring, boundary surfaces are grounded to ensure a smooth surface vertical to the axis.

(2) Procedure of the heat treatment

Because of their low initial permeability, samples were thermally cracked. Samples were put in an oven (ENS) and temperature was increased at a rate of 140°C/h to the target temperature of 930°C. Then the target temperature was kept constant for 2 hours. After samples were cooled down to room air temperature.

(3) Sample Characteristics

The intact samples have a mean density of 2670 kg/m^3 and the porosity varies between 1.5%~2.3%. The porosity was estimated by comparing the weight of a water-saturated sample with the weight of the same sample dried in a vacuum at 40˚C for 4 days. Permeability is of the order of $10^{-21}m^2$. The P wave velocity of the andesite samples is 5400 m/s ± 200m/s.

For the heat-treated samples, the porosity varies between 3.1%~3.5%, permeability is in the range of $8.2*10^{-18}$~$9*10^{-18}$ m^2. The P wave velocity of heat-treated samples is 3700m/s ± 200m/s.

(4) Sample preparation

For the experiment of fluid injection with acoustic surveys, 4 strain gauges of type *Tokyo Sokki TML* type FCB 2-11 are glued on the sample surface. These gauges are each composed of one axial and one radial gauge. Neoprene tubing is used to separate the sample from oil confining medium. 12 P-wave and 4 polarized S-wave sensors (1 MHz eigen frequency) were glued on the surface of the rock and sealed in the jacket.

4.2.2 Experiment Methods

(1) Experiment apparatus

Experiments were performed on a conventional triaxial cell installed in the Laboratoire de Geologie at the Ecole Normale Superieure in Paris. (Ougier-Simonin et al. 2011 ; Fortin et al. 2011, Nicolas et al. 2016). Active acoustic surveys and passive acoustic emissions (AE) were recorded (Thompson et al., 2006; Schubnel et al., 2007; Ougier-Simonin et al. 2011; Nicolas et al. 2016). Pore pressure could be controlled at the top and the bottom of the sample with two micro-volumetric pumps (Quizix) with an accuracy of about 10^{-2} MPa (Brantut et al., 2011; Ougier-Simonin et al., 2011; Nicolas et al., 2016).

(2) Experimental Procedure

Two specific experiments are presented below:

In the first experiment on the heat-treated sample, confining pressure is first increased up to 40 MPa and then decreased at 5 MPa. Then the sample is fully saturated, and the pore pressure is maintained constant to 2 MPa. Confining pressure is then increased at constant pressure rate of $10^{-6}s^{-1}$ to make sure the sample is deformed under drained conditions (Fortin et al.2011; Nicolas et al. 2016) up to 40MPa. P wave velocity and permeability are measured during hydrostatic loading. At last, pore pressure is increased up to 35 MPa and differential loading is increased on the sample up to macroscopic failure. Mechanical and acoustic data are recorded during the experiment.

For the second experiment, figure 4.1 shows the procedure of loading. First the heat-treated andesite sample is first fully saturated, then hydrostatic loading is applied on the sample up to 40MPa. Differential stress is increased close to the stress state of dilatancy point, then the sample is kept under this stress state for 12 hours to make sure that no creep is taking place. At last water is injected into the sample from the bottom at a constant pore pressure of 35MPa

(dirac). The fluid pressure diffused through the sample; leading to the rupture of the specimen. Mechanical data, ultrasonic velocities and acoustic emissions were recorded during the experiment.

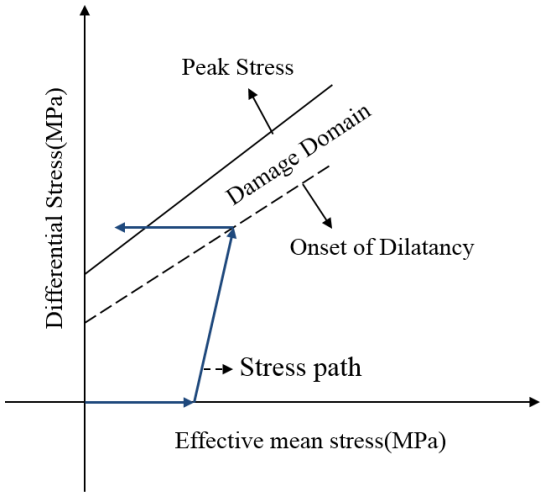

Figure 4.1 Illustration of experiment scheme (adapted from Schubnel et al. 2007)

4.3. Results

4.3.1 Mechanical properties of heat-treated andesite under hydrostatic loading

(1) Mechanical properties and P wave evolution of heat-treated sample under hydrostatic loading in dry condition

Under dry conditions, the P wave velocity increased of 600m/s when the confining pressure is increased from 12.5MPa to 40MPa. The crack density change during this process is obtained using effective medium theory in discussion part 4.4.1. Compared with the intact rocks, the heat treated samples show a large P wave velocity change during the hydrostatic loading under dry conditions. The intact rocks show a small change under hydrostatic loading due to the small

original porosity (absence of pre-existing crack in the intact sample). During this experiment the volumetric strain decreased of 0.4% (closure of the thermal cracks)

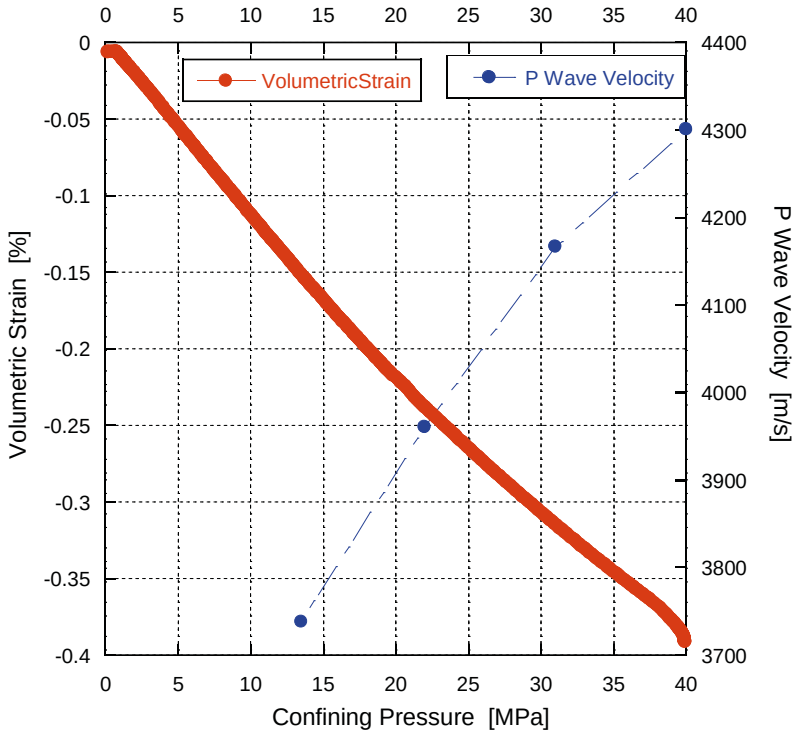

Figure 4.2 Mechanical properties and ultrasonic velocities of heat-treated samples under hydrostatic loading in dry condition.

(2) Mechanical properties and P wave evolution of heat-treated andesite under hydrostatic loading in saturated conditions

The fluid has a large effect on the P wave velocity: i) Under saturated condition, the P wave velocity increased of 140m/s while the effective confining pressure is increased from 20MPa to 37.5MPa, showing an effect of fluid pressure sustaining the micro cracks. ii) In addition, in saturated conditions and under the same confining pressure, the sample has a relatively high P wave velocity compared to the sample in dry condition (compare figure 4.3 with figure 4.2).

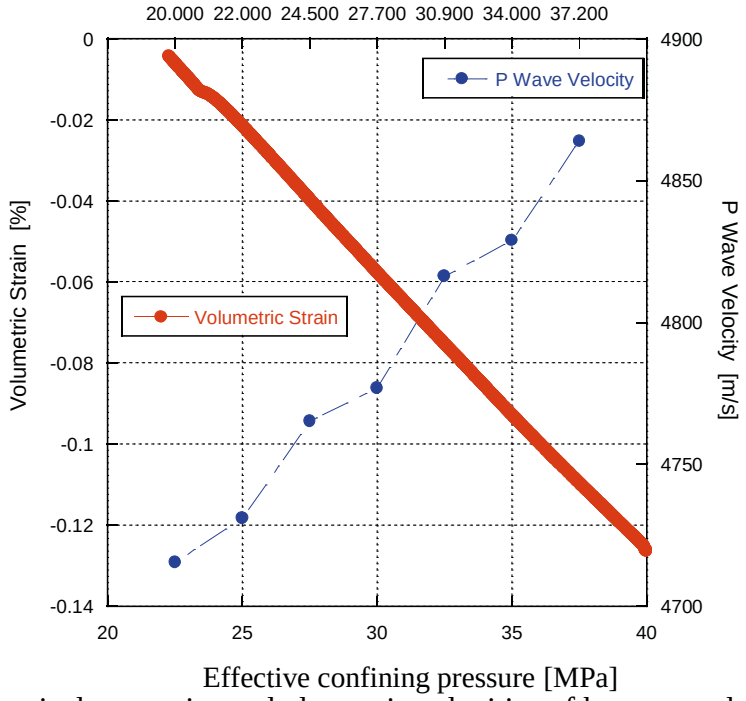

Figure 4.3 Mechanical properties and ultrasonic velocities of heat-treated andesite samples under hydrostatic loading in saturated conditions.

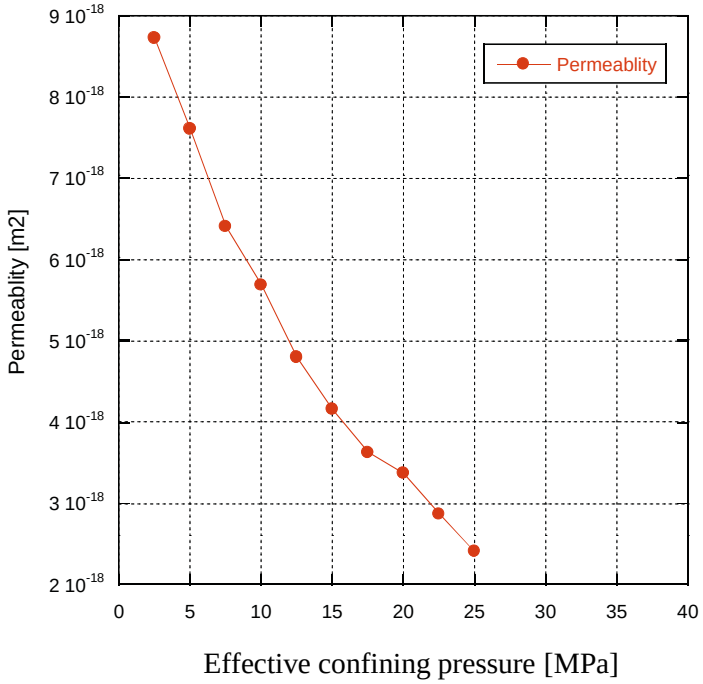

Figure 4.4 Permeability of heat-treated andesite samples under hydro-loading.

Permeability is measured during the hydrostatic loading of the heat-treated andesite sample. A large decrease of permeability is observed as shown in Figure 4.4. Permeability is measured with constant flow method. As shown in figure 4.4, the permeability decreased from $9*10^{-18}m^2$

to $2.5*10^{-18}m^2$ as the effective confining pressure is increased from 2.5MPa to 25MPa. Aspect ratio and crack aperture could be deduced from permeability measurement using effective medium theory, this part is discussed in 4.4.2.

4.3.2 Differential loading of heat-treated andesite sample under saturated condition.

(1) Mechanical data—axial strain and volumetric strain

Tri-axial deformation experiments were performed under saturated condition under a confining pressure of 40MPa and a pore pressure of 35 MPa on heat treated (at 930°C) andesite samples. As shown in figure 4.5(a), crack closure effect is observed at the start of loading, indicated by the beginning of the stress-strain curve which is concave. The stress-strain curve shows a brittle behavior.

(2) P wave velocity evolution

The P wave velocity increases at the beginning of the differential loading (figure 4.5(b)), denoting the closure of cracks. At a differential loading of Q=75MPa, the P wave velocity is constant (cracks are fully closed) until Q=230MPa, then it starts to decrease, indicating the onset of dilatancy. The P wave velocity decreases of 20% from onset of dilatancy to failure.

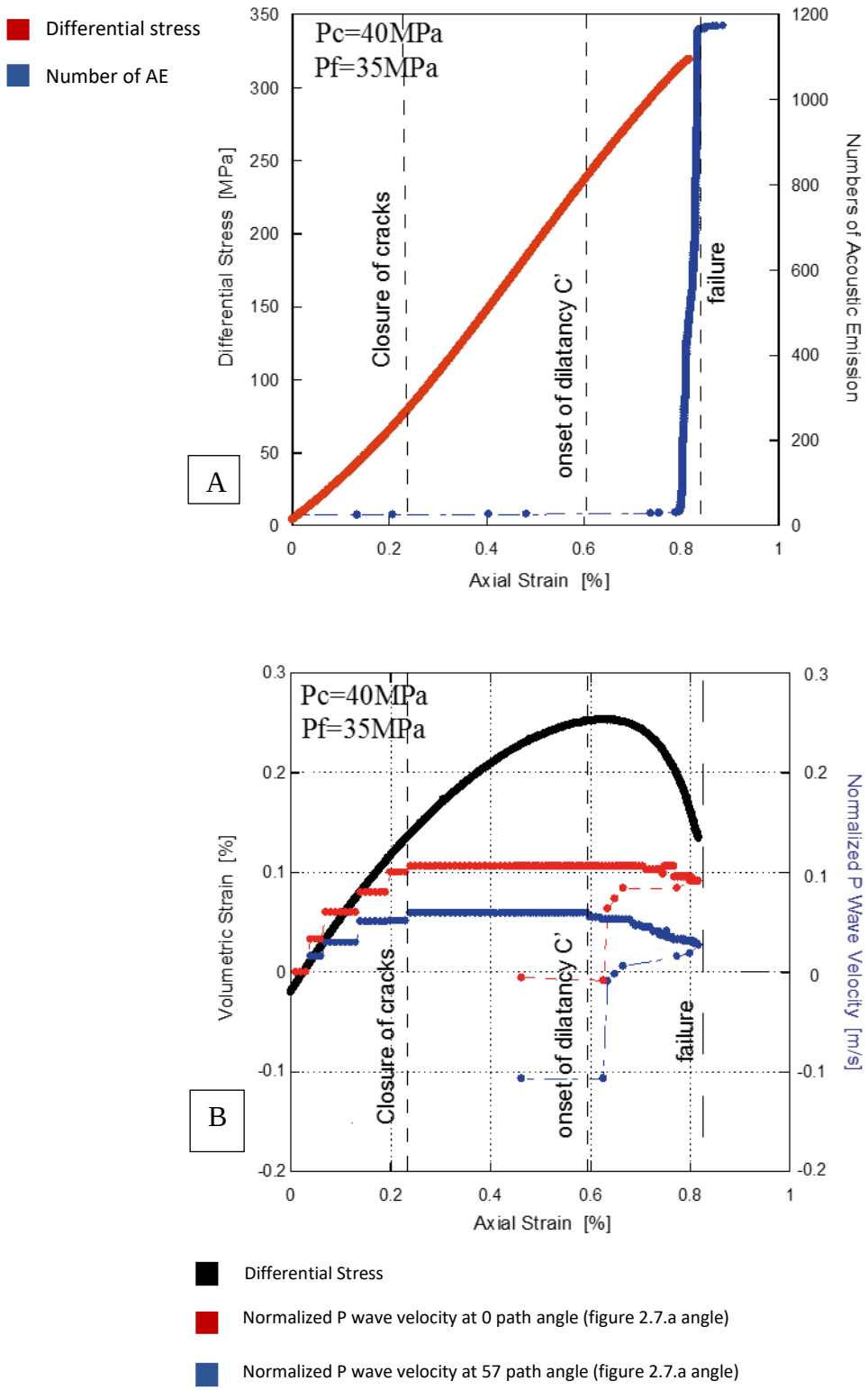

Figure 4.5.a Mechanical data and acoustic emission of heat-treated andesite sample in saturated condition under tri-axial deformation; **b** P wave velocity evolution with strain under triaxial deformation.

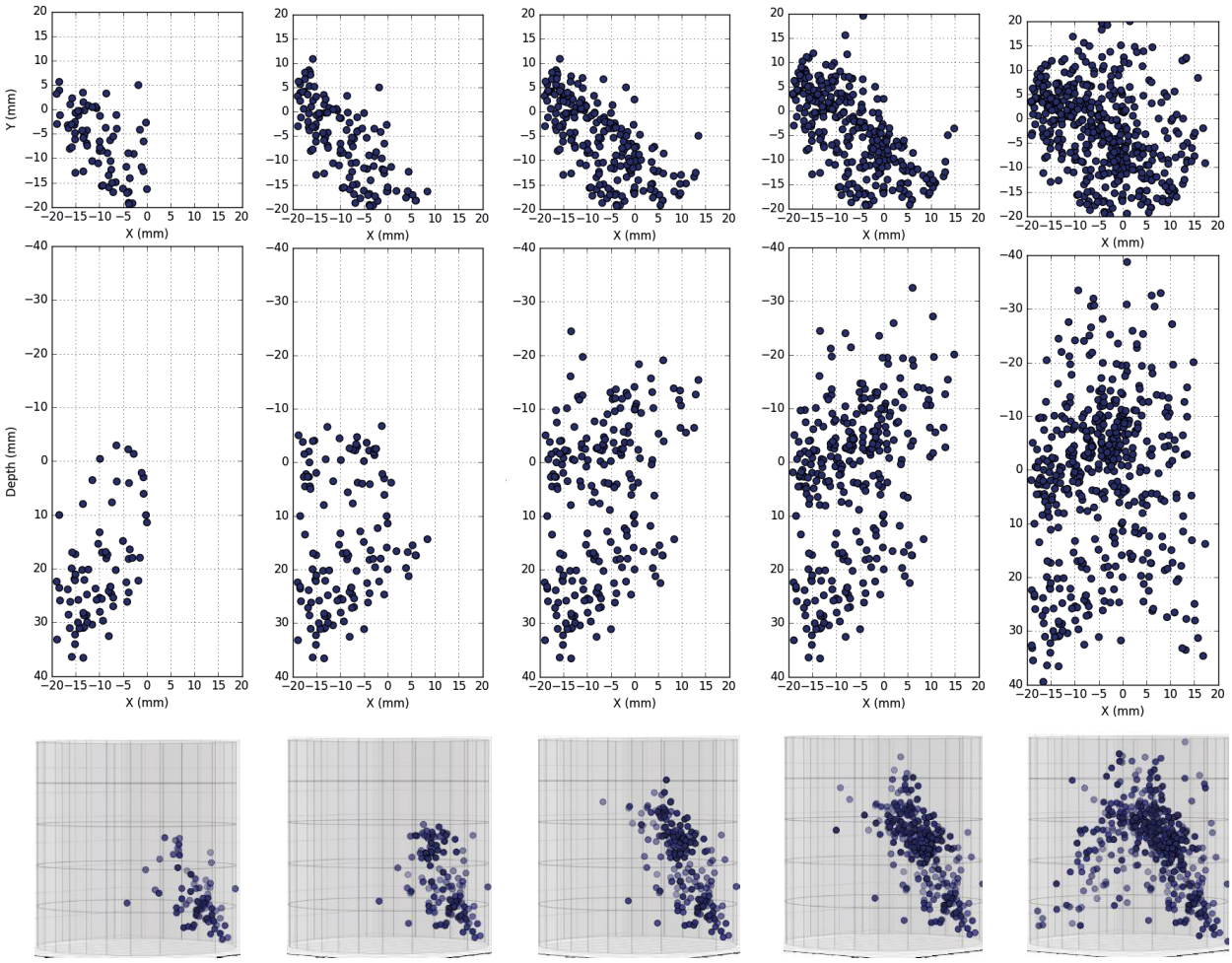

(a) 0~250s (b) 0~350s (c) 0~450s (d) 0~650s (e) 0~800s

(i) Sample after experiment with a fork shaped fracture

Figure 4.6: a~e: Location of the Acoustic Emissions **i**: The sample after experiment with a fork shaped fracture network, there is a good agreement with the location of AE.

(3) AE location

During tri-axial deformation, under a confining pressure of 40MPa and pore pressure of 35MPa the heat treated (at 930°C) andesite sample developed fork-shaped faults at failure. The acoustic emission location (figure 4.6 a-e) of faults shows a good agreement with the faults shown on sample after deformation (figure 4.6.i). The main fracture propagated within 600 seconds (figure 4.6. a~e).

(4) Peak stress of heat-treated andesite samples

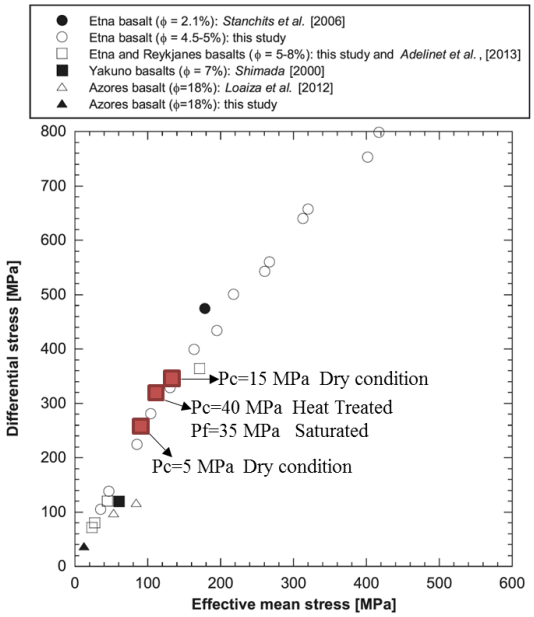

Figure 4.6.g Peak stresses for basalt samples and andesite samples. Zhu et al. (2016)

The peak stress of andesite under saturated condition with an effective confining pressure of 5MPa and in dry condition with confining pressure of 5MPa and 15MPa are plotted in figure 4.6.g. It has been shown that the results are consistent with researches accomplished by other researchers in basalt samples (Zhu et al., 2016).

4.3.3 Fluid injection induced rupture on heat-treated andesite sample

(1) Pore pressure at boundaries

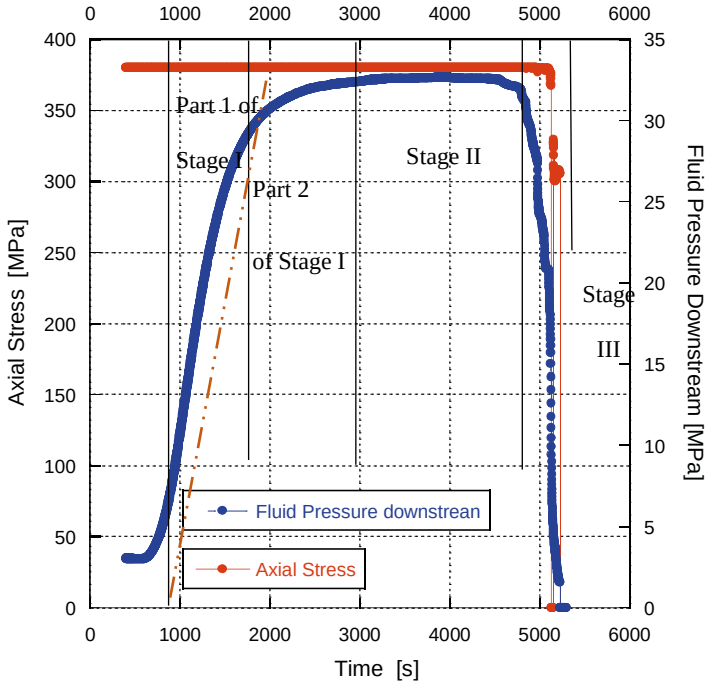

Figure 4.7 Fluid pressure at downstream during experiment on heat-treated andesite sample under fluid injection.

In this experiment, the confining pressure (40MPa) and axial stress (370MPa) are fixed. The fluid pressure at upstream (lower boundary) is increased suddenly from 1 to 35MPa, and then maintained constant at 35 MPa. The upper boundary condition is a fluid reservoir with a constant volume (dead volume). Figure 4.7 shows the fluid pressure evolution at the downstream (upper boundary) (blue curve).

As is shown in figure 4.7, from 300s to 700s, downstream fluid pressure is constant and flow to the fluid filling the dead volume. The injection volume suddenly increases at 300s (figure 4.9) while downstream fluid pressure remains constant, and the volumetric strain also increases (figure 4.8.b).

Stage I is from 700s to 2700s. From 700s to 1500s, the downstream fluid pressure increases linearly, at a constant rate of 0.029MPa/s, due to fluid diffusion. From 1500s to 2700s, downstream fluid pressure increases at a decreasing rate.

Stage II is from 2700s to 4500s. During this time period, downstream fluid pressure measured at downstream is almost constant.

Stage III is failure. From 4500s to 5200s, the downstream fluid pressure downstream begins to decrease until the main fracture went through the whole sample.

(2) Mechanical data—axial strain and volumetric strain

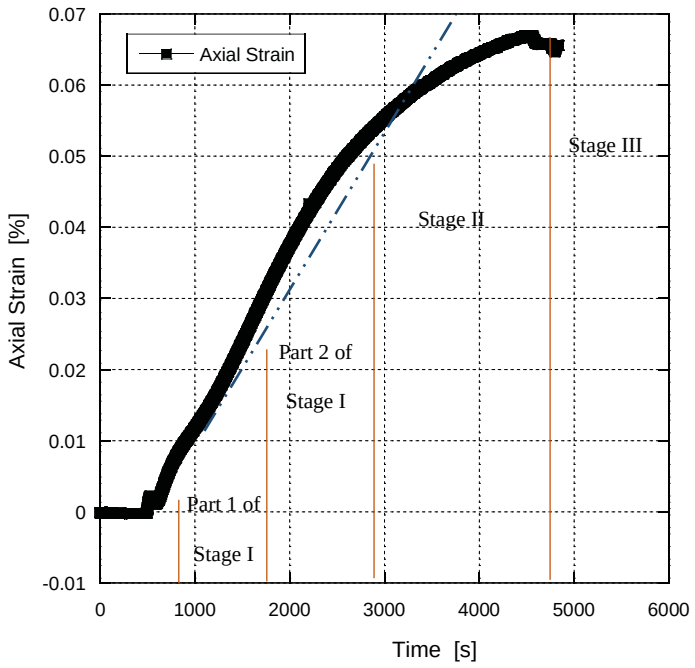

Figure 4.8.a Axial strain evolution during fluid injection.

As shown in figure 4.8.a, the axial strain increases by 0.065% from the start of the injection to the rupture. The axial strain increases linearly with time from the start of injection to 2700s at a constant rate. 2700s corresponds to the end of stage I, and the start of stage II. After stage I, the axial strain increases at a decreasing rate, exhibiting non-linear characteristics in stage II, until rupture.

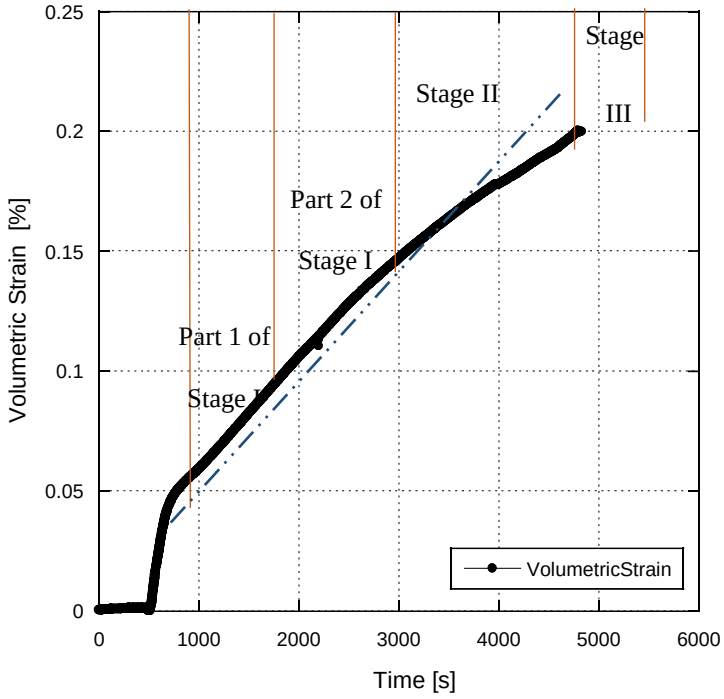

Figure 4.8.b Volumetric strain of heat-treated andesite sample during fluid injection.

From figure 4.8.b, it is shown that the volumetric strain has a dilation of 0.2% from the start of the injection to the rupture. In the stage I (from 700s to 2700s), the volumetric strain increases from 0.05% to 0.14 %.The volumetric strain increases linearly from 700s to 1500s (the first part of stage I). In this part, pore pressure measured at downstream increases linearly as shown in figure 4.7 at a constant rate. From 1500s to 2700s (the second part of stage I), the pore pressure increases of only 4.5MPa, and the volumetric strain increases of 0.05%. From 2700s to 4500s (stage II, 4500s is the start of the rupture process), the pore pressure has a slight increase of 1.5MPa, while the volumetric strain increases of 0.062%.

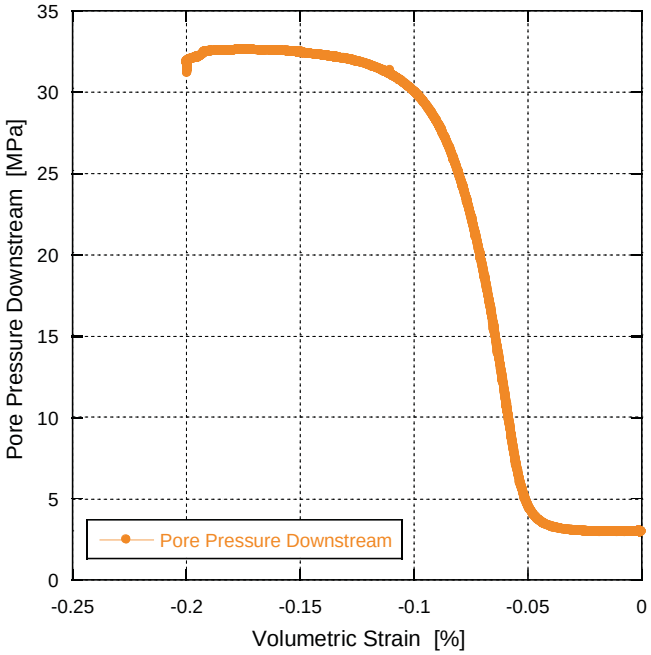

Figure 4.8.c Volumetric strain of heat-treated andesite sample during fluid injection

(3) Injected volume

Figure 4.9 shows that injected volume of fluid increased of 2ml from the start of the injection to the start of rupture process (end of stage II).

Before 300s, the injection volume increases suddenly, due to the filling of the dead volume at the upstream and downstream.

From 300s to 1500s (first part of stage I which corresponds to the linear increase in the downstream pore pressure - Figure 4.7), injected volume increases at a decreasing rate, with a total increase of 0.5ml.

From 1500s to 2700s (second part of stage I, corresponding to the nonlinear increase in the pore pressure downstream), the total volume of injected water is 0.2ml, with an almost constant rate of 0.17ul/s.

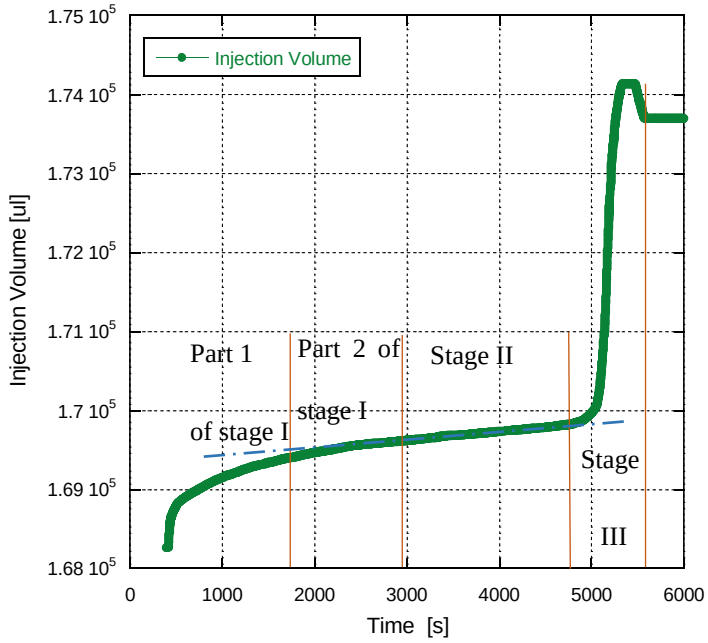

Figure 4.9 Injected volume evolution versus time during fluid injection

From 2700s to 4500s (stage II, corresponding to an almost constant pressure before rupture), the total volume of injected water is 0.1ml, with a constant rate of 0.05ul/s.

From 4500s to 5000s (first part of stage III, corresponding to the beginning of the rupture), the total volume of injected water is 0.1ml, with an increasing rate. If we define t=5000s as main shock, the recorded acoustic emission events before this time are foreshocks and after this are aftershocks.

From 5000s to 5200s (second part of stage III, corresponding to the rupture process), the injected volume of fluid increases at a constant high rate (16ul/s) due to the propagation of the fracture, and drops as the main fracture has propagated through the whole sample.

(4) P wave velocity evolution

Water was injected in the bottom part at constant fluid pressure of 35 MPa (Dirac), the fluid pressure was measured at the upper boundary of the sample in a dead volume.

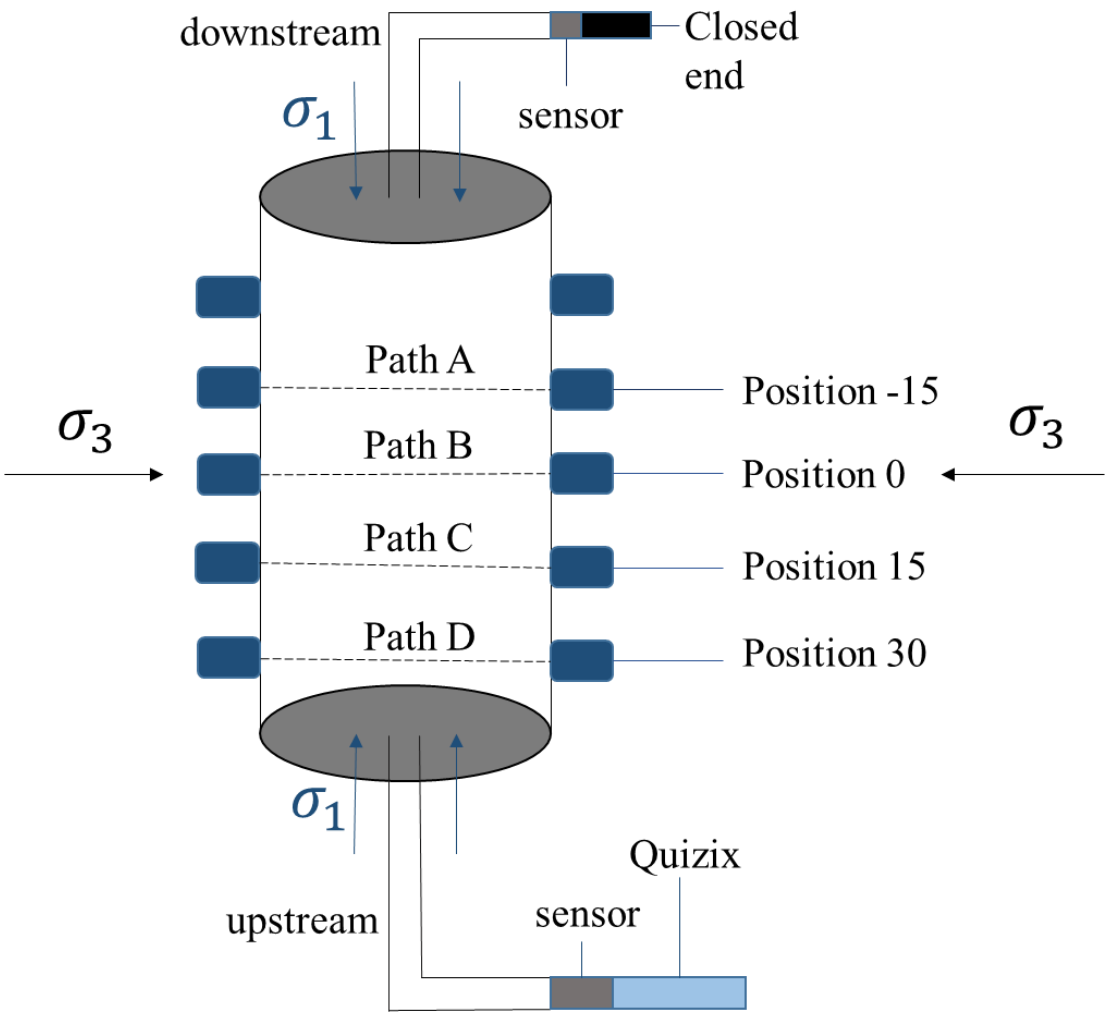

Figure 4.10.a P wave velocity measurement at different positions during experiment of fluid injection

Radial P-wave velocity (normal to the axial stress) was measured during fluid injection. Figure 4.10.a shows the position of ray paths A, B, C, D for the P wave velocity measurements. For example, path A denotes a horizontal measurement of P wave velocity at the position of -15 mm along vertical axis; this measurement is closed to the downstream. Path B is a measurement done in the middle of the sample (figure 10.a position of 0). Path D denotes a measurement at the position + 30 mm; this measurement is closed to the upstream.

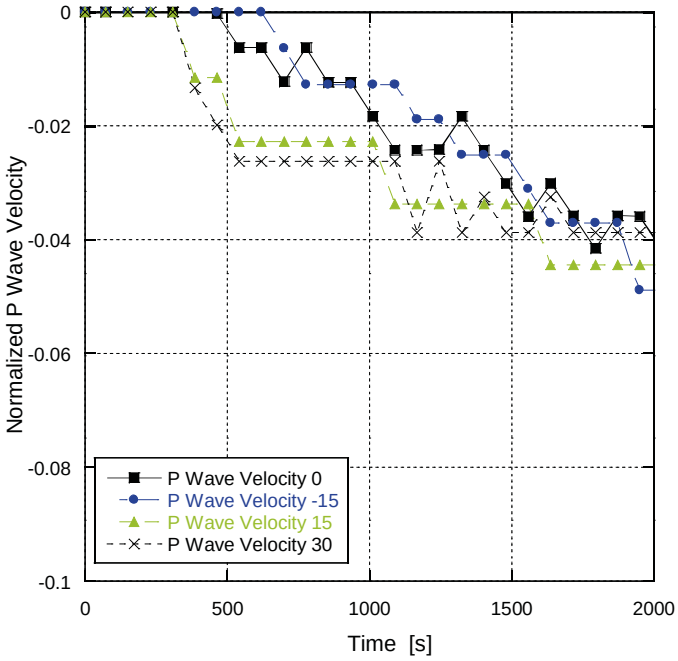

Figure 4.10.b Evolution of horizontal P wave velocity measured at different position during experiment of fluid injection

As the fluid is injected (at around 300s) (figure 4.10.b), a clear decrease of the P-wave velocity is observed on all the ray paths. In addition, there is a clear sequence when looking at the position of the P wave measurements between 300s and 1500s: at the beginning of the injection, P wave velocity measured at path A (figure 4.10.a and 4.10.b) is the latest to start decreasing. A decrease of 2.5% is measured from 300s to 1500s. The P wave velocity measured at path B, decreased earlier than P wave velocity measured at path A (with a total decrease of 3%). The P wave velocity measured at path C starts to decrease earlier than the P wave velocity measured at path A, B, but later than path D with a total decrease of 3%. P wave velocity measured at path D starts to decrease earliest. This time range between 300s and 1500s corresponds to the first part in stage I (Figure 4.9), where fluid pressure measured in the downstream increases linearly (figure 4.7), and the injected volume increases (figure 4.9) nonlinearly. This sequence of P-wave velocity decrease indicates a fluid pressure diffusion from the upstream part to the downstream part of the sample.

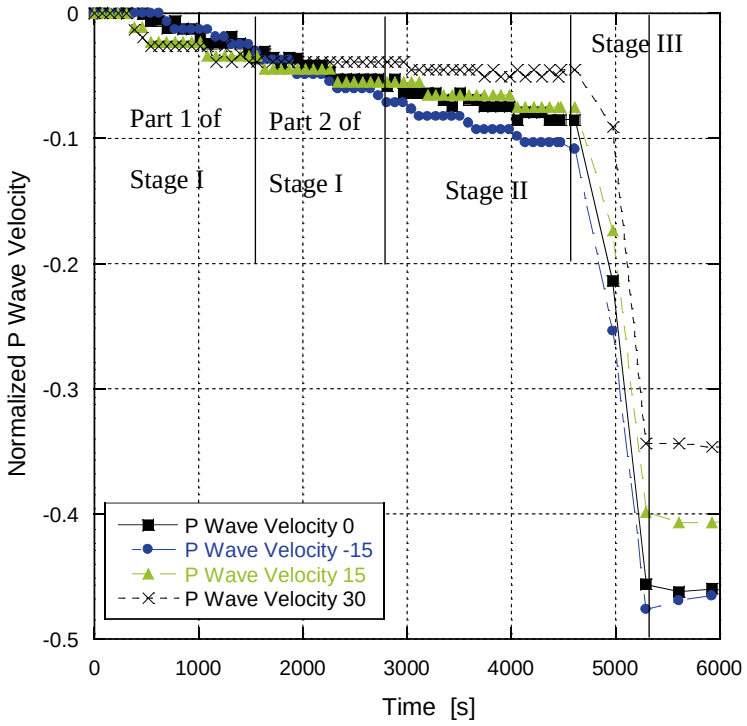

Figure 4.10.c P wave velocity evolution during experiment of fluid injection induced rupture on heat treated andesite sample

From 1500s to 2700s (Part 2 of stage I – Figure 4.10.c), the P wave velocity measured at different positions (figure 4.10.c) kept decreasing. The P wave velocity measured at path A decreased of 4%, while the P wave velocity measured at path B decreased of 3% ; and P wave velocity measured at path C decreased of 2.5%, and P wave velocity measured at path D decreased of 0.2%. The largest decrease in P wave velocity is at a position close to the downstream path (path A; -15 mm). The P wave velocity measured close to the upstream (path D) has nearly no decrease during this stage. The sequence of magnitude of decrease at different positions is reversed compared to the beginning of the injection experiment.

The P wave velocity measured at path D has no change, indicating that the development of cracks almost stopped at the upstream end part of the sample. The other parts (path A, B, C) of the sample almost have the same decrease in P wave velocity, showing that during this stage, the cracks develop mainly in the middle part of the sample and at the downstream part of the sample.

From 2700s to 4500s, the P wave velocity measured at path A (-15 position, downstream) has a decrease of 2%, the P wave velocity measured at path B (0 position) and position C (15 position) have a decrease of 1%, the P wave velocity measured at path D (30 position, upstream) has a decrease of 0.2%. The P wave velocity measured at downstream has the largest decrease while the P wave velocity measured at upstream has almost no change. These results show that the crack development is mainly active at the downstream part of the sample, while at the upstream part of the sample, the crack development almost stopped. In the middle part of the sample, cracks kept developing, but less active compared to the downstream part of the sample.

From 4500s to 5200s (stage III, corresponding to the rupture process), the P wave velocity at different positions of the sample keeps decreasing, with an amount of 40%~45% of decrease.

(5) Acoustic Emission number

From 500s to 1500s (first part of stage I), the log number of acoustic emission events increased from 0 to 0.75. From 1500s to 2700s (part 2 of stage I), the log number of acoustic emission events increased from 0.75 to 1.45. From 2700s to 4500s (stage II), the log number of acoustic emission events increased from 1.45 to 1.75. The number of events during stage II are much less than during stage I (the diffusion process), which is consistent with the P wave velocity decrease. (P wave velocity decrease in stage II are much less than that of stage I). From 4500s to 5200s (stage III, rupture process), the log number of acoustic emissions increased from 1.75 to 3.5. AE numbers indicate cracks opening and initiation and propagation of new cracks during fluid injection.

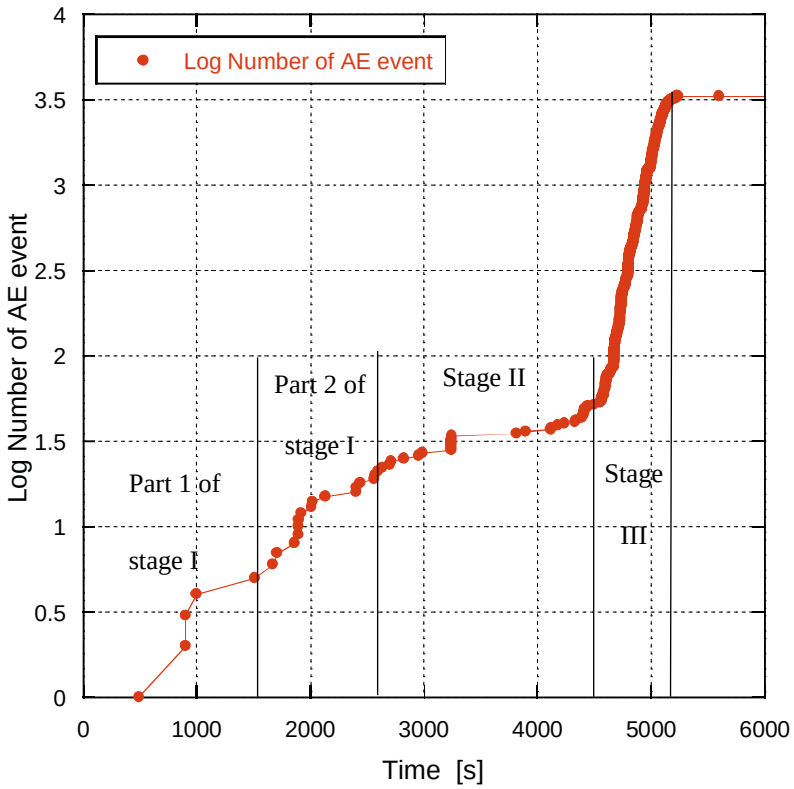

Figure 4.11.a Number of acoustic emissions during fluid injection

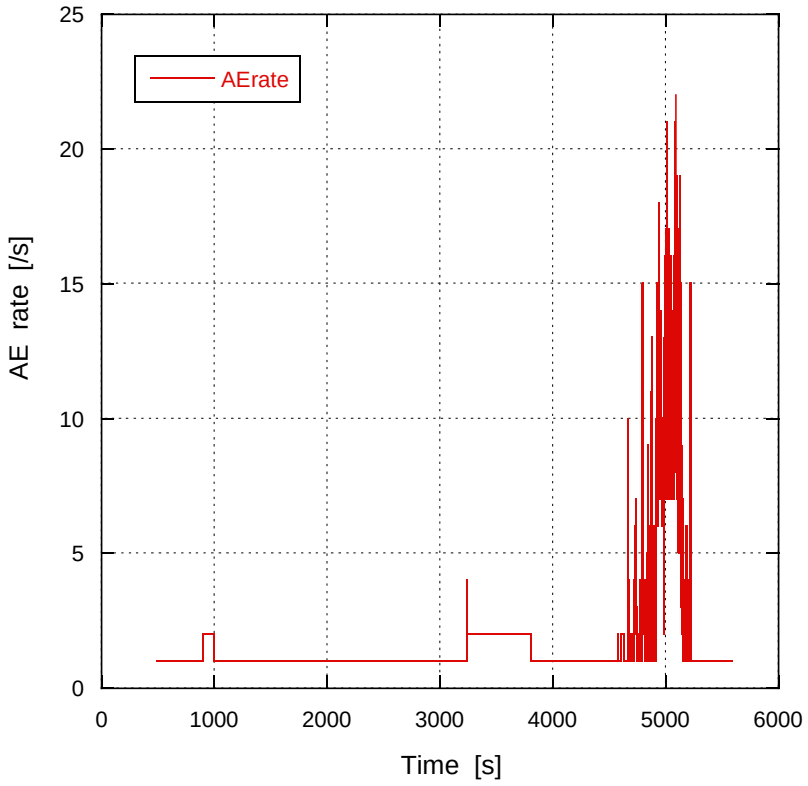

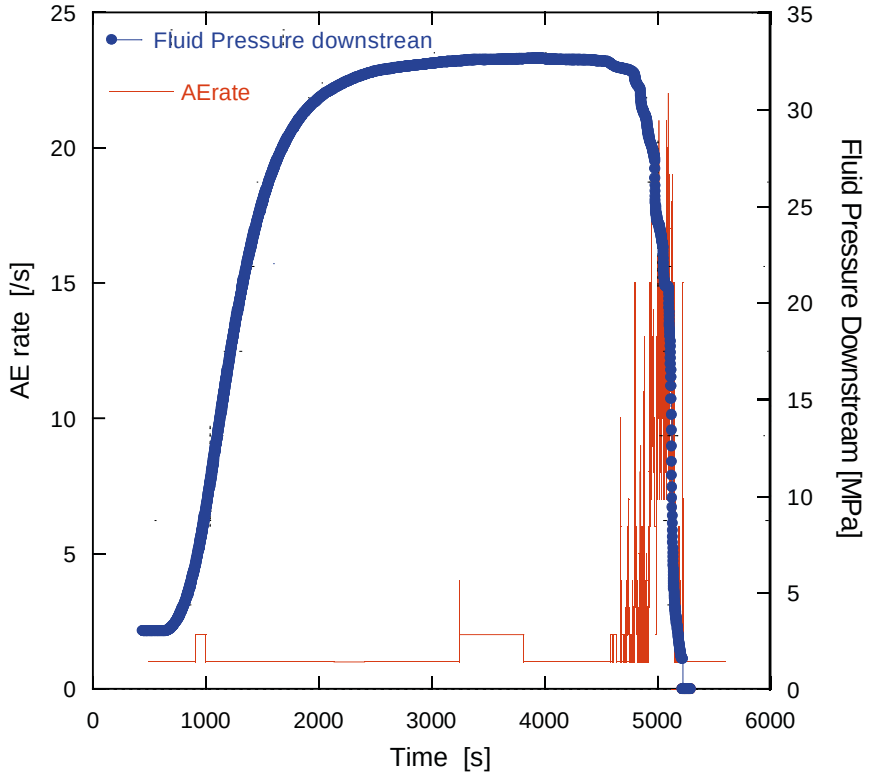

Figure 4.11.b AE rate during fluid injection

During fluid injection, the event number shows two points of burst (Figure 4.11.b), the first point is at 3200s, where pore fluid pressure reaches the highest value. The second point is at 4500s (stage III, beginning of rupture), at a stage where pore fluid pressure begins to decrease. AE rate is maximum at 5000s, where the axial stress begins to drop (rupture).

(6) AE location

Acoustic Emissions are located with an algorithm considering the P wave velocity change in time. To do the velocity model, the sample is separated in five parts, according to the positions of sensors.

The sample developed two fractures, with an angle of 60º (figure 4.12.m). The first fracture initiates from the downstream part, which is consistent with the P wave velocity measurements (P wave velocity keeps decreasing at downstream part in stage II).

The first fracture developed in a stable manner from 4500s to 4900s, with a fracture tip velocity of 0.1mm/s (figure 4.12 a-c). The fracture propagated unstably at t=4900s, forming a fracture through the whole sample. Then, at t=5050s another fracture is initiated from the middle part of the sample, with an angle close to the one observed on the first fracture (figure 4.12 d-i). The second fracture is formed in 50 seconds across the whole sample, in an unstable manner.

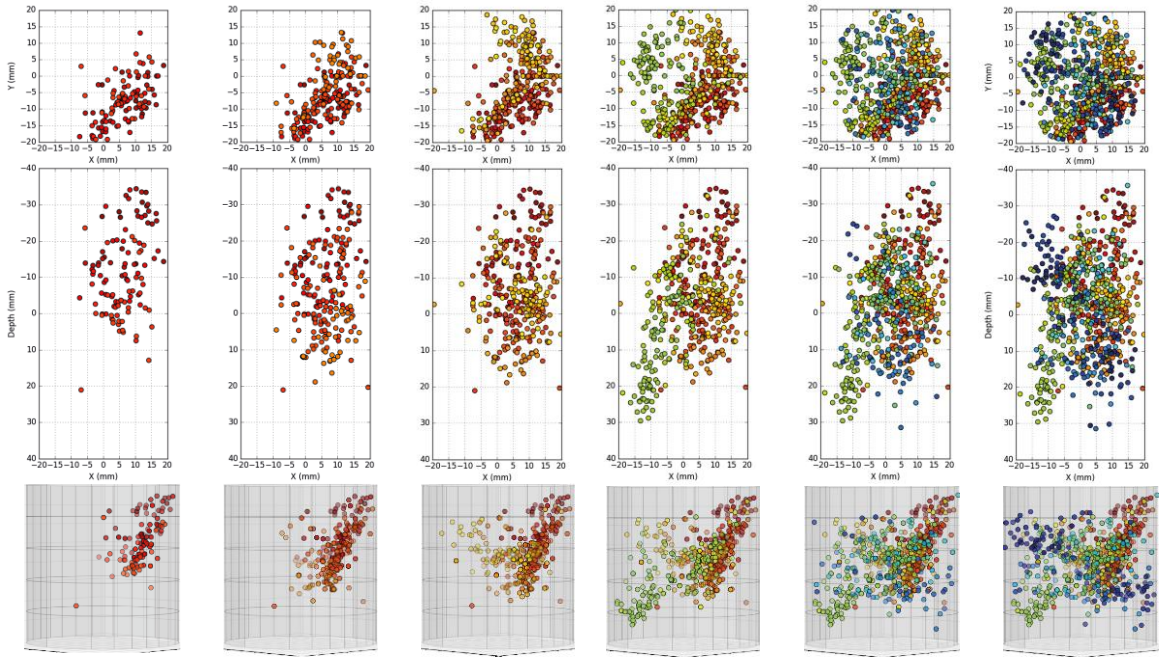

(a) 4500s~4800s (b) 4500s~4850s (c) 4500s~4900s (d) 4500s~4950s (e) 4500s~5050s (i) 4500s~5250s

(m) sample with two faults after experiment

Figure 4.12: a~i: Location of Acoustic Emissions in the experiment of fluid-injection induced rupture. m: The sample after the experiment has two fractures, in good agreement with the AE locations.

From 4950s to 5050s, events are observed around fault zone (fluid may begin to dissipate into the surrounding damaged zone of the fault).

As shown in figure 4.12, the fractures observed in the sample after deformation (figure 4.12.m) are in good agreement with the location of the acoustic emission (figure 4.12.i).

4.4 Discussion

4.4.1 Crack density inverted from hydrostatic loading under dry condition

Considering the effect of both cracks and pores, and the assumption of non-interaction, effective medium theory is employed to calculate crack density of heat treated andesite during hydrostatic loading (Mori and Tanaka, 1973; Kachanov, 1993; Sayers and Kachanov 1995; Shafiro and Kachanov, 1997; Schubnel and Gueguen, 2003; Fortin et al. 2007)

$$\frac{K_o}{K} = 1 + \frac{\rho}{1-p}\frac{h}{1-2v_o}\left\{1 - \frac{v_o}{2}\right\} + \frac{p}{1-p}\frac{3(1-v_o)}{2(1-2v_o)} \tag{4-1}$$

$$\frac{G_o}{G} = 1 + \frac{\rho}{1-p}\frac{h}{1+v_o}\left\{1 - \frac{v_o}{5}\right\} + \frac{p}{1-p}\frac{15(1-v_o)}{7-5v_o} \tag{4-2}$$

h is a factor describing the penny-shaped geometry.

$$h = \frac{16(1-v_o^2)}{9(1-v_o/2)} \tag{4-3}$$

K_0 is the bulk modulus of solid skeleton, v_0 is the Poisson ratio of solid skeleton; these moduli can be estimated using the data obtained on intact andesite sample.

K and G are estimated using the ultrasonic velocities measured during the hydrostatic loading of heat treated (at 930°C) andesite. The porosity parameter p of heat treated andesite samples is 3.7%. ρ is the crack density which could be inverted using equations 4-1, 4-2 and 4-3.

Figure 4.13 shows the evolution of the crack density on the dry sample with pressure, and decrease from 0.75 to 0.4 as pressure increase from 12 to 40 MPa. Note that for crack density larger than 0.5, the non-interaction assumption is not really appropriate.

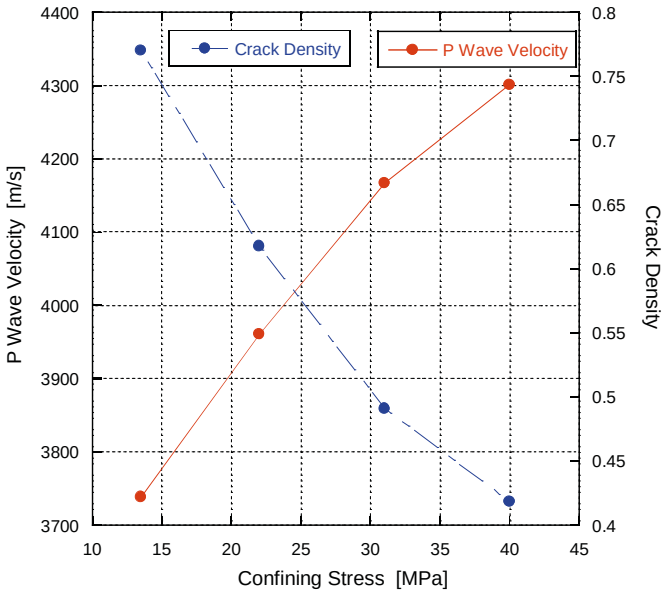

Figure 4.13 inverted crack density in the experiment of heat-treated andesite under hydro-loading in dry condition.

4.4.2 Aspect ratio/crack length/crack aperture inverted from hydro-loading under saturated conditions

The pressure at which cracks close is (Walsh, 1965; Jaeger et al., 2007; Ougier-Simonin et al., 2011)

$$\sigma_{close} = \frac{\pi \xi E_o}{4(1 - {v_o}^2)} \tag{4-4}$$

Under saturated conditions, from the data of heat treated andesite samples during hydrostatic loading (figure 4.2, 4.3) and differential loading (figure 4.5), it is assumed that the pressure for closing the cracks $\sigma_{close}$is 75MPa (75MPa is the value extrapolated with pressure-volumetric curve), E_0 is the Young modulus of the intact rock estimated as 70GPa, $v_0$is the Poisson ratio

of the intact rock estimated as 0.22, ξ is the mean aspect ratio. It could be calculated with equation (4) that aspect ratio ξ is 0.001.

Dienes and Gueguen, [1989] gave the relation between permeability k and microstructure parameters. The permeability k of a material with an isotropic distribution of the crack could be expressed as (Gueguen and Dienes 1989; Ougier-Simonin et al. 2011).

$$k = \frac{2}{15} f w^2 \xi \rho_c \tag{4-5}$$

k is permeability, f is percolation fraction, assumed to be 1 (Dienes and Gueguen 1989), w is crack aperture, ρ_c is crack density. It could be calculated that the aperture is ~0.27μm. With the aspect ratio, it could be estimated that the crack length is 270μm, which is the size of phenocrysts in samples we use in these experiments.

4.4.3 Fluid injection into heat treated saturated andesite sample

(1) Different stages and corresponding physical processes in fluid injection experiment

The behavior in the injection experiment could be decomposed into four parts.

Stage I is a diffusion process influenced by the dead volume at downstream. During this process, P wave velocities at different positions of the sample decreased which might due to crack opening, and the axial strain and volumetric strain increased linearly, indicating an elastic regime.

In stage II, the fluid pressure measured at downstream is almost constant. But P wave velocity kept decreasing at different positions of the sample, the injected volume increased with a constant rate, the volumetric strain started to increase nonlinearly. This process indicates that while the stress state is constant on a macro scale, cracks kept propagating at a low rate through the whole sample (slow crack propagation). The pore pressure at micro scale is possibly not

constant in the whole sample, a competition between crack development and fluid pressure build up might have occurred.

In stage II, cracks begin to develop heterogeneously in the whole sample. During this stage, mainly the downstream end of the sample is active in crack development. From the P velocity decrease, it could be deduced that at the upstream end of the sample, cracks almost stopped developing, the pore pressure might have remained constant at this part. At the downstream part of the sample, cracks kept developing. This is also confirmed with the acoustic location in figure 4.12, which shows that the main fracture starts from the downstream end of the sample.

In stage III, rupture process begins. As shown in figure 4.12, 5000s is the point where the main fracture suddenly propagated through the whole sample. The acoustic numbers recorded from 4500s to 5000s reflected the propagation of the tip of the main fracture. The acoustic emissions recorded from 5000s to 5200s reflects several processes: firstly, as the main fracture suddenly formed and went through whole sample, the fluid pressure dissipated into the new fracture and the damaged zone. Then another fracture at the same angle (with respect to the axial stress of the sample) is formed. The fluid then dissipated in the fracture surface and surrounding zone (injected volume increases suddenly in figure 4.9 and fluid pressure drops in figure 4.7). Fluid dissipation could cause local slip on the main fault after. After 1 hour under almost constant stress (32MPa-32.8MPa), once the fluid pressure in the sample reach a certain value (32.8MPa), the micro cracks begin to interact and develop unstably, which finally leads to the rupture.

(2) Time dependent behavior in the injection-induced rupture experiment

Stage II is a time dependent process, with stress state and fluid pressure remaining almost constant, it took approximately 2000s-3000s for the strain to keep increasing until the final failure. The volumetric strain increased nonlinearly of 0.1% with the fluid pressure increasing

from 32MPa to 32.8MPa in 3000 seconds. As P wave velocity kept decreasing, acoustic numbers kept increasing, cracks kept developing.

Following Mallet et al. [2014], the time to rupture could be modeled. This model is built on the basis of subcritical crack growth and wing crack model. The time to rupture τ(3000s in our experiment under constant stress state) could be expressed as

$$\tau = \frac{\lambda}{I_0}\exp(\frac{E_a + 2\gamma s}{kT}) \tag{4-6}$$

I_0 is a characteristic speed, assumed to be the product of interatomic distance b and the atomic vibration frequency υ, I_0~10^4m/s [Lawn and Wilshaw, 1975]. E_a is the activation energy, is assumed to be 25 kj/mol (Mallet et al. 2014). γ is the thermodynamic surface energy (for water), in the range of 1.0J/m^2(Gueguen et al.1990). s is an elementary surface of a crack jump, in the range of 3.2*10^{-20}m^2 (Darot and Gueguen, 1986). T is temperature (room temperature K).k is Boltzmann constant. Thus, λ could be estimated using equation 4-6 and $\lambda = 153\mu m$; taking into account that:

$$\lambda = \frac{\pi E_0 kT}{4s\sigma'^2} \tag{4-7}$$

where E_0 is young's modulus. This lead to σ' = 0.3MPa (with E_0 to be 50GPa).

In addition, Ashby and Sammis, (1990) give the following expression:

$$\sigma' = \sigma_i' - \sigma_3' \tag{4-8}$$

$$\sigma_i' = \frac{F_w}{d^2} \tag{4-9}$$

d is the average space between cracks (an assumption is made about the stress interaction σ_i' to be constant). And F_w is:

$$F_w = (A_1\sigma_1' - A_3\sigma_3')a^2 \tag{4-10}$$

where a is crack radius, assumed to be ~ (100μm-300μm)/2. σ_1' is $\sigma_1 - p$, σ_3' is $\sigma_3 - p$ (pore pressure is changing both in space and time, but in stage II, we can assume that the whole sample has reached the same pressure). Finally, A_1 and A_3 are expressed as (Ashby and Sammis, 1990)

$$A_1 = \frac{\pi\sqrt{\beta}}{\sqrt{3}}((1+\mu^2)^{1/2} - \mu) \tag{4-11}$$

$$A_3 = A_1\left(\frac{(1+\mu^2)^{\frac{1}{2}} + \mu}{(1+\mu^2)^{\frac{1}{2}} - \mu}\right) \tag{4-12}$$

$\beta = 0.1$. μ is friction coefficient, referred in basalt, in a range of 0.55~0.65, A_1 is in the range of 0.31~0.34, A_3 is in the range of 0.97~1.05, F_w is in the range of 0.005Pam^2~0.015Pam^2.

With the estimation of σ' and F_w, d_c could be estimated to be $129\mu m$~$223\mu m$, which is consistent the size of phenocrysts. If activation energy E_a is 70kj/mol (value for basalt from Heap et al. 2009), d_c is $0.1\mu m$, so activation energy has a large influence on the value of d_c. Crack interactions are dominant when crack has a critical crack length I_c, as this stage, crack mean spacing is characterized by a critical distance d_c. I_c is estimated to be equal to d_c. So the d in σ_i' is calculated as d_c.

In this case τ while λ is calculated to be in the range of

Finaly, in stage II, the crack length change with time could be expressed as

$$I(t) - I_c = -\lambda\ln(1 - \mathrm{t}/\tau) \tag{4-13}$$

Which is

$$I(t) = -153\ln\left(1 - \frac{t}{3000}\right) + 150 \tag{4-14}$$

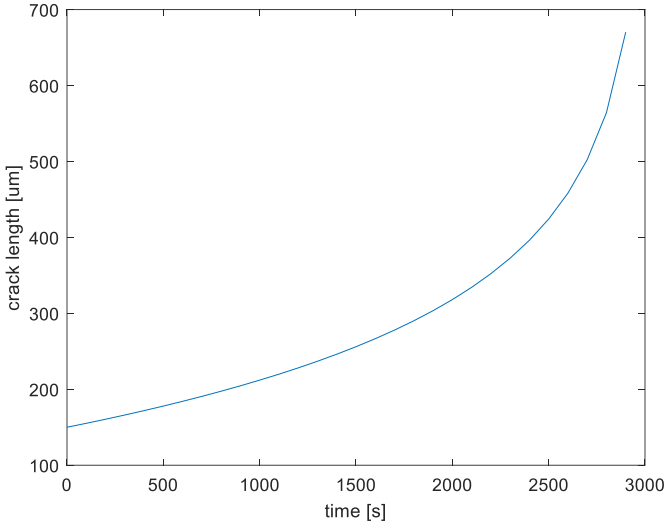

Figure 4.14 crack length change with time in stage II.

The mean crack length at the rupture is in the range of 0.650 mm. Note that following the approach of Mallet et al. [2014]. The volumetric strain could also be modeled with the subcritical crack growth and wing crack.

4. 5 Conclusions

(1) Under saturated conditions, P wave velocity of heat treated (at 930°C) andesite measured under hydro-loading has a slight increase compared to dry conditions.

(2) Under saturated conditions, crack density of heat-treated andesite sample is inverted, aspect ratio is estimated to be 0.001, and crack aperture $0.27\mu m$.

(3) Permeability of heat treated (at 930°C) andesite sample has shown a large decrease ($9*10^{-18}m^2$~$2*10^{-18}m^2$ under hydro-loading (0MPa~25MPa).

(4) Heat-treated andesite samples have shown a brittle characteristic under saturated conditions and falls on the line of failure despite different porosities.

(5) A time dependent behavior was observed in the fluid-injection induced rupture experiment.

(6) Heterogeneity of crack development was observed before rupture. More cracks were developed at downstream end while upstream end remains silent. The rupture began from the downstream end.

(7) Critical crack space is inverted and estimated to be in the range of $129\mu m$~$223\mu m$. Crack length growth with time is inverted during stage II where stress state was constant.

Chapter V Permeability Evolution and Its Effect on Fluid Pressure Temporal Spatial Distribution during Fluid Injection

Abstract

Chapter V investigates the fluid pressure diffusion in rock submitted to stresses close to the criticality. We performed a fluid injection experiment on the thermally treated andesite and monitored pore pressure in a space-time domain. Firstly, hydrostatic loading is applied on the sample to 40MPa, then differential loading was increased until stress state reaches beginning of dilatancy. Then, fluid pressure was increased at one boundary of the sample and kept at a constant value (35 MPa), until the whole sample reaches failure. We employed optic fiber sensors to measure the fluid pressure at different positions of the sample during the pressure diffusion process, axial strain and radial strain are recorded during the whole process. After experiment, CT-scan was performed on the sample after fluid injection experiment to observe the fractures formed after experiment. Spatiotemporal pattern of seismicity related to hydraulic diffusion. Our results show that (1) Permeability heterogeneity is observed during the fluid-injection experiment. (2) Subcritical crack growth influences the permeability and pore pressure spatial temporal distribution. (3) A numerical simulation reproduces well the fluid injection experiment

5.1 Introduction

Fluid pressure variation associated with seismicity can be observed in natural processes such as seasonality of ground water recharge (Hainzl *et al.* 2006; Saar and Manga, 2003), water level fluctuations in water reservoirs (Chander, 1997; Talwani 1997), in petroleum exploration (Davies et al., 2013; Rutqvist et al., 2013) , geothermal field (Baisch et al., 2010; Deichmann

and Giardini, 2009; Brodsky et al., 2000; Prejean et al. ,2004; Giardini 2009), wastewater disposal (Horton, 2012; Kim, 2013; Keranen et al., 2014; Frohlich et al, 2014), or CO_2 sequestration (Zoback and Gorelick, 2012; Mazzoldi et al., 2012; Cappa and Rutqvist, 2011). It has been also shown that fluid pressure variation influence earthquake faulting activity (Yamashita 1998; El Hariri et al., 2010) over long space and time scales (Hummel and Müller, 2009; Shapiro *et al*., 1997, 2003;).

Seismicity activity associated with fluid pressure variation depends on the diffusivity and mechanical properties of rocks (failure criterium) (Do Nascimento et al., 2005; Shapiro *et al*., 1997, 2003). In a recent model, Hummel and Müller, (2009) included the permeability change during the fluid pressure diffusion. Yilmaz et al. (1994) investigated pore fluid pressure distribution in fractured and compliant rocks by simulating 1-D pore-fluid pressure profiles with a pressure-dependent permeability. In addition, pore pressure propagation is also highly influenced by the permeability heterogeneity (Lee et al., 1998; Clifton et al., 2003; Do Nascimento et al., 2005). Thus, it is important to account for geological complexity when estimating the transmission of fluid pressure variations while investigating seismicity activity (Simpson and Narasimhan, 1992; Lee et al., 1998; Do Nascimento et al., 2005).

To investigate the link between pore fluid pressure diffusion and seismicity activity, we performed fluid injection experiments on the thermally treated andesite and monitored pore pressure in time and in different locations. First, hydrostatic loading is increased on the sample to 40MPa, then differential loading is increased until a stress state close to the beginning of dilatancy. Finally, fluid pressure is increased at one boundary of the sample and kept at a constant value (35 MPa), until the whole sample reaches failure. We employed optic fiber sensors to measure the fluid pressure at different positions of the sample during the pressure diffusion process. In addition axial strain and radial strain are recorded during the whole

process. After the experiment, a CT-scan was performed on the sample to observe the fractures formed after experiment.

5.2 Methodology

5.2.1 Sample preparation

Samples were cored with a length of 100mm and a diameter of 50mm. All samples are cored parallel in the same block. After coring, boundary surfaces are grounded to ensure a smooth surface vertical to the axis.

The sample is andesite from Deshaies Quarry (La Guadeloupe, French Antillas). It is composed of a fine groundmass with phenocrysts. The sample has a porosity of 1.5%. Initial P-wave velocity in the sample was measured at room pressure, with a value around 5400m/s. Permeability is of the order of $10^{-21}m^2$. To increase its permeability, the sample was heat-treated with a programmable Meker MHT-3 furnace. The sample was heated at a rate of 140°C/h, up to 930°C, kept 2 h at this temperature, and then cooled down to room temperature (approximately in 10 hours), to avoid thermal shock effect. The cracks induced are due to the different thermal expansion coefficients of minerals (Fredrich and Wong, 1986; Browning et al., 2016).

To measure the pore pressure in the rock specimen submitted to confining pressure, three holes were drilled on the surface of the sample with a depth of 25mm to bury the optic fiber sensors rock at 1/4, 2/4 and 3/4 of the height of the sample. Then, three fiber optic sensors are placed into the holes that were previously drilled. The combination of the fiber optic sensors with the pressure sensors of the Quizix system allow five independent pressure measurements at five points along the sample (0, 2.5, 5.0, 7.5 and 10 cm). Heat-shrinkable tubing made is used to separate the sample from oil confining medium (Reinsch et al., 2012; Blöger et al., 2014).

5.2.2 Experiment apparatus

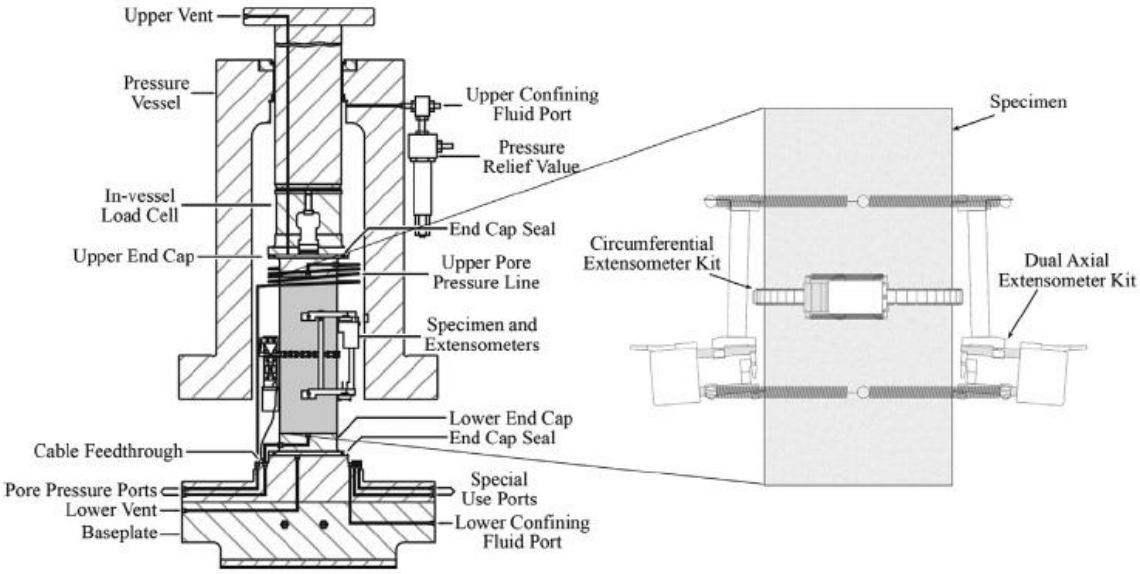

Figure 5.1 Tri-axial cell (MTS 815) at GFZ potsdam (Blöger et al., 2014)

Figure 5.2 Sample assembly on tri-axial cell at GFZ Potsdam, Germany (Reinsch et al., 2012)

Experiments were performed on the triaxial cell (MTS 815) (figure 5.1) at GFZ, Potsdam (Blöger et al., 2014; Pei et al., 2017). Strains are measured with extensometers including one

axial and two radial (figure 5.1). Axial displacement is also measured with displacement transducers (DCDT) mounted between the moving piston and a fixed platen. Volumetric strain is calculated as $\varepsilon_v = \varepsilon_a + 2\varepsilon_r$ where ε_a and ε_r are the axial and radial strains, respectively.

Pore pressure and pore fluid volume are controlled by a micro-volume pump both at the upper part and down part of the sample (Quizix 106 6000-Series) with an accuracy of about 10^{-2} MPa and 10^{-4} ml/min, respectively (Blöger et al., 2014). The tubing volume between the pumps and the sample is approximately 100 ml.

5.2.3 Optical Fibers

(1) Sensing Principle

The fiber optic sensor (FOPS) used for this application consists of a miniature all-silica extrinsic Fabry-Perot cavity (EFPI) pressure sensor with an encapsulated Fibre Bragg Grating (FBG) (Bremer et al., 2010, Reinsch et al., 2012) (Figure 5.3). The 200µm fiber was cleaved and polished using raw polishing paper of several hundred micrometers, in order to avoid light reflections at the outer surface of the 200µm fiber. The length of the sensor is about 0.5cm and its outer diameter is about 230µm (Reinsch et al., 2012). Hence, the fiber optic sensor provides a simple, miniature and robust sensor to measure pressure and temperature within a rock specimen. The theoretical discussion of the sensing principle is based on Reinsch et al., (2012) and Bremer et al., (2010). Monochromatic light is sent in the fiber optic and propagates to the head. Incident light is reflected twice (figure 5.3) (Reinsch et al., 2012, Bremer et al., 2010): (1) First, part of light is reflected at the entrance into the EFPI cavity (glass/air interface) and (2) the transmitted light is reflected at the termination of the cavity (air/glass interface). Light reflected at the end of the cavity is partly transmitted back into the fiber and interferes with light reflected from the first reflection (Reinsch et al., 2012, Bremer et al., 2010). The phase shift between the two reflected signals depends on the cavity length, which is function of the

pressure and temperature (temperature is maintained constant during our experiments). Before being used in experiments, the fiber optics need to be calibrated to achieve the relation between pressure and cavity length (phase shift evolution with pressure). A thorough theoretical discussion of the principle of this sensor can be found in Bremer et al. (2010) and details on the experimental setup are given in Reinsch et al. (2012).

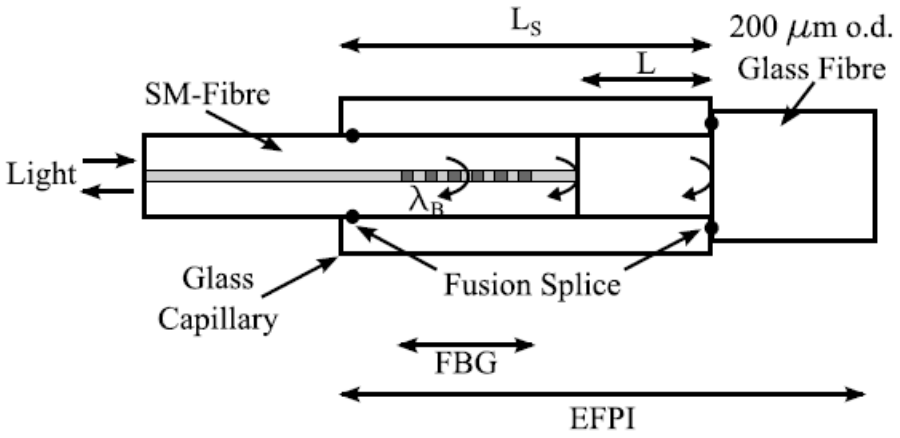

Figure 5.3 Configuration of fibre optic sensors (Reinsch et al., 2012)

(2) Interrogation system

The interrogation system is shown in Figure 5.4 (Reinsch et al., 2012). The interrogation system consists of a broad-band light source (BBS) (INO FBS-C), an optical circulator, a fibre optic switch (JDS Fitel) and an optical spectrum analyser (OSA) (ANDO AQ6330) (Reinsch et al., 2012). Light from the BBS is guided through the optical circulator to the optical switch, which is used to interrogate the fibre optic sensor and an optical mirror, sequentially. The mirror signal is used for normalisation of the measured signal from the FOPS (Reinch et al., 2012). The reflected light from the FOPS/mirror is then guided back to the optical circulator, from where the signal is transferred to the OSA. The OSA captures and normalises the reflected

FOPS spectrum. A computer is used to acquire and analyse the spectrum and operating the switch. An example of a normalized spectrum is depicted in Figure 5.4.

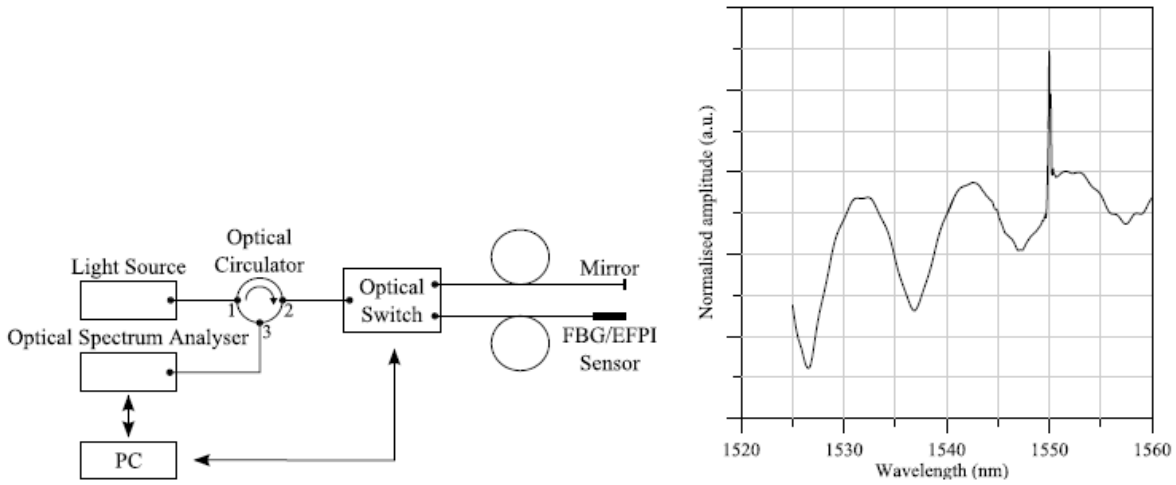

(a) Interrogation System. (b) Normalized Spectrum.

Figure 5.4 Configuration of interrogation system (Reinsch et al., 2012)

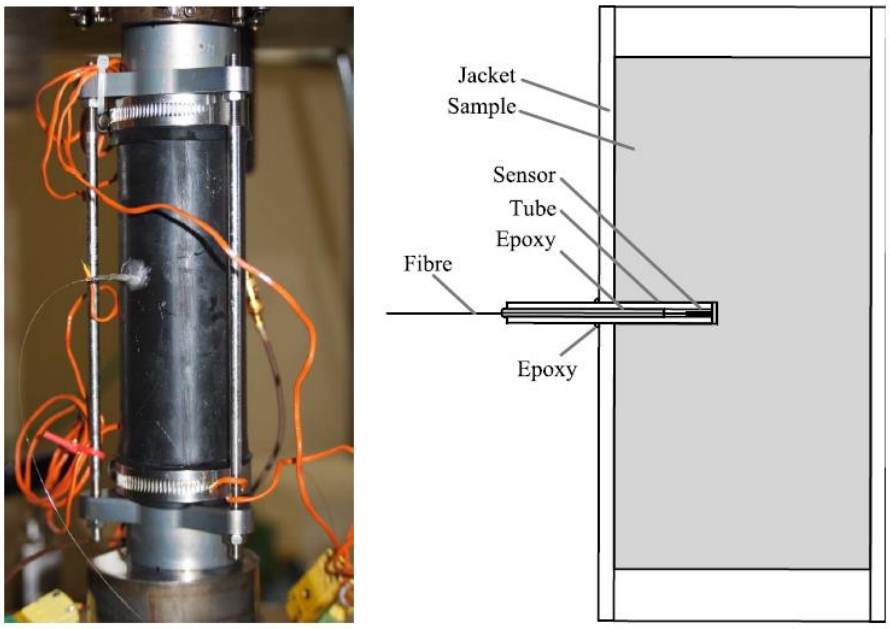

(a) Sample Preparation. (b) Sketch.

Figure 5.5 Configuration of fibre optic sensors assembly (Reinsch et al., 2012).

(3) Assembly fibre optic sensors on samples and MTS

Using a needle, a hole has been poked through the jacket at the position of the drill-hole (figure 5.5). The sensor has been embedded through this hole approximately 25mm deep into the rock sample, leaving a void space of 12 mm^3 which is less than 0.05% of the pore volume (Reinsch et al., 2012).

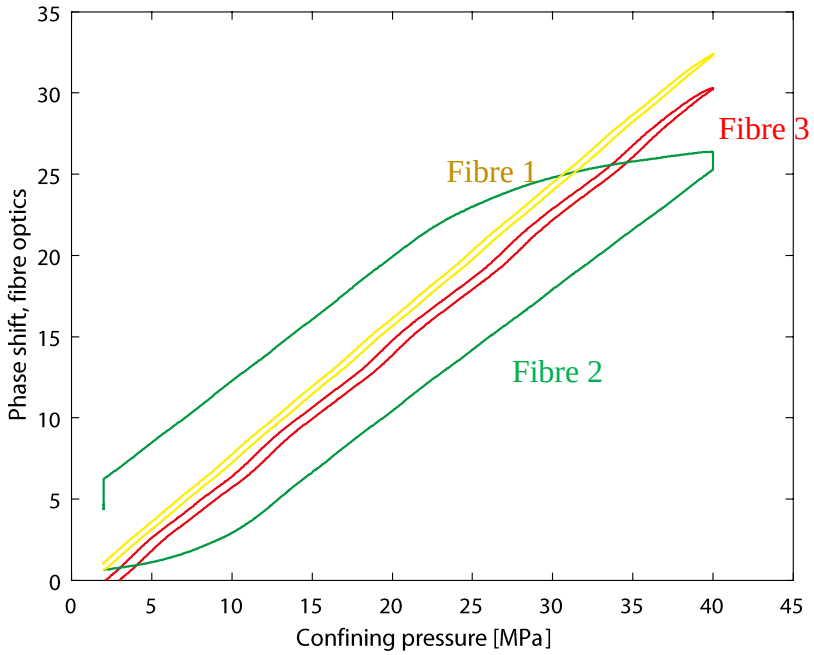

Figure 5.6 Calibration of fiber optic sensors

(4) Calibration of Optical Fibers

For calibration, the three fibre optic sensors were placed within the oil in the pressure chamber. Temperature of oil was controlled and maintained constant at 30°C. The pressure was increased from 2MPa to 40 MPa at a rate of 0.25 MPa/min while data from the sensors was recorded with a time resolution of 15 s, thus one measurement is made approximately each 0.06 MPa. The sensor responses to an increase of pressure were tested and the sensors response is shown to be linear as a function of pressure (Figure 5.6) for two of the sensors (Fibres 1 and 3). Fibre 2 shows a hysteresis that could be explained by a small leak in the Fabry-Perot cavity. The response of Fibre 2 seems to be correct and linear after an initial non-linear response (Figure 5.6). From the experiment on the rock, this sensor will be used only in the linear response

domain. With the calibration information, it is possible to correlate phase shift changes to pressure changes. Note that the precision can be estimated to be around 0.5 MPa.

5.3 Results

5.3.1 Fluid pressure temporal spatial distribution

In this experiment, pore pressure is measured (i) at point A - Upstream (figure 5.7), at point B (position -25mm) where pore pressure is measured by a fiber optic, at point C (position 0 mm) where pore pressure is measured by a fiber optic, at point D (position +25mm) where pore pressure is measured by a fiber optic, and at point E - downstream (figure 5.7).

Before fluid injection, hydrostatic pressure was increase to 40 MPa, and differential loading was applied on the sample till 379 MPa. The axial strain and radial strain increase due to the differential loading (i.e. between t=0 and 3500 s), at the beginning of the experiment are shown in figure 5.7 (Top). Before fluid injection, the axial strain is 0.06% while volumetric strain is 0.004% (figure 5.7).

At t=4700s, the upstream pore pressure is increased to 35 MPa and maintained constant at this pressure. As soon as the upstream pressure is increased, the pore pressure increased almost immediately in B, C and D. Then, the whole sample reaches an equilibrium and the fluid pressure at downstream increases very slowly (figure 5.7), the pore pressure at positions C and D keeps constant (figure 5.7). During this stage, the pore pressure in B decreases slightly, which may be related to the initiation and propagation of cracks in the area of B.

Then, the fluid pressure at downstream (position E) begin to build up, with a change in the slope at a t=15000 s. This is correlated with an increased in the pore pressure at different positions and a decrease in the volumetric strain (figure 5.7). From the point where pore pressure in the whole sample began to increase till rupture, the volumetric strain decreased of

0.28% (figure 5.7), denoting that the cracks initiate and propagate during this stage. As the pore pressure at position C, D, E reaches 20 MPa and the pore pressure at position B reaches 35 MPa, the rupture begins (figure 5.7).

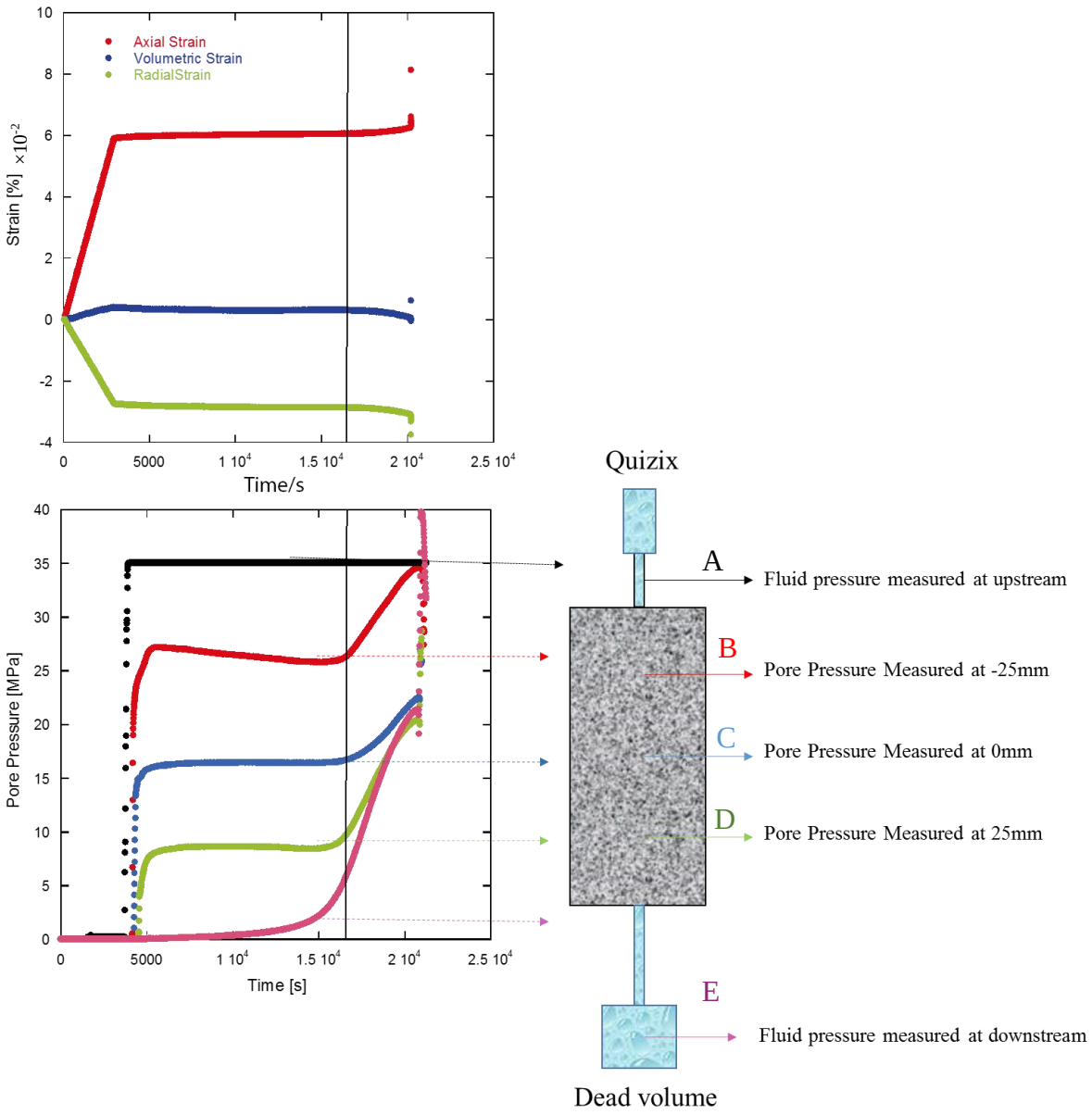

Figure 5.7 Pore pressure evolution at different positions of samples and strain evolution during fluid injection experiment

The injection rate evolution during the fluid injection is shown in figure 5.8. At the beginning of the fluid injection, the injection rate is high (figure 5.8). As fluid diffuse from upstream to downstream and reach the equilibrium (fluid is filling the dead volume), the injection rate decreases from 10^{-1}ml/s to 10^{-3}ml/s (figure 5.8) and keeps constant (figure 5.8).

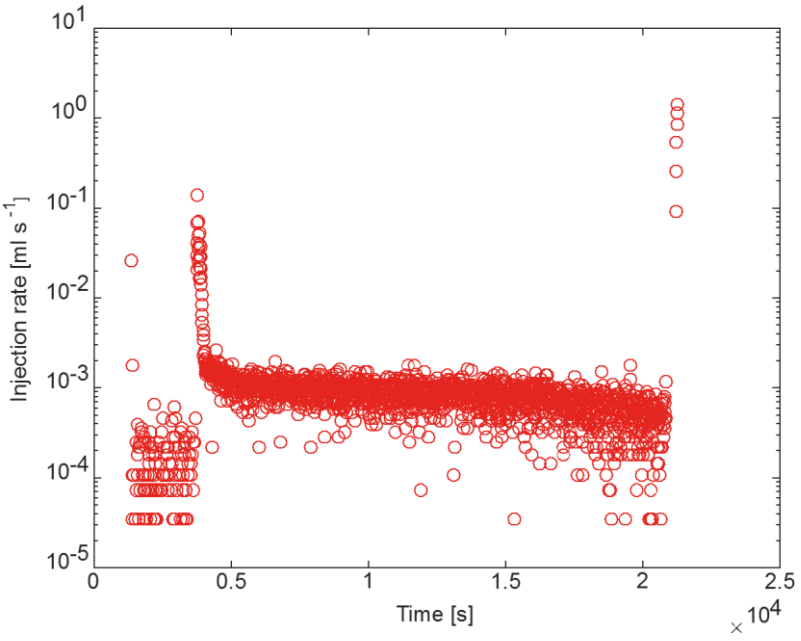

Figure 5.8 Injection rate evolution during fluid injection experiment

5.3.2 Permeability variation space & time

Assuming that the injection rate through the whole sample is the same and constant during the fluid injection (figure 5.8), it is possible to evaluate the following ratio

$$k = \frac{Q\mu L}{A\Delta P} \tag{5-1}$$

Where Q is the flow through the sample, μ is the fluid viscosity, L is a length, A is the cross-sectional area and ΔP is the difference in pore pressure. A is 0.002m^2 and μ is the fluid viscosity 1.0518×10^{-3} Pa·S, Q is estimated using the injection rate, and q= 10^{-9}m^3/s. Note that the flow is transient, thus k is not the exact permeability, the ratio defined in (5-1) gives us an idea of the evolution of the permeability in time and in space. Indeed, it is possible to defined k at

different parts of the sample with the fluid pressure measured by optic fiber sensors at different positions of the sample.

Figure 5.9.A and figure 5.9.B show the evolution of k at two different parts of the sample with time (between B and C for Fig 5.9.A and between C and D for Fig 5.9.B). Figure 5.9.A shows that k remains almost constant in the area BC. However, Figure 5.9. B shows that k increases largely in the area CD, indicating the creation of connected crack network between C and D. Figure 5.9 reflects the spatial difference of fluid conductivity and the heterogeneity of crack development through the whole sample.

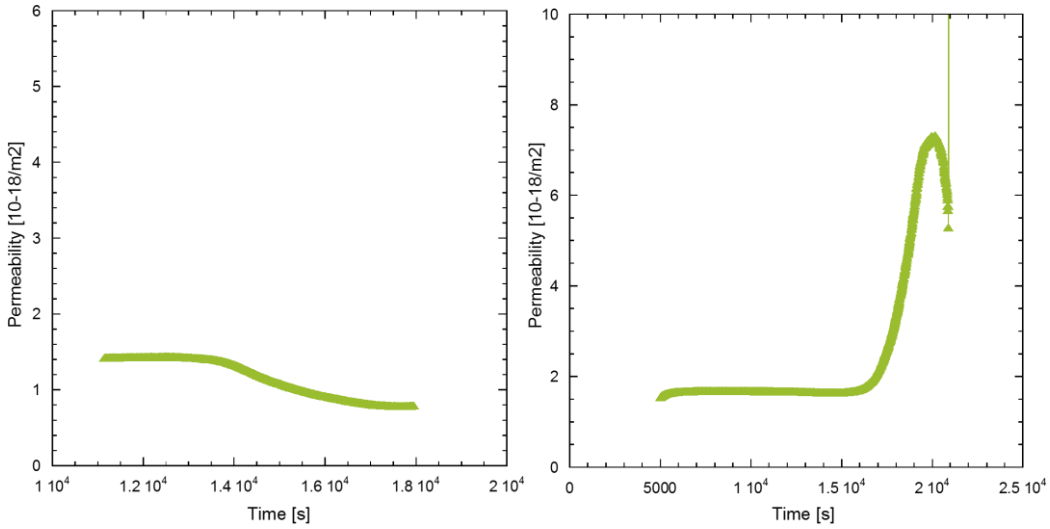

Figure 5.9.A permeability evolution in B-C part of sample**; B** Permeability evolution in C-D part of sample

5.3.3 A clear heterogeneity of crack development (CT images)

In order to have an insight into the fracture network formed during fluid injection experiment, CT scan was performed at IFPEN on the sample after experiment. Three planes were scanned, including transverse plane, coronel plane and sagittal plane which are vertical to the directions of σ_1, σ_2, σ_3.

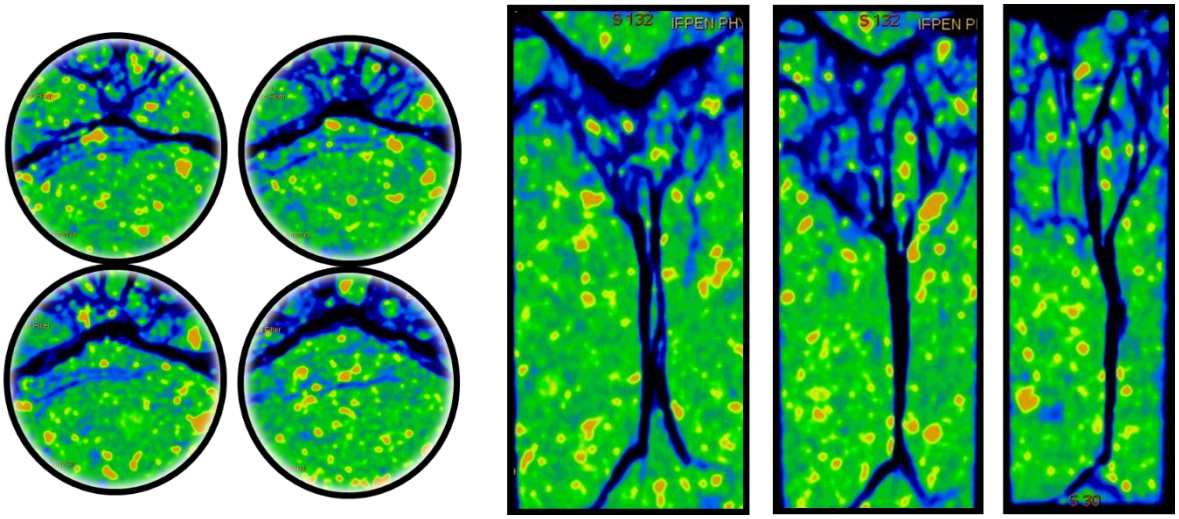

Figure 5.10.A Coronal Plane **Figure 5.10.B** Tranverse Plane

Figure 5.10 CT scan of samples after fluid injection experiment

As is shown in the figure 5.10.A, 5.10.B, the fracture formed after fluid injection has shown a large heterogeneity in the whole sample. Half of the sample (zone between A and C) developed dense fractures network at different scales and fractures connect well with each other. The other half part of the sample has developed a single main fracture with a secondary fracture close to the boundary. These results implicate that damage zone in the upper part of the sample may have developed during the diffusion process and fractures connect well before the rupture, which corresponds well with the results of pore pressure evolution shown in figure 5.7 (pore pressure measured at position C, D, E slowly tends to the same value before rupture).

5.4 Discussion

The hydraulic diffusivity D is (Klute and Dirksen, 1986):

$$D \sim \frac{kBK_d}{\eta\alpha} \tag{5-2}$$

where k is permeability, B is Skempson's coefficient, K_d is the drained bulk modulus, η is the fluid viscosity and α is Biot's coefficient. η=1.0518×10^-3Pa·S, K_d=9 GPa. We will assume that Skempton's coefficient is and Biot's coefficient is 1.

5.4.1 boundary condition

For the upstream boundary condition, the pressure is increased instantaneity $p = p_0$= 35 Pa. At $t = 0$ and remains constant for ≥ 0 ; it is a Dirichlet-type boundary condition :

$$P(x, t < 0) = 0, p(x = 0, t \geq 0) = 35MPa$$

For the downstream boundary condition, we have to take into account the effect of the dead volume. The condition is due to mass conservation and:

$$S_d \frac{\partial p_p}{\partial t}_{x=L} + \frac{kA}{\eta} \frac{\partial p_p}{\partial x}_{x=L} = 0 \quad (5\text{-}3)$$

L is the sample length 0.1m, S_d is the downstream reservoir storage capacity

$$S_d = \frac{V_1}{K_f} \quad (5\text{-}4)$$

Where V_1 is reservoir volume. The water bulk modulus is K_f2.25GPa. k is the permeability, η=1.0518×10^{-3}Pa·S, A is surface area 0.002m^2.

5.4.2 Equation setup

Continuity equation expressing the fluid-mass conservation is

$$\frac{\partial \phi \rho_f}{\partial t} = -\nabla q \rho_f \quad (5\text{-}5)$$

ρ_f is the fluid density, q is filtration velocity and ϕ is the rock porosity. $\phi\rho_f$ is proportional to the pore pressure perturbation P_p and can be substituted by $\rho_0 P_p S_r$, where S_r is the storage coefficient of the rock and ρ_0 is reference fluid density.

Darcy law is given by:

$$q = -\frac{k}{\eta} \nabla P_p \quad (5\text{-}6)$$

Diffusivity is defined by:

$$D = \frac{k\rho_f}{S_r \eta \rho_0} \tag{5-7}$$

The combination of mass conservation and Darcy low leads to the diffusivity equation (written here in one dimension):

$$\frac{\partial P_p}{\partial t} = D \frac{\partial^2}{\partial x^2} P_p \tag{5-8}$$

The initial diffusion coefficient value is D_0=9×10^{-6}m^2, with a permeability value of 1×10^{-18}m^2.

5.4.3 Solution of pore pressure at different positions and time

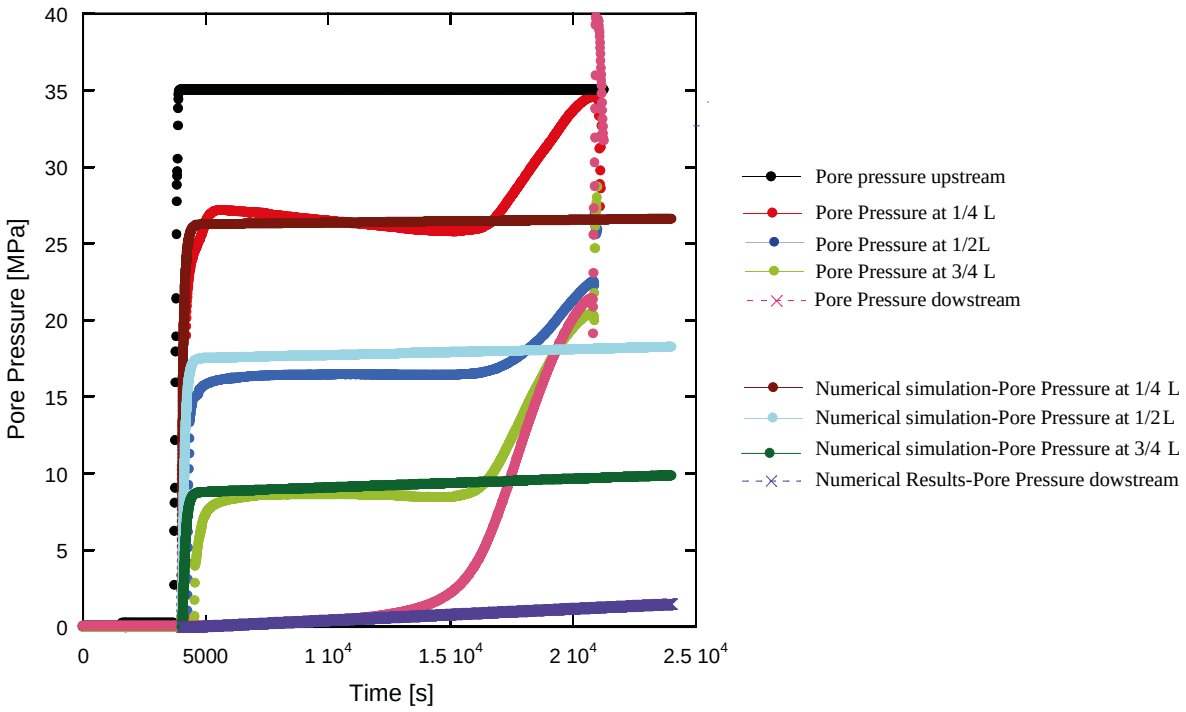

Figure 5.11 Comparison of model results and experiment data.

A numerical solution is obtained using comsol. In a first approach, we consider a permeability constant is space and in time.

With a constant permeability of 1×10^{-18}m^2, the numerical solution is shown in figure 5.11. The numerical solution agrees well with experiment data until around 12000s. Indeed, at this time,

fluid pressure at downstream deviates from the numerical simulation, showing that the modeling with constant permeability may be not applicable any more.

Let's assume a permeability distribution as shown in figure 5.12: the permeability has been increased of 2 order of magnitude $k=10^{-16}m^2$, except between L=0.2 and 0.4, where $k=5\times10^{-17}m^2$.

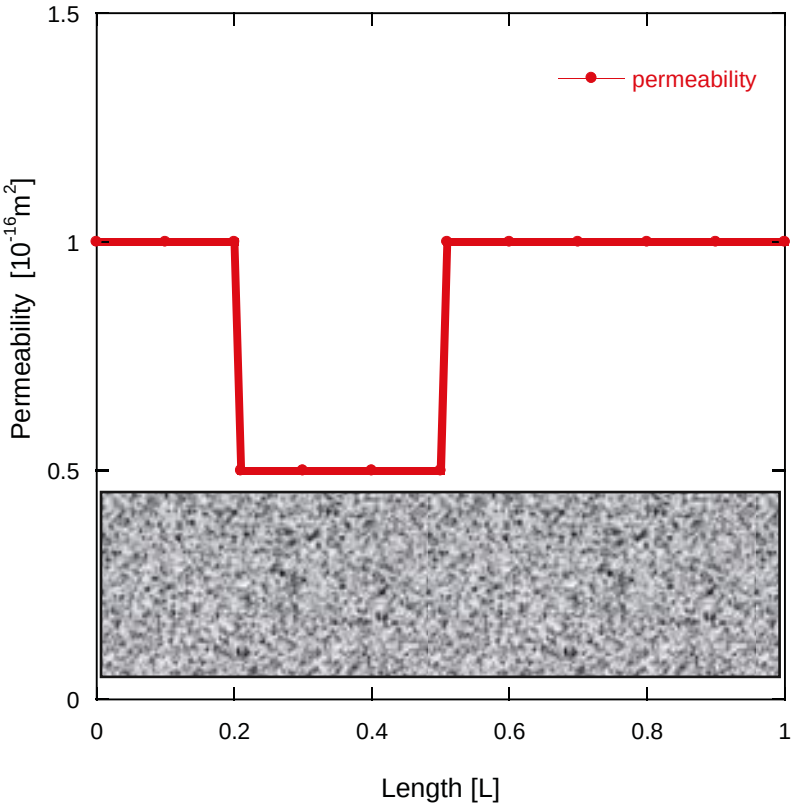

Figure 5.12 Assumed permeability in the sample after 12000s

With the permeability distribution described in figure 5.12, the numerical simulation is plotted in figure 13 for t>16 000s. Note that t=16000s, corresponds to the D' point where dilatancy over dominates compaction. It is shown (figure 5.13) that the result agrees well with experiment data.

Why does the permeability change at a constant effective stress state? One explanation is that under constant stress state subcritical crack growth takes place. Subcritical crack growth occurred until it reaches the length where the interactions between cracks are strong (D').

Cracks begin to coalescence and grow, thus the permeability is enhanced and pore pressure at different positions begin to increase (as is shown in the numerical simulation).

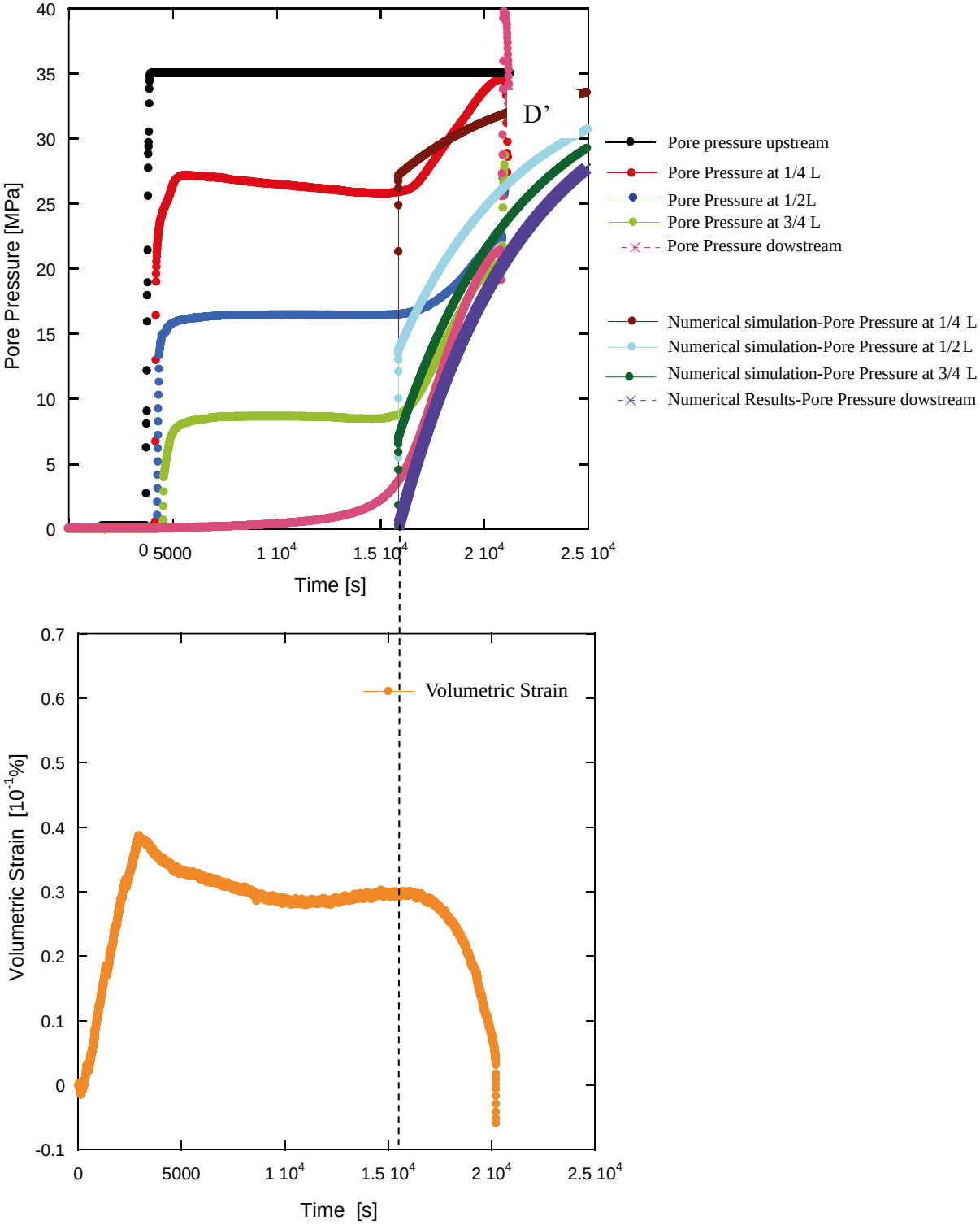

Figure 5.13 Comparison of experiment data and model result with an assumed heterogeneous permeability

In the experiment, the time from where fluid begin to increase (D') to rupture is 4000s (figure 5.13). This value is consistent with the time to rupture of 2000s-3000s obtained in chapter IV. In addition, the numerical simulation with the assumed permeability distribution agrees well with experiment data and verifies that permeability is heterogeneous in the sample.

5.5 Conclusions

(1) Permeability heterogeneity is observed during the fluid-injection experiment.

(2) Subcritical crack growth influences the permeability and pore pressure spatial temporal distribution.

(3) A numerical simulation reproduces well with the fluid injection experiment.

Conclusions

The main results of this dissertation are concluded as follows.

Thermal effect on mechanical properties of geothermal/volcano systems

(1) Due to thermal treatment, the P wave velocity decreased by up to 50% as temperature of heat treatment varies from room temperature up to 1100°C. Crack density increases up to 0.6.

(2) A clay content as low as 1.5% in the intact rock leads to partial melting for a temperature of heat treatment > 500°C. Partial melting modifies the microstructure and the characteristics of the rocks.

(3) A small amount of crack sealing changes the distribution of the crack size. The ultrasonic velocity is weakly modified, but the mechanical strength is enhanced.

(4) Thermal treatment could have strengthening effect on the rocks depending on the original microstructure of the rock and the mineral content. This is counter-intuitive but might be linked to the presence of clay in the andesite.

Hydrothermal effect of alteration on the properties of geothermal system

(1) Elastic moduli of altered andesite increases compared to heat treated andesite.

(2) Peak stress of altered andesite decreases compared to heat treated andesite. The weakening is stronger as alteration is higher.

(3) Using XRD results, we show that smectite appeared in the altered andesite (heat treated andesite has no smectite).

(4) Smectite is observed to precipitate in cracks.

(5) A decrease of the friction coefficient in cracks due to the presence of smectite might explain the mechanical weakening of altered sample.

Fluid pressure variation induced seismicity

(1) Permeability of heat treated (at 930°C) andesite sample has shown a large decrease ($9\times10^{-18}m^2$~$2\times10^{-18}m^2$ under hydrostatic loading (0MPa~25MPa).

(2) Heat treated andesite samples have shown a brittle characteristic under saturated conditions and falls on the Mohr-Coulomb envelop of the intact samples.

(3) A time dependent behavior was observed in the fluid-injection induced rupture experiment.

(4) Heterogeneity of crack development was observed before rupture. More cracks were developed at downstream while upstream remains silent. The rupture began from the downstream end.

(5) Critical crack space is inverted and estimated to be in the range of $129\mu m$~$223\mu m$. Crack length growth with time is inverted during stage II where stress state was constant.

Spatiotemporal pattern of seismicity related to hydraulic diffusion

(1) Permeability heterogeneity is observed during the fluid-injection experiment.

(2) Subcritical crack growth influences the permeability and pore pressure spatial temporal distribution.

(3) A numerical simulation reproduces well the fluid injection experiment.

References

Chapter I References

Ashby, M.F.A. and Hallam, S.D., 1986. The failure of brittle solids containing small cracks under compressive stress states. *Acta Metallurgica*, *34*(3), pp.497-510.

Ashby, M.F. and Sammis, C.G., 1990. The damage mechanics of brittle solids in compression. *Pure and Applied Geophysics*, *133*(3), pp.489-521.

Baud, P., Zhu, W. and Wong, T.F., 2000. Failure mode and weakening effect of water on sandstone. *Journal of Geophysical Research: Solid Earth*, *105*(B7), pp.16371-16389.

Bernabe, Y., 1987. The effective pressure law for permeability during pore pressure and confining pressure cycling of several crystalline rocks. *Journal of Geophysical Research: Solid Earth*, *92*(B1), pp.649-657.

Bhat, H.S., Sammis, C.G. and Rosakis, A.J., 2011. The micromechanics of westerley granite at large compressive loads. *Pure and Applied Geophysics*, *168*(12), pp.2181-2198.

Bieniawski, Z.T., 1967, October. Mechanism of brittle fracture of rock: part I—theory of the fracture process. In *International Journal of Rock Mechanics and Mining Sciences & Geomechanics Abstracts* (Vol. 4, No. 4, pp. 395-406). Pergamon.

Bouysse, P. and Westercamp, D., 1990. Subduction of Atlantic aseismic ridges and Late Cenozoic evolution of the Lesser Antilles island arc. *Tectonophysics*, *175*(4), pp.349-380.

Bouchot, V., Sanjuan, B., Calcagno, P., Gloaguen, E., Thinon, I., Gailler, L., Baltassat, J.M., Bourgeois, B., Lerouge, C., Gadalia, A. and Bourdon, E., 2011, March. The high-temperature geothermal system of Bouillante (Guadeloupe, French West Indies). In *19ème Conférence géologique de la Caraïbe 2011*.

Brace, W.F., Paulding Jr, B.W. and Scholz, C.H., 1966. Dilatancy in the fracture of crystalline rocks. *Journal of Geophysical Research*, *71*(16), pp.3939-3953.

Brace, W., Walsh, J.B. and Frangos, W.T., 1968. Permeability of granite under high pressure. *Journal of Geophysical research*, *73*(6), pp.2225-2236.

Brace, W.F. and Orange, A.S., 1968. Further studies of the effects of pressure on electrical resistivity of rocks. *Journal of Geophysical research*, *73*(16), pp.5407-5420.

Bristow, J.R., 1960. Microcracks, and the static and dynamic elastic constants of annealed and heavily cold-worked metals. *British Journal of Applied Physics*, *11*(2), p.81.

Byerlee, J.D. and Brace, W.F., 1968. Stick slip, stable sliding, and earthquakes—effect of rock type, pressure, strain rate, and stiffness. *Journal of Geophysical Research*, *73*(18), pp.6031-6037.

Coyner, K.B., 1984. *Effects of stress, pore pressure, and pore fluids on bulk strain, velocity, and permeability in rocks*(Doctoral dissertation, Massachusetts Institute of Technology).

Crank, J., 1979. *The mathematics of diffusion*. Oxford university press.

Dake, L.P., 1978. Fundamentals of Reservoir Engineering, No. 8. Amsterdam: Developments in Petroleum Science.

Darot, M. and Gueguen, Y., 1986. Slow crack growth in minerals and rocks: Theory and experiments. *pure and applied geophysics*, *124*(4-5), pp.677-692.

Deshpande, V.S. and Evans, A.G., 2008. Inelastic deformation and energy dissipation in ceramics: a mechanism-based constitutive model. *Journal of the Mechanics and Physics of Solids*, *56*(10), pp.3077-3100.

Davidson, J.P., 1983. Lesser Antilles isotopic evidence of the role of subducted sediment in island arc magma genesis. *Nature*, *306*(5940), p.253.

Fatt, I. and Davis, D.H., 1952. Reduction in permeability with overburden pressure. *Journal of Petroleum Technology*, *4*(12), pp.16-16.

Feuillet, N., Manighetti, I. and Tapponnier, P., 2001. Active arc-transverse normal faulting in Guadeloupe (French Lesser Antilles). *Comptes rendus de lacademie des sciences serie II fascicule A-sciences de la terre et des planetes*, *333*(9), pp.583-590.

Feuillet, N., Manighetti, I., Tapponnier, P. and Jacques, E., 2002. Arc parallel extension and localization of volcanic complexes in Guadeloupe, Lesser Antilles. *Journal of Geophysical Research: Solid Earth*, *107*(B12), pp.ETG-3.

Fortin, J., Guéguen, Y. and Schubnel, A., 2007. Effects of pore collapse and grain crushing on ultrasonic velocities and Vp/Vs. *Journal of Geophysical Research: Solid Earth*, *112*(B8).

Fortin, J., Stanchits, S., Dresen, G. and Guéguen, Y., 2006. Acoustic emission and velocities associated with the formation of compaction bands in sandstone. *Journal of Geophysical Research: Solid Earth*, *111*(B10).

Fortin, J., Stanchits, S., Vinciguerra, S. and Guéguen, Y., 2011. Influence of thermal and

mechanical cracks on permeability and elastic wave velocities in a basalt from Mt. Etna volcano subjected to elevated pressure. *Tectonophysics*, *503*(1-2), pp.60-74.

Gavrilenko, P. and Gueguen, Y., 1989. Pressure dependence of permeability: a model for cracked rocks. *Geophysical Journal International*, *98*(1), pp.159-172.

Germanovich, L.N. and Astakhov, D.K., 2004. Stress-dependent permeability and fluid flow through parallel joints. *Journal of Geophysical Research: Solid Earth*, *109*(B9).

Geertsma, J., 1957. The effect of fluid pressure decline on volumetric changes of porous rocks.

Griffith, A.A. and Eng, M., 1921. VI. The phenomena of rupture and flow in solids. *Phil. Trans. R. Soc. Lond. A*, *221*(582-593), pp.163-198.)

Gibowicz, S.J. and Kijko, A., 1994. An Introduction to Mining Seismicity.

Guéguen, Y. and Schubnel, A., 2003. Elastic wave velocities and permeability of cracked rocks. *Tectonophysics*, *370*(1-4), pp.163-176.

Guéguen, Y. and Sarout, J., 2009. Crack-induced anisotropy in crustal rocks: predicted dry and fluid-saturated Thomsen's parameters. *Physics of the Earth and Planetary Interiors*, *172*(1-2), pp.116-124.

Guéguen, Y., Adelinet, M., Ougier-Simonin, A., Fortin, J. and Schubnel, A., 2011. How cracks modify permeability and introduce velocity dispersion: Examples of glass and basalt. *The Leading Edge*, *30*(12), pp.1392-1398.

Guéguen, Y. and Sarout, J., 2011. Characteristics of anisotropy and dispersion in cracked medium. *Tectonophysics*, *503*(1-2), pp.165-172.

Hallbauer, D.K., Wagner, H.N.G.W. and Cook, N.G.W., 1973, November. Some observations concerning the microscopic and mechanical behaviour of quartzite specimens in stiff, triaxial compression tests. In *International Journal of Rock Mechanics and Mining Sciences & Geomechanics Abstracts*(Vol. 10, No. 6, pp. 713-726). Pergamon.

Inglis, C.E., 1913. Stresses in a plate due to the presence of cracks and sharp corners. *Trans Inst Naval Archit*, *55*, pp.219-241.)

Irwin, G.R., 1957. Analysis of stresses and strains near the end of a crack traversing a plate. *J. appl. Mech.*

Jaeger, J., Cook, N.G. and Zimmerman, R., 2007. Poroelasticity and thermoelasticity. *Fundamentals of Rock Mechanics*, pp.168-204.

Johnson, H.H. and Paris, P.C., 1968. Sub-critical flaw growth. *Engineering Fracture*

Mechanics, *1*(1), pp.3-45.

Jones Jr, F.O., 1975. A laboratory study of the effects of confining pressure on fracture flow and storage capacity in carbonate rocks. *Journal of Petroleum Technology*, *27*(01), pp.21-27.

Jones, F.O. and Owens, W.W., 1980. A laboratory study of low-permeability gas sands. *Journal of petroleum Technology*, *32*(09), pp.1-631.

Jones Jr, F.O., 1975. A laboratory study of the effects of confining pressure on fracture flow and storage capacity in carbonate rocks. *Journal of Petroleum Technology*, *27*(01), pp.21-27.

Kachanov, M., Tsukrov, I. and Shafiro, B., 1994. Effective moduli of solids with cavities of various shapes. *Applied Mechanics Reviews*, *47*(1S), pp.S151-S174.

Kemeny, J.M. and Cook, N.G., 1987. Determination of rock fracture parameters from crack models for failure in compression.

Lawn, B. and Wilshaw, R., 1975. Indentation fracture: principles and applications. Journal of materials science, 10(6), pp.1049-1081.

Mallet, C., Fortin, J., Guéguen, Y. and Bouyer, F., 2015. Brittle creep and subcritical crack propagation in glass submitted to triaxial conditions. Journal of Geophysical Research: Solid Earth, 120(2), pp.879-893.

Martin, C.D. and Chandler, N.A., 1994, December. The progressive fracture of Lac du Bonnet granite. In *International Journal of Rock Mechanics and Mining Sciences & Geomechanics Abstracts* (Vol. 31, No. 6, pp. 643-659). Pergamon.

Martin, C.D. and Christiansson, R., 2009. Estimating the potential for spalling around a deep nuclear waste repository in crystalline rock. *International Journal of Rock Mechanics and Mining Sciences*, *46*(2), pp.219-228.

Mathieu, L., de Vries, B.V.W., Mannessiez, C., Mazzoni, N., Savry, C. and Troll, V.R., 2013. The structure and morphology of the Basse Terre Island, Lesser Antilles volcanic arc. *Bulletin of volcanology*, *75*(3), p.700.

Nemat-Nasser, S. and Horii, H., 1982. Compression-induced nonplanar crack extension with application to splitting, exfoliation, and rockburst. *Journal of Geophysical Research: Solid Earth*, *87*(B8), pp.6805-6821.

Nemat-Nasser, S. and Obata, M., 1986. Rate-dependent, finite elasto-plastic deformation of

polycrystals. *Proc. R. Soc. Lond. A*, *407*(1833), pp.343-375.

Newman, J.N. and Wu, T.Y., 1973. A generalized slender-body theory for fish-like forms. *Journal of Fluid Mechanics*, *57*(4), pp.673-693.

Nicolas, A., Fortin, J., Regnet, J.B., Dimanov, A. and Guéguen, Y., 2016. Brittle and semi-brittle behaviours of a carbonate rock: influence of water and temperature. *Geophysical Journal International*, *206*(1), pp.438-456.

Nur, A.M.O.S. and Walder, J.O.S.E.P.H., 1990. Time-dependent hydraulics of the Earth's crust. In *The role of fluids in crustal processes* (Vol. 113). National Academy Press Washington, DC.

Ougier-Simonin, A., Fortin, J., Guéguen, Y., Schubnel, A. and Bouyer, F., 2011. Cracks in glass under triaxial conditions. *International Journal of Engineering Science*, *49*(1), pp.105-121.

Ougier-Simonin, A., Gueguen, Y., Fortin, J., Schubnel, A. and Bouyer, F., 2010. Damage and cracking in glass under pressure; Endommagement et fissuration du verre en compression triaxiale.

Orowan, E., 1949. Fracture and strength of solids. *Reports on progress in physics*, *12*(1), p.185.

Parlange, M.B. and Katul, G.G., 1992. An advection-aridity evaporation model. *Water Resources Research*, *28*(1), pp.127-132.

Perol, T. and Bhat, H.S., 2016. Micromechanics-based permeability evolution in brittle materials at high strain rates. *Pure and Applied Geophysics*, *173*(8), pp.2857-2868.

Richart, F.E., Brandtzaeg, A. and Brown, R.L., 1928. *A study of the failure of concrete under combined compressive stresses*. University of Illinois at Urbana Champaign, College of Engineering. Engineering Experiment Station.

Sammis, C.G. and Ashby, M.F., 1986. The failure of brittle porous solids under compressive stress states. *Acta metallurgica*, *34*(3), pp.511-526.

Samper, A., Quidelleur, X., Boudon, G., Le Friant, A. and Komorowski, J.C., 2008. Radiometric dating of three large volume flank collapses in the Lesser Antilles Arc. *Journal of Volcanology and Geothermal Research*, *176*(4), pp.485-492.

Sayers, C.M. and Kachanov, M., 1995. Microcrack-induced elastic wave anisotropy of brittle rocks. *Journal of Geophysical Research: Solid Earth*, *100*(B3), pp.4149-4156

Scholz, C.H., 1968. The frequency-magnitude relation of microfracturing in rock and its relation to earthquakes. *Bulletin of the seismological society of America*, *58*(1), pp.399-

415.

Simmons, G. and Brace, W.F., 1965. Comparison of static and dynamic measurements of compressibility of rocks. *Journal of geophysical research*, *70*(22), pp.5649-5656.

Tada, H., Paris, P.C. and Irwin, G.R., 1985. Handbook for stress analysis of cracks. Del Research.

Topponnier, P., and Brace, WF (1976). *Development of Stress-induced Microeraeks in Westerly*.

Walsh, J.B., 1965. The effect of cracks on the uniaxial elastic compression of rocks. *Journal of Geophysical Research*, *70*(2), pp.399-411.

Wang, X.Q., Schubnel, A., Fortin, J., Guéguen, Y. and Ge, H.K., 2013. Physical properties and brittle strength of thermally cracked granite under confinement. *Journal of Geophysical Research: Solid Earth*, *118*(12), pp.6099-6112.

Wawersik, W.R. and Brace, W.F., 1971. Post-failure behavior of a granite and diabase. *Rock mechanics*, *3*(2), pp.61-85.

Wawersik, W.R. and Fairhurst, C., 1970, September. A study of brittle rock fracture in laboratory compression experiments. In *International Journal of Rock Mechanics and Mining Sciences & Geomechanics Abstracts* (Vol. 7, No. 5, pp. 561-575). Pergamon.

Westergaard, H.M., 1939. Bearing pressures and cracks. *Journal of applied mechanics*, *6*(2), pp.A49-A53.

Wong, T.F., David, C. and Zhu, W., 1997. The transition from brittle faulting to cataclastic flow in porous sandstones: Mechanical deformation. *Journal of Geophysical Research: Solid Earth*, *102*(B2), pp.3009-3025.

Yale, D.P. and Nur, A., 1985. Network modeling of flow, storage, and deformation in porous rocks. In *SEG Technical Program Expanded Abstracts 1985* (pp. 91-94). Society of Exploration Geophysicists.

Yilmaz, Ö., Nolen-Hoeksema, R.C. and Nur, A., 1994. Pore pressure profiles in fractured and compliant rocks 1. *Geophysical prospecting*, *42*(6), pp.693-714.

Zimmerman, R.W., Somerton, W.H. and King, M.S., 1986. Compressibility of porous rocks. *Journal of Geophysical Research: Solid Earth*, *91*(B12), pp.12765-12777.

Chapter II References

Adelinet, M., Fortin, J., & Guéguen, Y. (2011). Dispersion of elastic moduli in a porous-cracked rock: Theoretical predictions for squirt-flow. *Tectonophysics, 503*(1-2), 173-181.

Ashby, M. F. A., & Hallam, S. D. (1986). The failure of brittle solids containing small cracks under compressive stress states. *Acta Metallurgica*, *34*(3), 497-510.

Ashby, M. F., & Sammis, C. G. (1990). The damage mechanics of brittle solids in compression. *Pure and Applied Geophysics*, *133*(3), 489-521.

Baud, P., Wong, T. F., & Zhu, W. (2014). Effects of porosity and crack density on the compressive strength of rocks. *International Journal of Rock Mechanics and Mining Sciences*, *67*, 202-211.

Bowen, N. L. (1912). The order of crystallization in igneous rocks. *The Journal of Geology*, *20*(5), 457-468.

Bowen, N. L. (1913). The melting phenomena of the plagioclase feldspars. *American Journal of Science*, (210), 577-599.

Bouysse, P. and Westercamp, D., 1990. Subduction of Atlantic aseismic ridges and Late Cenozoic evolution of the Lesser Antilles island arc. *Tectonophysics*, *175*(4), pp.349-380.

Brace, W.F., Pauling, B.W., and Scholz C. (1966), Dilatancy in fracture of crystalline rock, *Journal of Geophysical Research, 71,* 3939. 9.

Brantut, N., Sulem, J., & Schubnel, A. (2011). Effect of dehydration reactions on earthquake nucleation: Stable sliding, slow transients, and unstable slip. *Journal of Geophysical Research: Solid Earth*, *116*(B5).

Brotons, V., Tomás, R., Ivorra, S. and Alarcón, J.C., 2013. Temperature influence on the physical and mechanical properties of a porous rock: San Julian's calcarenite. *Engineering Geology*, *167*, pp.117-127

Byerlee, J. (1978). Friction of rocks. In Rock friction and earthquake prediction (pp. 615-626). Birkhäuser, Basel.

Chaki, S., Takarli, M., & Agbodjan, W. P. (2008). Influence of thermal damage on physical properties of a granite rock: porosity, permeability and ultrasonic wave evolutions. *Construction and Building Materials*, *22*(7), 1456-1461.

Cotterell, B., & Rice, J. (1980). Slightly curved or kinked cracks. *International journal of*

fracture, 16(2), 155-169.

Darot, M., & Reuschlé, T. (2000). Effect of pore and confining pressures on VP in thermally pre-cracked granites. *Geophysical research letters*, *27*(7), 1057-1060.

Davidge, R. W., & Green, T. J. (1968). The strength of two-phase ceramic/glass materials. *Journal of Materials Science*, *3*(6), 629-634.

Faoro, I., Vinciguerra, S., Marone, C., Elsworth, D., & Schubnel, A. (2013). Linking permeability to crack density evolution in thermally stressed rocks under cyclic loading. *Geophysical Research Letters*, *40*(11), 2590-2595.

Farquharson, J., Heap, M.J., Varley, N.R., Baud, P. and Reuschlé, T., 2015. Permeability and porosity relationships of edifice-forming andesites: a combined field and laboratory study. *Journal of Volcanology and Geothermal Research*, *297*, pp.52-68.

Faulkner, D. R., & Rutter, E. H. (2003). The effect of temperature, the nature of the pore fluid, and subyield differential stress on the permeability of phyllosilicate-rich fault gouge. *Journal of Geophysical Research: Solid Earth*, *108*(B5).

Feuillet, N., Manighetti, I. and Tapponnier, P., 2001. Active arc-transverse normal faulting in Guadeloupe (French Lesser Antilles). *Comptes Rendus De Lacademie Des Sciences Serie Ii Fascicule A-Sciences De La Terre Et Des Planetes*, *333*(9), pp.583-590.

Feuillet, N., Manighetti, I., Tapponnier, P. and Jacques, E., 2002. Arc parallel extension and localization of volcanic complexes in Guadeloupe, Lesser Antilles. *Journal of Geophysical Research: Solid Earth*, *107*(B12), pp.ETG-3.

Fortin, J., Stanchits, S., Vinciguerra, S., & Guéguen, Y. (2011). Influence of thermal and mechanical cracks on permeability and elastic wave velocities in a basalt from Mt. Etna volcano subjected to elevated pressure. *Tectonophysics*, *503*(1-2), 60-74.

Fredrich, J. T., & Wong, T. F. (1986). Micromechanics of thermally induced cracking in three crustal rocks. *Journal of Geophysical Research: Solid Earth*, *91*(B12), 12743-12764.

Friedman, M., Handin, J., Higgs, N. G., & Lantz, J. R. (1979, January). Strength and ductility of four dry igneous rocks at low pressures and temperatures to partial melting. In *20th US Symposium on Rock Mechanics (USRMS)*. American Rock Mechanics Association.

Géraud, Y. (1994). Variations of connected porosity and inferred permeability in a thermally cracked granite. *Geophysical Research Letters*, *21*(11), 979-982.

Glover, P.W.J., Baud, P., Darot, M., Meredith, P., Boon, S.A., LeRavalec, M., Zoussi, S. and

Reuschle, T., 1995. α/β phase transition in quartz monitored using acoustic emissions. *Geophysical Journal International*, *120*(3), pp.775-782.

Greene-Kelly, R. (1953) Irreversible dehydration in montrnorillonite. Part II: Clay Mineral Bull. 1, 52-56.

Greil, P. (2012). Generic principles of crack-healing ceramics. *Journal of Advanced Ceramics, 1*(4), 249-267.

Guéguen, Y., & Dienes, J. (1989). Transport properties of rocks from statistics and percolation. *Mathematical geology*, *21*(1), 1-13.

Guéguen, Y. and Sarout, J., 2009. Crack-induced anisotropy in crustal rocks: predicted dry and fluid-saturated Thomsen's parameters. *Physics of the Earth and Planetary Interiors*, *172*(1-2), pp.116-124.

Guéguen, Y. & Kachanov, M., 2011. Effective elastic properties of cracked rocks—an overview, in *Mechanics of Crustal Rocks,* pp. 73–125, eds Leroy, Y.M. & Lehner, F.K., Springer.

Gupta, T. K. (1976). Crack healing and strengthening of thermally shocked alumina. *Journal of the American Ceramic Society, 59*(5‐6), 259-262.

Heap, M. J., Lavallée, Y., Petrakova, L., Baud, P., Reuschle, T., Varley, N. R., & Dingwell, D. B. (2014). Microstructural controls on the physical and mechanical properties of edifice-forming andesites at Volcán de Colima, Mexico. *Journal of Geophysical Research: Solid Earth*, *119*(4), 2925-2963.

Heap, M.J., Farquharson, J.I., Baud, P., Lavallée, Y. and Reuschlé, T., 2015. Fracture and compaction of andesite in a volcanic edifice. *Bulletin of volcanology*, *77*(6), p.55.

Heap, M.J. and Kennedy, B.M., 2016. Exploring the scale-dependent permeability of fractured andesite. *Earth and Planetary Science Letters*, *447*, pp.139-150.

Homand-Etienne, F. and Houpert, R., 1989, March. Thermally induced microcracking in granites: characterization and analysis. In *International Journal of Rock Mechanics and Mining Sciences & Geomechanics Abstracts* (Vol. 26, No. 2, pp. 125-134). Pergamon.

Jaud, P. and Lamethe, D., 1985. The Bouillante geothermal power-plant, Guadeloupe. *Geothermics*, *14*(2-3), pp.197-205.

Kachanov, M., Tsukrov, I. and Shafiro, B., 1994. Effective moduli of solids with cavities of various shapes. *Applied Mechanics Reviews*, *47*(1S), pp.S151-S174.

Kant, M.A., Ammann, J., Rossi, E., Madonna, C., Höser, D. and Rudolf von Rohr, P., 2017. Thermal properties of Central Aare granite for temperatures up to 500° C: Irreversible changes due to thermal crack formation. *Geophysical Research Letters*, *44*(2), pp.771-776.

Kemeny, J. M., & Cook, N. G. (1991). Micromechanics of deformation in rocks. In Toughening mechanisms in quasi-brittle materials (pp. 155-188). Springer, Dordrecht.

Keshavarz, M., Pellet, F. L., & Loret, B. (2010). Damage and changes in mechanical properties of a gabbro thermally loaded up to 1,000 C. *Pure and Applied Geophysics*, *167*(12), 1511-1523.

Malek, Z., Balek, V., Garfinkel-Shweky, D., and Yariv S. (1997). The study of the dehydration and dehydroxylation of smectites by emanation thermal analysis. *Journal of Thermal Analysis*, Volume 48, Issue 1, pp 83–92.

Mallet, C., Fortin, J., Guéguen, Y. and Bouyer, F., 2013. Effective Elastic Properties of Cracked Solids: An Experimental Investigation. *International Journal of Fracture*, 182(2).

Mallet, C., Fortin, J., Guéguen, Y., & Bouyer, F. (2014). Evolution of the crack network in glass samples submitted to brittle creep conditions. *International Journal of Fracture*, *190*(1-2), 111-124.

Nara, Y., Morimoto, K., Hiroyoshi, N., Yoneda, T., Kaneko, K., & Benson, P. M. (2012). Influence of relative humidity on fracture toughness of rock: implications for subcritical crack growth. *International Journal of Solids and Structures, 49*(18), 2471-2481.

Nasseri, M. H. B., Schubnel, A., Benson, P. M., & Young, R. P. (2009). Common evolution of mechanical and transport properties in thermally cracked westerly granite at elevated hydrostatic pressure. In *Rock Physics and Natural Hazards* (pp. 927-948). Birkhäuser Basel.

Nasseri, M. H. B., Schubnel, A., & Young, R. P. (2007). Coupled evolutions of fracture toughness and elastic wave velocities at high crack density in thermally treated Westerly granite. *International Journal of Rock Mechanics and Mining Sciences*, *44*(4), 601-616.

Nemat-Nasser, S., & Horii, H. (1982). Compression-induced nonplanar crack extension with application to splitting, exfoliation, and rockburst. *Journal of Geophysical Research: Solid Earth*, *87*(B8), 6805-6821.

Nichols, F.A., and W. W. Mullins (1965), Morphological changes of a surface of revolution due to capillarity- induced surface diffusion, *Journal of Applied Physics, 36,* 1826-1835.

Nicolas, A., Fortin, J., Regnet, J. B., Dimanov, A., & Guéguen, Y. (2016). Brittle and semi-brittle behaviours of a carbonate rock: influence of water and temperature. *Geophysical Journal International*, *206*(1), 438-456.

Ouchterlony, F. (1990). Fracture toughness testing of rock with core based specimens. *Engineering Fracture Mechanics, 35*(1-3), 351-366.

Ougier-Simonin, D.E.P.A., 2010. Characterisation of hydraulic fractures in limestones using X-ray microtomography. *Advances in x-ray tomography for geomaterials*, *118*, p.221.

Ougier-Simonin, A., Fortin, J., Guéguen, Y., Schubnel, A., & Bouyer, F. (2011). Cracks in glass under triaxial conditions. *International Journal of Engineering Science*, *49*(1), 105-121.

Roedder, E. (1981). Origin of fluid inclusions and changes that occur after trapping. In Fluid Inclusions: *Applications to Petrology*, Vol. 6, 101-137.

Russel, J., and V. Famer (1964) Infra-red spectroscopic study of the dehydration of montmorillonite and saponite. Clay Min. Bull. 5, 443.

Sayers, C.M. and Kachanov, M., 1995. Microcrack-induced elastic wave anisotropy of brittle rocks. *Journal of Geophysical Research: Solid Earth*, *100*(B3), pp.4149-4156.

Schubnel, A., Benson, P. M., Thompson, B. D., Hazzard, J. F., & Young, R. P. (2006). Quantifying damage, saturation and anisotropy in cracked rocks by inverting elastic wave velocities. In *Rock Damage and Fluid Transport, Part I* (pp. 947-973). Birkhäuser Basel.

Schubnel, A., Thompson, B. D., Fortin, J., Guéguen, Y., & Young, R. P. (2007). Fluid-induced rupture experiment on Fontainebleau sandstone: Premonitory activity, rupture propagation, and aftershocks. *Geophysical research letters*, *34*(19).

Sengun, N., 2014. Influence of thermal damage on the physical and mechanical properties of carbonate rocks. *Arabian Journal of Geosciences*, *7*(12), pp.5543-5551.

Simmons, G., & Richter, D. (1976). Microcracks in rocks. *The physics and chemistry of minerals and rocks*, 105-137.

Siratovich, P. A., Heap, M. J., Villenueve, M. C., Cole, J. W., & Reuschlé, T. (2014). Physical property relationships of the Rotokawa Andesite, a significant geothermal reservoir rock in the Taupo Volcanic Zone, New Zealand. *Geothermal Energy*, *2*(1), 10.

Siratovich, P., Cole, J., Heap, M., Villeneuve, M., Reuschlé, T., Swanson, K., Kennedy, B., Gravley, D. and Lavallée, Y., 2015. Experimental thermal stimulation of the Rotokawa Andesite.

Smith, D. L., and B. Evans (1984), Diffusional crack healing in quartz, *Journal of Geophysical Research, 89*, 4125– 4136.

Sprunt E.S., and A. Nur (1979), Micro-cracks and healing in granites: new evidence from cathodoluminescence, *Science, 205,* 495-497.

Swanenberg, H. E. C. (1980). Fluid inclusions in high-grade metamorphic rocks from SW Norway (Doctoral dissertation, Utrecht University).

Talukdar, M., Roy, D., and T. N. Singh. "Correlating mode-I fracture toughness and mechanical properties of heat-treated crystalline rocks." *Journal of Rock Mechanics and Geotechnical Engineering* 10.1 (2018): 91-101.

Thompson, B. D., Young, R. P., & Lockner, D. A. (2005). Observations of premonitory acoustic emission and slip nucleation during a stick slip experiment in smooth faulted Westerly granite. *Geophysical research letters*, *32*(10).

Thompson, B. D., Young, R. P., & Lockner, D. A. (2006). Fracture in Westerly granite under AE feedback and constant strain rate loading: nucleation, quasi-static propagation, and the transition to unstable fracture propagation. *Pure and applied geophysics*, *163*(5-6), 995-1019.

Trias, R., Ménez, B., Le Campion, P., Zivanovic, Y., Recourt, L., Lecoeuvre, A., Schmitt-Kopplin, P., Uhl, J., Gislason, S., Alfreðsson, H., Mesfin, K., Snæbjörnsdóttir, S., Aradóttir, E., Gunnarsson, I., Matter, J., Stute, M., Oelkers E., & Gérard, E., (2017) High reactivity of deep biota under anthropogenic CO2 injection into basalt, *Nature Communications*, *DOI: 10.1038/s41467-017-01288-8*

Tutluoglu, L., & Keles, C. (2011). Mode I fracture toughness determination with straight notched disk bending method. *International Journal of Rock Mechanics and Mining Sciences, 48*(8), 1248-1261.

Villemant, B., Komorowski, J.C., Dessert, C., Michel, A., Crispi, O., Hammouya, G., Beauducel, F. and De Chabalier, J.B., 2014. Evidence for a new shallow magma intrusion at La Soufrière of Guadeloupe (Lesser Antilles): insights from long-term geochemical monitoring of halogen-rich hydrothermal fluids. *Journal of Volcanology and Geothermal Research*, *285*, pp.247-277.

Vinciguerra, S., Trovato, C., Meredith, P. G., & Benson, P. M. (2005). Relating seismic velocities, thermal cracking and permeability in Mt. Etna and Iceland basalts. *International Journal of Rock Mechanics and Mining Sciences*, *42*(7-8), 900-910.

Violay M., Heap M., Acosta M. and C. Madonna (2017) Porosity evolution at the brittle ductile transition in the continental crust: implications for deep hydro-geothermal circulation. *Scientific Reports | DOI:10.1038/s41598-017-08108-5*

Walsh, J. B. (1965). The effect of cracks on the uniaxial elastic compression of rocks. *Journal of Geophysical Research*, *70*(2), 399-411.

Wang, X. Q., Schubnel, A., Fortin, J., Guéguen, Y., & Ge, H. K. (2013). Physical properties and brittle strength of thermally cracked granite under confinement. *Journal of Geophysical Research: Solid Earth*, *118*(12), 6099-6112.

Wong, T. F., Fredrich, J. T., & Gwanmesia, G. D. (1989). Crack aperture statistics and pore space fractal geometry of Westerly granite and Rutland quartzite: Implications for an elastic contact model of rock compressibility. *Journal of Geophysical Research: Solid Earth*, *94*(B8), 10267-10278.

Wong, T. F., Wong, R. H., Chau, K. T., & Tang, C. A. (2006). Microcrack statistics, Weibull distribution and micromechanical modeling of compressive failure in rock. *Mechanics of Materials, 38*(7), 664-681.

Zhu, W., Baud, P., Vinciguerra, S., & Wong, T. F. (2016). Micromechanics of brittle faulting and cataclastic flow in Mount Etna basalt. *Journal of Geophysical Research: Solid Earth*, *121*(6), 4268-4289.

Chapter III References

Adelinet, M., Fortin, J., Gue´guen, Y., Schubnel, A., & Geoffroy, L., 2010. Frequency and fluid effects on elastic properties of basalt: Experimental investigations, *Geophysical Research Letters*, 37(2).

Adelinet, M., Dorbath, C., Le Ravalec, M., Fortin, J., & Gue´guen, Y., 2011. Deriving microstructure and fluid state within the Icelandic crust from the inversion of tomography data, *Geophysical research letters*, 38(3).

Adelinet, M., Fortin, J., Schubnel, A., & Gue´guen, Y., 2013. Deformation modes in an Icelandic basalt: from brittle failure to localized deformation bands, *Journal of Volcanology and Geothermal Research*, 255, 15–25.

Anderson, E. M., 1937. Ix. The dynamics of the formation of cone-sheets, ring-dykes, and caldron-subsidences, *Proceedings of the Royal Society of Edinburgh*, 56, 128–157.

Ashby, M. & Hallam, S., 1986. The failure of brittle solids containing small cracks under compressive stress states, *Acta Metallurgica*, 34(3), 497 – 510.

Ashby, M. & Sammis, C. G., 1990. The damage mechanics of brittle solids in compression, *Pure and Applied Geophysics*, 133, 489–521.

Atkinson, B. K., 1984. Subcritical crack growth in geological materials, *Journal of Geophysical Research: Solid Earth*, 89(B6), 4077–4114.

Ayling, M. R., Meredith, P. G., & Murrell, S. A., 1995. Microcracking during triaxial deformation of porous rocks monitored by changes in rock physical properties, I. Elastic-wave propagation measure-ments on dry rocks, *Tectonophysics*, 245(3), 205–221.

Baud, P., Schubnel, A., & Wong, T.-f., 2000. Dilatancy, compaction, and failure mode in Solnhofen limestone, *Journal of Geophysical Research: Solid Earth*, 105(B8), 19289–19303.

Bhat, H., Sammis, C., & Rosakis, A., 2011. The micromechanics of Westerley granite at large compressive loads, *Pure and Applied Geophysics*, 168(12), 2181–2198.

Bhat, H. S., Rosakis, A. J., & Sammis, C. G., 2012. A micromechanics based constitutive model for brittle failure at high strain rates, *Journal of Applied Mechanics*, 79(3), 031016.

Bos, B. & Spiers, C. J., 2002. Frictional-viscous flow of phyllosilicate-bearing fault rock: Microphysical model and implications for crustal strength profiles, *Journal of Geophysical Research: Solid Earth*, 107(B2).

Brantut, N., Schubnel, A., & Gue´guen, Y., 2011. Damage and rupture dynamics at the brittle-ductile transition: The case of gypsum, *Journal of Geophysical Research: Solid Earth*, 116(B1).

Brenguier, F., Campillo, M., Takeda, T., Aoki, Y., Shapiro, N., Briand, X., Emoto, K., & Miyake, H., 2014.Mapping pressurized volcanic fluids from induced crustal seismic velocity drops, *Science*, 345(6192), 80–82.

Bristow, J. R., 1960. Microcracks, and the static and dynamic elastic constants of annealed and heavily cold-worked metals, *British Journal of Applied Physics*, 11(2), 81.

Browne, P., 1978. Hydrothermal alteration in active geothermal fields, *Annual Review of Earth and Planetary Sciences*, 6(1), 229–248.

Budiansky, B. & O'Connell, R. J., 1976. Elastic moduli of a cracked solid, *International Journal of Solids and Structures*, 12(2), 81 – 97.

Byerlee, J., 1978. Friction of rocks, in *Rock friction and earthquake prediction*, pp. 615–626, Springer.

Carpenter, B., Marone, C., & Saffer, D., 2011. Weakness of the san andreas fault revealed by samples from the active fault zone, *Nature Geoscience*, 4(4), 251.

Chester, F. M., Rowe, C., Ujiie, K., Kirkpatrick, J., Regalla, C., Remitti, F., Moore, J. C., Toy, V., Wolfson-Schwehr, M., Bose, S., Kameda, J., Mori, J. J., Brodsky, E. E., Eguchi, N., & Toczko, S., 2013. Structure and composition of the plate-boundary slip zone for the 2011 Tohoku-Oki earthquake, *Science*, 342(6163), 1208.

Collettini, C., Niemeijer, A., Viti, C., & Marone, C., 2009. Fault zone fabric and fault weakness, *Nature*, 462(7275), 907.

Connor, C. B., Sparks, R., Mason, R., Bonadonna, C., & Young, S., 2003. Exploring links between physical and probabilistic models of volcanic eruptions: The Soufriere Hills Volcano, Montserrat, *Geophysical research letters*, 30(13).

Darot, M., Gue´guen, Y., & Baratin, M., 1992. Permeability of thermally cracked granite, *Geophys. Res. Lett.*, 19, 869–872.

De la Cruz-Reyna, S. & Reyes-Da´vila, G. A., 2001. A model to describe precursory material-failure phenomena: applications to short-term forecasting at Colima volcano, Mexico, *Bulletin of Volcanology*, 63(5), 297–308.

Denlinger, R., 1990. A model for dome eruptions at Mount St. Helens, Washington based on subcritical crack growth, in *Lava flows and domes*, pp. 70–87, Springer.

Deshpande, V. & Evans, A. G., 2008. Inelastic deformation and energy dissipation in ceramics: A mechanism-based constitutive model, *Journal of the Mechanics and Physics of Solids*, 56, 3077–3100.

Drits, V., Besson, G., & Muller, F., 1995. An improved model for structural transformation of heat-treated aluminous dioctahedral 2:1 layer silicates, *Clays and Clay minerals*, 43(6), 718–731.

Dvorak, J. J. & Dzurisin, D., 1997. Volcano geodesy: The search for magma reservoirs and the formation of eruptive vents, *Reviews of Geophysics*, 35(3), 343–384.

Fortin, J., Schubnel, A., & Gue´guen, Y., 2005. Elastic wave velocities and permeability evolution during compaction of Bleurswiller sandstone, *International Journal of Rock Mechanics and Mining Sciences*, 42(7), 873–889.

Fortin, J., Stanchits, S., Dresen, G., & Gue´guen, Y., 2006. Acoustic emission and velocities associated with the formation of compaction bands in sandstone, *Journal of Geophysical Research: Solid Earth*, 111(B10).

Fortin, J., Gue´guen, Y., & Schubnel, A., 2007. Effects of pore collapse and grain crushing on ultrasonic velocities and Vp/Vs, *Journal of Geophysical Research: Solid Earth*, 112(B8).

Fortin, J., Stanchits, S., Dresen, G., & Gueguen, Y., 2009. Acoustic emissions monitoring during in-elastic deformation of porous sandstone: comparison of three modes of deformation, *Pure and Applied Geophysics*, 166(5-7), 823–841.

Fortin, J., Stanchits, S., Vinciguerra, S., & Gue´guen, Y., 2011. Influence of thermal and mechanical cracks on permeability and elastic wave velocities in a basalt from Mt. Etna volcano subjected to elevated pressure, *Tectonophysics*, 503(1), 60–74.

Fredrich, J. T. & Wong, T.-f., 1986. Micromechanics of thermally induced cracking in three crustal rocks, *Journal of Geophysical Research: Solid Earth*, 91(B12), 12743–12764.

Fredrich, J. T., Evans, B., & Wong, T.-F., 1989. Micromechanics of the brittle to plastic transition in Carrara marble, *Journal of Geophysical Research: Solid Earth*, 94(B4), 4129–4145.

Frolova, J., Ladygin, V., Rychagov, S., & Zukhubaya, D., 2014. Effects of hydrothermal alterations on physical and mechanical properties of rocks in the Kuril–Kamchatka island arc, *Engineering Geology*, 183, 80–95.

Geoffroy, L. & Dorbath, C., 2008. Deep downward fluid percolation driven by localized crust dilatation in iceland, *Geophysical research letters*, 35(17).

Glover, P., Baud, P., Darot, M., Meredith, P., Boon, S., LeRavalec, M., Zoussi, S., & Reuschle, T., 1995. α/β phase transition in quartz monitored using acoustic emissions, *Geophysical Journal International*,120(3), 775–782.

Grechka, V. & Kachanov, M., 2006. Effective elasticity of fractured rocks: A snapshot of the work in progress, *Geophysics*, 71, W45–W58.

Greene-Kelly, R., 1953. Irreversible dehydration in montmorillonite, *Clay Minerals*, 2, 52–56.

Grim, R. E. & Rowland, R. A., 1944. Differential thermal analysis of clays and shales, a control and prospecting method, *Journal of the American Ceramic Society*, 27(3), 65–76.

Gudmundsson, A., 2009. Toughness and failure of volcanic edifices, *Tectonophysics*, 471(1-2), 27–35.

Heap, M., Baud, P., Meredith, P., Vinciguerra, S., Bell, A., & Main, I., 2011. Brittle creep in basalt and its application to time-dependent volcano deformation, *Earth and Planetary Science Letters*, 307(1-2), 71–82.

Heap, M., Lavalle´e, Y., Petrakova, L., Baud, P., Reuschle, T., Varley, N., & Dingwell, D. B., 2014. Microstructural controls on the physical and mechanical properties of edifice-forming andesites at Volca´n de Colima, Mexico, *Journal of Geophysical Research: Solid Earth*, 119(4), 2925–2963.

Heap, M., Farquharson, J., Baud, P., Lavalle´e, Y., & Reuschle´, T., 2015. Fracture and compaction of andesite in a volcanic edifice, *Bulletin of volcanology*, 77(6), 55.

Heap, M. J., Vinciguerra, S., & Meredith, P., 2009. The evolution of elastic moduli with increasing crack damage during cyclic stressing of a basalt from Mt. Etna volcano, *Tectonophysics*, 471(1-2), 153–160.

Heap, M. J., Kennedy, B. M., Farquharson, J. I., Ashworth, J., Mayer, K., Letham-Brake, M., Reuschle´, T., Gilg, H. A., Scheu, B., Lavalle´e, Y., et al., 2017. A multidisciplinary approach to quantify the permeability of the Whakaari/White Island volcanic hydrothermal system (Taupo Volcanic Zone, New Zealand), *Journal of Volcanology and Geothermal Research*, 332, 88–108.

Hyndman, R. D., Yamano, M., & Oleskevich, D. A., 1997. The seismogenic zone of subduction thrust faults, *Island Arc*, 6(3), 244–260.

Keshavarz, M., Pellet, F., & Loret, B., 2010. Damage and changes in mechanical properties of a gabbro thermally loaded up to 1,000 C, P*ure and Applied Geophysics*, 167(12), 1511–1523.

Le´vy, L., Gibert, B., Sigmundsson, F., Flo´venz, O. G., Hersir, G. P., Briole, P., & Pezard, P. A., 2018. The role of smectites in the electrical conductivity of active hydrothermal systems: electrical properties of core samples from Krafla volcano, Iceland, *Geophysical Journal International*, 215(3), 1558–1582.

Mackenzie, R., 1957. The montmorillonite differential thermal curve. i.-general variability in the dehydroxylation region, *Bulletin du Groupe francais des argiles*, 9(4), 7–15.

Main, I. G., 1999. Applicability of time-to-failure analysis to accelerated strain before earthquakes and volcanic eruptions, *Geophysical Journal International*, 139(3), F1–F6.

Malek, Z., Balek, V., Garfinkel-Shweky, D., & Yariv, S., 1997. The study of the dehydration and dehydroxylation of smectites by emanation thermal analysis, *Journal of thermal*

analysis, 48(1), 83–92.

Mallet, C., Fortin, J., Gue´guen, Y., & Bouyer, F., 2013. Effective elastic properties of cracked solids: An experimental investigation., *International journal of fracture*, 182(2).

Mallet, C., Fortin, J., Guguen, Y., & Bouyer, F., 2015. Brittle creep and subcritical crack propagation in glass submitted to triaxial conditions, *Journal of Geophysical Research: Solid Earth*, 120(2), 879–893.

Massonnet, D. & Sigmundsson, F., 2000. Remote sensing of volcano deformation by radar interferometry from various satellites, *Remote sensing of active volcanism*, pp. 207–221.

Mavko, G., Mukerji, T., & Godfrey, N., 1995. Predicting stress-induced velocity anisotropy in rocks, *Geophysics*, 60(4), 1081–1087.

McTigue, D., 1987. Elastic stress and deformation near a finite spherical magma body: resolution of the point source paradox, *Journal of Geophysical Research: Solid Earth*, 92(B12), 12931–12940.

Meier, L. & Kahr, G., 1999. Determination of the cation exchange capacity (cec) of clay minerals using the complexes of copper(ii) ion with triethylenetetramine and tetraethylenepentamine, *Clays and Clay Minerals*, 47(3), 386–388.

Meller, C. & Kohl, T., 2014. The significance of hydrothermal alteration zones for the mechanical behavior of a geothermal reservoir, *Geothermal Energy*, 2(1), 12.

Meunier, A., 2005. Clays, Springer Science & Business Media.

Mogi, K., 1958. Relations between the eruptions of various volcanoes and the deformations of the ground surfaces around them., *Earthquake research institute*, 36, 99–134.

Moore, D. E. & Lockner, D. A., 2007. Friction of the smectite clay montmorillonite, *The seismogenic zone of subduction thrust faults*, pp. 317–345.

Nara, Y. & Kaneko, K., 2005. Study of subcritical crack growth in andesite using the double torsion test, *International Journal of Rock Mechanics and Mining Sciences*, 42(4), 521–530.

Nara, Y., Morimoto, K., Hiroyoshi, N., Yoneda, T., Kaneko, K., & Benson, P. M., 2012. Influence of relative humidity on fracture toughness of rock: implications for subcritical crack growth, *International Journal of Solids and Structures*, 49(18), 2471–2481.

Nara, Y., Yamanaka, H., Oe, Y., & Kaneko, K., 2013. Influence of temperature and water on subcritical crack growth parameters and long-term strength for igneous rocks, *Geophysical*

Journal International, 193(1), 47–60.

Navelot, V., Ge´raud, Y., Favier, A., Diraison, M., Corsini, M., Lardeaux, J.-M., Verati, C., de Le´pinay, J. M., Legendre, L., & Beauchamps, G., 2018. Petrophysical properties of volcanic rocks and impacts of hydrothermal alteration in the guadeloupe archipelago (west indies), *Journal of Volcanology and Geothermal Research*, 360, 1–21.

Nemat-Nasser, S. & Horii, H., 1982. Compression-induced nonplanar crack extension with application to splitting, exfoliation, and rock burst, *Journal of Geophysical Research: Solid Earth*, 87(B8), 6805–6821.

Nicolas, A., Girault, F., Schubnel, A., Pili, E´., Passele`gue, F., Fortin, J., & Deldicque, D., 2014. Radon emanation from brittle fracturing in granites under upper crustal conditions, *Geophysical Research Letters*, 41(15), 5436–5443.

Nicolas, A., Fortin, J., Regnet, J., Dimanov, A., & Gue´guen, Y., 2016. Brittle and semi-brittle behaviours of a carbonate rock: influence of water and temperature, *Geophysical Journal International*, 206(1), 438–456.

Nicolas, A., Fortin, J., & Gue´guen, Y., 2017a. Micromechanical constitutive model for low-temperature constant strain rate deformation of limestones in the brittle and semi-brittle regime, *Geophysical Journal International*, 211(1), 300–321.

Nicolas, A., Fortin, J., Regnet, J., Verberne, B., Plu¨mper, O., Dimanov, A., Spiers, C., & Gue´guen, Y., 2017b. Brittle and semi-brittle creep of tavel limestone deformed at room temperature., *Journal of Geophysical Research: Solid Earth*, 122(6): 4436-4459.

Ohnaka, M., 1975. Frictional characteristics of typical rocks, *Journal of Physics of the Earth*, 23(1),87–112.

Ougier-Simonin, A., Fortin, J., Gue´guen, Y., Schubnel, A., & Bouyer, F., 2011. Cracks in glass under triaxial conditions, *International Journal of Engineering Science*, 49(1), 105–121.

Pagli, C., Sigmundsson, F., Arnado´ttir, T., Einarsson, P., & Sturkell, E., 2006. Deflation of the Askja volcanic system: constraints on the deformation source from combined inversion of satellite radar interferograms and GPS measurements, *Journal of Volcanology and Geothermal Research*, 152(1-2), 97–108.

Passele`gue, F. X., Fabbri, O., Dubois, M., & Ventalon, S., 2014. Fluid overpressure along an Oligocene out-of-sequence thrust in the Shimanto Belt, SW Japan, *Journal of Asian Earth Sciences*, 86, 12–24.

Pedersen, R. & Sigmundsson, F., 2004. InSAR based sill model links spatially offset areas of deformation and seismicity for the 1994 unrest episode at Eyjafjallajo¨kull volcano, Iceland, *Geophysical Research Letters*, 31(14).

Perol, T. & Bhat, H. S., 2016. Micromechanics-based permeability evolution in brittle materials at high strain rates, *Pure and Applied Geophysics*, 173(8), 2857–2868.

Pola, A., Crosta, G., Fusi, N., Barberini, V., & Norini, G., 2012. Influence of alteration on physical properties of volcanic rocks, *Tectonophysics*, 566, 67–86.

Ratdomopurbo, A. & Poupinet, G., 1995. Monitoring a temporal change of seismic velocity in a volcano: Application to the 1992 eruption of Mt. Merapi (Indonesia), *Geophysical research letters*, 22(7), 775–778.

Reyes, A. G., 1990. Petrology of philippine geothermal systems and the application of alteration mineralogy to their assessment, *Journal of Volcanology and Geothermal Research*, 43(1-4), 279–309.

Rimsaite, J., 1975. Natural alteration of mica and reactions between released ions in mineral deposits, *Clays and clay minerals*, 23(3), 247–55.

Russell, J. & Farmer, V., 1964. Infra-red spectroscopic study of the dehydration of montmorillonite and saponite, *Clay Minerals Bulletin*, 5(32), 443–464.

Saffer, D. M., Frye, K. M., Marone, C., & Mair, K., 2001. Laboratory results indicating complex and potentially unstable frictional behavior of smectite clay, *Geophysical Research Letters*, 28(12), 2297–2300.

Sayers, C. M. & Kachanov, M., 1995. Microcrack-induced elastic wave anisotropy of brittle rocks, *Journal of Geophysical Research: Solid Earth*, 100(B3), 4149–4156.

Siratovich, P., Heap, M., Villeneuve, M., Cole, J., Kennedy, B., Davidson, J., & Reuschle´, T., 2016. Mechanical behaviour of the Rotokawa Andesites (New Zealand): Insight into permeability evolution and stress-induced behaviour in an actively utilised geothermal reservoir, *Geothermics*, 64, 163–179.

Siratovich, P. A., Heap, M. J., Villenueve, M. C., Cole, J. W., & Reuschle´, T., 2014. Physical property relationships of the Rotokawa Andesite, a significant geothermal reservoir rock in the Taupo Volcanic Zone, New Zealand, *Geothermal Energy*, 2(1), 10.

Skjerlie, K. P. & Johnston, A. D., 1992. Vapor-absent melting at 10 kbar of a biotite-and amphibole-bearing tonalitic gneiss: implications for the generation of a-type granites,

Geology, 20(3), 263–266.

Stanchits, S., Vinciguerra, S., & Dresen, G., 2006. Ultrasonic velocities, acoustic emission characteristics and crack damage of basalt and granite, *Pure and Applied Geophysics*, 163(5-6), 975–994.

Tada, H., Paris, P. C., & Irwin, G. R., 2000. The Stress Analysis of Cracks Handbook. The American Society of Mechanical Engineers.

Taut, T., Kleeberg, R., & Bergmann, J., 1998. Seifert software: The new seifert rietveld program bgmn and its application to quantitative phase analysis, *Materials Structure*, 5(1), 57–66.

Tutluoglu, L. & Keles, C., 2011. Mode I fracture toughness determination with straight notched disk bending method, *International Journal of Rock Mechanics and Mining Sciences*, 48(8), 1248–1261.

Vajdova, V., Baud, P., & Wong, T.-F., 2004. Compaction, dilatancy, and failure in porous carbonate rocks, *Journal of Geophysical Research: Solid Earth*, 109(B5).

Vinciguerra, S., Trovato, C., Meredith, P., & Benson, P., 2005. Relating seismic velocities, thermal cracking and permeability in mt. etna and iceland basalts, *International Journal of Rock Mechanics and Mining Sciences*, 42(7-8), 900–910.

Walsh, J. B., 1965. The effect of cracks on the compressibility of rock, *Journal of Geophysical Research*, 70(2), 381–389.

Walwer, D., Calais, E., & Ghil, M., 2016. Data-adaptive detection of transient deformation in geodetic networks, *Journal of Geophysical Research: Solid Earth*, 121(3), 2129–2152.

Wang, X.-Q., Schubnel, A., Fortin, J., David, E., Gue´guen, Y., & Ge, H.-K., 2012. High Vp/Vs ratio: Saturated cracks or anisotropy effects?, *Geophysical Research Letters*, 39(11).

Wang, X.-Q., Schubnel, A., Fortin, J., Gue´guen, Y., & Ge, H.-K., 2013. Physical properties and brittle strength of thermally cracked granite under confinement, *Journal of Geophysical Research: Solid Earth*, 118(12), 6099–6112.

Wong, T.-f., David, C., & Zhu, W., 1997. The transition from brittle faulting to cataclastic flow in porous sandstones: Mechanical deformation, *Journal of Geophysical Research: Solid Earth*, 102(B2), 3009–3025.

Wyering, L., Villeneuve, M., Wallis, I., Siratovich, P., Kennedy, B., Gravley, D., & Cant, J., 2014. Mechanical and physical properties of hydrothermally altered rocks, Taupo Volcanic Zone, New Zealand, *Journal of Volcanology and Geothermal Research*, 288, 76–93.

Yamaguchi, A., Sakaguchi, A., Sakamoto, T., Iijima, K., Kameda, J., Kimura, G., Ujiie, K., Chester, F. M., Fabbri, O., Goldsby, D., Tsutsumi, A., Li, C.-F., & Curewitz, D., 2011. Progressive illitization in fault gouge caused by seismic slip propagation along a megasplay fault in the Nankai Trough, *Geology*, 39(11), 995–998.

Zhan, W. & Guggenheim, S., 1995. The dehydroxylation of chlorite and the formation of topotactic product phases, *Clays and clay minerals*, 43(5), 622–629.

Zhu, W., Baud, P., & Wong, T.-f., 2010. Micromechanics of cataclastic pore collapse in limestone, *Journal of Geophysical Research: Solid Earth*, 115(B4).

Zimbelman, D., Rye, R. O., & Breit, G., 2005. Origin of secondary sulfate minerals on active andesitic stratovolcanoes, *Chemical Geology*, 215(1-4), 37–60.

Chapter IV References

Acosta, M., Passelègue, F. X., Schubnel, A., & Violay, M. (2018). Dynamic weakening during earthquakes controlled by fluid thermodynamics. *Nature communications*, *9*(1), 3074.

Ashby, M. F., & Sammis, C. G. (1990). The damage mechanics of brittle solids in compression. *Pure and Applied Geophysics*, *133*(3), 489-521.

Blanpied, M. L., Lockner, D. A., & Byerlee, J. D. (1995). Frictional slip of granite at hydrothermal conditions. *Journal of Geophysical Research: Solid Earth*, *100*(B7), 13045-13064.

Brantut, N., Sulem, J., & Schubnel, A. (2011). Effect of dehydration reactions on earthquake nucleation: Stable sliding, slow transients, and unstable slip. *Journal of Geophysical Research: Solid Earth*, *116*(B5).

Dienes, J. K. (1982, January). Permeability, percolation and statistical crack mechanics. In *The 23rd US Symposium on Rock Mechanics (USRMS)*. American Rock Mechanics Association.

Darot, M., & Gueguen, Y. (1986). Slow crack growth in minerals and rocks: Theory and experiments. *pure and applied geophysics*, *124*(4-5), 677-692.

Ellsworth, W. L. (2013). Injection-induced earthquakes. *Science*, *341*(6142), 1225942.

Elsworth, D., Spiers, C. J., & Niemeijer, A. R. (2016). Understanding induced seismicity. *Science*, *354*(6318), 1380-1381.

Frohlich, C. (2012). Two-year survey comparing earthquake activity and injection-well

locations in the Barnett Shale, Texas. *Proceedings of the National Academy of Sciences*, *109*(35), 13934-13938.

Frohlich, C., & Brunt, M. (2013). Two-year survey of earthquakes and injection/production wells in the Eagle Ford Shale, Texas, prior to the Mw4. 8 20 October 2011 earthquake. *Earth and Planetary Science Letters*, *379*, 56-63.

Frohlich, C., Ellsworth, W., Brown, W. A., Brunt, M., Luetgert, J., MacDonald, T., & Walter, S. (2014). The 17 May 2012 M4. 8 earthquake near Timpson, East Texas: An event possibly triggered by fluid injection. *Journal of Geophysical Research: Solid Earth*, *119*(1), 581-593.

Fletcher, J. B., & Sykes, L. R. (1977). Earthquakes related to hydraulic mining and natural seismic activity in western New York State. *Journal of Geophysical Research*, *82*(26), 3767-3780.

Faoro, I., Vinciguerra, S., Marone, C., Elsworth, D., & Schubnel, A. (2013). Linking permeability to crack density evolution in thermally stressed rocks under cyclic loading. *Geophysical Research Letters*, *40*(11), 2590-2595.

Fortin, J., Stanchits, S., Vinciguerra, S., & Guéguen, Y. (2011). Influence of thermal and mechanical cracks on permeability and elastic wave velocities in a basalt from Mt. Etna volcano subjected to elevated pressure. *Tectonophysics*, *503*(1-2), 60-74.

Fortin, J., Guéguen, Y., & Schubnel, A. (2007). Effects of pore collapse and grain crushing on ultrasonic velocities and Vp/Vs. *Journal of Geophysical Research: Solid Earth*, *112*(B8).

Giardini, D. (2009). Geothermal quake risks must be faced. *Nature*, *462*(7275), 848

Guéguen, Y., & Schubnel, A. (2003). Elastic wave velocities and permeability of cracked rocks. *Tectonophysics*, *370*(1-4), 163-176.

Gueguen, Y., & Dienes, J. (1989). Transport properties of rocks from statistics and percolation. *Mathematical geology*, *21*(1), 1-13.

Gueguen, Y., Reuschlé, T., & Darot, M. (1990). Single-crack behaviour and crack statistics. In *Deformation Processes in Minerals, Ceramics and Rocks* (pp. 48-71). Springer, Dordrecht.

Horton, S. (2012). Disposal of hydrofracking waste fluid by injection into subsurface aquifers triggers earthquake swarm in central Arkansas with potential for damaging earthquake. *Seismological Research Letters*, *83*(2), 250-260.

Heap, M. J., Lavallée, Y., Petrakova, L., Baud, P., Reuschle, T., Varley, N. R., & Dingwell, D. B. (2014). Microstructural controls on the physical and mechanical properties of edifice-forming andesites at Volcán de Colima, Mexico. *Journal of Geophysical Research: Solid Earth*, *119*(4), 2925-2963.

Heap, M. J., Baud, P., Meredith, P. G., Vinciguerra, S., Bell, A. F., & Main, I. G. (2011). Brittle creep in basalt and its application to time-dependent volcano deformation. *Earth and Planetary Science Letters*, *307*(1-2), 71-82.

Justinic, A. H., Stump, B., Hayward, C., & Frohlich, C. (2013). Analysis of the Cleburne, Texas, earthquake sequence from June 2009 to June 2010. *Bulletin of the Seismological Society of America*, *103*(6), 3083-3093.

Keranen, K. M., Savage, H. M., Abers, G. A., & Cochran, E. S. (2013). Potentially induced earthquakes in Oklahoma, USA: Links between wastewater injection and the 2011 Mw 5.7 earthquake sequence. *Geology*, *41*(6), 699-702.

Kranz, R. L., Saltzman, J. S., & Blacic, J. D. (1990, October). Hydraulic diffusivity measurements on laboratory rock samples using an oscillating pore pressure method. In *International Journal of Rock Mechanics and Mining Sciences & Geomechanics Abstracts* (Vol. 27, No. 5, pp. 345-352). Pergamon.

Kachanov, M. (1993). Elastic solids with many cracks and related problems. In *Advances in applied mechanics* (Vol. 30, pp. 259-445). Elsevier.

Kachanov, M. (1993). Elastic solids with many cracks and related problems. In *Advances in applied mechanics* (Vol. 30, pp. 259-445). Elsevier.

Lockner, D., & Byerlee, J. D. (1977). Hydrofracture in Weber sandstone at high confining pressure and differential stress. *Journal of Geophysical research*, *82*(14), 2018-2026.

Lawn, B., & Wilshaw, R. (1975). Indentation fracture: principles and applications. *Journal of materials science*, *10*(6), 1049-1081.

McGarr, A. (2014). Maximum magnitude earthquakes induced by fluid injection. *Journal of Geophysical Research: solid earth*, *119*(2), 1008-1019.

McGarr, A., & Barbour, A. J. (2017). Wastewater disposal and the earthquake sequences during 2016 near Fairview, Pawnee, and Cushing, Oklahoma. *Geophysical Research Letters*, *44*(18), 9330-9336.

McClure, M. W., & Horne, R. N. (2014). An investigation of stimulation mechanisms in

Enhanced Geothermal Systems. *International Journal of Rock Mechanics and Mining Sciences*, *72*, 242-260.

Masuda, K., Nishizawa, O., Kusunose, K., Satoh, T., Takahashi, M., & Kranz, R. L. (1990). Positive feedback fracture process induced by nonuniform high-pressure water flow in dilatant granite. *Journal of Geophysical Research: Solid Earth*, *95*(B13), 21583-21592.

Mori, T., & Tanaka, K. (1973). Average stress in matrix and average elastic energy of materials with misfitting inclusions. *Acta metallurgica*, *21*(5), 571-574.

Mallet, C., Fortin, J., Guéguen, Y., & Bouyer, F. (2014). Evolution of the crack network in glass samples submitted to brittle creep conditions. *International Journal of Fracture*, *190*(1-2), 111-124.

Nur, A., & Booker, J. R. (1972). Aftershocks caused by pore fluid flow?. *Science*, *175*(4024), 885-887.

Nicolas, A., Fortin, J., Regnet, J. B., Dimanov, A., & Guéguen, Y. (2016). Brittle and semi-brittle behaviours of a carbonate rock: influence of water and temperature. *Geophysical Journal International*, *206*(1), 438-456.

Ougier-Simonin, A., Fortin, J., Guéguen, Y., Schubnel, A., & Bouyer, F. (2011). Cracks in glass under triaxial conditions. *International Journal of Engineering Science*, *49*(1), 105-121.

Pereira, J. M., & Arson, C. (2013). Retention and permeability properties of damaged porous rocks. *Computers and Geotechnics*, *48*, 272-282.

Pola, A., Crosta, G. B., Fusi, N., & Castellanza, R. (2014). General characterization of the mechanical behaviour of different volcanic rocks with respect to alteration. *Engineering Geology*, *169*, 1-13.

Shirzaei, M., Ellsworth, W. L., Tiampo, K. F., González, P. J., & Manga, M. (2016). Surface uplift and time-dependent seismic hazard due to fluid injection in eastern Texas. *Science*, *353*(6306), 1416-1419.

Segall, P., & Lu, S. (2015). Injection-induced seismicity: Poroelastic and earthquake nucleation effects. *Journal of Geophysical Research: Solid Earth*, *120*(7), 5082-5103.

Stanchits, S., Mayr, S., Shapiro, S., & Dresen, G. (2011). Fracturing of porous rock induced by fluid injection. *Tectonophysics*, *503*(1-2), 129-145.

Schubnel, A., Thompson, B. D., Fortin, J., Guéguen, Y., & Young, R. P. (2007). Fluid-induced rupture experiment on Fontainebleau sandstone: Premonitory activity, rupture propagation,

and aftershocks. *Geophysical research letters*, *34*(19).

Sayers, C. M., & Kachanov, M. (1995). Microcrack-induced elastic wave anisotropy of brittle rocks. *Journal of Geophysical Research: Solid Earth*, *100*(B3), 4149-4156.

Schubnel, A., & Guéguen, Y. (2003). Dispersion and anisotropy of elastic waves in cracked rocks. *Journal of Geophysical Research: Solid Earth*, *108*(B2).

Shafiro, B., & Kachanov, M. (1997). Materials with fluid-filled pores of various shapes: effective elastic properties and fluid pressure polarization. *International Journal of Solids and Structures*, *34*(27), 3517-3540.

Talwani, P., & Acree, S. (1985). Pore pressure diffusion and the mechanism of reservoir-induced seismicity. In *Earthquake Prediction* (pp. 947-965). Birkhäuser, Basel.

Thompson, B. D., Young, R. P., & Lockner, D. A. (2006). Fracture in Westerly granite under AE feedback and constant strain rate loading: nucleation, quasi-static propagation, and the transition to unstable fracture propagation. *Pure and Applied Geophysics*, *163*(5-6), 995-1019.

Wassing, B. B. T., Van Wees, J. D., & Fokker, P. A. (2014). Coupled continuum modeling of fracture reactivation and induced seismicity during enhanced geothermal operations. *Geothermics*, *52*, 153-164.

Wu, L., Cui, C., Geng, N., & Wang, J. (2000). Remote sensing rock mechanics (RSRM) and associated experimental studies. *International Journal of Rock Mechanics and Mining Sciences*, *37*(6), 879-888.

Wong, T. F., Ko, S. C., & Olgaard, D. L. (1997). Generation and maintenance of pore pressure excess in a dehydrating system 2. Theoretical analysis. *Journal of Geophysical Research: Solid Earth*, *102*(B1), 841-852.

Walsh, J. B. (1965). The effect of cracks on the compressibility of rock. *Journal of Geophysical Research*, *70*(2), 381-389.

Vinciguerra, S., Meredith, P. G., & Hazzard, J. (2004). Experimental and modeling study of fluid pressure-driven fractures in Darley Dale sandstone. *Geophysical research letters*, *31*(9).

Zoback, M. D., & Harjes, H. P. (1997). Injection-induced earthquakes and crustal stress at 9 km depth at the KTB deep drilling site, Germany. *Journal of Geophysical Research: Solid Earth*, *102*(B8), 18477-18491.

Zhu, W., Baud, P., Vinciguerra, S., & Wong, T. F. (2016). Micromechanics of brittle faulting and cataclastic flow in Mount Etna basalt. *Journal of Geophysical Research: Solid Earth*, *121*(6), 4268-4289.

Chapter V References

Baisch, S., Vörös, R., Rothert, E., Stang, H., Jung, R. and Schellschmidt, R., 2010. A numerical model for fluid injection induced seismicity at Soultz-sous-Forêts. *International Journal of Rock Mechanics and Mining Sciences*, *47*(3), pp.405-413.

Blöcher, G., Reinsch, T., Hassanzadegan, A., Milsch, H. and Zimmermann, G., 2014. Direct and indirect laboratory measurements of poroelastic properties of two consolidated sandstones. *International Journal of Rock Mechanics and Mining Sciences*, *67*, pp.191-201.

Bremer, K., Lewis, E., Leen, G., Moss, B., Lochmann, S., Mueller, I., Reinsch, T. and Schroetter, J., 2010, November. Fibre optic pressure and temperature sensor for geothermal wells. In *Sensors, 2010 IEEE* (pp. 538-541). IEEE.

Brodsky, E.E., Roeloffs, E., Woodcock, D., Gall, I. and Manga, M., 2003. A mechanism for sustained groundwater pressure changes induced by distant earthquakes. *Journal of Geophysical Research: Solid Earth*, *108*(B8).

Browning, J., Meredith, P. and Gudmundsson, A., 2016. Cooling-dominated cracking in thermally stressed volcanic rocks. *Geophysical Research Letters*, *43*(16), pp.8417-8425.

Cappa, F. and Rutqvist, J., 2011. Impact of CO2 geological sequestration on the nucleation of earthquakes. *Geophysical Research Letters*, *38*(17).

Chander, R., 1997. On categorising induced and natural tectonic earthquakes near new reservoirs. *Engineering Geology*, *46*(2), pp.81-92.

Clifton, A.E., Pagli, C., Jónsdóttir, J.F., Eythorsdóttir, K. and Vogfjörð, K., 2003. Surface effects of triggered fault slip on Reykjanes Peninsula, SW Iceland. *Tectonophysics*, *369*(3-4), pp.145-154.

Darcy, H., 1856. *Les fontaines publiques de la ville de Dijon: exposition et application...* Victor Dalmont.

Davies, R., Foulger, G., Bindley, A. and Styles, P., 2013. Induced seismicity and hydraulic fracturing for the recovery of hydrocarbons. *Marine and petroleum geology*, *45*, pp.171-

185.

Deichmann, N. and Giardini, D., 2009. Earthquakes induced by the stimulation of an enhanced geothermal system below Basel (Switzerland). *Seismological Research Letters*, *80*(5), pp.784-798.

Do Nascimento, A.F., Lunn, R.J. and Cowie, P.A., 2005. Numerical modelling of pore-pressure diffusion in a reservoir-induced seismicity site in northeast Brazil. *Geophysical Journal International*, *160*(1), pp.249-262.

El Hariri, M., Abercrombie, R.E., Rowe, C.A. and Do Nascimento, A.F., 2010. The role of fluids in triggering earthquakes: observations from reservoir induced seismicity in Brazil. *Geophysical Journal International*, *181*(3), pp.1566-1574.

Fredrich, J.T. and Wong, T.F., 1986. Micromechanics of thermally induced cracking in three crustal rocks. *Journal of Geophysical Research: Solid Earth*, *91*(B12), pp.12743-12764.

Frohlich, C., Ellsworth, W., Brown, W.A., Brunt, M., Luetgert, J., MacDonald, T. and Walter, S., 2014. The 17 May 2012 M4.8 earthquake near Timpson, East Texas: An event possibly triggered by fluid injection. *Journal of Geophysical Research: Solid Earth*, *119*(1), pp.581-593.

Giardini, D., 2009. Geothermal quake risks must be faced. *Nature*, *462*(7275), p.848.

Hainzl, S., Kraft, T., Wassermann, J., Igel, H. and Schmedes, E., 2006. Evidence for rainfall-triggered earthquake activity. *Geophysical Research Letters*, *33*(19).

Horton, S., 2012. Disposal of hydrofracking waste fluid by injection into subsurface aquifers triggers earthquake swarm in central Arkansas with potential for damaging earthquake. *Seismological Research Letters*, *83*(2), pp.250-260.

Hummel, N. and Müller, T.M., 2009. Microseismic signatures of non-linear pore-fluid pressure diffusion. *Geophysical Journal International*, *179*(3), pp.1558-1565.

Keranen, K.M., Weingarten, M., Abers, G.A., Bekins, B.A. and Ge, S., 2014. Sharp increase in central Oklahoma seismicity since 2008 induced by massive wastewater injection. *Science*, *345*(6195), pp.448-451.

Klute, A. and Dirksen, C., 1986. Hydraulic conductivity and diffusivity: Laboratory methods. *Methods of soil analysis: part 1—physical and mineralogical methods*, (methodsofsoilan1), pp.687-734.

Lee, M.K. and Wolf, L.W., 1998. Analysis of fluid pressure propagation in heterogeneous rocks:

Implications for hydrologically-induced earthquakes. *Geophysical Research Letters*, *25*(13), pp.2329-2332.

Mazzoldi, A., Rinaldi, A.P., Borgia, A. and Rutqvist, J., 2012. Induced seismicity within geological carbon sequestration projects: maximum earthquake magnitude and leakage potential from undetected faults. *International Journal of Greenhouse Gas Control*, *10*, pp.434-442.

Pimienta, L., Fortin, J., Borgomano, J.V. and Guéguen, Y., 2016. Dispersions and attenuations in a fully saturated sandstone: Experimental evidence for fluid flows at different scales. *The Leading Edge*, *35*(6), pp.495-501.

Prejean, S.G., Hill, D.P., Brodsky, E.E., Hough, S.E., Johnston, M.J.S., Malone, S.D., Oppenheimer, D.H., Pitt, A.M. and Richards-Dinger, K.B., 2004. Remotely triggered seismicity on the United States west coast following the M w 7.9 Denali fault earthquake. *Bulletin of the Seismological Society of America*, *94*(6B), pp.S348-S359.

Reinsch, T., Blöcher, G., Milsch, H., Bremer, K., Lewis, E., Leen, G. and Lochmann, S., 2012. A fibre optic sensor for the in situ determination of rock physical properties. *arXiv preprint arXiv:1208.1233*.

Rutqvist, J., Rinaldi, A.P., Cappa, F. and Moridis, G.J., 2013. Modeling of fault reactivation and induced seismicity during hydraulic fracturing of shale-gas reservoirs. *Journal of Petroleum Science and Engineering*, *107*, pp.31-44.

Saar, M.O. and Manga, M., 2003. Seismicity induced by seasonal groundwater recharge at Mt. Hood, Oregon. *Earth and Planetary Science Letters*, *214*(3-4), pp.605-618.

Shapiro, S.A., Huenges, E. and Borm, G., 1997. Estimating the crust permeability from fluid-injection-induced seismic emission at the KTB site. *Geophysical Journal International*, *131*(2), pp.F15-F18.

Shapiro, S.A., Patzig, R., Rothert, E. and Rindschwentner, J., 2003. Triggering of seismicity by pore-pressure perturbations: Permeability-related signatures of the phenomenon. In *Thermo-Hydro-Mechanical Coupling in Fractured Rock* (pp. 1051-1066). Birkhäuser, Basel.

Simpson, D.W. and Narasimhan, T.N., 1990. Inhomogeneities in rock properties and their influence on reservoir induced seismicity. *Gerlands Beitr. Geophys*, *99*, pp.205-219.

Talwani, P., 1997. On the nature of reservoir-induced seismicity. *Pure and Applied Geophysics*, *150*(3-4), pp.473-492.

Yilmaz, Ö., Nolen-Hoeksema, R.C. and Nur, A., 1994. Pore pressure profiles in fractured and compliant rocks 1. *Geophysical prospecting*, *42*(6), pp.693-714.

Zoback, M.D. and Gorelick, S.M., 2012. Earthquake triggering and large-scale geologic storage of carbon dioxide. *Proceedings of the National Academy of Sciences*, *109*(26), pp.10164-10168.

RÉSUMÉ

Comprendre et connaitre les propriétés physiques et le comportement mécanique de l'andésite est important pour des applications industrielles comme la géothermie ou le stockage de CO_2 mais aussi pour comprendre différents processus naturels. Tout d'abord, les effets de la fissuration thermique sur les propriétés physiques et les processus de rupture de l'andésite ont été étudiés via des expériences triaxiales à taux de déformation constant et à température ambiante. Deuxièmement, nous avons effectué des recherches sur les effets de l'altération sur le comportement physique et la minéralogie. Enfin, une série d'expériences a été réalisée afin d'étudier l'effet de la variation de la pression du fluide i) sur le comportement mécanique des échantillons d'andésite et ii) sur les activités d'émissions acoustiques.

MOTS CLÉS

Fissure thermique; injection de fluide; propriété physique; propriété mécanique

ABSTRACT

The physical properties and mechanical behavior of andesite are of interest in the context of geothermal reservoir, CO2 sequestration and for several natural processes. The effects of thermal crack damage on the physical properties and rupture processes of andesite were investigated under triaxial deformation at room temperature. Secondly we did research on the effect of alteration on physical behavior and mineralogy. At last a series of experiments were performed in order to investigate the effect of fluid pressure variation i) on the mechanical behavior of andesite samples and ii) on acoustic emissions activities

KEYWORDS

Thermal crack; fluid injection; physical property; mechanical property